CALIFORNIA INSTITUTE OF TECHNOLOGY

EARTHQUAKE ENGINEERING RESEARCH LABORATORY

EXPERIMENTAL AND FINITE ELEMENT STUDIES OF A LARGE ARCH DAM

By

Ziyad H. Duron

Report No. EERL 87-02

A Report on Research Supported by Grants from the National Science Foundation

Pasadena, California

1987

This investigation was sponsored by Grant Nos. EAR83-17257 and CES-8619908 from the National Science Foundation under the supervision of J. F. Hall. Any opinions, findings, conclusions or recommendations expressed in this publication are those of the author and do not necessarily reflect the views of the National Science Foundation.

EXPERIMENTAL AND FINITE ELEMENT STUDIES OF A LARGE ARCH DAM

Thesis by

Ziyad H. Duron

In Partial Fulfillment of the Requirements
for the Degree of
Doctor of Philosophy

California Institute of Technology
Pasadena, California

1988

(Submitted September 11, 1987)

ACKNOWLEDGMENTS

I would like to thank my thesis advisor, John Hall, for his valued help and advice during the past four years. His dedication, leadership and sincerity will always be appreciated.

I would also like to thank the many people who had a part in my work here and made my stay so enjoyable. In particular, I wish to thank Mike Dowling for his friendship and companionship.

My thanks also go to SOPS and to the staff of Thomas Laboratory. Sharon Beckenbach, Crista Potter, and Cecilia Lin were simply outstanding in helping me to produce this thesis. A special thanks goes to Raul Relles, Garrett Jeong and Bill Donlon for everything they did for me.

I have truly been blessed to have parents such as mine, who have been so instrumental and involved in my life. No words can express my appreciation and no man could be more fortunate.

Finally, I would like to thank my wife, Suzanne, for without her, my success here would not have been possible. Her dedication and love for me can never be doubted and I hope that I will continue to be worthy of her love.

ABSTRACT

Forced vibration field tests and finite element studies have been conducted on Morrow Point (arch) Dam in order to investigate dynamic dam-water interaction and water compressibility. Design of the data acquisition system incorporates several special features to retrieve both amplitude and phase of the response in a low signal to noise environment. These features contributed to the success of the experimental program which, for the first time, produced field evidence of water compressibility; this effect seems to play a significant role only in the symmetric response of Morrow Point Dam in the frequency range examined. In the accompanying analysis, frequency response curves for measured accelerations and water pressures as well as their resonating shapes are compared to predictions from the current state-of-the-art finite element model for which water compressibility is both included and neglected. Calibration of the numerical model employs the antisymmetric response data since they are only slightly affected by water compressibility, and, after calibration, good agreement to the data is obtained whether or not water compressibility is included. In the effort to reproduce the symmetric response data, on which water compressibility has a significant influence, the calibrated model shows better correlation when water compressibility is included, but the agreement is still inadequate. Similar results occur using data obtained previously by others at a low water level. A successful isolation of the fundamental water resonance from the experimental data shows significantly different features from those of the numerical water model, indicating possible inaccuracy in the assumed geometry and/or boundary conditions for the reservoir. However, the investigation does suggest possible directions in which the numerical model can be improved.

TABLE OF CONTENTS

CHAPTER 1

Introduction

The earthquake design of concrete arch dams is a very important problem, especially since failure of the structure could result in major loss of life. An integral part of any design process is, of course, the analytical technique that is used to obtain design values such as maximum stresses and displacements of the dam under various load conditions. The results of such an analysis can be used by the engineer to evaluate the adequacy of the design of the dam and to make appropriate modifications if needed. If the design is incorrect, or does not meet the required specifications, improvements to the design must be made.

The success of any analysis procedure is ultimately judged on its ability to reproduce or predict observed behavior. While the state-of-the-art has advanced rapidly over the last twenty years, the gathering of experimental data for use in comparison studies has lagged behind. For example, mathematical models for the water domain have progressed from simple lumped added masses [1] to finite element formulations that include water compressibility and a special transmitting boundary for infinite reservoir geometries [2,3,4]. However, no serious comparisons have ever been made between forced vibration field data and results of analyses that include water compressibility [5]. Such a comparison is part of this investigation, which has the overall objective of examining the dynamic dam-water interaction for Morrow Point Dam, a large arch dam in Colorado. Carried out simultaneously with the work reported here have been forced vibration field tests and analyses of Santa Anita Dam, an arch dam in California, where the focus was on dam-foundation interaction. Except for a few features of the experimental technique, the results for Santa Anita Dam are not included here and will be reported in the near future.

A typical mathematical model used in correlation studies with field data employs finite elements for the dam and lumped added masses for the water which are determined from incompressible water behavior. However, the lumped mass approach has been shown to significantly overestimate the added mass effect of the water [6]. Only recently have finite element discretizations of the actual water domains appeared (Emosson arch Dam [7], Techi arch Dam [8], Xiang Hong Dian gravity arch Dam [9], Quan Shui arch Dam [10], and Monticello arch Dam [11]), but they have not included water compressibility except for a few results in [11].

In the majority of correlations with data from forced vibration field tests, measured resonant frequencies and shapes are compared to computed eigenvalues and eigenvectors (or to computed resonating shapes). An additional exercise, which can be very informative, is to compute the forced vibration responses of the dam as functions of excitation frequency for comparison to the measured frequency response functions. Such studies have been conducted on only three dams : Xiang Hong Dian, Quan Shui, and Monticello [11]. Amplitude and phase of the frequency response functions are useful quantities to measure but have been reported only for Kolnbrein arch Dam [12].

Measurements of dynamic water pressure are fundamental to understanding dam-water interaction, but are rarely obtained (Fujiwara gravity Dam [13], Pine Flat gravity Dam [14], Xiang Hong Dian, Quan Shui, and Monticello [11,15]). Only in three of these investigations were serious attempts made to compare the measured pressure profiles at the resonances with computed profiles (Xiang Hong Dian, Quan Shui, and Monticello [11]). Apparently, comparisons have never been made between measured and computed frequency response functions for dynamic water pressure.

Another informative exercise in investigating dam-water interaction is to check a mathematical model against field data obtained at significantly different water depths. Such data is available for Morrow Point arch Dam [16,17], Big Tujunga

Dam [18], Tonoyama arch Dam [19], Yahagi arch Dam [20], Kamishiiba arch Dam [13], Sazanamigawa arch Dam [13], Ambiesta arch Dam [21], Fiastra gravity arch Dam [22], Alpe Gera gravity Dam [23], Kolnbrein, Kops arch Dam [24], Yugoslavia No. 2 arch Dam [25], and Techi, but analyses have been reported only for Big Tujunga, Kolnbrein, Yugoslavia No.2 and Techi. Unfortunately, the more detailed studies mentioned above have been carried out at a single water depth.

It is interesting to note that results from previous investigations have shown no glaring deficiencies in the mathematical models that suggested water compressibility to be a necessary feature that must be included to obtain reasonable correlation with forced vibration data. One must keep in mind that parameters such as concrete modulus, foundation modulus, and damping values are adjusted for best fit, a process that may partially compensate for neglecting water compressiblity, especially if the fit is made at only a single water depth. In any case, the experience with forced vibration field studies seems at odds with the results from analyses using earthquake excitations, which predict strong differences in the computed responses of an arch dam when water compressiblity is included or neglected [2,3]. As a result, there exists considerable disagreement over the importance of water compressibility in the dynamic response of concrete dams.

In order to further investigate the role of water compressibility under forced vibration excitations, detailed field tests and finite element analyses have been carried out on Morrow Point Dam, which was also the subject of the analyses in [2,3]. This dam is a relatively thin arch dam which means that dam-water interaction is significant, and the resonant frequencies of the dam and water are such that water compressibility would be expected to play a noticeable role in the dam response. It should be stated that water compressibility may be somewhat more important for Morrow Point Dam than for an "average" concrete dam, which may partially explain the discrepancies between field correlation studies and the analysis results

of [2,3]. Features of the present investigation include the following.

1. Water is modeled by the finite element method with compressibility included and a transmitting boundary to represent an infinite reservoir.
2. Measured and computed results are compared for resonant frequencies, resonating shapes of dam acceleration and dynamic water pressure, and frequency response functions for dam acceleration and dynamic water pressure, including both amplitude and phase.
3. The present field tests were carried out with a nearly full reservoir. The investigation is extended to include forced vibration data obtained previously [16] at a much lower water level.

Chapter 2 details the experimental apparatus used to conduct the forced vibration tests at Morrow Point and Santa Anita Dams. The vibration generators and the transducers used to measure acceleration responses on the dam and the adjacent foundation as well as hydrodynamic pressures generated in the reservoir are discussed. The design and operation of the data acquisition system used during testing are also described.

The experimental procedure and details such as the placement of the vibration generators (shakers) and transducers are presented in Chapter 3. Only the general procedure necessary for proper testing is discussed; details common to all types of experimental investigations are omitted. Implementation of a mode elimination technique that was effective in reducing modal interference observed during testing at Santa Anita Dam is also discussed.

Chapter 4 describes the response analysis procedure that was adopted for use in the correlation study of Morrow Point Dam. The technique is a frequency domain solution that treats the dam-foundation and water domains as substructures and discretizes them using finite elements [2]. The basic formulation and mathematical framework of the procedure are presented. A discussion on the frequency behavior

of infinite fluid domains is included in order to provide a better understanding of the findings presented in the next chapter.

Results from forced vibration tests at Morrow Point Dam are presented in Chapter 5. A full description of the tests and the kinds of responses obtained are given. The tests were conducted with a full reservoir and were designed to investigate the interactions between the dam and the reservoir water. Dynamic water pressures on the upstream face of the dam as well as accelerations along the crest were measured. The second half of the chapter discusses results from a correlation study in which the analysis procedure described in Chapter 4 is used to reproduce the experimental results. Comparisons are made for the computed antisymmetric and symmetric responses of the dam assuming incompressible and compressible water conditions. Direct evidence of water compressibility and the successful isolation of the fundamental symmetric water mode is presented. Correlations with data obtained from previous forced vibration tests on Morrow Point Dam with a low water level are also discussed. The chapter concludes with a summary of the effects of water depth on the response of the dam. Chapter 6 lists conclusions and some suggestions for future work. A complete data set of the experimental results is contained in Appendix I.

CHAPTER 2

EXPERIMENTAL APPARATUS

2.1 Introduction

Although field tests on arch dams have been carried out many times in the past, a non-traditional approach to forced vibration testing was adopted for the experiments at Santa Anita and Morrow Point Dams [26]. Typically, tests are performed with large operating staffs and a significant amount of test equipment, including various types of transducers and associated signal conditioners, spectrum analyzers, photorecording oscilloscopes, and digital data systems that convert analog signals to digital information which is then stored on magnetic tape.

The testing system described in this chapter was designed to operate efficiently using a minimum number of components and to aid the investigations of the dynamic interactions that take place between the dam and foundation, and between the dam and reservoir water. These objectives placed the following requirements on the system.

1. Accurate determination of response in a low signal-to-noise ratio environment must be made. Such responses include motions near and beyond the dam-foundation interface and dynamic pressures in the reservoir.
2. Both amplitude and phase of the response must be determined. The phase quantity of interest is the phase lag of the response relative to the excitation force.
3. The data set should include complete frequency sweeps at a large number of stations. The volume of data generated necessitates the use of an automated data acquisition and processing system.

2.2 System Components

2.2.1 Vibration Generators

The vibration generator system shown in Figure 2.1 is used to supply sinusoidal force excitations to the dam. The system, originally designed and developed approximately 25 years ago at the California Institute of Technology, consists of two control consoles and two shakers and was manufactured by Kinemetrics in Pasadena, California. Each shaker is capable of producing a force of up to 5,000 pounds at frequencies from 2.5 Hz to 10.0 Hz. The force is generated by counter-rotating buckets that can be loaded with varying amounts of lead weights and is a function of both the mass of the weights and the square of the excitation frequency. The two units can be operated separately or synchronously, in phase or out of phase, in a master-slave configuration. When operated together, the desired phase relationship can be maintained to within 2 degrees. The buckets can be aligned so that any line of action (in the horizontal plane) of the force is possible. A synchro signal is used in the calculation of the phase lag of the response to the excitation force. The location and orientation of the vibration generators is discussed in Chapter 3.

2.2.2 Transducers

The steady state responses induced in the dam and its adjacent foundation are measured using force balance accelerometers, Model FBA-11, also manufactured by Kinemetrics (see Figure 2.2). Other instruments such as velocity meters, seismometers, and different types of accelerometers have been used in previous field tests on dams. The accelerometers used were chosen because their high output facilitates accurate measurement of both amplitude and relative phase. The FBA-11 is a uniaxial accelerometer that can be oriented to measure either horizontal or vertical surface accelerations and is enclosed in a watertight housing weighing only 1.5 pounds, making the unit very practical and easy to handle. It is a highly sensitive,

low frequency, low power, spring-mass device with a natural frequency of 50 Hz and damping adjusted to 70% critical. A full scale range of ±0.1g at ±2.5volts dc was used for the tests at Santa Anita and Morrow Point Dams. The FBA-11s have a flat frequency response up to 25 Hz but produce a phase shift that varies linearly from 3.6 degrees at 2 Hz to 18 degrees at 10 Hz.

Calibration tests were performed to determine the relative response characteristics of the accelerometers. An LVDT (linear variable differential transformer) output was used as a reference against which the FBA response was compared. An Electro-seis, whose input is controlled by a signal generator, provided a common excitation to both the LVDT and FBA. The tests consisted of exciting the Electro-seis sinusoidally over a frequency range of 2 Hz to 10 Hz and monitoring the response signals from the LVDT and FBA. Comparisons between the relative response amplitudes and phases were made using the data acquisition system described in the next section. Appropriate care was taken to convert the LVDT displacement responses to corresponding acceleration responses. The results of this test showed that the response characteristics of any two FBA-11s do not vary by more than 4%; thus, calibration is not essential. This is a marked advantage over some other motion sensing transducers. For example, any two Model SS-1 Ranger Seismometers can have sufficiently different natural frequencies and damping to require that calibrations be performed at all frequencies of interest.

Water pressures in the reservoir are measured using LC-32 hydrophones (see Figure 2.3) provided by Celesco Transducer Products in Canoga Park, California. The transducer element is lead zirconate titanate, which senses dynamic pressure only, and is housed in a watertight neoprene sheath that effectively eliminates short-circuiting problems. These hydrophones are extremely sensitive and are capable of detecting a 7 microvolt peak signal. This sensitivity made operating under less than calm conditions somewhat difficult; however, a portion of the cable below

the water surface was shielded from environmental effects to improve the signal-to-noise ratio (see Chapter 3). Typically, the hydrophone itself will have a flat response from 1 Hz to 1 kHz, will not produce a phase shift in the low frequency range of interest, and will have an output constant of 0.5 volts/psi. However, the actual response characteristics will vary as a function of cable length. Attempts to obtain response characteristics and to determine appropriate output constants are described in Chapter 5.

2.2.3 Data Acquisition System

The data acquistion system was designed not only for efficient data retrieval and recording, but also for on-site data processing to help monitor and evaluate the testing. Figure 2.4 shows the system in operation on Morrow Point Dam. The system is compact and is easily transferred from station to station along the dam crest if needed. The A to D converter, amplifiers, and filters, as well as other accessory equipment, were designed and constructed at the California Institute of Technology. Because of its modular make-up and exclusive use of solid-state electronics, the data acquisition system has proven to be reliable and nearly maintenance-free. Considerable cost savings were realized over commercial products.

The main components of the system are shown in block diagram form in Figure 2.5. The FBA console supplies power to the FBAs and transfers the signals to the amplifier unit where gains from 5 to 500 can be selected. The hydrophones do not require a separate power supply but do require proper impedance matching through charge amplifiers. No phase shift is introduced in the amplification process for either the FBAs or the hydrophones.

Once amplified, the signals are band-passed to eliminate DC levels and unwanted high frequency noise. The DC components result from FBA signal drift, which can vary significantly during the day because of changing temperature and sun conditions. The high frequency noise can be caused by windy conditions or

installations in and around the dam, such as power plant stations, gate valves, etc. These frequencies are usually much higher than those associated with the vibration modes of the dam and are therefore filtered out. The low-pass cutoff frequency (fhco) is chosen to give the cleanest signal and to prevent aliasing.

A schematic diagram of a typical band-pass filter is shown in Figure 2.6. The circuit consists of a passive high pass R-C network in cascade with an active second-order low pass filter. The high pass section has a cutoff frequency (flco) of 0.02 Hz. This cutoff frequency removes the DC levels of a signal without distorting its low frequency components. The cutoff frequency for the low pass filter is adjustable between 10 Hz and 100 Hz. The high pass filter has a 6db/octave falloff below flco while the low pass filter falls off at 12db/octave beyond fhco. The phase shift through a band-pass filter at any frequency is the sum of the shift angles due to the high pass and low pass sections.

Filter characteristics (gain vs. frequency and phase shift vs. frequency) are shown in Figure 2.7. The fhco was chosen as 70 Hz at Santa Anita Dam, which is below the Nyquist frequency (equal to one half the sampling frequency, see below). To avoid aliasing, fhco must not exceed the Nyquist frequency. High noise levels at lower frequencies were encountered at Morrow Point Dam, and fhco was reduced to 10 Hz. As seen from Figure 2.7, negligible signal attenuation is present between 2 Hz and 10 Hz with fhco=70 Hz; however, with fhco=10 Hz, approximately 22% of the signal amplitude is lost at 10 Hz. Filtering also produces a phase shift which, in the frequency range from 2 Hz to 10 Hz, varies linearly from −3 degrees to 10 degrees when fhco=70 Hz and from 14 degrees to 90 degrees when fhco=10 Hz.

The filtered signals are output on a multichannel Hewlett-Packard chart recorder and are digitized by an A to D converter. The A to D is a 16 channel, 12 bit integrated circuit design with two eight channel multiplexers, which are arranged in a 16 channel, single-ended configuration. Data sampling can take place every

35 microseconds without loss of full-scale accuracy. The actual sampling interval selected equals 390 microseconds, which is multiplexed through 16 channels, giving a sample interval of 6240 microseconds per channel. This interval corresponds to a sampling frequency of 160 Hz. The Nyquist frequency is 80 Hz, which can be used as an upper bound on fhco. This sampling frequency yields 80 samples per cycle at 2 Hz or 16 samples at 10 Hz for each channel of data. Two hundred samples per channel are taken which corresponds to 2.5 cycles of sampled data at 2 Hz and 12.5 cycles at 10 Hz.

Interactive software residing in a Zenith-120 microcomputer allows the user to evaluate and monitor overall system performance and also provides on-site data reduction capabilities. At each excitation frequency, a sine curve is fit to each channel of sampled data by a least-squares algorithm to determine amplitude, phase, and signal offset. A precise value of the frequency is calculated by counting the number of sample intervals between zero crossings of the shaker synchro signal for which there is no offset or noise. Each sample point is the amplitude of the response at the sample time and is assumed to consist of harmonic and DC components, as

$$x_{1+(n-1)} = A \sin\left(w(n-1)dt\right) + B \cos\left(w(n-1)dt\right) + C \ ,$$

where $n = 1, \ldots, NS$ (NS = number of samples.)

dt = sample interval

w = excitation frequency

A, B = the amplitudes of the harmonic components

C = the offset (DC component).

In matrix form, the response at a station can be written as

$$\begin{bmatrix} \sin(w*0\,dt) & \cos(w*0\,dt) & 1 \\ \vdots & \vdots & \vdots \\ \sin(w*(n-1)dt) & \cos(w*(n-1)dt) & 1 \\ \vdots & \vdots & \vdots \\ \sin(w*(NS-1)dt) & \cos(w*(NS-1)dt) & 1 \end{bmatrix} \begin{Bmatrix} A \\ B \\ C \end{Bmatrix} = \begin{Bmatrix} x_1 \\ \vdots \\ x_{1+(n-1)} \\ \vdots \\ x_{1+(NS-1)} \end{Bmatrix} .$$

Values for A, B and C are obtained via a least-squares algorithm, and the response can now be characterized as

$$x(t) = D\sin(wt + \theta) + C\ ,$$

where $D = \sqrt{(A^2 + B^2)}$ and is the amplitude of the response

$\theta = \arctan(B/A)$ and is the phase of the response relative to the sampling initiation time.

The amplitude D is normalized by the exciting force: g/kip for the accelerometers and psi/kip for the hydrophones. The difference in θ between a transducer signal and the shaker synchro signal gives the phase lag relative to the exciting force. Because of the DC filtering process, the offset in the transducer signals, C, will always be small.

The data are then stored in a $5\frac{1}{4}$ inch floppy disk file, which contains values of frequency, amplitude, and phase for the recorded station responses. The digitized data can also be stored on disk, if desired. Calibrations and corrections applied to the data to yield the true amplitude and phase of the response are described in Chapter 5. The filter correction for phase is avoided by filtering the shaker synchro signal in the same way the transducer signals are filtered. Plot routines are available which output frequency response curves at the end of each frequency sweep. Data retrieval, processing, and output for eight channels require approximately 30 seconds for each frequency.

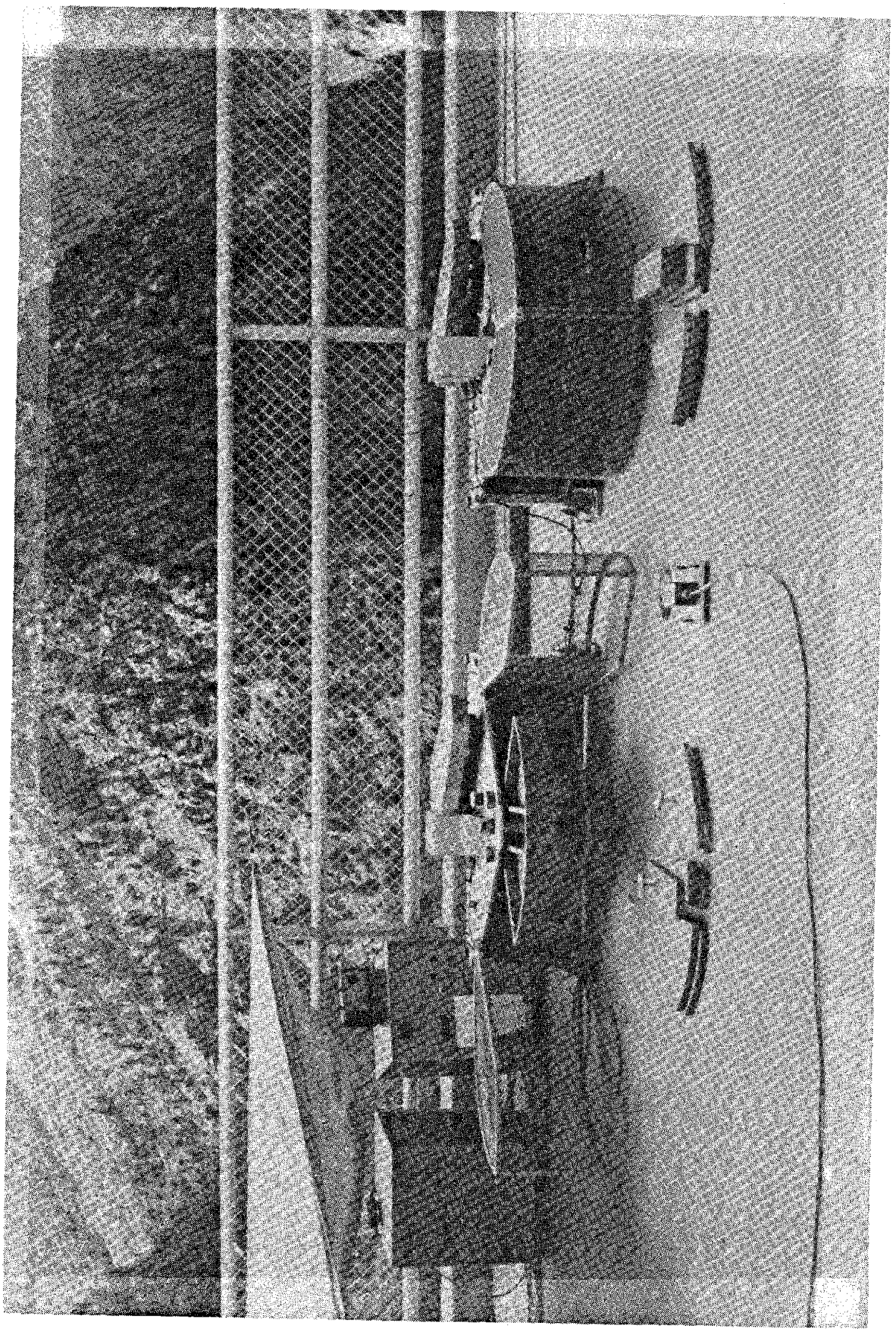

Figure 2.1 Vibration generator system, shown in place on Morrow Point Dam.

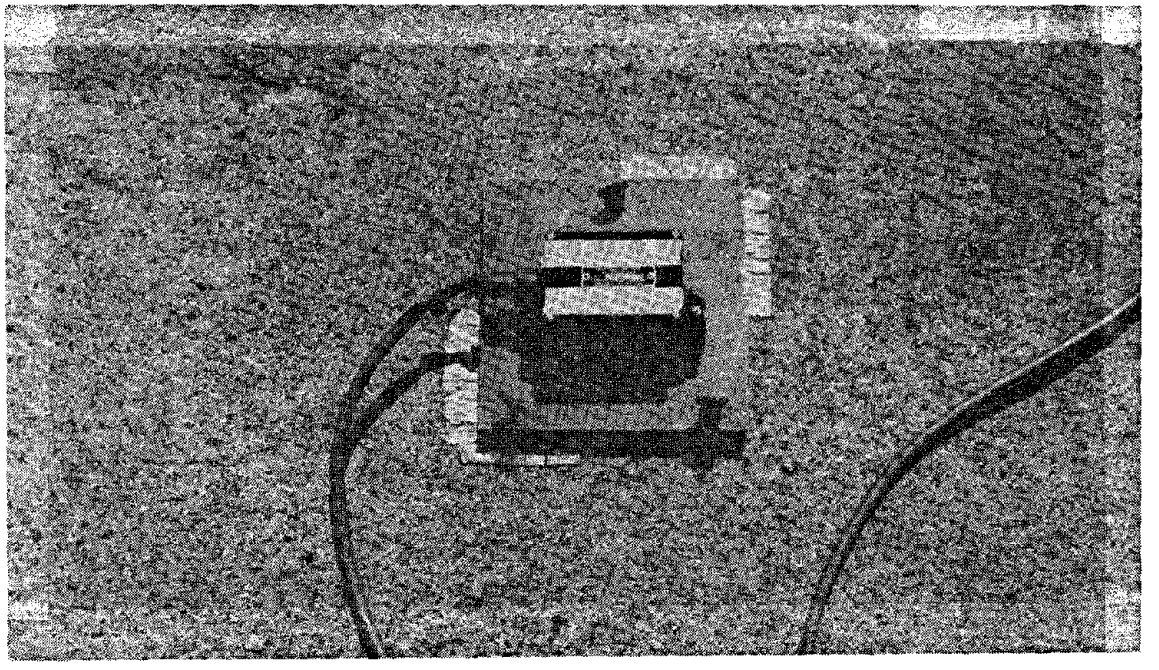

Figure 2.2 Force balance accelerometer, Model FBA-11, mounted on leveling plate.

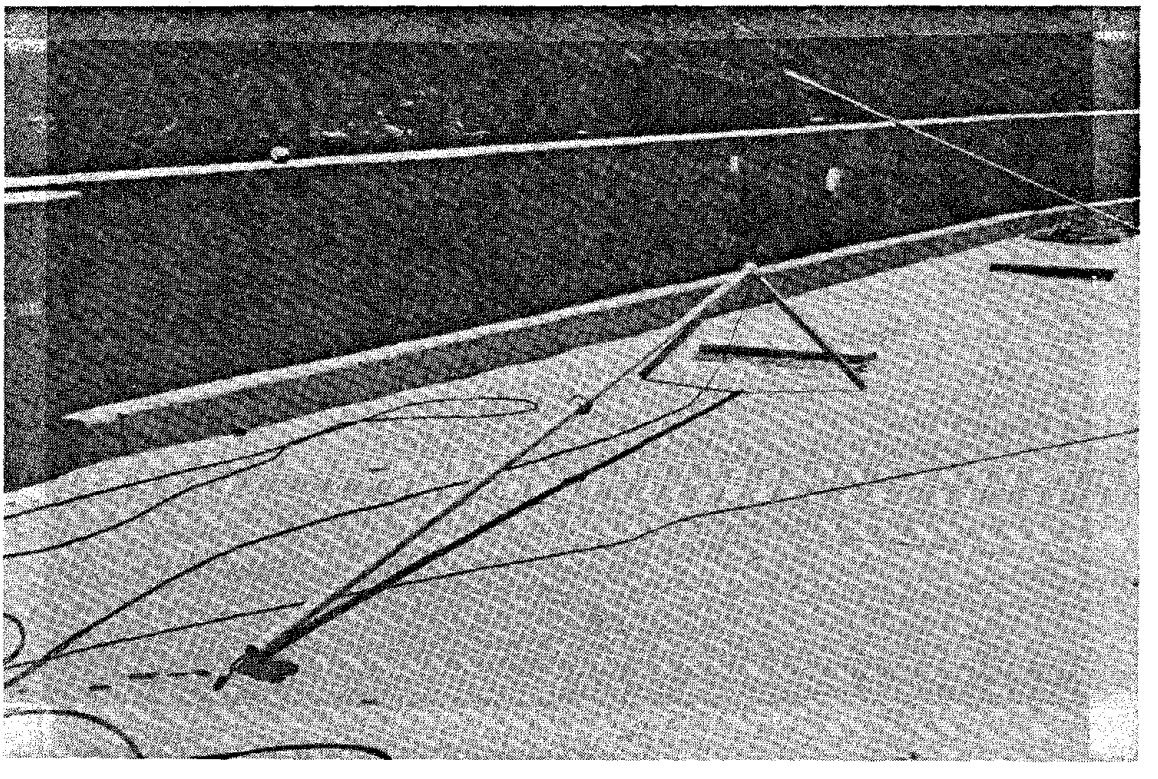

Figure 2.3 Hydrophone shown with pipe used for water wave isolation.

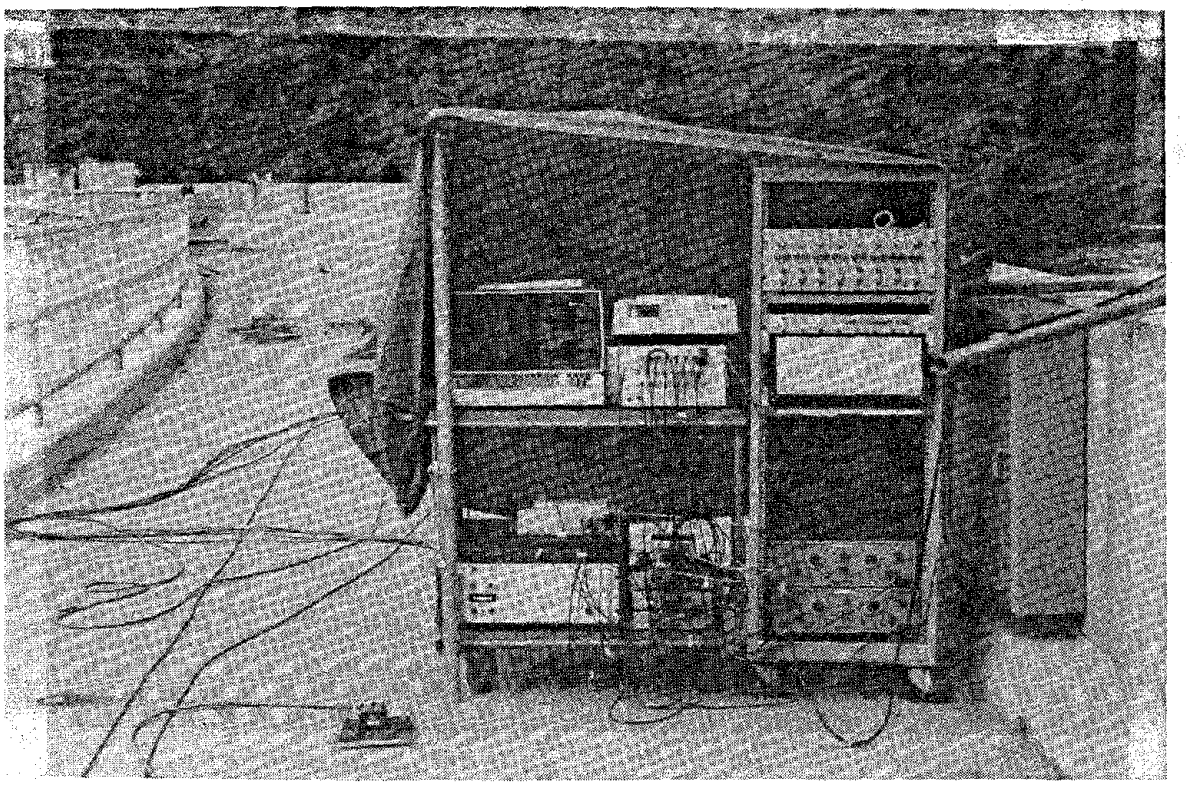

Figure 2.4 Data acquisition system, shown in place on Morrow Point Dam.

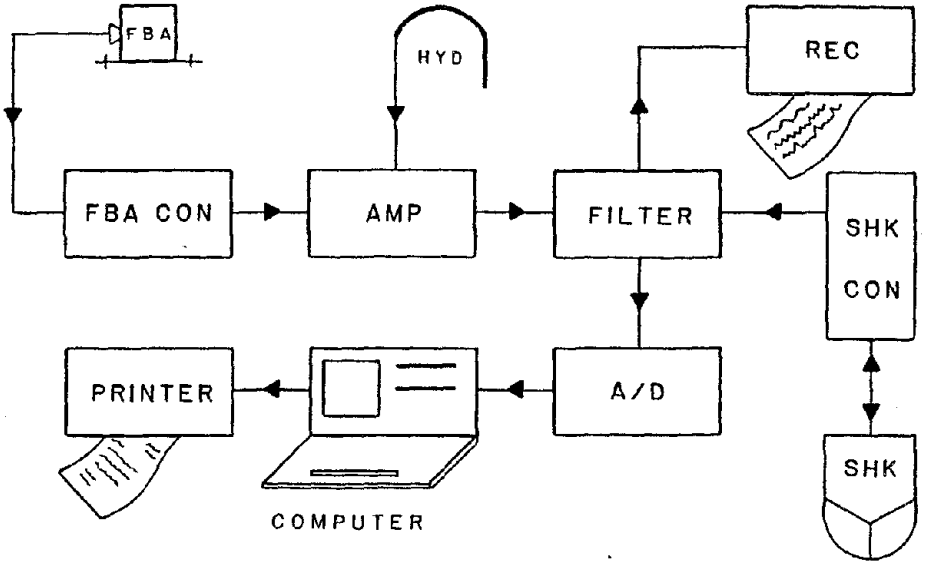

Figure 2.5 Block diagram of data acquisition system.

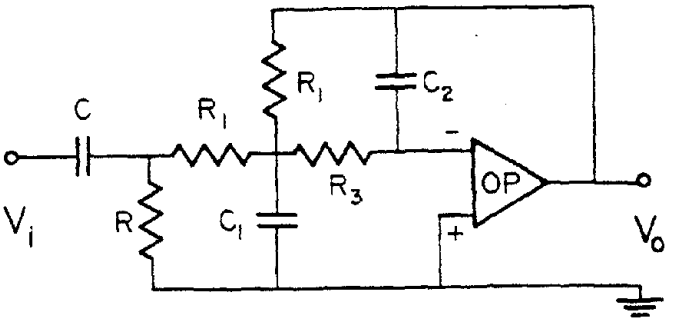

Figure 2.6 Schematic diagram for a band-pass filter.

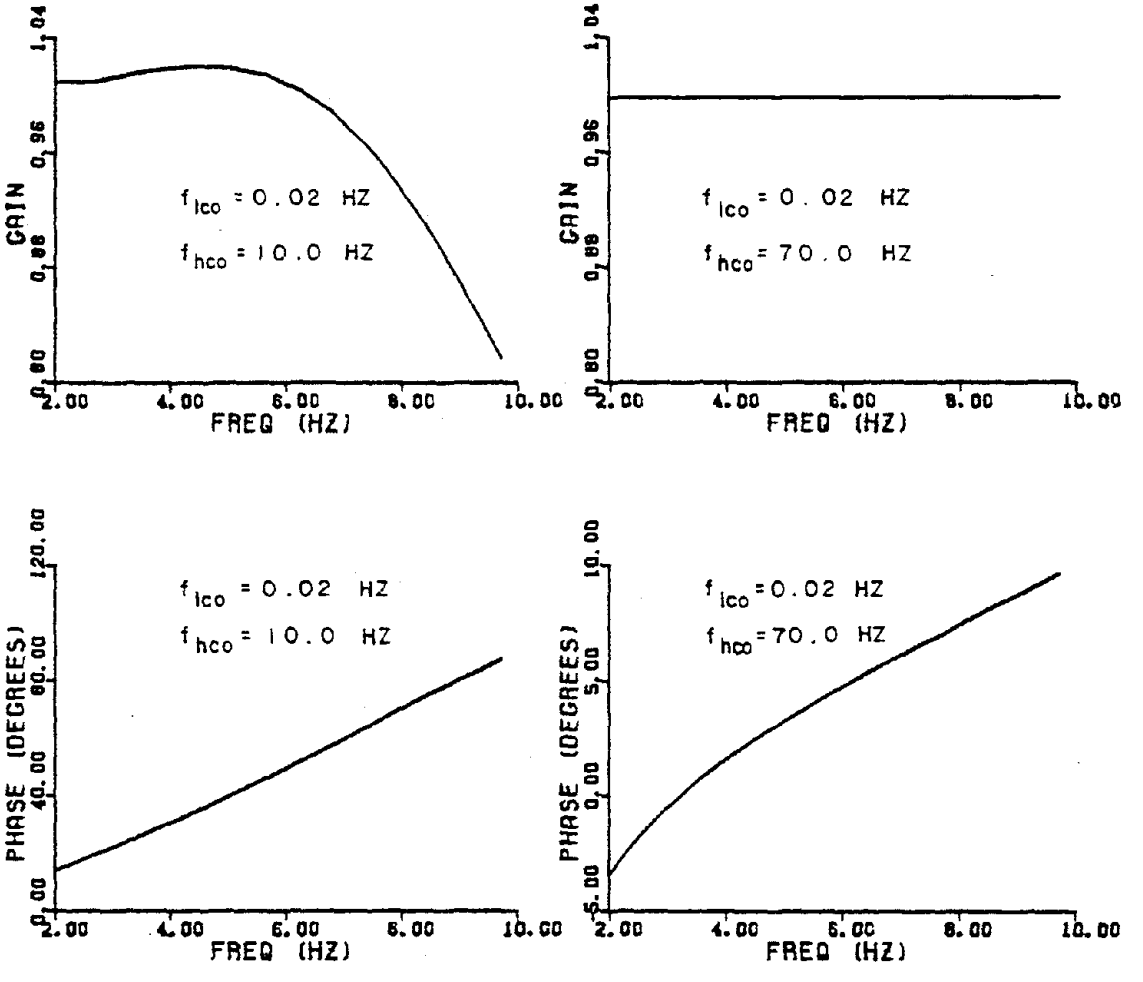

Figure 2.7 Characteristics of the band-pass filters used at Morrow Point Dam (left) and Santa Anita Dam (right).

CHAPTER 3

EXPERIMENTAL PROCEDURE

3.1 Introduction

The experimental procedure described here is used to determine the steady-state responses of the dam, the foundation, and the water in the reservoir to a given sinusoidal exciting force. The procedure is simplified through the use of the data acquisition system, which controls the retrieval and processing of data. The user is responsible for ensuring proper installation and operation of the shakers and motion transducers [26].

3.2 Shaker Location and Orientation

Two shakers (or a single shaker if only one is used) are bolted on the dam crest at the centerline. Symmetric responses are excited with the force aligned in the stream (radial) direction, and antisymmetric responses are excited with the force aligned in the cross-stream (tangential) direction. This configuration differs from the more traditional one in which two shakers, one on each side at some distance from the centerline with their forces aligned in the radial directions, are operated in phase to excite symmetric responses and out of phase to excite antisymmetric responses. With the centerline location scheme, the technique of adjusting the directions of the forces to eliminate a given mode (see below) is simplified because only a single direction need be adjusted.

The symmetry of the dam is, of course, never perfect but is usually present to a degree so that all modes that are observed can be classified as either symmetric or antisymmetric. The result of nonperfect symmetry is that antisymmetric modes are excited to some degree in the symmetric shake and vice-versa. Elimination of

the fundamental antisymmetric mode in the symmetric shake and elimination of the fundamental symmetric mode in the antisymmetric shake are desirable objectives which result in a cleaner set of data.

Elimination of any mode can be accomplished if the direction of the force is made perpendicular to the direction of motion of that mode at the shaker location. Figure 3.1 shows a sketch of Santa Anita Dam. Note that the dam does not exhibit good symmetry about its centerline, and the dashed line crest shapes represent the fundamental symmetric mode at 6.3 Hz and the fundamental antisymmetric mode at 6.6 Hz. With the direction of the force aligned along F1 in the stream direction, the measured response from the FBA at the shaker location will contain contributions from both fundamental symmetric and antisymmetric modes. In order to eliminate the antisymmetric response, for example, in the symmetric shake, the direction of motion of the first antisymmetric mode at the shaker location must be identified. This direction is indicated along F2 in Figure 3.1. If the direction of the force is adjusted to act perpendicular to F2, elimination of the first antisymmetric mode will result.

Figure 3.2 shows the results of the mode elimination technique at Santa Anita Dam. The two curves represent acceleration responses at a station on the dam crest where both the fundamental symmetric and fundamental antisymmetric modes have sizable radial components. The response to the symmetric shake contains no visible trace of the fundamental antisymmetric mode and was obtained after adjusting the direction of force 40 degrees off the stream direction. Similarly, the response to the antisymmetric shake contains no visible trace of the fundamental symmetric mode and was obtained after adjusting the direction of force 5 degrees off the cross-stream direction. These adjusted directions for the force are determined by trial and error and are used throughout the entire series of tests.

3.3 Determination of Vibration Frequencies

Preliminary tests are conducted in which a survey of the dam response is made using an FBA located next to the shaker at the dam centerline on the crest. The FBA is aligned in the radial direction for the symmetric shake and in the tangential direction for the antisymmetric shake. The FBA response signal is monitored on the chart recorder while the frequency of the shaker is swept from 2 Hz to 10 Hz. In this manner, the resonant frequencies of the dam can be quickly identified. Results from preliminary tests at Morrow Point Dam identified symmetric resonant frequencies at 3 Hz, 4 Hz, 5.5 Hz, and 6.7 Hz. These values compared favorably with the actual resonances at 2.95 Hz, 3.9 Hz, 5.4 Hz, and 6.7 Hz.

The resonant frequencies determined during the preliminary sweeps are used to set appropriate frequency increments for use during the forced vibration testing. Typically, a small frequency increment, 0.1 Hz or less, is used to accurately define the resonant peaks, whereas a much larger increment is used for frequencies far from resonance. The automated and efficient operation of the data acquisition system allowed an increment of 0.1 Hz or less to be maintained throughout the tests at Santa Anita and Morrow Point Dams without substantially increasing the duration of any particular test.

3.4 Test Procedure

Prior to the start of each frequency sweep, all FBAs are placed and balanced at the recording stations. The accelerometers are attached to aluminum plates that are supported off the ground by three adjustable screws in tripod fashion as shown in Figure 2.2. This arrangement facilitates the balancing procedure and ensures secure placement at recording stations, especially on non-level surfaces. To balance an FBA, a ± 12 volt DC power supply is connected and the output is monitored using a digital voltmeter. The tilt of the aluminum plates is adjusted via the screws until the measured voltage is minimized. Without these platforms, the adjustment to balance the FBA must be made internally and is very sensitive and difficult.

The hydrophones, one of which is shown in Figure 2.3, are placed by lowering them down the upstream face of the dam using the attached cable. In windy conditions, surface waves, white caps and bobbing driftwood disturb the cable, and a considerable amount of noise (including low frequency noise not eliminated by the filters) appears on the hydrophone signal. Some relief was obtained at Morrow Point Dam by placing the cable inside a 3 inch diameter aluminum pipe that extended 3 feet below the water surface, and by manually keeping the driftwood away. This allowed testing to proceed under moderately windy conditions, i.e., wind speeds under 15 miles per hour.

At each frequency, sufficient time is allowed for the shakers and the response signals at the various stations to stabilize. Data acquisition is then initiated by the user by activating the data processing routine. Checks in the experimental procedure are required so that various components of the system are not saturated by large signals. This occurs at 2.5 volts for the FBAs (because of excessive signal drift), 15 volts for the filters (because of excessive signal amplification), and 2.5 volts for the A to D converter (because of excessive amplification). Saturation of the FBAs and filters produces signal clipping which is easily detected by examining the

traces on the chart recorder. The data processing program detects saturation of the A to D by monitoring the signal amplitudes. Saturation is relieved by reducing the amplification or by rebalancing the FBA. Rebalancing an FBA during a frequency sweep can be performed without stopping the shakers since critical DC drift levels (approximately 2.0 volts) greatly exceed the acceleration response portion of the signal (approximately 10 millivolts to 200 millivolts).

A typical frequency sweep contains about 60 frequencies (between 2 Hz and 10 Hz) at which the amplitude and phase of each channel are computed. Approximately 90 minutes are required for each frequency sweep. This value includes the time it takes to make five changes of weights in the shaker buckets in order to maintain a near maximum excitation force. Additional time, often considerable, is required to place the FBAs and hydrophones. Most of the testing at Santa Anita and Morrow Point Dams was carried out by an operating staff of two persons.

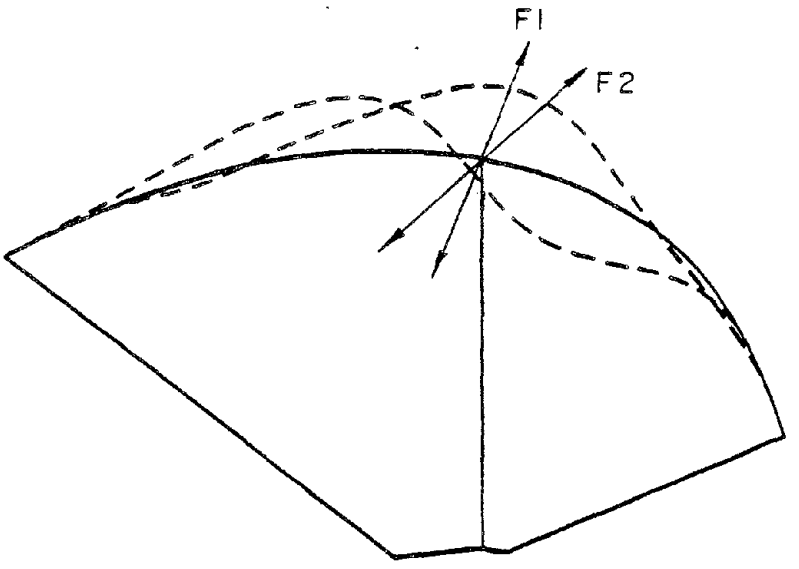

Figure 3.1 Sketch of Santa Anita Dam. Shown are the fundamental symmetric and antisymmetric modes at 6.3 Hz and 6.6 Hz, respectively. Elimination of the antisymmetric response at the shaker location occurs after adjusting the shaker force perpendicular to F2.

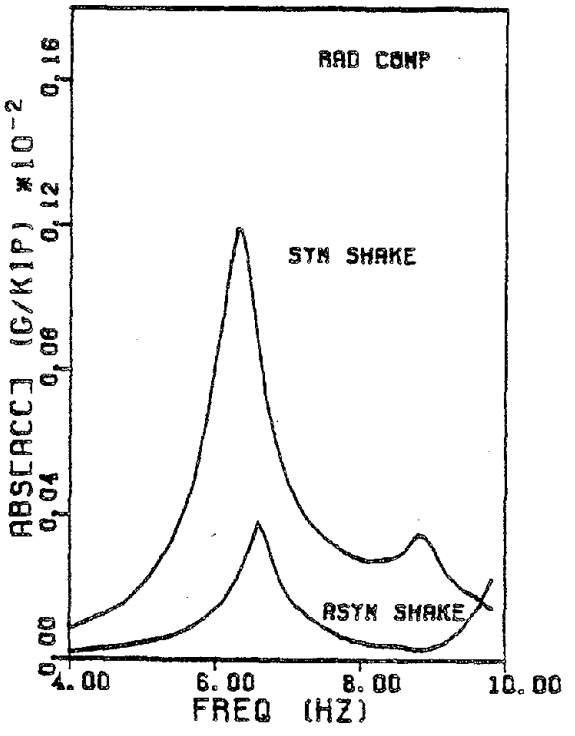

Figure 3.2

Results of the mode elimination technique performed at Santa Anita Dam. Radial components of acceleration amplitude at same location on the dam crest for both symmetric and antisymmetric shakes are shown.

CHAPTER 4

RESPONSE ANALYSIS TECHNIQUE

4.1 Introduction

Most of the early work concerning the earthquake analysis of arch dams neglected any dam-water interaction effects, and a two-part solution scheme was adopted. The first part was aimed at identifying hydrodynamic pressures resulting from the motion of a rigid dam. Standard solution techniques were then used to obtain the response of the dam subjected to both ground motions and the predetermined, time-varying hydrodynamic pressures.

Such an uncoupled approach is only valid if the dam is very stiff; however, in typical arch dam systems, the dam vibrations and hydrodynamic pressures will modify each other to a considerable extent. Early attempts to model these interactions neglected water compressibility and represented the water as added masses attached to the dam. The finite element computer program ADAP [27], as introduced in 1973, is an example of this approach. The program was later extended to include a finite element model of the water which, because of the incompressibility assumption, could be reduced to an added mass matrix assembled into the dam equations [6].

Early attempts by Hatano [28] and Priscu [29,30] to include water compressibility in the arch dam-water interaction problem employed a time domain, finite difference discretization of shell equations for the dam and of the pressure wave equation for the water. Inclusion of water compressibility, however, makes the results sensitive to the location of the upstream reservoir boundary. The physically preferred geometry of a reservoir extending to infinity in the upstream direction was not realized until Porter [31] extended Kotsubo's [32] analytical treatment of an in-

finite water domain. The analytical treatment restricted the reservoir geometry to constant depth with vertical side walls extending radially away from the dam. It also restricted the analysis to the frequency domain.

Porter's solution technique, adapted from earlier work on concrete gravity dams [33], efficiently employed vibration modes of a finite element representation of the dam without water as generalized coordinates, and incorporated effects of the water by a substructure technique in which hydrodynamic terms computed from the water domain substructure were included in the equations of motion of the dam. Later, Hall [2] replaced the analytically treated water domain with a finite element discretization that used a special transmitting boundary so that infinite water domains of realistic geometry could be modeled. The analysis procedure has since been refined by Fok [3], and a computer program for earthquake analysis is available [4].

In an effort to reproduce the observed experimental responses of Morrow Point Dam, the analysis procedure of [2] is adopted. The reference contains details of the derivation and implementation of the procedure, and only a brief description of the main features and mathematical framework is presented here. Loading is specialized to that of shakers mounted on the dam.

4.2 System Overview

Figure 4.1 shows an arch dam-foundation-water system. The water domain is characterized by a finite irregular region adjacent to the dam, which is followed by a region of uniform cross section that extends to infinity in the upstream direction. Interactions occurring between the dam and the water, the dam and its foundation, and between the water and the foundation rock under the reservoir are accounted for. Linear elastic behavior throughout the system is assumed.

To properly account for water compressibility, the pressure wave equation is used to describe the water behavior. A radiation boundary condition is imposed on the reservoir floor and sides, which approximately accounts for energy loss into the underlying foundation medium. A transmitting boundary solution is available to model infinite water domains and requires that the reservoir geometry maintain a uniform cross-section beyond some distance upstream from the dam where the transmitting boundary is located. In the infinite uniform region, use is made of continuum solutions in the upstream direction to account for the propagation of pressure waves. Regular finite elements are employed in the irregular region between the dam and the transmitting boundary.

The interaction between the dam and its adjacent foundation rock is approximately accounted for by the common procedure of including a portion of the foundation in the finite element mesh of the dam and assuming the rock to be massless. The choice of a massless foundation material allows foundation flexibility to be incorporated into the solution without complications that arise from wave propagation effects which may introduce unrealistic low frequency resonances in the system. Radiation damping is approximately lumped into the damping values assigned to the modes of the dam-foundation system which are also used as generalized coordinates to express the system response. These assumptions pertaining to dam-foundation interaction did not prevent reasonable agreement from being obtained between anal-

ysis results and field data from previous forced vibration studies [9,10]. Included in these comparisons were motions at the dam-foundation interface.

4.3 Dam–Foundation Substructure

The dam is idealized as an assemblage of thick-shell finite elements whose material properties are characterized by Young's modulus, E_d, Poisson's ratio, ν_d, and the unit weight of concrete, w_d. The foundation rock is modeled with three-dimensional solid brick elements with properties E_r, ν_r, and a zero mass density. Along the dam-foundation interface, a transition element is used to connect the thick shell elements in the dam to the solid elements in the foundation.

This finite element discretization results in a set of linear differential equations in time t which describes the dam-foundation behavior and are:

$$M\ddot{\underset{\sim}{x}}(t) + C\dot{\underset{\sim}{x}}(t) + K\,\underset{\sim}{x}(t) = \underset{\sim}{F}(t) - \underset{\sim}{Q}(t)\,, \tag{4.1}$$

where M is the mass matrix (dam only)

C is the damping matrix of the dam and foundation (classical damping is assumed)

K is the stiffness matrix of the dam and foundation

$\underset{\sim}{F}(t)$ is the excitation vector containing the shaker forces

$\underset{\sim}{Q}(t)$ is the hydrodynamic force vector

$\underset{\sim}{x}(t)$ is the vector of displacement degrees of freedom (DOF) of the dam and foundation.

The effect of the reservoir water in contact with the dam is expressed in the above equation by the unknown hydrodynamic force vector $\underset{\sim}{Q}(t)$, which has nonzero terms only at the dam-water interface. An expression for the vector $\underset{\sim}{Q}(t)$ is determined from an analysis of the water substructure as explained in the next section.

The set of N coupled equations (N, the total number of DOF of the dam–foundation substructure) can be transformed into a set of uncoupled equations

through the normal coordinate transformation defined by

$$\underset{\sim}{x}(t) = \sum_{j=1}^{J} \underset{\sim}{\phi}_j Y_j(t) \ , \tag{4.2}$$

where $\underset{\sim}{\phi}_j$ is the jth modal eigenvector obtained from the undamped eigenvalue problem associated with the dam-foundation system, and $Y_j(t)$ is the generalized displacement of the jth mode. The expansion in equation 4.2 is complete if J equals N. It should be noted that for most types of loadings, including the shaker excitations considered here, contributions of the various modes are generally greatest for the lowest ones and tend to decrease for the higher ones. Good accuracy in the solution, therefore, is possible for values of J less than N.

Applying the transformation (equation 4.2) to equation 4.1 results in J uncoupled modal equations, the jth of which is written as

$$M_j \ddot{Y}_j(t) + C_j \dot{Y}_j(t) + K_j Y_j(t) = \underset{\sim}{\phi}_j^T \underset{\sim}{F}(t) - \underset{\sim}{\phi}_j^{f\,T} \underset{\sim}{Q}^f(t) \ , \tag{4.3}$$

where the usual expressions for the generalized mass, damping and stiffness are

$$M_j = \underset{\sim}{\phi}_j^T M \underset{\sim}{\phi}_j = 1 \qquad \text{if } \underset{\sim}{\phi}_j \text{ are } M \text{ normalized} \tag{4.4}$$

$$C_j = 2\zeta_j \omega_j \tag{4.5}$$

$$K_j = \omega_j^2 \ , \tag{4.6}$$

and where ω_j and ζ_j are the natural frequency and the critical damping ratio associated with the jth vibration mode of the dam-foundation system; $\underset{\sim}{\phi}_j^f$ lists the components of the jth mode for all nodes along the dam-water interface, and $\underset{\sim}{Q}^f(t)$ lists the hydrodynamic forces (ordered to correspond to $\underset{\sim}{\phi}_j^f$) for the interface nodes. The values ζ_j are assumed to include all sources of damping associated with the dam and foundation rock including radiation.

If the system is subjected to harmonically varying loads, $\underset{\sim}{F}(t)$, expressed as

$$\underset{\sim}{F}(t) = \underset{\sim}{\bar{F}}(\omega)\, e^{i\omega t} \ , \tag{4.7}$$

then the responses to this harmonic loading can also be assumed to be harmonic after sufficient time, but not necessarily in phase with the excitation, and can be written as

$$Y_j(\mathrm{t}) = \bar{Y}_j(\omega)\, e^{i\omega \mathrm{t}} \tag{4.8}$$

$$\underset{\sim}{Q}^f(\mathrm{t}) = \underset{\sim}{\bar{Q}}^f(\omega)\, e^{i\omega \mathrm{t}} \,. \tag{4.9}$$

$\underset{\sim}{\bar{F}}(\omega)$, $\bar{Y}_j(\omega)$ and $\underset{\sim}{\bar{Q}}^f(\omega)$ are the frequency response functions for the excitation and the dam and water pressure responses, and ω is the circular frequency associated with all quantities. Note that $\bar{Y}_j(\omega)$ and $\underset{\sim}{\bar{Q}}^f(\omega)$ can in general be complex and will contain both amplitude and phase information of the response.

Upon substitution of equations 4.7 to 4.9 into equation 4.3, the set of J uncoupled modal equations is transformed into the frequency domain. The jth equation becomes

$$[-\omega^2 M_j + i\omega C_j + K_j]\, \bar{Y}_j(\omega) = \underset{\sim}{\phi}_j^T\, \underset{\sim}{\bar{F}}(\omega) - \underset{\sim}{\phi}_j^{f^T}\, \underset{\sim}{\bar{Q}}^f(\omega) \,. \tag{4.10}$$

The quantity $\underset{\sim}{\bar{Q}}^f(\omega)$ remains to be defined.

4.4 Water Substructure

The pressure wave equation in terms of the dynamic pressure p (positive in compression) is used to describe the water behavior

$$\frac{\partial^2 p}{\partial x^2} + \frac{\partial^2 p}{\partial y^2} + \frac{\partial^2 p}{\partial z^2} = \frac{1}{C^2} \frac{\partial^2 p}{\partial^2 \mathrm{t}} , \tag{4.11}$$

which is valid for small displacements, irrotational motion, and inviscid flow, and C is the velocity of pressure waves in water. The boundary conditions are

$$\frac{\partial p}{\partial n}(s,t) = -\frac{w}{g} a_n(s,t) \quad \text{along the dam-water interface} \tag{4.12}$$

$$\frac{\partial p}{\partial n}(s',t') = q \frac{\partial p}{\partial \mathrm{t}}(s',t') \quad \text{along the reservoir floor and sides} \tag{4.13}$$

$$p = 0 \quad \text{at the free surface} , \tag{4.14}$$

where w = unit weight of water; g = gravitational acceleration; s,t and s',t' are coordinates along the dam-water interface and along the reservoir floor and sides, respectively; $a_n(s,t)$ is the normal component of the dam acceleration at the dam-water interface; n denotes the inward normal direction to a boundary; and q is the coefficient that defines the amount of energy loss due to water–foundation interaction. In addition to these boundary conditions, the solution must also satisfy the radiation condition for water domains extending to infinity in the upstream direction.

Considering a one-dimensional wave propagation from the water into the foundation, q can be expressed as

$$q = \frac{w}{w_f C_f} , \tag{4.15}$$

where w_f and C_f are the unit weight and dilatational wave speed in the adjacent foundation medium. Alternatively, q can be defined by a reflection coefficient, α, as

$$q = \frac{1}{C} \frac{1-\alpha}{1+\alpha} , \tag{4.16}$$

where α is the ratio of reflected to incident wave amplitude of a pressure wave striking the foundation.

The harmonic pressure responses can be written as

$$p(x,y,z,\mathrm{t}) = \bar{p}(x,y,z,\omega)\, e^{i\omega \mathrm{t}} \,, \tag{4.17}$$

and substitution of equation 4.17 into the governing wave equation yields

$$\frac{\partial^2 \bar{p}}{\partial x^2} + \frac{\partial^2 \bar{p}}{\partial y^2} + \frac{\partial^2 \bar{p}}{\partial z^2} + \frac{\omega^2}{C^2}\,\bar{p} = 0 \,, \tag{4.18}$$

which is the Helmholtz equation. The boundary conditions are now

$$\frac{\partial \bar{p}}{\partial n}\,(s,t,\omega) = -\frac{w}{g} a_n(s,t,\omega) \tag{4.19}$$

$$\frac{\partial \bar{p}}{\partial n}\,(s',t',\omega) = i\omega q \bar{p}(s',t',\omega) \tag{4.20}$$

and

$$\bar{p}(\omega) = 0 \quad \text{at the free surface .} \tag{4.21}$$

The harmonic acceleration of the dam in its jth mode, $a_n(s,t,\omega)$, is obtained from

$$a_n(s,t,\omega) = \sum_{j=1}^{J} -\omega^2 \phi_j^f(s,t)\, \bar{Y}_j(\omega) \,, \tag{4.22}$$

where $\phi_j^f(s,t)$ is the continuous distribution of $\underset{\sim}{\phi_j^f}$ over the dam-water interface. Solution of the boundary value problem defined by equations 4.18 to 4.22 yields the frequency response function for the hydrodynamic pressures in the reservoir which can be expressed as

$$\bar{p}(x,y,z,\omega) = \sum_{j=1}^{J} -\omega^2 \bar{Y}_j(\omega)\, \bar{p}_j(x,y,z,\omega) \,, \tag{4.23}$$

where $\bar{p}_j(x,y,z,\omega)$ is the solution due to $\phi_j^f(s,t)$ and is computed from the finite element water model. Note that in equations 4.22 and 4.23, $\bar{Y}_j(\omega)$ is unknown.

A similar expression can be written for the complex frequency response function for the hydrodynamic force vector, $\underset{\sim}{\bar{Q}}^f(\omega)$, on the upstream face of the dam, which appears in equation 4.10

$$\underset{\sim}{\bar{Q}}^f(\omega) = \sum_{j=1}^{J} -\omega^2 \bar{Y}_j(\omega)\, \underset{\sim}{\bar{Q}}_j^f(\omega) \tag{4.24}$$

where $\underset{\sim}{\bar{Q}}_j^f(\omega)$ is the static equivalent of the pressure function $\bar{p}_j(x, y, z, \omega)$ at the dam-water interface. Substitution of 4.24 into equation 4.10 and assembly of the J equations into matrix form yields

$$S(\omega)\, \underset{\sim}{\bar{Y}}(\omega) = \underset{\sim}{\bar{L}}(\omega)\ , \tag{4.25}$$

where

$$S_{jk}(\omega) = -\omega^2\, \underset{\sim}{\phi}_j^{f^T}\, \underset{\sim}{\bar{Q}}_k^f(\omega)\ , \quad j \neq k \tag{4.26}$$

$$S_{jj}(\omega) = -\omega^2\, M_j + i\omega C_j + K_j - \omega^2\, \underset{\sim}{\phi}_j^{f^T}\, \underset{\sim}{\bar{Q}}_j^f(\omega) \tag{4.27}$$

and

$$\bar{L}_j(\omega) = \underset{\sim}{\phi}_j^T\, \underset{\sim}{\bar{F}}(\omega)\ . \tag{4.28}$$

Notice that $S(\omega)$ is not a diagonal matrix since the eigenvectors, $\underset{\sim}{\phi}_j$, do not uncouple the dam-foundation-water system. Recall that $\underset{\sim}{\phi}_j$ are obtained from the undamped eigenvalue problem associated with the dam–foundation substructure. The modal equations are therefore recoupled as a result of the hydrodynamic terms that appear on the left side of equation 4.25.

The solution to equation 4.25 yields the responses of the generalized coordinates in the frequency domain. Since the experimental results are obtained as steady-state responses, the computed results of interest are obtained from equations 4.2 and 4.8 for the dam and 4.17 and 4.23 for the water pressure.

4.5 Effects of Water Compressibility

The presence of the water is included in equation 4.25 through the terms $\underset{\sim}{\bar{Q}}_j^f(\omega)$ which, if water compressibility is included, are frequency-dependent and complex-valued. Their real parts represent added mass, and their imaginary parts represent added damping. The damping is due to radiation upstream (for an infinite reservoir) and absorption along the reservoir floor and sides. If $\alpha = 1.0$ for an infinite reservoir, then damping can exist only above a critical frequency f_I associated with the infinite uniform portion (its fundamental resonant frequency) because only above f_I can travelling waves exist. (f denotes a frequency in Hz.)

To examine the frequency behavior of infinite water domains, consider the two-dimensional reservoirs shown in Figures 4.2(a) and 4.2(b), one of which is shallower adjacent to the dam face (line a–b) than in the infinite region and the other which is deeper. Along the reservoir floor, $\alpha = 0.9$. Figure 4.3 shows the modulus, phase, and the real and imaginary parts of the hydrodynamic force $R(\omega)$ on the dam face for the two reservoirs. $R(\omega)$ is normalized with the static force, $R_{st} = \frac{1}{2} w H_0^2$, and f is normalized with the fundamental resonant frequency of the infinite uniform region, $f_I = \frac{C}{4H}$. The dashed line curves are associated with the reservoir in Figure 4.2(a), and the solid line curves represent the water behavior in Figure 4.2(b). The excitation consists of a rigid harmonic motion of the dam in the horizontal direction $\left(a_n(s,t) = 1 \cdot e^{i\omega t}\right)$. The behavior of $R(\omega)$ should be characteristic of that of the $\underset{\sim}{\bar{Q}}_j^f(\omega)$ terms for the two types of reservoirs.

The fundamental resonant frequency f_{wat} of the water body of Figure 4.2(a) occurs at f_I, and the resonance evolves from a standing wave (real part) to a travelling wave (imaginary part) with a phase shift approaching 90°. Thus, a large amount of radiation damping is present above $f_{\text{wat}} = f_I$. Resonance of the water body of Figure 4.2(b) takes place at a frequency f_{wat} below f_I and has some features typical of those of a bounded domain, i.e., positive and negative real peaks and a

centered imaginary peak. However, the imaginary part does not die out above the resonance, although it is smaller than in the previous case. This "mixed" resonance undergoes a phase shift that exceeds 90°.

If the water domain is considered to be incompressible and the reservoir floor and sides rigid, as is commonly assumed, then $C = \infty$ in equation 4.18, and $q = 0$ in equation 4.20. Under these conditions, the hydrodynamic terms are frequency-independent and real-valued and reduce the effect of the water to a frequency independent added mass with no damping. The incompressible water response is identical to the compressible water response at zero frequency.

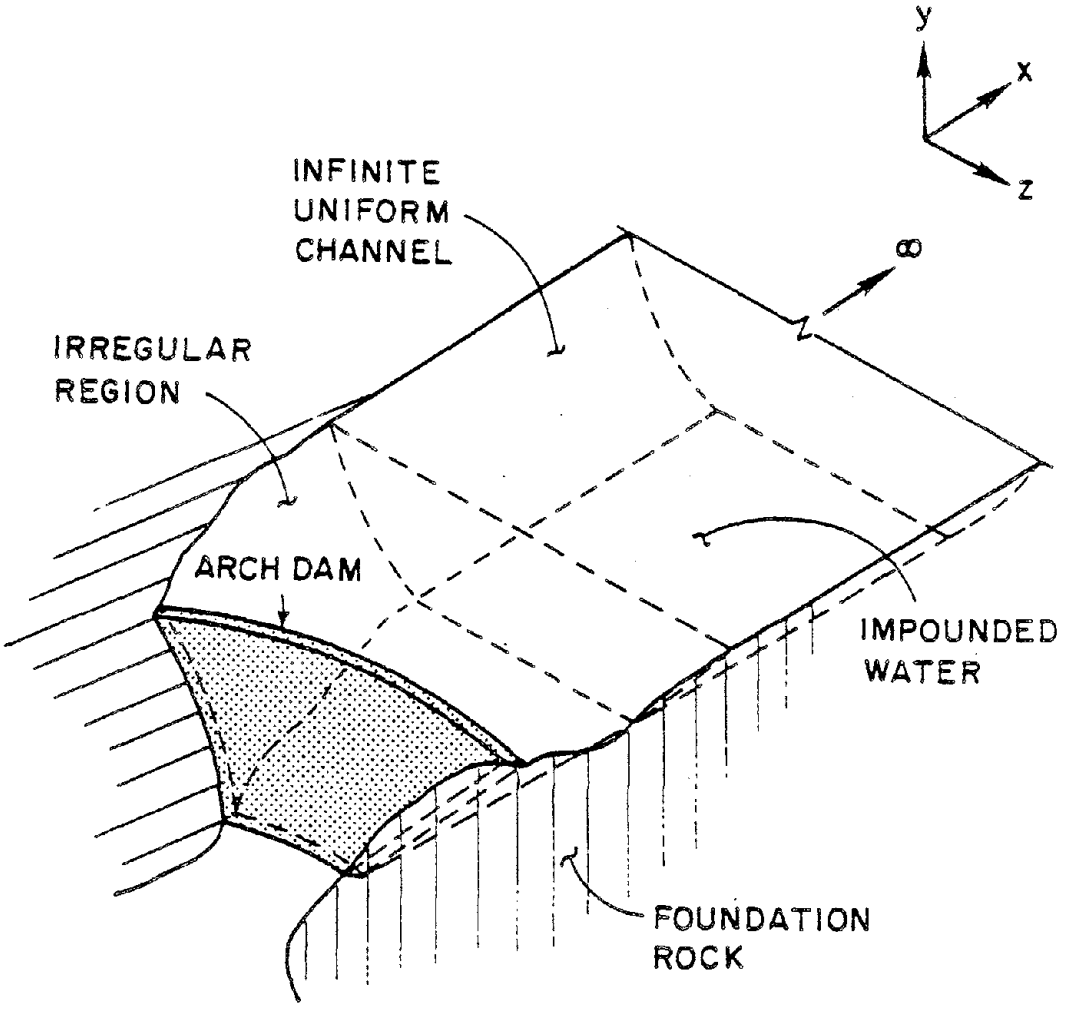

Figure 4.1 Typical arch dam-foundation-reservoir system. Taken from reference [3].

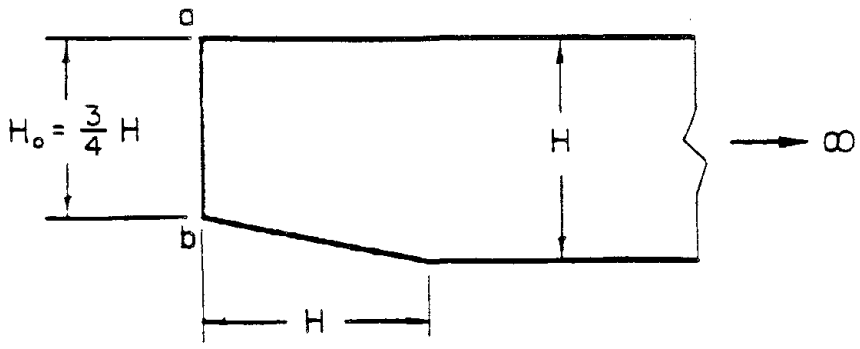

(a) Reservoir with sloped floor and $H_0 < H$ adjacent to dam face.

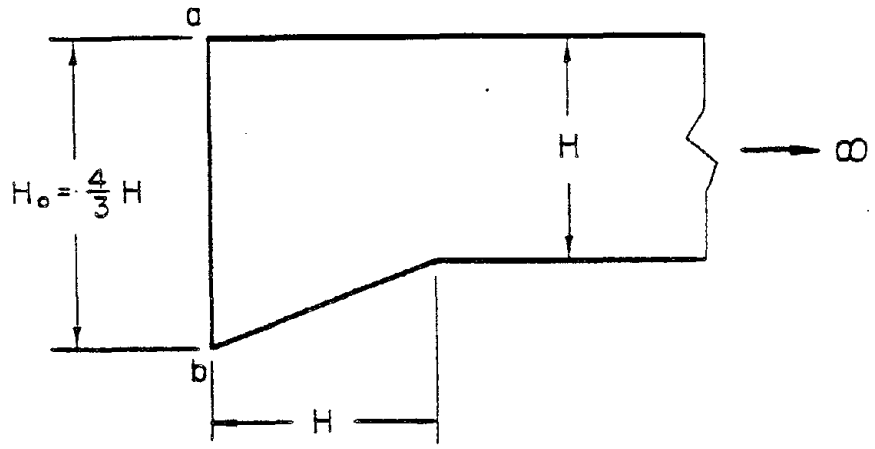

(b) Reservoir with sloped floor and $H_0 > H$ adjacent to dam face.

Figure 4.2 Two-dimensional infinite water domains.

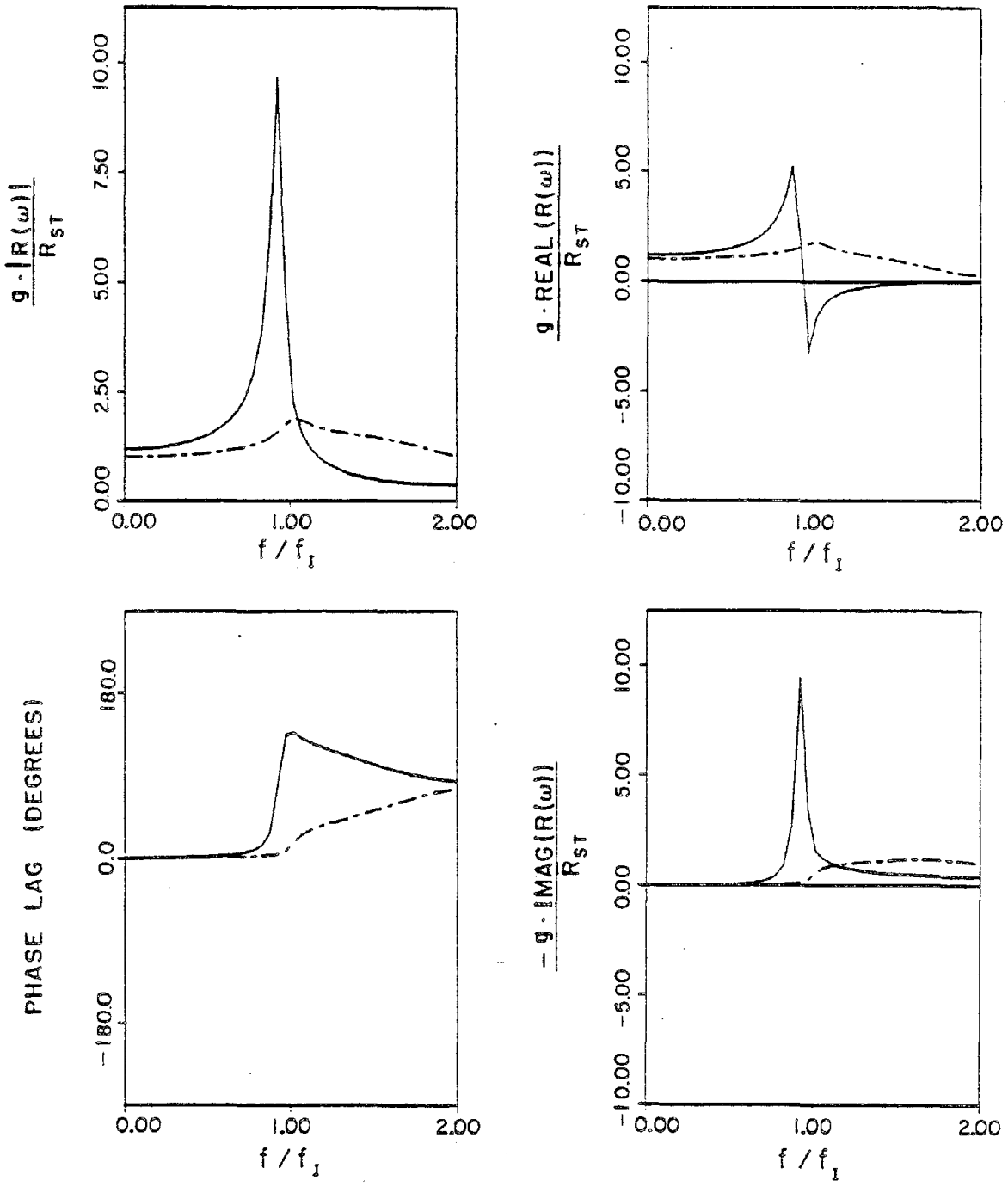

Figure 4.3 Comparison of $R(\omega)$ computed for the reservoirs shown in Figure 4.2. Shown are the magnitude, phase, real and imaginary parts. The solid curves represent the results associated with the geometry of Figure 4.2(b) and the dashed curves were computed using the geometry of Figure 4.2(a).

CHAPTER 5

CORRELATION STUDY OF MORROW POINT DAM

5.1 Introduction

Results from forced vibration tests on Morrow Point Dam are presented in this chapter. The objective of these tests was to examine the dynamic interactions that occur between the dam and the reservoir water. Correlation studies to evaluate the ability of the analysis procedure (outlined in Chapter 4) to reproduce these results are also discussed.

The chapter begins with a description of Morrow Point Dam, its foundation, and reservoir in Section 5.2. This is followed (in Section 5.3) by a discussion on the types of steady-state responses measured during the tests and a description of data reduction and calibration procedures. Data samples are also presented, which indicate the type and quality of data taken. The finite element discretization of the arch dam system and a discussion on the choice of material properties associated with the models is presented in Section 5.4.

Section 5.5 describes the results of a correlation study between the observed and computed behavior of the dam at full reservoir. The antisymmetric response behavior is investigated first by attempting to calibrate the analysis procedure with the experimental data. Once satisfactory agreement is obtained, comparisons between the observed and computed symmetric responses are made. The importance of water compressibility effects in the forced vibration response of the dam is also discussed. Direct evidence of water compressibility from the experimental data is presented in Section 5.6.

Results from previous forced vibration tests on Morrow Point Dam (conducted

in 1969 and in 1972) are discussed in Section 5.7. Correlations with data obtained at a low water level are presented. The effects of water depth on the reponse of the dam are summarized in Section 5.8.

5.2 System Description

5.2.1 Dam

Morrow Point Dam is one of three dams of the Curecanti Unit, Colorado River Storage Project [34]. The Curecanti Unit not only provides storage for hydroelectric power generation along a 40 mile stretch of the Gunnison River, but also provides storage for irrigation, recreation, and flood control. The dam is located on the Gunnison River in Montrose County near the village of Cimmaron, Colorado, which is twenty-two miles east of Montrose, Colorado (see Figure 5.1).

Morrow Point Dam, shown in Figure 5.2, was the first double-curvature thin arch dam built by the Bureau of Reclamation. Construction began in 1963 and was completed in January 1968. The dam was built with vertical contraction joints spaced at 40 foot centers except at the center (Block 10), which is 30 feet wide. The joints simplified the construction procedure and allowed the concrete to contract during the cooling period without cracking. The vertical joints were grouted before filling the reservoir.

The dam is 465 feet tall with a crest length of 724 feet and is 12 feet thick at the crest and 52 feet thick at the base. The crest and base elevations are 7165 feet and 6700 feet, respectively. There are four orifice-type free-fall spillways located at the top center of Morrow Point Dam. Water flowing through the openings falls approximately 350 feet into a concrete-lined stilling basin. The spillways are capable of discharging 41,000 cubic feet of water per second at a water surface elevation of 7165 feet.

5.2.2 Foundation

The dam sits in a U-shaped canyon, which was 200 feet wide at the base and 550 feet wide at the crest prior to construction. The canyon walls are fairly smooth and have very little overburden. During excavation along the dam–foundation interface, bolt holes were drilled in both keyways and rock bolts were installed. In two unstable areas at the top of the left keyway, 1 inch groutable bolts were used, and 0.75 inch nongroutable bolts were used in the remainder of the left keyway and in all of the right keyway. Alluvial material in the valley floor is rounded sand, gravel, cobbles, and boulders.

5.2.3 Reservoir

The reservoir has a capacity of 117,165 acre-feet (52 million cubic feet) at a normal water surface elevation of 7160 feet and is approximately 11 miles long. Morrow Point Dam is the middle dam of three along the Gunnison River, and even though three small creeks do enter the reservoir far upstream, it is likely that sediment deposition is minor in the vicinity of the dam. Figure 5.3 shows the topography of the site at Morrow Point. Although the dam exhibits good symmetry about the plane of centers, the reservoir geometry is not symmetric. The entire reservoir is underlain by rocks that are considered impermeable.

5.3 Experimental Investigations

5.3.1 Location of Vibration Generators and Transducers

The forced vibration tests carried out at Morrow Point Dam followed the general procedure previously described in Chapter 3. Two vibration generators (shakers) were used during the testing and were placed side by side on the dam crest at the center block (Block 10). Symmetric responses were obtained by orienting the shaker buckets in the upstream-downstream direction, and antisymmetric responses were obtained by orienting the buckets in the cross-stream direction. The mode

elimination technique was not necessary because of the good symmetry present in the dam. A typical frequency sweep was made up of 0.1 Hz intervals from 2 Hz to 8 Hz with a finer spacing near resonances as necessary. In order to maintain a near-maximum excitation force, five changes of weights in the buckets were used during each frequency sweep.

Acceleration responses were measured at 17 stations along the dam crest and at 3 stations down the crown cantilever at Block 10 (Figure 5.4); the latter were located in galleries inside the dam. Four separate frequency sweeps were required to obtain the responses along the crest since only five accelerometers were available for each test. Only the radial component of acceleration at each station for both the symmetric and antisymmetric shake was measured. Because of the symmetry of the dam, it was assumed that no significant radial responses would be obtained along the cantilever section at Block 10 in the antisymmetric shake; therefore, these responses were measured only during the symmetric shake. A reference FBA was maintained at the shaker location at Block 10 and was oriented in the radial direction for the symmetric responses and in the tangential direction for the antisymmetric responses.

Hydrodynamic pressure responses were obtained at 12 stations on the upstream face of the dam during the symmetric shake and at 12 stations during the antisymmetric shake (Figure 5.4). A series of 12 frequency sweeps was performed since only two hydrophones were available for each test. The original hydrophones had cable lengths of 150 feet and 300 feet. In order to obtain measurements down to a 300 foot water depth, it was necessary to remove a 30 foot section from the 150 foot cable and to splice it onto the 300 foot cable. Pressure responses at depths of 50 feet and 100 feet were obtained using the hydrophone with 120 feet of cable, and responses between 100 feet and 300 feet were obtained using the second hydrophone with 330 feet of cable.

5.3.2 Data Reduction and Calibration

The steady-state responses obtained on the dam and in the reservoir are characterized (see Section 2.2.3) as:

$$x_i(t) = D_i \sin(\omega t + \theta_i) \ ,$$

where $x_i(t)$ = the steady-state response at station i,

D_i = the amplitude of the response, either acceleration or hydrodynamic pressure,

θ_i = the phase of the response relative to the exciting force,

ω = the excitation frequency in rad/sec.

Values for the amplitude and phase of the response were obtained from the least-squares algorithim sine curve fit described in Chapter 3.

Accelerometer data were corrected for amplitude and phase distortions encountered during the band-pass filtering process and normal operation of the FBAs. The band-pass cutoff frequencies during the tests were set at flco=0.02 Hz and fhco=10 Hz. Signal attenuations that resulted in a 22% decrease in amplitude at 10 Hz were accounted for. Filtering also produces a phase shift; however, since both the FBA and shaker signals were filtered in the same way, no filter-induced phase shifts were present. Figure 5.5 shows the frequency response curves for a typical FBA used at Morrow Point Dam. No signal attenuation is present between 2 Hz and 10 Hz; however, the FBA does alter the phase of the response in a linear manner. This phase shift was accounted for.

Hydrodynamic pressure data were also corrected for amplitude and phase distortions. Signal attenuations resulting from the filtering process were accounted for; however, since both the hydrophone and shaker signals were filtered in the same manner, no filter-induced phase shifts were introduced. Calibration of the dynamic pressure responses was complicated by the dependence of hydrophone char-

acteristics on cable length and the uncertainty in the volts/psi output constants. Manufacturer specifications for the LC-32 hydrophone do not include attenuation characteristics below 5 kHz and no phase-shift information is available. As a result, field and laboratory hydrophone calibration tests were performed. The field tests were carried out at Morrow Point Dam and were designed to yield relative gain and phase-shift characteristics of the hydrophones, while the laboratory tests were aimed at identifying proper output constants.

The procedure for the field calibration tests involved placing both hydrophones on the upstream face of Block 10 at a depth of 50 feet. A single frequency sweep was run in which symmetric pressure responses were obtained. Responses from the hydrophone with 330 feet of cable relative to those of the one with 120 feet of cable are given in Figure 5.6 in terms of amplitude (AC) and phase (PHC) correction factors. Values for AC and PHC are determined as follows:

$$\mathrm{AC} = \frac{\mathrm{A_{ref}}}{\mathrm{A_{330}}}$$

and

$$\mathrm{PHC} = \theta_{330} - \theta_{\mathrm{ref}} \ ,$$

where $\mathrm{A_{ref}}$, θ_{ref} = amplitude and phase of the response measured by the reference hydrophone (the one with 120 feet of cable),

$\mathrm{A_{330}}$, θ_{330} = amplitude and phase of the response measured by the hydrophone with 330 feet of cable.

Linear functions were fit to the data; a zero function for PHC resulted.

Prior to these calibration tests, but after all data presented in this report were collected, attempts were made to measure pressure responses at water depths down to 400 feet which required that an additional 100 feet of cable be spliced onto the original 300 foot cable. During the course of these measurements, it is possible that water seeped into the spliced cable, which may explain the scatter in the

calibration data (see Figure 5.6). This scattering, which introduces uncertainties into the hydrophone calibrations, is not indicative of the quality of the pressure responses presented here.

Following the field calibration tests, an appropriate output constant for the reference hydrophone was determined from laboratory tests. The output constant, used to convert the response amplitude from volts to psi, was obtained by moving the hydrophone up and down in a bucket of water. An amplitude of 0.39 volts/psi, which appeared to be nearly independent of frequency in the range of interest, and a zero phase shift were found. This information together with the linear fits to the data in Figure 5.6 was sufficient to correct the dynamic pressure data.

5.3.3 Data Samples

The frequency response data presented in this section demonstrate the type and quality obtained during the forced vibration tests at Morrow Point Dam. Only a small portion of the data is shown here; a complete set is contained in Appendix I. Discussions and interpretations of the data are presented in Section 5.5.

Samples of acceleration and dynamic pressure responses are shown in Figure 5.7. Responses are at Block 10 for the symmetric shake. The acceleration response is the radial component on the dam crest, and the dynamic pressure is at a depth of 50 feet. Four symmetric resonances of the dam with frequencies of 2.95 Hz, 3.95 Hz, 5.4 Hz, and 6.7 Hz are present. As expected, corresponding water resonances also occur. Although not shown here (see Section 5.5), antisymmetric resonances occur at frequencies of 3.30 Hz and 6.21 Hz.

During the second symmetric resonance, accelerations reached 0.0009 g at the dam crest, and dynamic water pressures reached 0.010 psi. Accurate determination of amplitude and phase for acceleration and dynamic pressure amplitudes down to 2.0E–06 g and 3.0E–04 psi, respectively, was obtained. Figure 5.8 shows three sample traces from the chart recorder for dynamic pressures. The least-squares

algorithm accurately fit amplitudes of 0.004 psi, 0.00075 psi, and 0.001 psi. The top two traces are typical of calm conditions, while the bottom trace is typical of moderately windy conditions when wave action disturbed the aluminum pipe housing the hydrophone cable.

5.3.4 Water Level

During the forced vibration testing the water level remained fairly constant at elevation 7156 (9 feet below the crest). Elevations for the earlier UCB tests performed in 1969 and 1972 were 7007 ft and 7160 ft (158 and 5 feet below the crest). These elevations together with that of the canyon bottom are shown in Figure 5.9.

5.4 Idealization of Morrow Point Dam

The finite element models of the dam, foundation, and water used in the analysis of Morrow Point Dam are described below. A full 3-D analysis of the arch dam system was not performed because of cost and computer storage limitations. Instead, separate 3-D analyses were conducted with two geometrically symmetric finite element models, each representing part of the system to one side of the plane of centers (see Figure 5.3) with either symmetric or antisymmetric boundary conditions employed at the center plane. The two models are referred to as the right-hand side (RHS) and left-hand side (LHS) models, the point of view being downstream. Both employ the same dam and foundation mesh geometries but differ according to the reservoir geometry and foundation material properties that are chosen to match those on the side being modeled. It was hoped that the results from the two analyses would envelop those from a full analysis.

5.4.1 Dam

Generation of the finite element mesh for Morrow Point Dam is simplified because it is a single-centered variable thickness arch dam and, thus, characterized

by horizontal circular sections on the upstream and downstream sides of the dam. The finite element mesh appears in Figure 5.10 and is symmetric about the $x - y$ plane. The element utilized is a shell element with quadratic shape functions and eight nodes located at mid-thickness. Element thicknesses can be computed from auxiliary upstream and downstream coordinates or can be specified in the input data. Abrupt changes in thickness at the spillway section of the dam, although not depicted in Figure 5.10, are modeled by assigning appropriate thicknesses to the corresponding nodes in the mesh.

Five degrees of freedom are associated with each node: three translations and two rotations of the through-thickness nodal line about axes perpendicular to its own axis. Normal stresses perpendicular to the dam mid-thickness plane are set to zero. The plane b-e-g-f-a in Figure 5.10 defines the dam-fluid interface in the LHS model and the plane b-e-d-f-a is the dam-fluid interface in the RHS model. The dam–foundation interface is defined by the plane c-i-h and the plane of symmetry is the $z = 0$ plane (a-f-h), where appropriate boundary conditions are applied in the analysis.

The material properties used in the dam model were obtained from a core testing program conducted by the Bureau of Reclamation [35]. In order to monitor the physical properties and effects of age on concrete placed in the dam, 10 inch diameter cores at various locations were extracted for testing at 60 days, 180 days, 1 year, 5 years, and 10 years after placement. Tests were conducted to determine the density and elastic properties on all cores. Density was determined in the usual manner by weighing each core and submerging it in water to obtain the volume of the sample. Young's modulus of elasticity and Poisson's ratio were measured with dial gases mounted on an extensometer-compressometer frame, which monitored longitudinal and lateral deformations as the core was loaded. Based on the results of these tests, the initial value for Young's modulus used in the dynamic analysis

was 5.0E + 06 psi and a value of 0.2 was used for Poisson's ratio. The unit weight of the concrete was taken as 150 pcf.

5.4.2 Foundation

An appropriate portion of the foundation region is idealized using linear three-dimensional solid finite elements and is shown in Figure 5.11. Like the dam, the foundation mesh is symmetric about the $x-y$ plane. The mesh is constructed with planes cut into the adjacent foundation normal to the dam–foundation interface at nodal locations. Each normal plane approximates a semicircle whose radius equals the dam height; this extent yields a converged dam–foundation eigensolution when foundation mass is omitted.

Material properties for the foundation were obtained from field and laboratory tests conducted by the Bureau of Reclamation. Detailed descriptions and results of the foundation investigations are given in reference [36]. The variation in Young's modulus throughout the foundation adjacent to the dam is shown in Figures 5.12–14 and was reproduced to the extent possible in the finite element model. An average value is 3.8E+06 psi. Poisson's ratio was set to 0.2 and the unit weight of the foundation rock was taken to be zero.

5.4.3 Water Domain

The LHS and RHS water meshes shown in Figure 5.15 are constructed in horizontal layers bounded by contour lines in the reservoir and the upstream face of the dam (see Figure 5.3). The element employed is a linear brick element with one pressure degree of freedom per node. Each water mesh extends back 663 feet from the upstream face of the dam and has a maximum depth of 388 feet. Beyond 663 feet, the transmitting boundary solution for an infinite fluid domain is appropriately applied since the reservoir is fairly uniform in cross-section (Figure 5.3). The infinite fluid domain is also modeled to a depth of 388 feet.

The finite element model can be used to represent compressible or incompressible fluid behavior. Boundary conditions include the absorptive condition along the reservoir floor and sides and the transmitting condition on the upstream boundary which allows transmission of pressure waves in the upstream direction. For incompressible fluid behavior, the reservoir floor and sides are taken to be rigid. Since it is assumed that sedimentation in the reservoir is light, the only medium considered there is water.

The reflection coefficient α that enters the absorptive boundary condition along the reservoir floor and sides is expressed by equations 4.15 and 4.16. Taking Young's modulus of the foundation to be 3.8E+06 psi, Poisson's ratio as 0.2, and the unit weight as 125 pcf, $\alpha = 0.68$ results. However, for reasons stated in Section 5.5.4.2, the higher value $\alpha = 0.9$ is used in all computations with the compressible water model, which means a 90% reflection for a pressure wave normally incident to the reservoir floor or sides.

Because of the irregular geometry present in the reservoir, computation of the nodal coordinates was time-consuming; however, a semi-automated mesh generator and a graphics terminal helped to simplify the procedure. The structure at the bottom of the reservoir (see Figure 5.15) is a coffer dam that was built to divert the river during construction and was left in place after the dam was completed. Its profile is included for completeness and does not significantly alter the response behavior.

5.5 Comparison of Experimental and Numerical Results, Full Reservoir

5.5.1 Preliminary Comments

Results from a correlation study using the observed behavior at Morrow Point Dam are discussed in this section. Numerical results are obtained from the analysis

procedure outlined in Chapter 4. As discussed in the previous section, parameters of the finite element models of the dam and foundation were obtained from actual field and laboratory tests. The objective of the finite element study was not only to match vibration characteristics at resonance, but also to match the actual frequency response curves.

The analysis of Morrow Point Dam was performed on the geometrically symmetric LHS and RHS 3-D models, and results from both are included in the comparisons. Predictions from the LHS model are compared with the experimental data obtained to the left of Block 10 (looking downstream) and, similarly, RHS results are compared with data obtained to the right of Block 10.

The correlation study was carried out by first calibrating the numerical models using experimental data obtained from the antisymmetric shake. The concrete and foundation rock stiffnesses were scaled equally to yield a match in the fundamental resonant frequency. Modal damping ratios for the dam–foundation substructure were then determined by matching experimental and numerical resonant peak amplitudes on the dam crest. Once satisfactory agreement was obtained, analyses of the dam were then performed for the symmetric shake using similar stiffnesses and damping. Both incompressible and compressible fluid behavior were considered.

The numerical results employed 12 modes of the dam-foundation substructure in all cases. Values of modal damping for the first two antisymmetric modes were chosen to fit the experimental data of the first two antisymmetric resonances at full reservoir. These values indicated the contribution to the damping from the dam-foundation substructure to be on the order of 1% to 1.5%. Therefore, damping values for the higher modes in the antisymmetric analyses (both incompressible and compressible water models) were set to 1.3%. For the symmetric analyses, where no fitting was performed, damping values for all dam-foundation modes were set to 1.5%, again in both the incompresssible and compressible water models.

The compressible water model employed in the calculations appeared to be of the type shown in Figure 4.2(a) in which the fundamental resonant frequency of the infinite uniform portion, f_I, equals that of the entire water domain, f_{wat}. This was true for both antisymmetric response ($f_I^a = f_{\text{wat}}^a = 7.06$ Hz LHS, $= 8.14$ Hz RHS) and symmetric response ($f_I^s = f_{\text{wat}}^s = 3.81$ Hz LHS, $= 4.14$ Hz RHS). These values will be used later to estimate the effect of water compressibility on the computed dam response.

In the following sections, plots are presented that contain frequency responses of dam accelerations on the crest and water pressures on the upstream face of the dam. Both amplitude and phase information are shown, and the amplitudes are normalized by the exciting force. In these plots, curves that appear as solid lines represent experimental data, while the numerical results are indicated by dashed curves.

Plots are also presented of the response shapes of the dam crest and center cantilever (radial component) and the water pressure at the resonant frequencies. In order to provide the best correlation to the experimental data, the comparisons are made with the computed resonating shapes that result from the shaker excitation and not with the system eigenvectors. To depict both amplitude and phase information, the shapes are plotted at five equally spaced time instants over a half cycle of response. For the antisymmetric response shapes, the initial time instant is taken when the response amplitude at a reference point (crest of Blocks 7 and 13 for dam response, Blocks 7 and 12 at a 100 foot depth for water pressure) reaches zero. For the symmetric response shapes, the initial time instant corresponds to maximum response amplitude at a reference point (crest of Block 10 for dam response and Block 10 at a 300 foot depth for water pressure). The plots of the measured and computed shapes are scaled to the same amplitude with the scale factors given in the figures.

Table 1 presents a summary of the resonant frequencies and damping values pertaining to Morrow Point Dam for the full reservoir case (water level 9 feet below the crest). Both experimental and numerical results are presented.

5.5.2 Antisymmetric Behavior

5.5.2.1 Incompressible Water Model

Figures 5.16 and 5.17 show measured and computed frequency response curves for crest acceleration. The Young's moduli of the dam and foundation were scaled uniformly by a factor E_{rat} to yield a match in the fundamental resonant frequency at 3.30 Hz. Required factors were close to unity; $E_{\text{rat}} = 0.93$ and 1.00 for the LHS and RHS models, respectively. The difference between these values arises from different added masses in the two models, greater on the right where the reservoir is narrower (see Figure 5.3) . Modal damping values for the first two resonances were obtained by matching the measured and computed resonant amplitudes at Block 13 for the RHS model and at Block 7 for the LHS model. Resulting values were 1.5% experimental (half-power determination), 1.62% LHS model and 1.47% RHS model for mode 1. Values for mode 2 were 3.3% experimental, 1.45% LHS model and 1.14% RHS model. Recall that the damping values for the numerical model are associated with modes of the dam-foundation system only.

The agreement between the measured and computed response curves in Figures 5.16 and 5.17 below 5 Hz, including the fundamental resonance, is very good. The 180 degree phase shift through the fundamental resonance is characteristic of a single degree-of-freedom oscillator and indicates that almost no modal interference is present there. The jagged peaks in the experimental phase curves around 5 Hz are considered to be inaccurate because of the relatively small crest accelerations measured there.

In the vicinity of the second resonance, the agreement is not as good. The

predicted resonant frequency exceeds the experimental value by 8% (average value from LHS and RHS models). The smaller analytical damping values are consistent with the shapes of the resonant peaks shown in the figures which are thinner than the experimental ones. This difference in damping values may be due to contamination of the measured antisymmetric resonance at 6.21 Hz from symmetric resonances at 5.4 Hz and 6.7 Hz. The phase plots in the vicinity of the second resonance indicate that some modal interference may be present.

The same level of agreement present in the acceleration response curves can be seen in the pressure responses in Figures 5.18 and 5.19 even though no further fitting of the experimental data has been performed. The influence of reservoir geometry on the relative amplitudes of the pressures accounts for the larger responses on the right side of the dam where the reservoir is narrower. Because the true reservoir geometry is between those of the finite element models, the effects of reservoir geometry on the predicted pressure responses may appear slightly exaggerated. Nonetheless, the good match obtained for the pressure comparison relieves some of the concerns expressed earlier regarding the hydrophone calibrations.

To further evaluate how well the numerical model can predict the observed dam response, a correlation between the calculated resonating shapes and those determined experimentally is presented in Figures 5.20 and 5.21 (dam crest) and in Figures 5.22 and 5.23 (pressure profile). The wiggles in the measured dam crest shapes are due to the four separate vibration tests used to measure the crest response; probably, the dam did not respond in exactly the same manner in each test. The similarity in the crest shapes between the first and second resonances can be explained by the fact that the second resonance is a higher cantilever mode (see UCB test results in reference [17]). This is also evident in the pressure profile of Figure 5.23. The crossover in the pressure profile near the 100 foot depth accounts for the small amplitudes at the second resonance in Figures 5.18 and 5.19. Overall,

the agreement between the computed and measured resonating shapes is very good at both resonances.

5.5.2.2 Compressible Water Model

With water compressibility neglected, the hydrodynamic effects on the dam response are equivalent to added mass terms, which are real-valued and independent of excitation frequency. A compressible water solution, however, introduces complex-valued, frequency-dependent, added mass terms. Actually, only the real part is added mass; the imaginary part represents added damping. The added damping results from pressure wave absorption along the reservoir floor and sides and from the energy radiation due to the propagation of pressure waves in the upstream direction.

The comparison between the computed and measured results as presented in Figures 5.16 to 5.23 for the incompressible water model is duplicated in Figures 5.24 to 5.27, 5.29 to 5.32 for the compressible water model. Values of E_{rat} to match the fundamental resonant frequency increased by only 2% over those used previously because the increase in the added mass from water compressibility was slight at this frequency significantly below $f^a_{\text{wat}} = 7.06$ LHS, 8.14 RHS. Numerical damping values to match the measured resonant peak amplitudes decreased by 12% (LHS) and 20% (RHS) at the fundamental resonance and by 28% (LHS) and 69% (RHS) at the second resonance due to the additional damping mechanism associated with compressible water.

The agreement between the measured and computed frequency response curves (see Figures 5.24 to 5.27) below 5 Hz is similar to that obtained with the incompressible water model since water compressibility has a negligible effect in this frequency range which is considerably below f^a_{wat}. Some improvement is seen at the second resonance regarding the frequency match where the difference is now only 2.6% (average value from LHS and RHS models), which is less than the 8% difference

obtained with the incompressible water model and is the result of the higher added mass near f^a_{wat}. This increased added mass is not evident in Figures 5.26 and 5.27 since the pressure response at the second resonance is small because of the crossover at the 100 foot depth, but it is evident in Figure 5.28 where the pressure response at Block 12 at 300 feet is shown. The comparison is shown for both incompressible and compressible models. As with the incompressible water model, very good agreement is obtained between the measured and computed resonating shapes in Figures 5.29 to 5.32.

5.5.3 Discussion of Water Compressibility Effects

In order to determine the effect of water compressibility on the dam response, the following general criteria are employed. Here, f_{wat} is the fundamental resonant frequency of the water only, and f_{dam} is the fundamental resonant frequency of the dam-foundation system without water. These criteria should be applied separately to symmetric and antisymmetric responses.

Criteria

If

$$\frac{f_{\text{wat}}}{f_{\text{dam}}} > 1.5 \,,$$

then the response of the dam is mostly independent of water compressibility effects at and below the fundamental resonant frequency of the dam-foundation-water system. Possible effects at higher frequencies may be present.

If

$$\frac{f_{\text{wat}}}{f_{\text{dam}}} < 1.1 \,,$$

then water compressibility effects on the dam-foundation-water system are pronounced.

If

$$1.1 < \frac{f_{\text{wat}}}{f_{\text{dam}}} < 1.5 \,,$$

water compressibility effects should fall somewhere between the two extremes above.

Morrow Point Dam

Applying these criteria to the behavior at Morrow Point Dam reveals the following. Values of f_{wat} and f_{dam} given below are averages from the RHS and LHS models.

Antisymmetric Response:

Based on the numerical results obtained from the compressible water solution, the fundamental frequency associated with the water is 7.6 Hz. The computed fundamental frequency of the dam and foundation (excluding water) is 4.1 Hz, which yields a ratio

$$\frac{f^a_{\text{wat}}}{f^a_{\text{dam}}} = \frac{7.6 \text{ Hz}}{4.1 \text{ Hz}} = 1.8 \, .$$

According to the above criteria, the antisymmetric response of the dam-foundation-water system should not be affected by water compressibility in its fundamental resonance. This is consistent with the findings of the correlation study. The effect of water compressibility seen at the higher resonance was mentioned as a possibility in the criteria.

Symmetric Response:

Numerical results presented in the next section indicate the fundamental frequency of the dam and foundation to be 4.2 Hz; that of the water is 3.97 Hz. The ratio associated with the symmetric response of the dam is

$$\frac{f^s_{\text{wat}}}{f^s_{\text{dam}}} = \frac{3.97 \text{ Hz}}{4.2 \text{ Hz}} = 0.95 \, ,$$

and it appears, then, that water compressibility effects will play a significant role in the response behavior.

Comment

The above results suggest an interesting procedure for investigating water compressibility effects. Since water compressibility will not significantly influence the antisymmetric response of Morrow Point Dam, experimental data from an antisymmetric shake can be used to calibrate a finite element model without concern over water compressibility effects. This calibration should result in reasonable values for Young's moduli and damping associated with the dam and the foundation. The calibrated model can then be used to reproduce the experimental data from a symmetric shake (where compressibility should be important) in two analyses—one incorporating and one neglecting water compressibility. Such a procedure is followed here and continues in the next section.

5.5.4 Symmetric Behavior

5.5.4.1 Incompressible Water Model

Figures 5.33 and 5.34 show the experimental and computed frequency responses for crest acceleration at Block 10 and pressure at a depth of 300 feet on Block 10 for the symmetric shake. Agreement between the observed and computed behavior from the incompressible water model is poor, including the correlation between resonant frequencies and peak amplitudes. It should be noted that the numerical model was the same one that successfully reproduced the antisymmetric forced vibration data (see Section 5.5.2.1). Similar damping values of 1.5% in all dam-foundation modes were used. The lower peak amplitudes in the experimental data, however, suggest that much higher damping is present (determined to be about 4% of critical for the first 3 resonances, see Table 1). If 1.5% is a reasonable value for the dam and foundation contributions (true for the antisymmetric response), then the presence of another damping mechanism is suggested. One possibility is that associated with water compressibility, which cannot be directly accounted for by an incompressible

water model. Of course, it is also possible that the amount of foundation radiation damping is greater under symmetric response than under antisymmetric response.

A comparison of the experimental and computed response shapes of the dam crest, center cantilever, and water pressure at the first three resonances is shown in Figures 5.35 to 5.43. The computed resonances at 3.30 Hz, 5.32 Hz and 6.07 Hz (average values from RHS and LHS models) correspond to the measured ones of 2.95 Hz, 3.95 Hz, and 5.4 Hz, respectively. This correlation demonstrates the poor accuracy in the computed resonant frequencies. In addition, a discrepancy exists in the cantilever shape of the dam at the second resonance (see Figure 5.39), where the expected higher cantilever mode (with its crossover) is missing in the experimental data, leaving a similarity in the measured response shapes of the dam at the first two resonances. Also, the experimental pressure response at the second resonance, which contains a crossover (see Figure 5.42), cannot be attributed to the shape of the dam response as is the case for the computed results. These points will be clarified in the following section.

5.5.4.2 Compressible Water Model

The numerical results presented in this section were obtained with a compressible water model and appear in Figures 5.44 to 5.54, which parallel Figures 5.33 to 5.43 for the incompressible water model. The numerical model used here is the same one used in Section 5.5.2.2 which successfully reproduced the antisymmetric forced vibration data, and except for the inclusion of water compressibilty and a 2% difference in E_{rat}, is the same as that used in the previous section. Also, as in the previous section, damping values are 1.5% in all dam-foundation modes and no fitting has been performed.

Examination of Figures 5.44 and 5.45 shows that the inclusion of water compressibilty has reduced the computed resonant peak amplitudes to reasonable levels and improved the match to the observed resonant frequencies (as compared to the

results with incompressible water of Figures 5.33 and 5.34). These improvements are attributed to the added damping from the compressible water and to the resonance of the hydrodynamic terms in equation 4.25 at the fundamental frequency of the water, f^s_{wat}, determined to be 3.81 Hz for the LHS model and 4.14 Hz for the RHS model. As these values equal f^s_1 for the respective models, the numerical water model appears to be of the class shown in Figure 4.2(a).

The amount of disagreement in Figures 5.44 and 5.45 indicates that considerable parameter adjustment of E_{rat}, α, and damping values would be required to achieve the quality of the match attained for the antisymmetric response. In this regard, the too highly damped second resonance in the numerical results would present a problem because even if the dam-foundation contribution to the damping were reduced to zero, the computed peak amplitude would still be only 60% of the measured amplitude. Thus, the amount of damping attributed to the compressible water appears to be overestimated by the finite element model in the frequency range above the fundamental water frequency, $f^s_{\text{wat}} = f^s_1$, which is where such damping is largest. Lowering α below 0.9 worsens the problem and raising it to 1.0 helps, but not much because the change in α is small; this is why a high value was chosen in the first place. The reservoir could conceivably be made bounded 5000 feet upstream where a bend exists in the river (see Figure 5.2), but with a reasonable α, pressure wave reflections would decay to small values by the time they returned to the dam. Thus, bounding the reservoir at this distance would have little effect on the computed dam response.

The resonating shapes of the dam response and water pressure (see Figures 5.46 to 5.54) show good agreement between the measured and computed results. The cantilever crossover in the computed shape at the second resonance (see Figure 5.50) has largely been eliminated, and is now much closer to the measured shape than that computed using incompressible water (see Figure 5.39). The question

of modal orthogonality, which arises because of the similar shapes of the first two dam resonances, can be addressed by considering the system mode shapes which include the water response, and it is the water that has distinctly different behaviors at the two resonances (see Figures 5.52 and 5.53). The crossover in the pressure response at the second resonance is probably due to f^s_{wat} being exceeded and the resulting presence of the second water mode, which contains the crossover. This feature cannot be duplicated by the incompressible water model.

5.6 Direct Evidence of Water Compressibility

The importance of water compressibility on the symmetric response seen in the previous section motivates the direct determination of f^s_{wat} from the experimental data so that a comparison with the computed value can be made. However, the observed resonances in the water pressure response coincide with the resonances of the dam-foundation-water system (see Figure 5.7, for example) and do not occur at the resonant frequencies of the water body itself. Because of this, several researchers have tried to isolate the fundamental resonance of the water body by normalizing a representative pressure frequency response with a representative dam acceleration frequency response [11,13]. Such an attempt is presented in Figures 5.55 using both experimental data and computed LHS results with compressible water. Shown are the magnitude, phase, real and imaginary parts of the normalized quantity. The pressure response selected is at Block 10 at a depth of 300 feet (symmetric shake, Figure 5.45) and the normalizing dam acceleration is taken at the crest of Block 10 (symmetric shake Figure 5.44).

Both sets of normalized pressure responses in Figure 5.55 show a resonant behavior. However, the resonant frequency indicated for the LHS water model is 3.35 Hz, which differs considerably from the known value of f^s_{wat} equal to 3.81 Hz. Also, the character of the resonance indicated for the LHS water model is not the

expected one since the water model is believed to be of the class shown in Figure 4.2(a). Therefore, based on the results with the numerical model, the normalized pressure method for determining f^s_{wat} is judged to be invalid. Note that the apparent resonances in Figure 5.55 both peak at the frequencies where the normalizing accelerations reach minimums (see Figure 5.44). Thus, the resonances of Figure 5.55 are thought to be artificial and not indicative of the true resonant behavior of either the LHS water model or the actual water domain. For the normalized pressure method to work, the shapes of the dam response (which excite the water) must not change in the frequency interval examined, and although this is not too far from the present case, the slight changes in the cantilever responses that do occur (see Figures 5.49 and 5.50) are apparently enough to prevent the water behavior from being revealed.

A theoretically valid procedure to isolate the response of a resonating water mode is to extract the modal amplitude from the water pressure response and to normalize it by the amplitude of the component of the dam acceleration which delivers a pure excitation to the water mode. This requires prior knowledge of the shape of the water mode and of the distribution of pressure and acceleration everywhere on the upstream face of the dam. With these criteria not met here, the pressures and accelerations measured at Block 10 are assumed to be representative of the distribution on the entire dam face. In addition, the vertical distribution of the fundamental water mode at Block 10 is assumed to be

$$\cos(\pi y/2H) \ ,$$

where y = vertical distance from the reservoir floor

H = water depth,

which is exactly true for a reservoir of constant depth with $\alpha = 1.0$. Thus, the

quantity

$$Z(\omega) = \frac{\int_0^H P_{\text{BLK10}}(y,\omega)\, \cos\frac{\pi y}{2H}\, dy}{\int_0^H a_{\text{BLK10}}(y,\omega)\, \cos\frac{\pi y}{2H}\, dy},$$

where $P_{\text{BLK10}}(y,\omega)$ = vertical distribution of pressure at Block 10

$a_{\text{BLK10}}(y,\omega)$ = vertical distribution of acceleration (radial component) at Block 10

will be used to isolate the fundamental resonance of the water. Plots of $|Z(\omega)|$, the phase of $Z(\omega)$, and the real and imaginary parts of $Z(\omega)$ are presented in Figure 5.56 for the experimental data and computed LHS results with compressible water.

The curves in Figure 5.56 obtained from the numerical results now peak at 3.88 Hz, which is near the computed value $f^s_{\text{wat}} = 3.81$ Hz for the LHS model. The resonant behavior is that expected for the fundamental water mode for the class of reservoir models shown in Figure 4.2(a) and is characterized by a transition from real (standing wave) below $f^s_{\text{wat}} = f^s_f$ to imaginary (traveling wave) beyond through a phase shift of 90 degrees. This successful isolation of the fundamental water resonance from the numerical results is due to the theoretical validity of the method and reasonableness of the two assumptions noted above. Thus, the curves in Figure 5.56 obtained from the experimental results are expected to represent the true behavior of the actual water domain.

Comparison between the curves in Figure 5.56 obtained from the experimental and numerical results shows significant differences in the resonant frequency, amplitude, and character of the resonance. However, the resonant frequency of the water obtained from the experimental data, 3.30 Hz, although lower than the computed value $f^s_{\text{wat}} = 3.81$ Hz, is not unreasonable and is consistent with the lower observed resonant frequencies of the system at the fundamental symmetric and second antisymmetric resonances (see Figures 5.44 and 5.24). Note that a lower f^s_{wat} implies a lower f^a_{wat}.

In addition, consider the concept of effective water depth

$$H_{\text{eff}} = \frac{C}{4f^s_{\text{wat}}},$$

as adapted from the exact expression for a reservoir of constant depth. With $f^s_{\text{wat}} = 3.81$ Hz (computed value), $H_{\text{eff}} = 310$ feet, and with the estimated actual value $f^s_{\text{wat}} = 3.30$ Hz, $H_{\text{eff}} = 358$ feet is obtained. Lowering the computed value for f^s_{wat} to 3.30 Hz would require increasing the effective depth of the water mesh from 310 feet to 358 feet, which would still be 29 feet less than the maximum water depth employed of 387 feet. Inclusion of the construction notch (mentioned in reference 34, see Figure 5.9) at the base of the dam would cause H_{eff} to increase; however, the notch was omitted from the analysis because of uncertainties concerning its profile around the dam and its continued existence. Note that steepening of the canyon walls would also raise H_{eff}. Although considerable effort was spent modeling the actual contours of the reservoir, improvement in the water mesh may still be possible. A more refined, perhaps full 3-D analysis, of the reservoir will be considered in the future.

The character of the resonance exhibited by the experimental curves in Figure 5.56 resembles the mixed resonance depicted in Figure 4.2(b) more than the other type of resonance shown in Figure 4.2(a) which is similar to that produced by the numerical water model. The positive and negative peaks of the real part (see Figure 5.56) are characteristic of a bounded domain, while the lingering imaginary part and the phase shift closer to 90 degrees than to 180 degrees are characteristic of an infinite domain. This behavior was shown to occur in Section 4.5 when the fundamental resonant frequency of the water, f_{wat}, was less than that of the infinite region, f_I, above which travelling waves can only exist. An increase in H_{eff} of the water mesh in the region between the dam and transmitting boundary would produce such a situation. Additional features of the experimental curves are

the higher resonant peak amplitude and smaller post resonance imaginary part as compared to the curves corresponding to the numerical results. The first feature may be due in part (as suggested by Figure 4.2(b)) to the water resonance occurring below f_I and may not imply that α is closer to 1.0. The second helps to explain the excessive damping in the second symmetric resonance of the numerical results. Thus, it is possible that reasonable modifications to the water mesh would lead to good agreement between the curves in Figure 5.56 and ultimately to an improvement in the comparison for the experimental and computed dam responses.

Factors other than reservoir geometry could also contribute to a lower f^s_{wat}. The through-thickness flexibility of the upstream face of the dam (not considered in the analysis) as well as the elasticity of the canyon (only pressure wave absorption included in the analysis) are two possibilities. If each of these factors contributes a 5% reduction in f^s_{wat}, then most of the desired change would be accounted for. Soft deposits (partially saturated) on the reservoir floor would have a similar effect. All of these possible factors deserve further investigation.

Finally, in light of possible errors in the experimental data and the relatively coarse spacing of the stations at Block 10 (see Figure 5.4), the interpretations of the experimental curves in Figure 5.56 should be viewed as preliminary until more complete and accurate data can be obtained. It is possible that a value for the fundamental water frequency higher than 3.30 Hz, which may be a little low, will result, as well as changes in the character of the resonance.

5.7 UCB Forced Vibration Tests on Morrow Point Dam

Researchers from the University of California in Berkeley performed forced vibration experiments on Morrow Point Dam in October 1969 [16] and again in June 1972 [17]. The early test was conducted with the water surface 158 feet below the crest, as shown in Figure 5.9. During the later test, the reservoir was nearly full,

approximately 4 feet above the level during the 1985 Caltech test. UCB employed two shakers of the same type as Caltech's but placed them 47 feet to each side of the centerline and operated them in phase for symmetric response and out of phase for antisymmetric response. Statham accelerometers, type A4, were used to measure the dam accelerations. No hydrodynamic pressure measurements were made.

Resonant frequencies and damping values obtained by UCB and Caltech at full reservoir agree well (see Table 2). This indicates that the dynamic properties of the dam remained unchanged for 13 years preceding 1985, which supports the effort described below to reproduce the 1969 UCB data with the finite element model calibrated using the 1985 Caltech data. UCB did miss the first and third symmetric resonances, the first presumably because of its depressed response (see Figure 5.7) and the third because of the existence of nodes of radial motion on the crest near the shaker locations (see Figure 5.48).

The comparison between the 1969 UCB experimental data at the lower water level and the computed results are presented in Figure 5.57 for the antisymmetric shake, in Figure 5.58 for the symmetric shake, and in Table 3. Except for the lower water level and the new shaker arrangement, the numerical models are the same ones used previously which were calibrated to the antisymmetric experimental data obtained by Caltech at water level 7156 feet. The computed antisymmetric responses at Blocks 8 and 14 (see Figure 5.57) were obtained with the LHS and RHS compressible water models, respectively. The LHS model results for the symmetric responses at Block 10 are presented in Figure 5.58 for both incompressible and compressible water models. No fitting of the numerical results to the data obtained at the low water level was done.

The agreement between the measured and computed antisymmetric responses in Figure 5.57 is considered to be reasonable and not too inferior to that obtained for the full reservoir case where fitting was performed. Water compressiblity effects

on the antisymmetric responses are negligible due to the high resonant frequency $f^a_{\text{wat}} = 11.67$ Hz (LHS and RHS average) resulting from the low water level. For the symmetric responses (Figure 5.58), the agreement is much poorer, especially with the incompressible water model, as was also the case with the full reservoir. One unusual feature of the experimental data is the close spacing of the first two measured resonant frequencies at 3.67 Hz and 4.52 Hz. This behavior is not reproduced in the numerical results, but could occur if f^s_{wat} (equal to 6.25 Hz LHS for the lower water level) were reduced. A decrease in f^s_{wat} would push the second resonant frequency down more than the first and improve the agreement between the observed resonant frequencies and those computed with the compressible water model. The smaller value for f^s_{wat} would also be consistent with the findings of the previous section.

5.8 Influence of Water Depth

Experimental and numerical results regarding the effect of water depth on the resonant frequencies of Morrow Point Dam are summarized in Table 4. The second resonant frequency for the symmetric response is sensitive to water compressibility since it is close to f^s_{wat}, and since the two frequencies cross as the water level is changed from 158 feet to 9 feet below the crest. A smaller f^s_{wat} would probably reduce the discrepancy in the frequency shift for the second symmetric resonance associated with the two levels (-12.6% experimental versus -18.1% numerical with water compressibility included). The important effect of the water on the dynamic response of Morrow Point Dam is reflected in the predicted 27% shift in fundamental frequency of symmetric response from empty to full reservoir conditions.

Mode	Experimental		Computed							
			Incompressible Water				Compressible Water			
			LHS		RHS		LHS		RHS	
	F(Hz)	ζ(%)	F(Hz)	ζ(%)	F(Hz)	ζ(%)	F(Hz)	ζ(%)	F(Hz)	ζ(%)
1A	3.30	1.5	3.31	1.62	3.31	1.47	3.31	1.42	3.31	1.18
2A	6.21	3.3	6.76	1.45	6.70	1.14	6.35	1.05	6.40	0.35
1S	2.95	4.0	3.29	---	3.31	---	3.05	---	3.10	---
2S	3.95	3.9	5.33	---	5.31	---	4.21	---	4.47	---
3S	5.40	4.3	6.11	---	6.03	---	5.96	---	5.88	---

Table 1. Resonant frequencies and damping values of Morrow Point Dam with full reservoir (water elevation 7156). Experimental damping values were determined by the half-power method, while values used in the analysis represent only the dam and foundation contribution needed to match the resonant peaks. The numerical model was fit to only the antisymmetric experimental data.

Mode	Caltech		UCB	
	F(Hz)	ζ(%)	F(Hz)	ζ(%)
1A	3.30	1.5	3.21	1.6
2A	6.21	3.3	6.05	2.5-3.5
1S	2.95	4.0	missed	
2S	3.95	3.9	3.93	3.0
3S	5.40	4.3	missed	
4S	6.70	3.4	6.73	3.8

Table 2. Summary of Data from Caltech (water elevation 7156) and 1972 UCB Forced Vibration Tests (water elevation 7160) at full reservoir.

Mode	Experimental		Computed			
			Incompresssible Water		Compressible Water	
	F(Hz)	ζ(%)	LHS	RHS	LHS	RHS
			F(Hz)	F(Hz)	F(Hz)	F(Hz)
1A	3.73	1.4	3.78	3.78	3.69	3.78
2A	6.67	1.8	7.16	7.16	6.93	6.93
1S	3.67	3.3	3.83	3.93	3.78	3.88
2S	4.52	2.3	5.79	5.84	5.22	5.36
3S	missed	---	6.62	6.73	6.57	6.70

TABLE 3. Resonant frequencies and damping values of Morrow Point Dam with partially full reservoir (water elevation 7007). Experimental damping values were determined by the half-power method. The numerical model was fit to only the antisymmetric experimental data at full reservoir (water elevation 7156).

Mode	Source	Empty Reservoir	Partial Res. (Hz)	Full Res. (Hz)	% Change Empty to Full	% Change Partial to Full
1A	FVT	---	3.73	3.30	---	-11.5
1A	FEM (comp)	4.10	3.74	3.31	-19.3	-11.5
1A	FEM (inc)	4.10	3.78	3.31	-19.3	-12.4
2A	FVT	---	6.67	6.21	---	-6.9
2A	FEM (comp)	8.19	6.93	6.38	-22.1	-7.9
2A	FEM (inc)	8.19	7.16	6.73	-17.8	-6.0
1S	FVT	---	3.67	2.95	---	-19.6
1S	FEM (comp)	4.23	3.84	3.08	-27.2	-19.8
1S	FEM (inc)	4.23	3.88	3.30	-21.9	-15.0
2S	FVT	---	4.52	3.95	---	-12.6
2S	FEM (comp)	7.04	5.30	4.34	-38.4	-18.1
2S	FEM (inc)	7.04	5.82	5.32	-24.4	-8.6

Table 4. Summary of resonant frequencies of Morrow Point Dam with empty, partially full (water elevation 7007) and full (water elevation 7156) reservoirs. The numerical model was fit only to the antisymmetric experimental data. Calculated values are averages from LHS and RHS models. FVT = forced vibration test, FEM = finite element model, comp = water compressibility included, inc = water compressibility neglected.

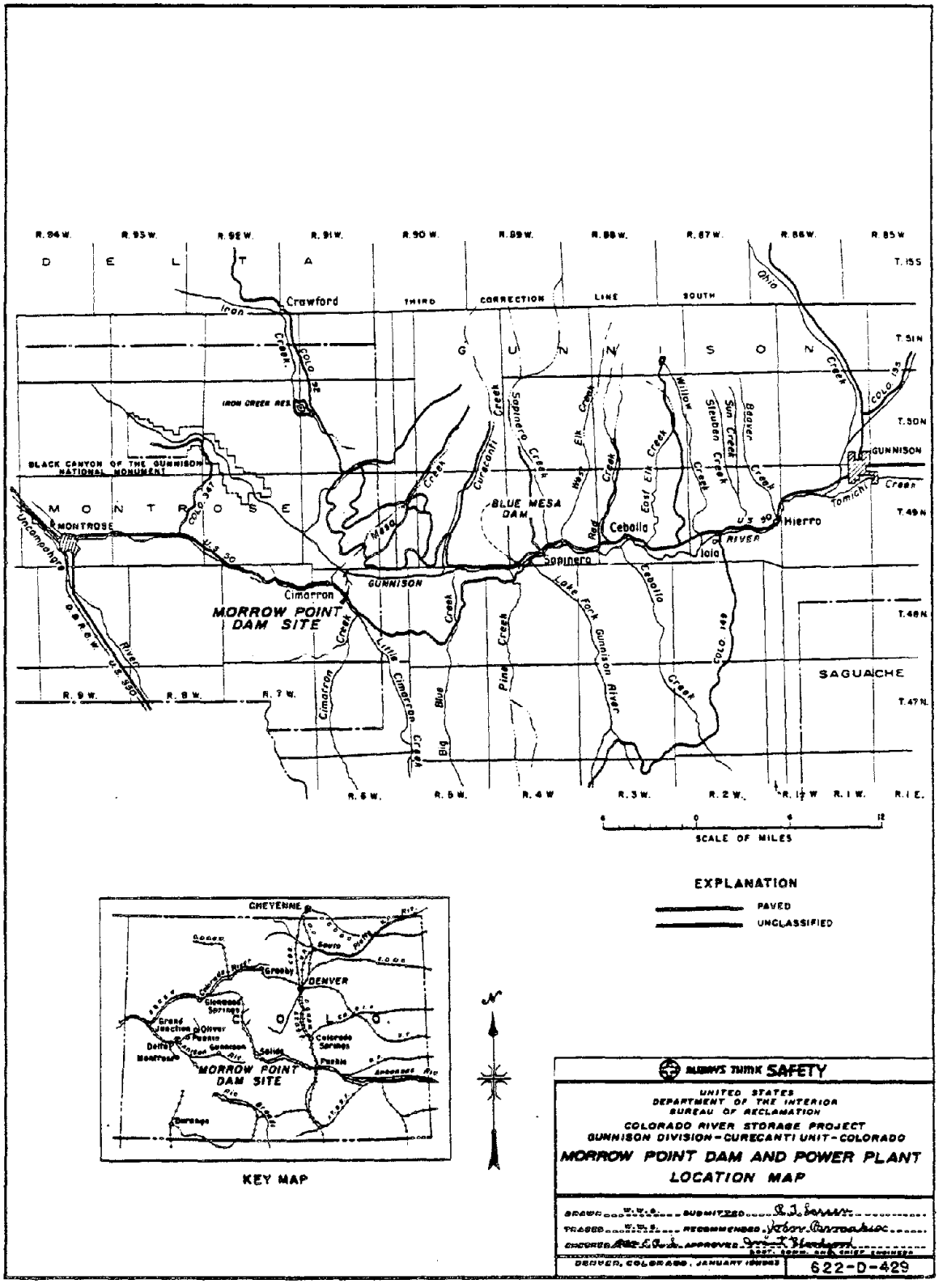

Figure 5.1 Location map of Morrow Point Dam. Taken from reference [36].

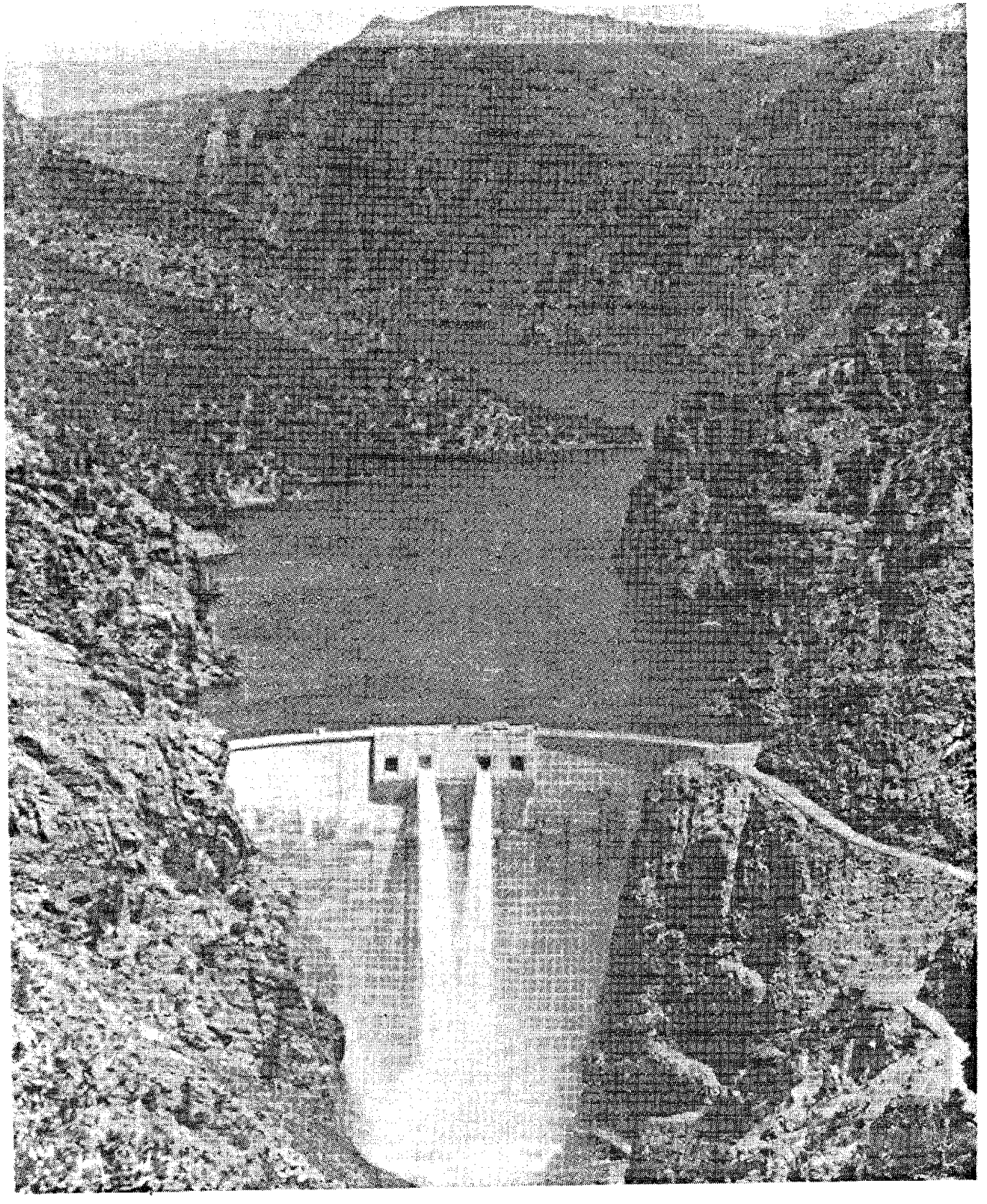

Figure 5.2 Aerial view of Morrow Point Dam and reservoir. Taken from reference [34].

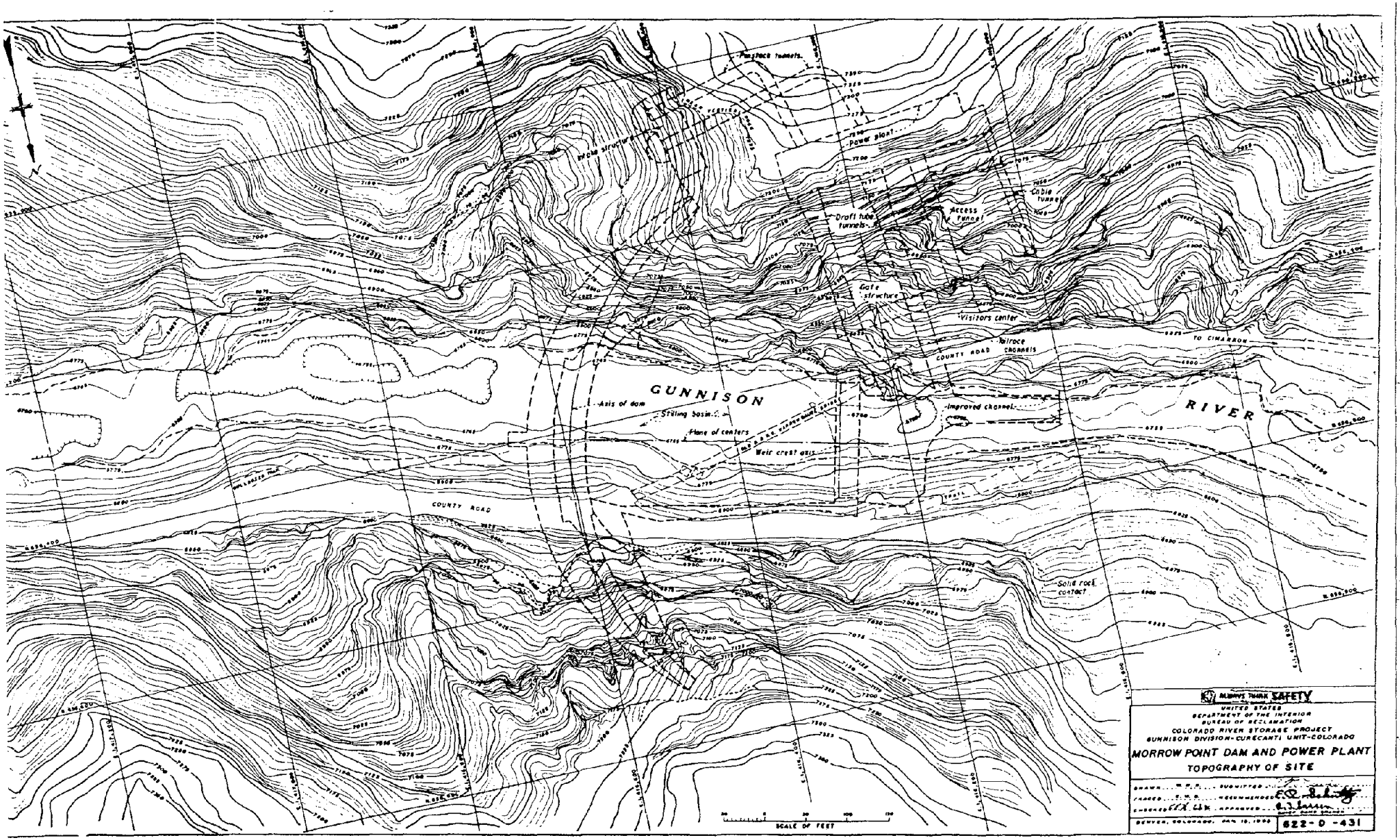

Figure 5.3 Topography of site at Morrow Point Dam. Taken from reference [34].

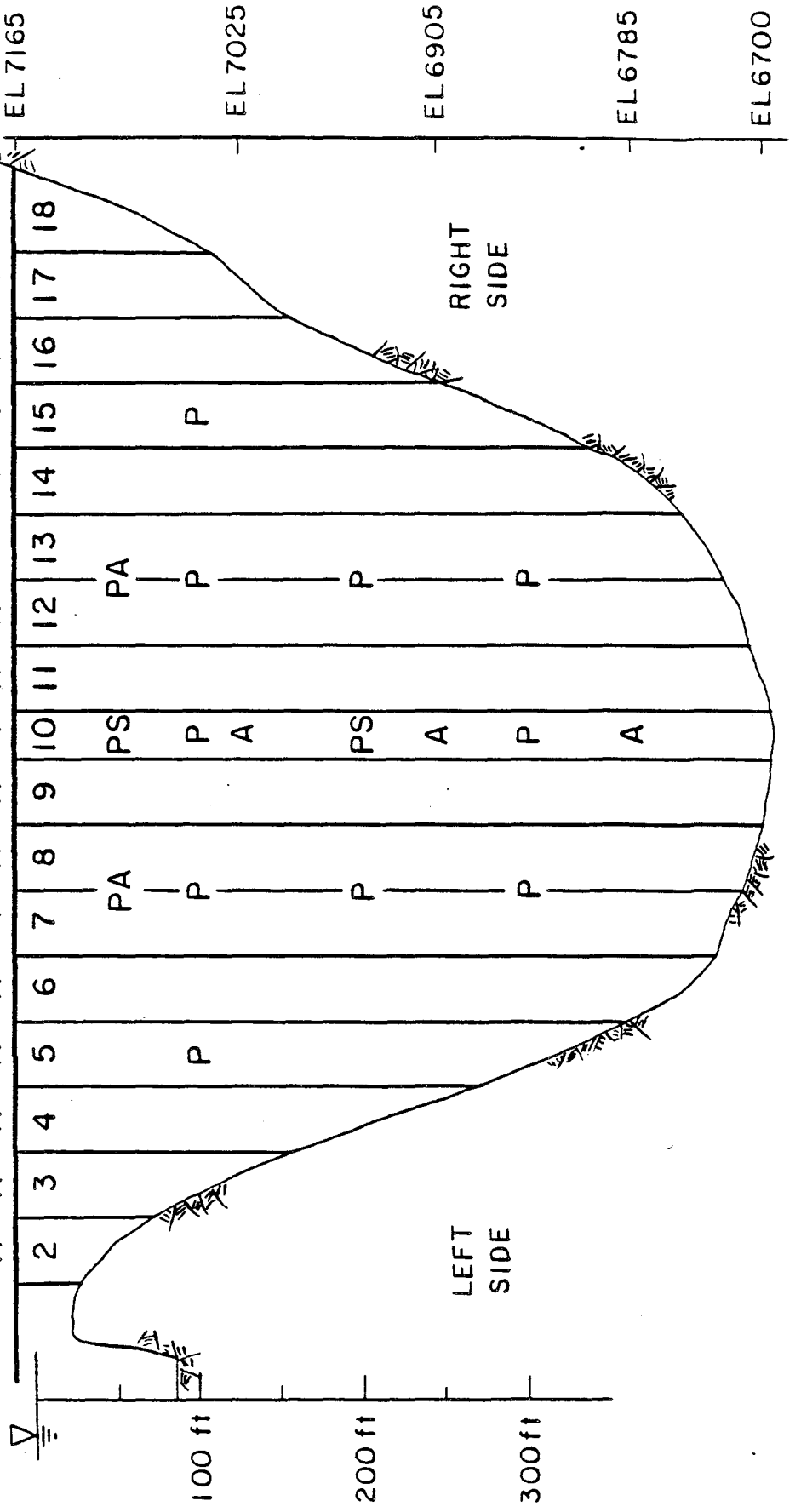

Figure 5.4 Stations at Morrow Point Dam where acceleration responses (A) and dynamic pressures (P) were measured. PS = symmetric shake only, PA = antisymmetric shake only.

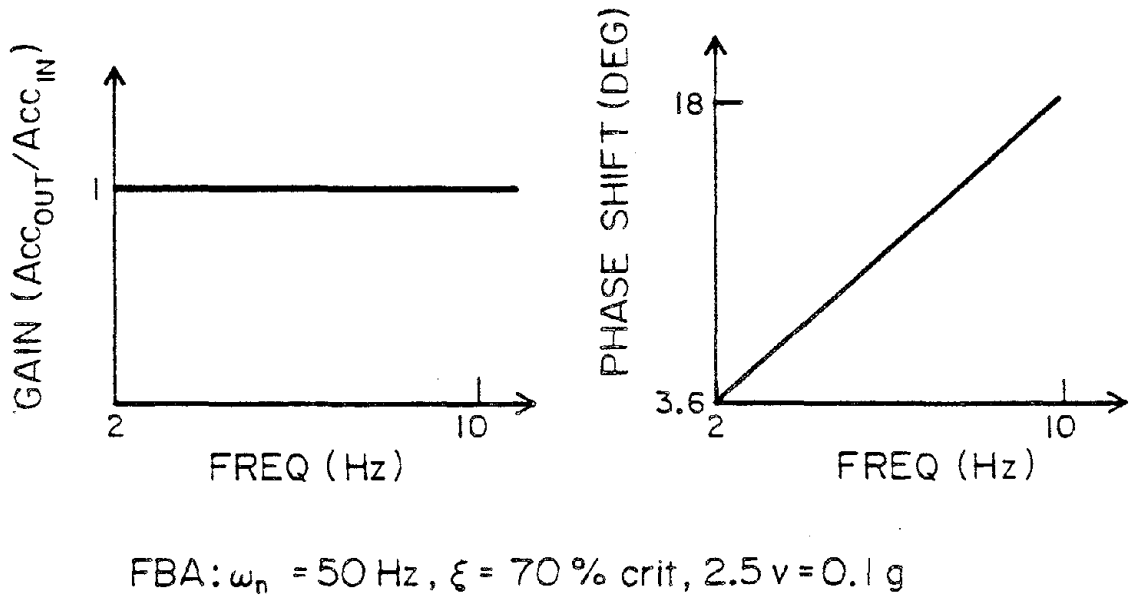

Figure 5.5 Frequency response curves for a typical FBA used at Morrow Point Dam. Characteristics are shown for the frequency range of interest.

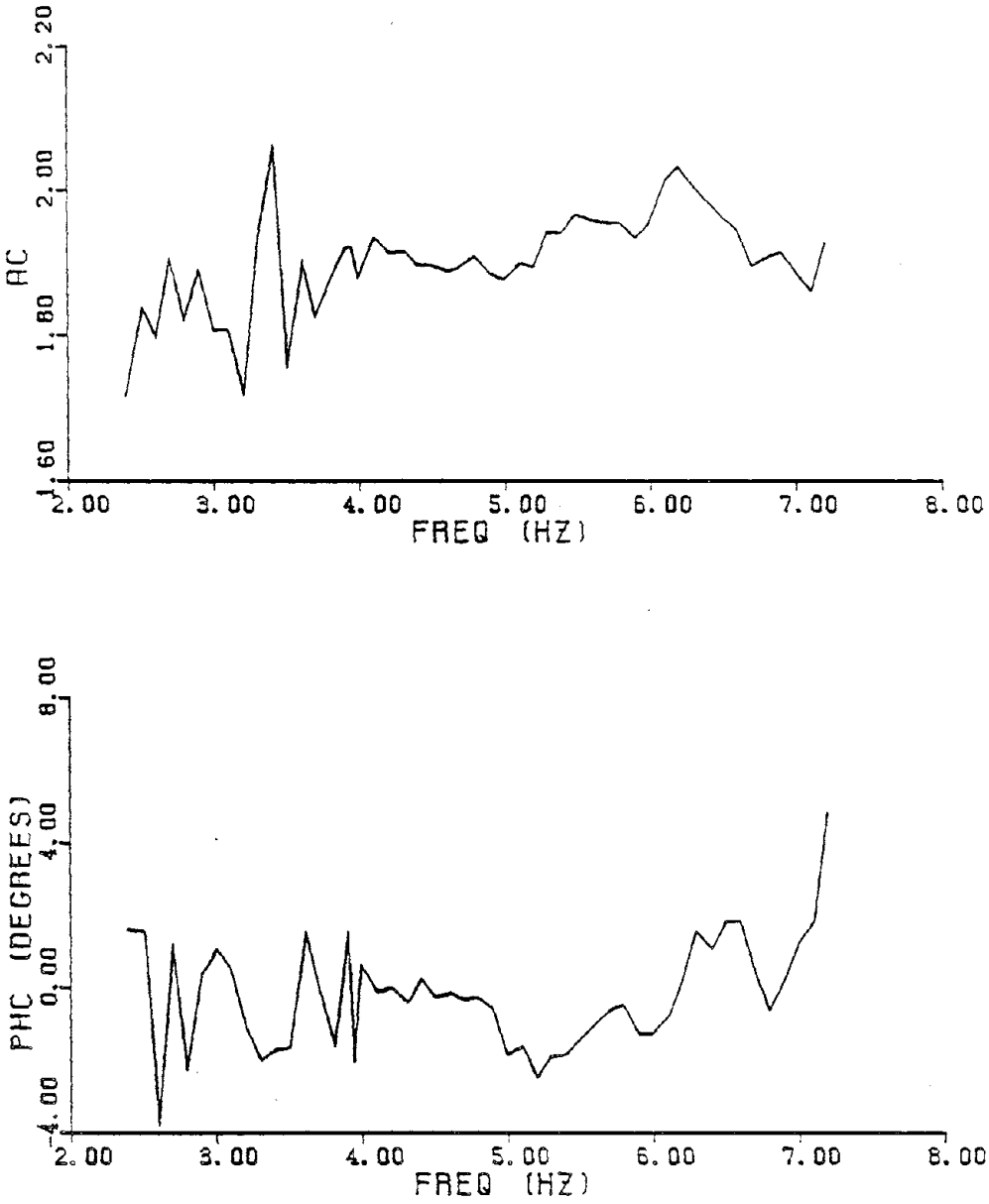

Figure 5.6 Frequency response curves for relative amplitude (AC) and phase angle (PHC) for the hydrophones with 120 feet (reference hydrophone) and 330 feet of cable.

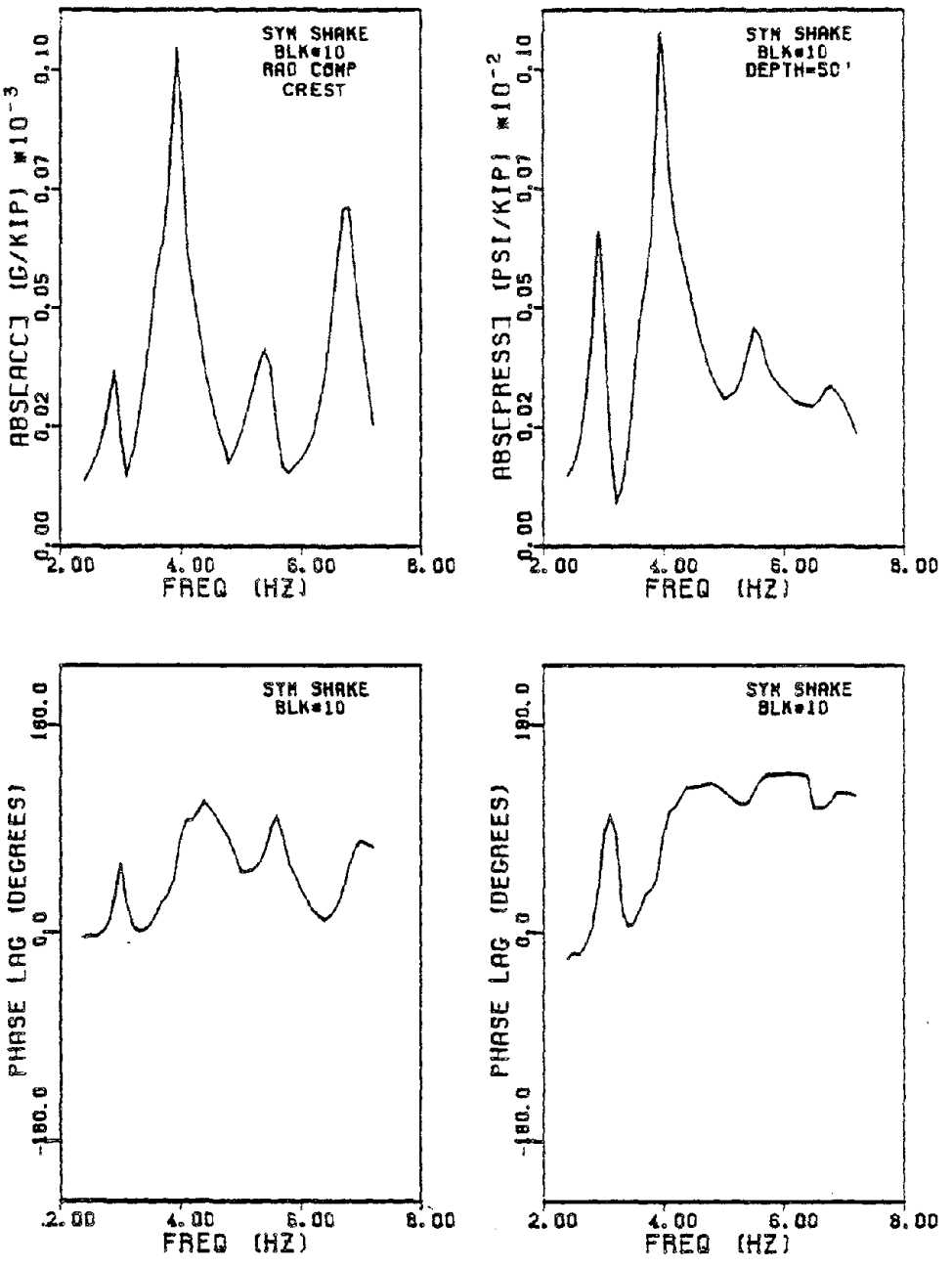

Figure 5.7 Frequency response curves obtained at Morrow Point Dam for the symmetric shake. Shown are the radial components of acceleration and phase on the crest at Block 10 and the pressure and phase at a depth of 50 feet.

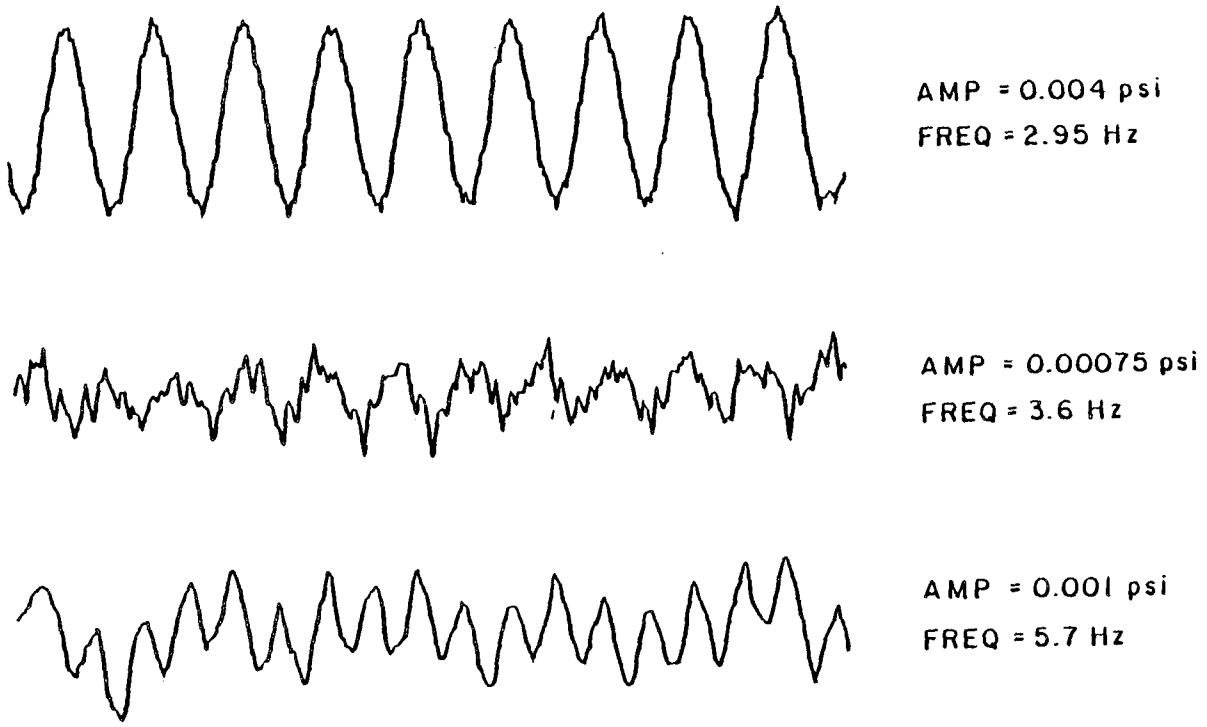

Figure 5.8 Sample dynamic pressure traces from Morrow Point Dam that indicate the quality of the signals obtained. Signal amplitudes, as determined by the least squares algorithm, are given on each trace. The top two traces were obtained under calm conditions; the bottom one was obtained under moderately windy conditions.

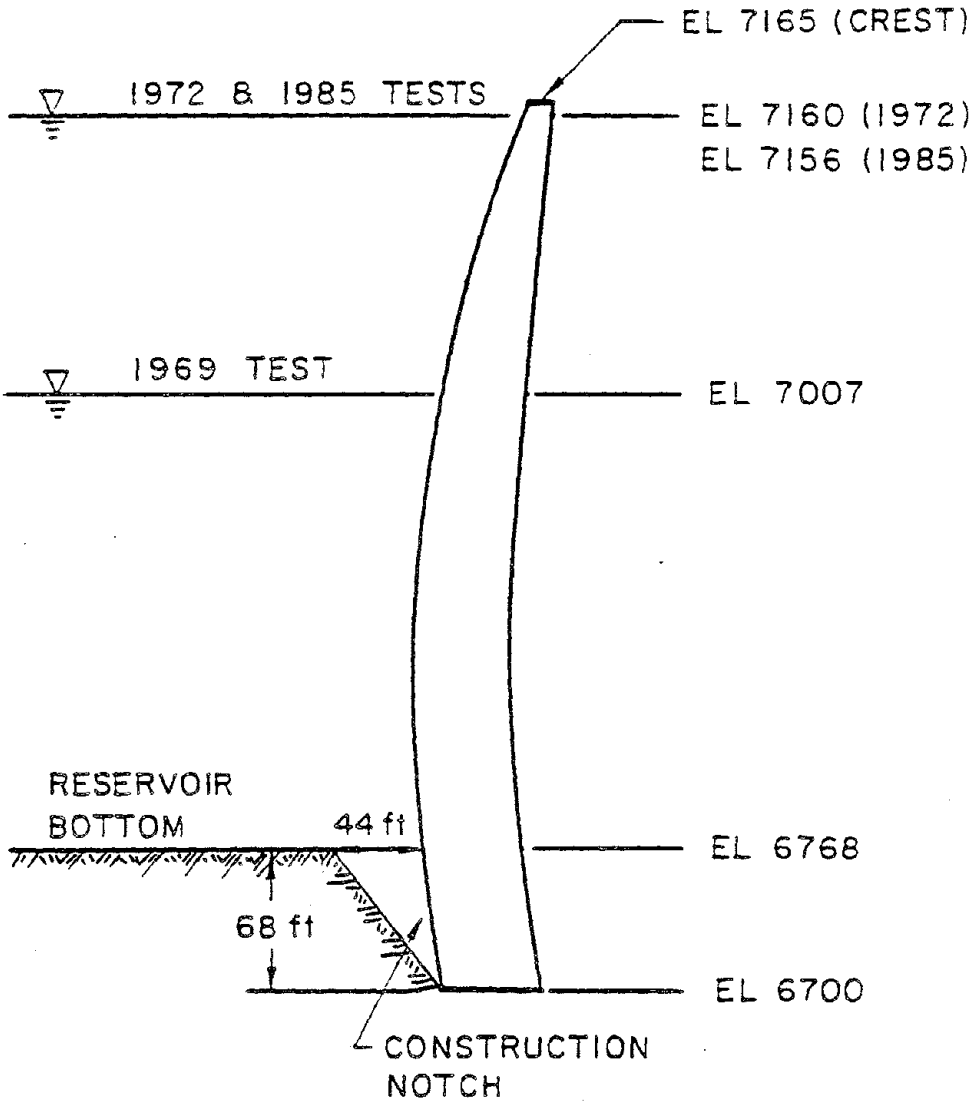

Figure 5.9 Section of Morrow Point Dam at the plane of centers showing water levels during various forced vibration tests.

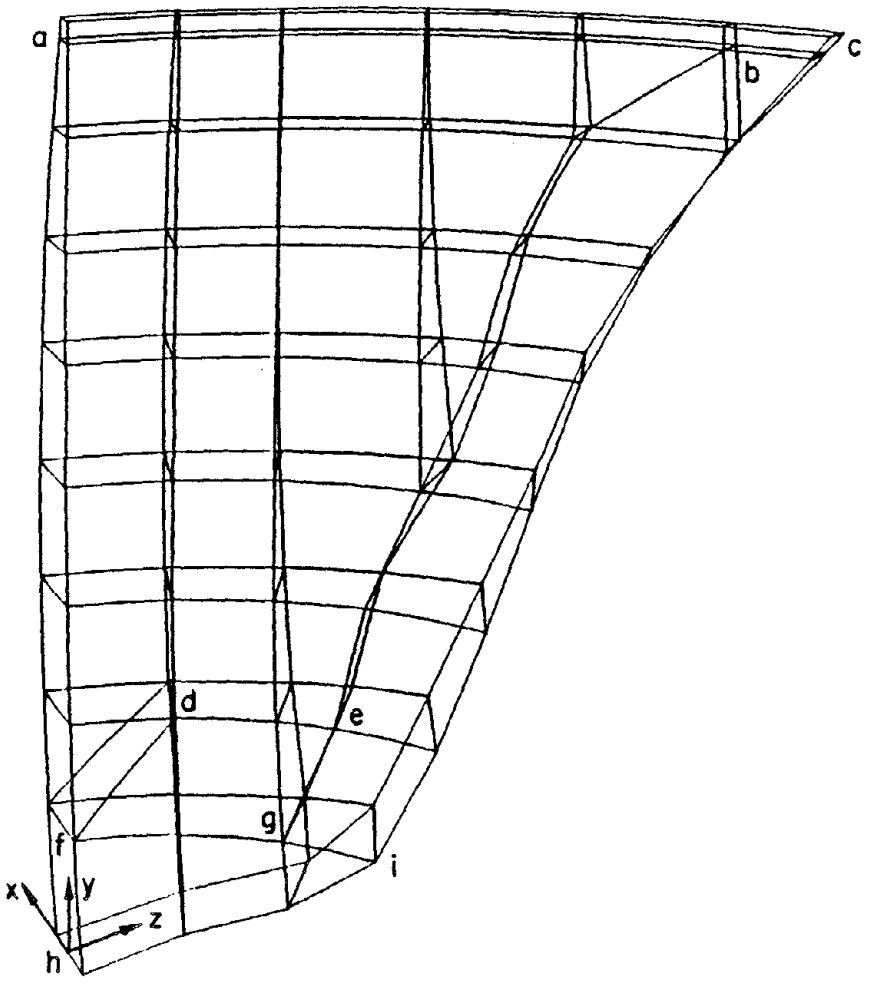

Figure 5.10 Finite element mesh of the symmetric half of Morrow Point Dam constructed with higher order thick shell elements. The dam-foundation interface is defined by c-i-h and the plane of symmetry is a-f-h. The dam-fluid interface is defined by region b-e-g-f-a for the LHS model and region b-e-d-f-a for the RHS model.

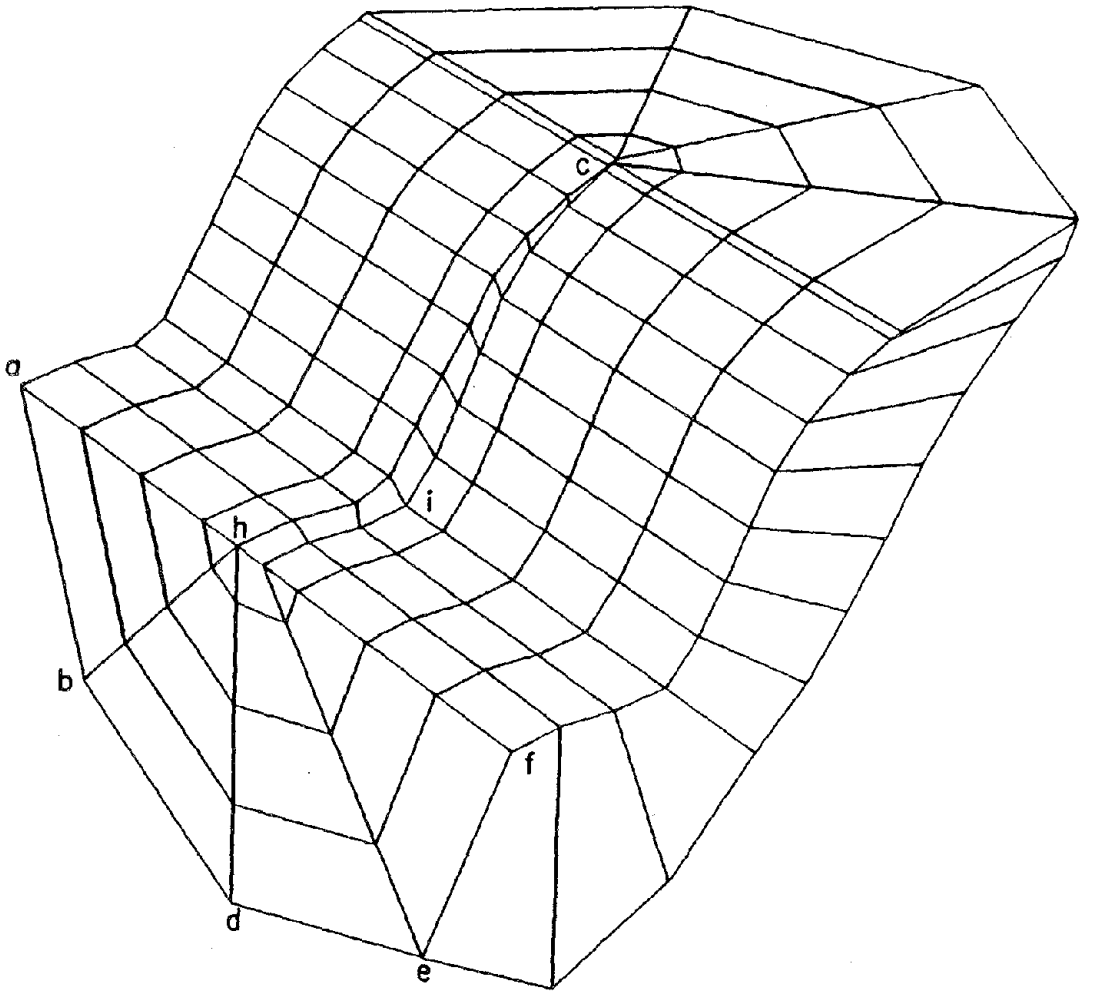

Figure 5.11 Finite element mesh of the foundation used in the symmetric 3-D analysis of Morrow Point Dam. The model is assumed to be massless and is composed of solid brick elements. The dam-foundation interface and plane of symmetry are defined by regions c-i-h and a-b-d-e-f-h, respectively.

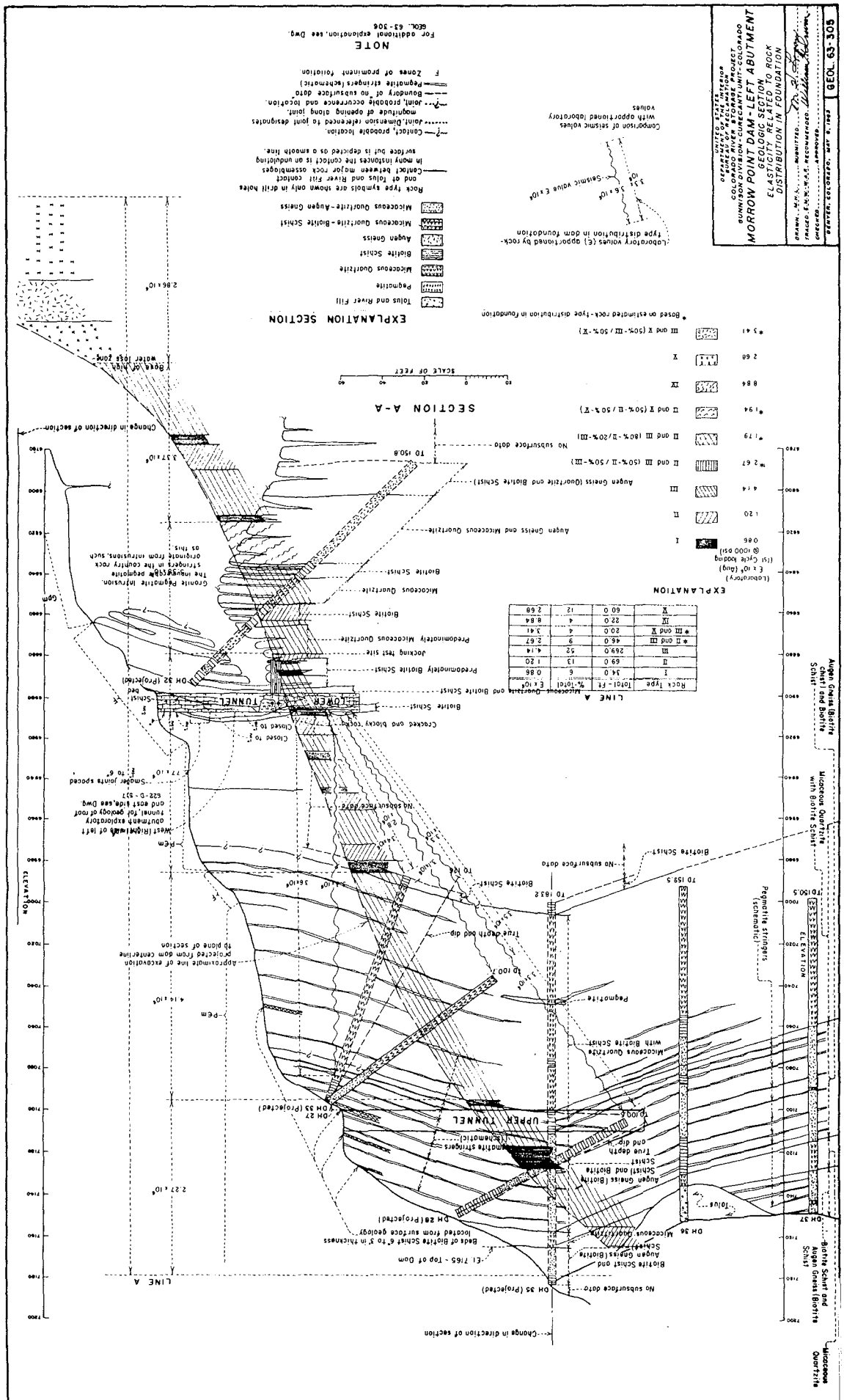

Figure 5.12 Left abutment—geologic section showing elasticity related to rock distribution. Taken from reference [36].

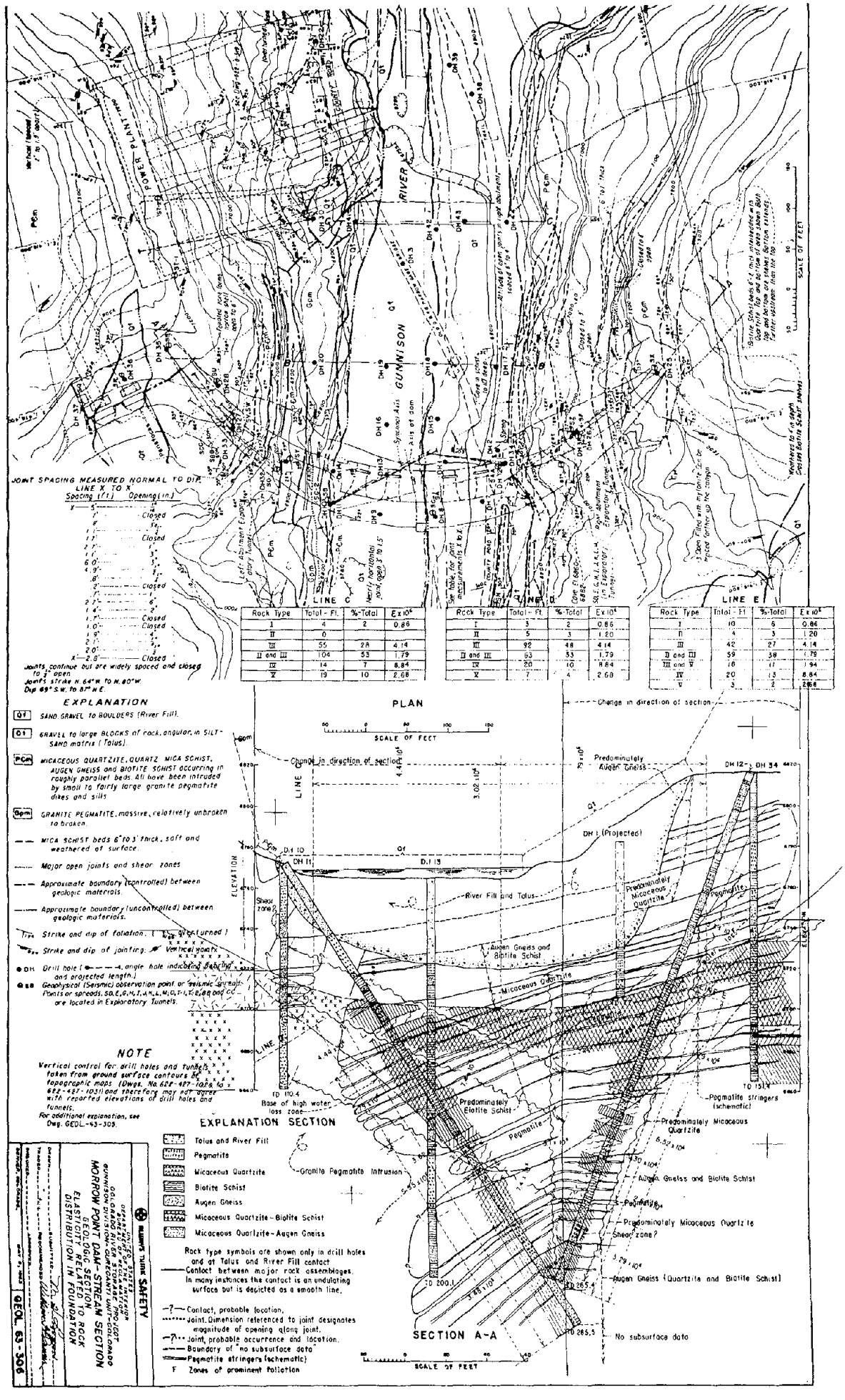

Rock Type	Total - Ft.	%-Total	Ex10⁶
I	4	2	0.86
II	0		
III	55	28	4.14
II and III	104	53	1.79
IV	14	7	8.84
V	19	10	2.68

Rock Type	Total - Ft.	%-Total	Ex10⁶
I	3	2	0.86
II	5	3	1.20
III	92	48	4.14
II and III	63	33	1.79
IV	20	10	8.84
V	7	4	2.68

Rock Type	Total - Ft.	%-Total	Ex10⁶
I	10	6	0.86
II	4	3	1.20
III	42	27	4.14
II and III	59	38	1.79
III and V	18	11	1.94
IV	20	13	8.84
V	3	2	2.68

Figure 5.13 Stream section—geologic section showing elasticity related to rock distribution. Taken from reference [36].

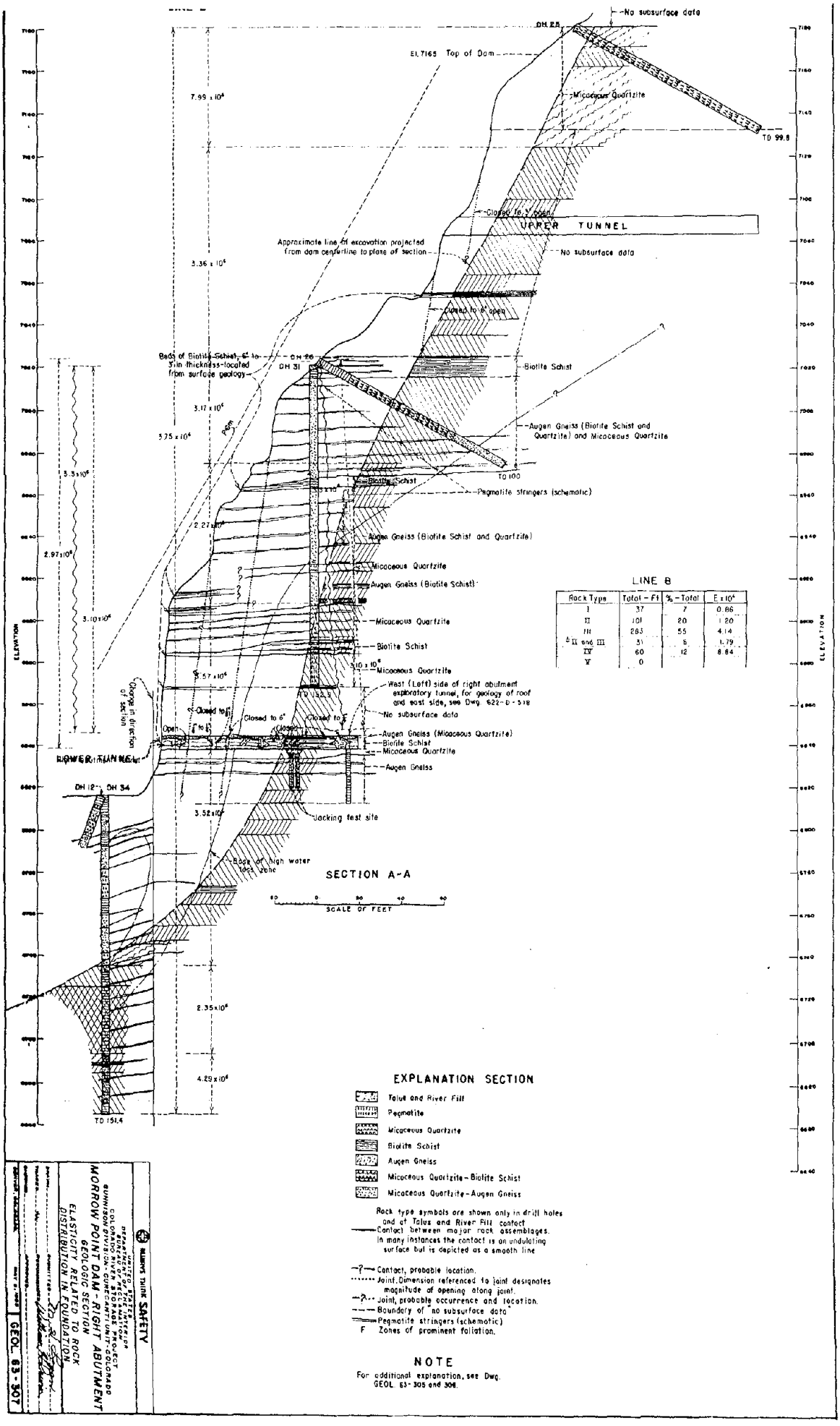

Figure 5.14 Right abutment—geologic section showing elasticity related to rock distribution. Taken from reference [36].

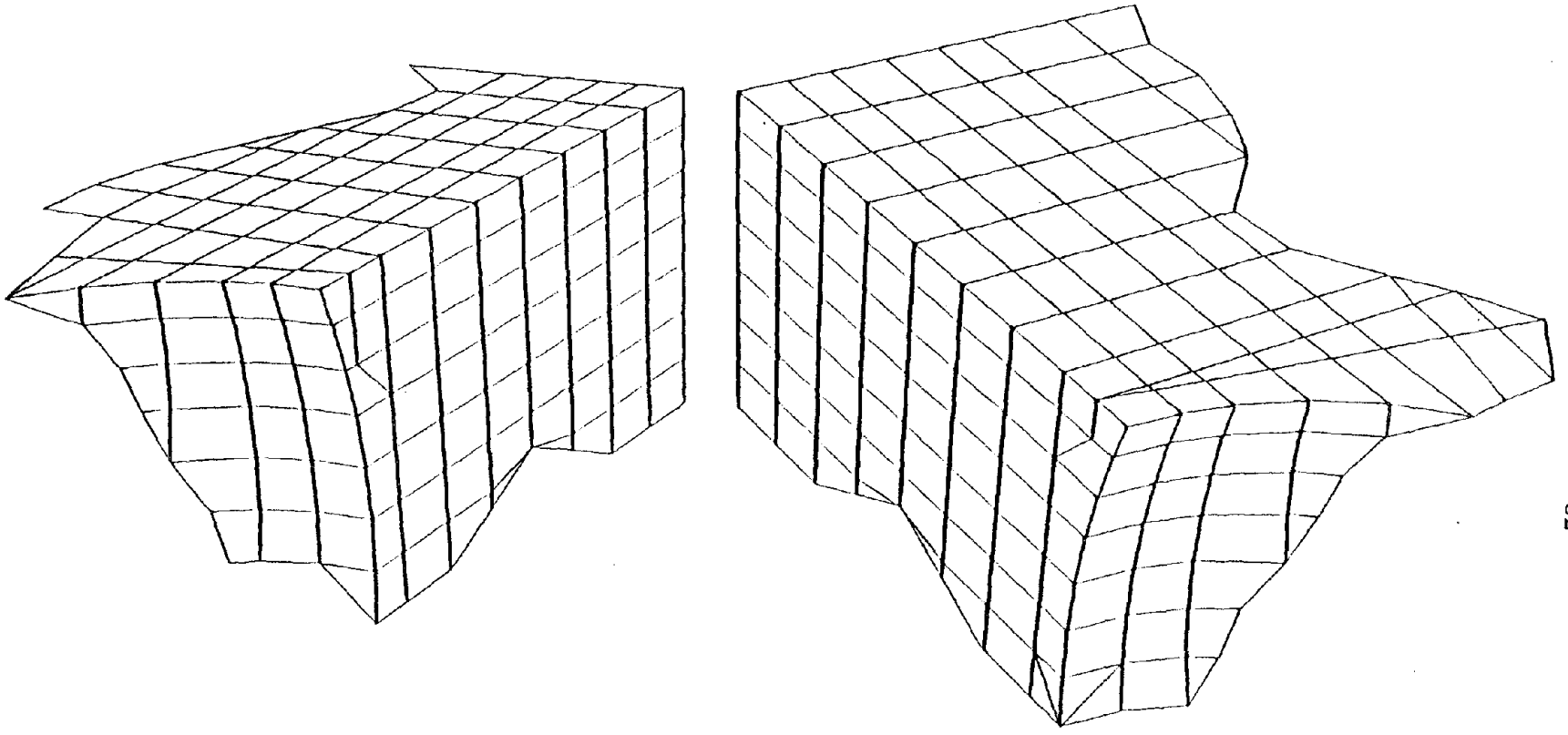

Figure 5.15 Finite element meshes of RHS (a) and LHS (b) water domains.

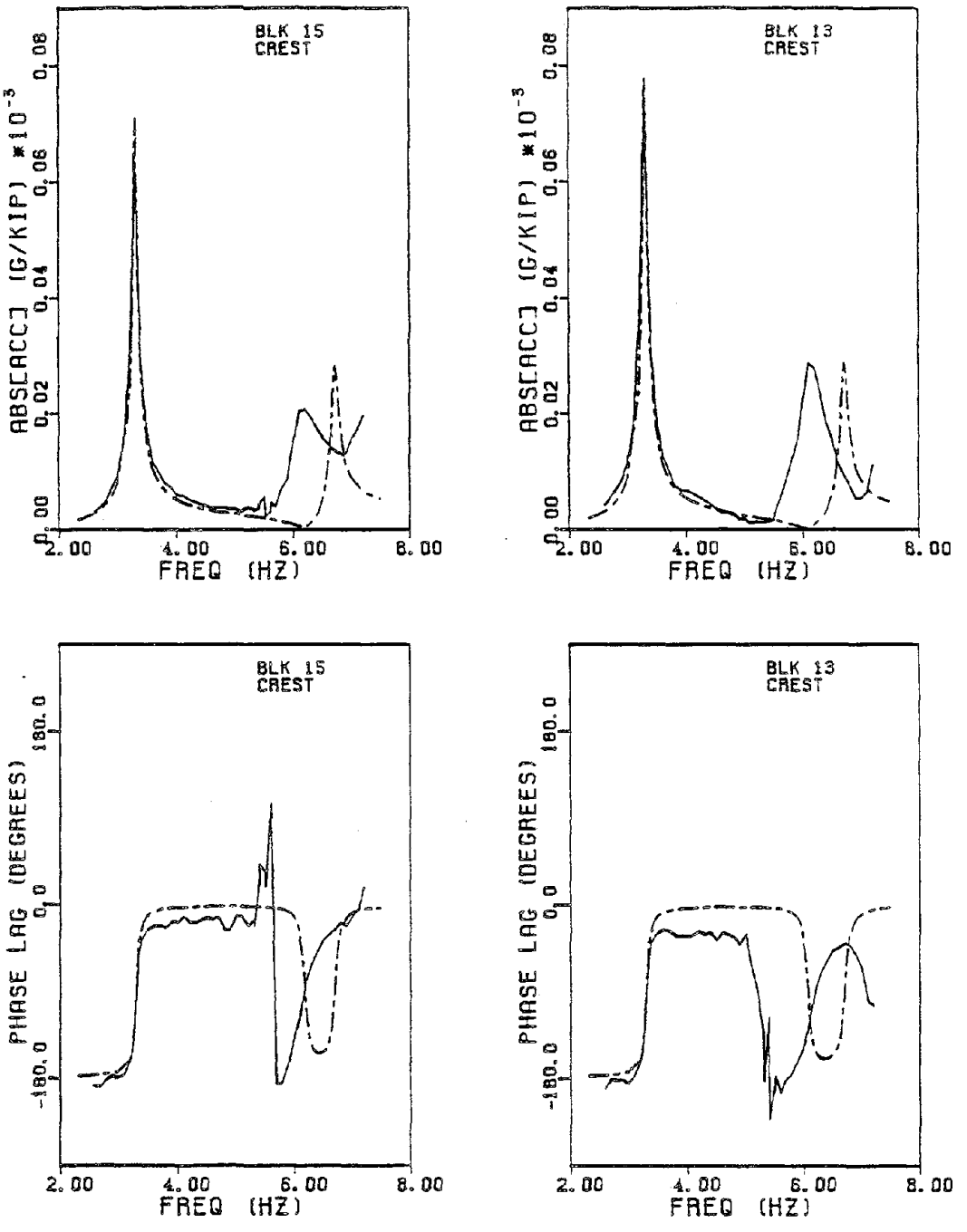

Figure 5.16 Measured and computed frequency response curves obtained for the antisymmetric shake at Blocks 15 and 13 on the dam crest. Shown are the radial components of acceleration and phase. The solid curves represent the experimental data and the dashed curves denote the computed response. An incompressible water model was used in the analysis.

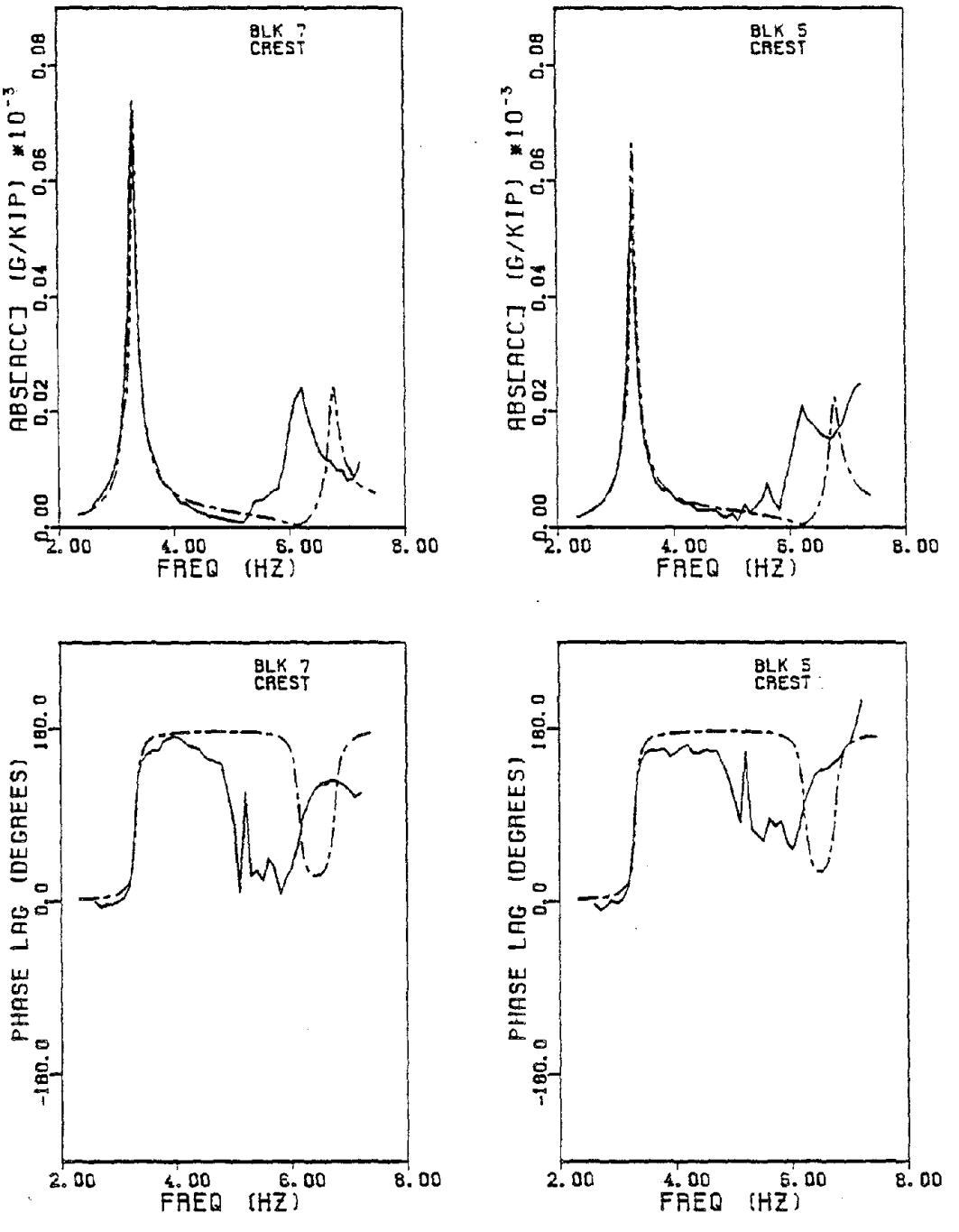

Figure 5.17 Measured and computed frequency response curves obtained for the antisymmetric shake at Blocks 7 and 5 on the dam crest. Shown are the radial components of acceleration and phase. The solid curves represent the experimental data and the dashed curves denote the computed response. An incompressible water model was used in the analysis.

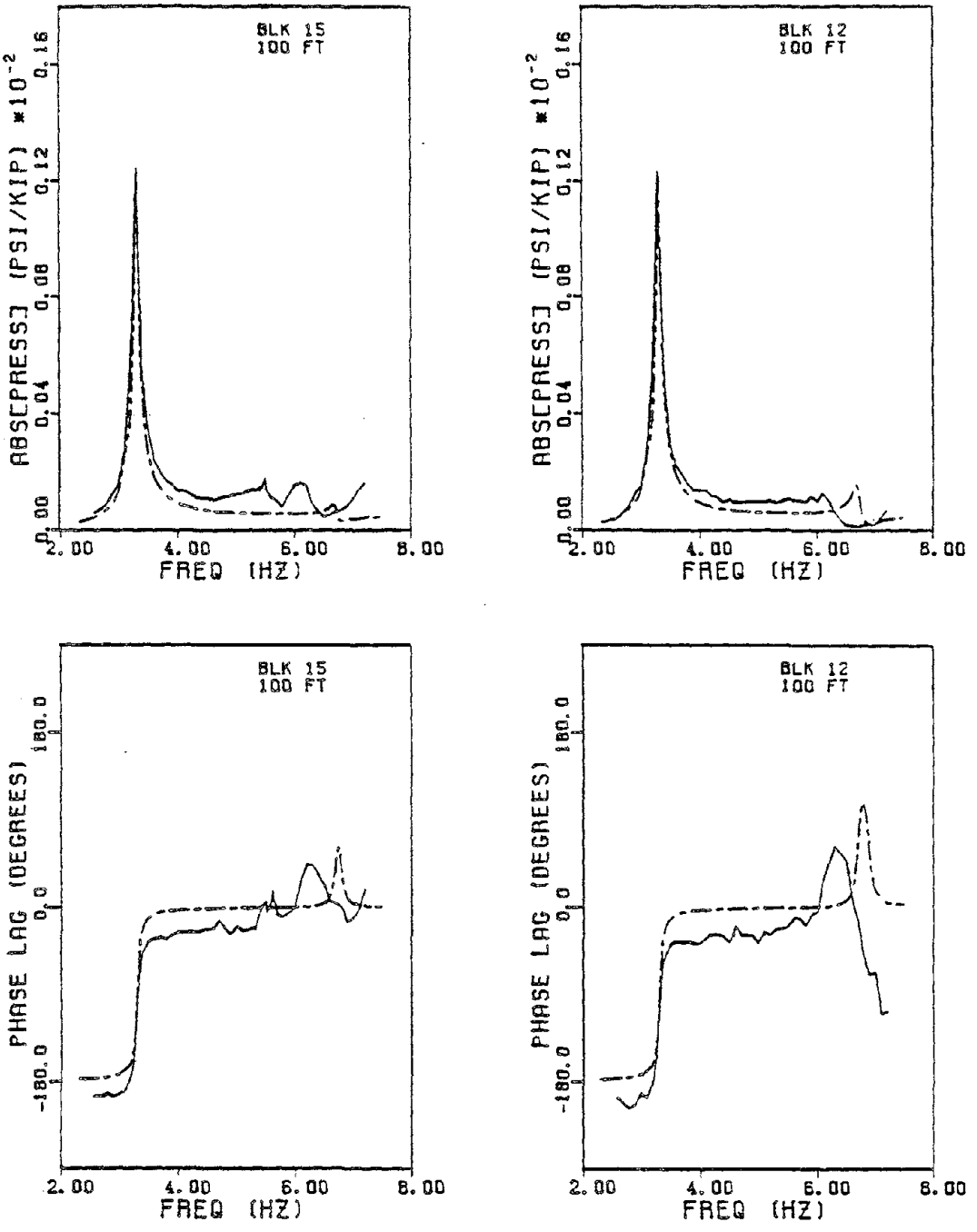

Figure 5.18 Measured and computed frequency response curves for hydrodynamic pressure and phase on the upstream face of the dam at Blocks 15 and 12 at a depth of 100 feet. The responses are obtained for the antisymmetric shake. The solid curves represent the experimental data and the dashed curves denote the computed responses obtained with an incompressible water model.

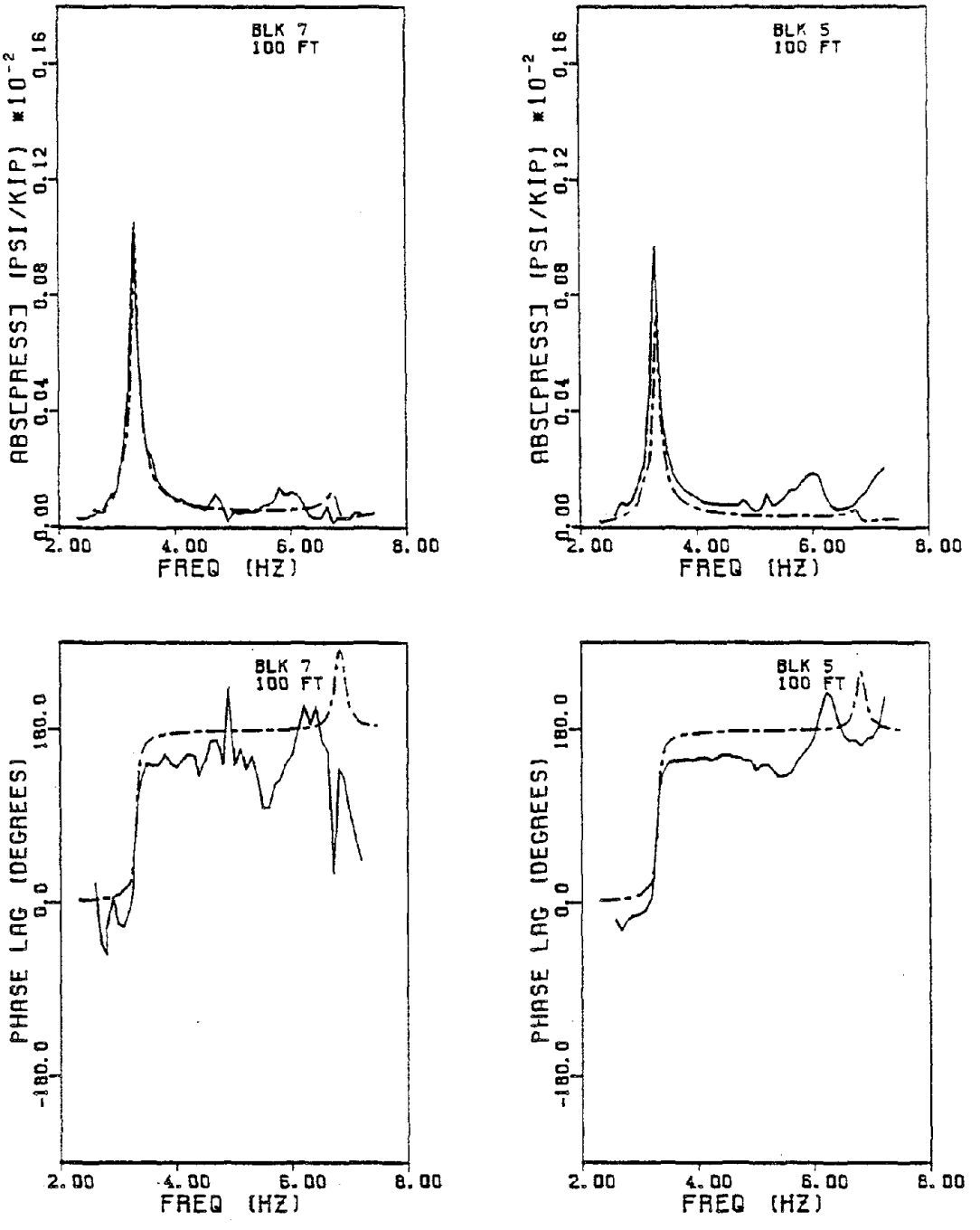

Figure 5.19 Measured and computed frequency response curves for hydrodynamic pressure and phase on the upstream face of the dam at Blocks 7 and 5 at a depth of 100 feet. The responses are obtained for the antisymmetric shake. The solid curves represent the experimental data and the dashed curves denote the computed responses obtained with an incompressible water model.

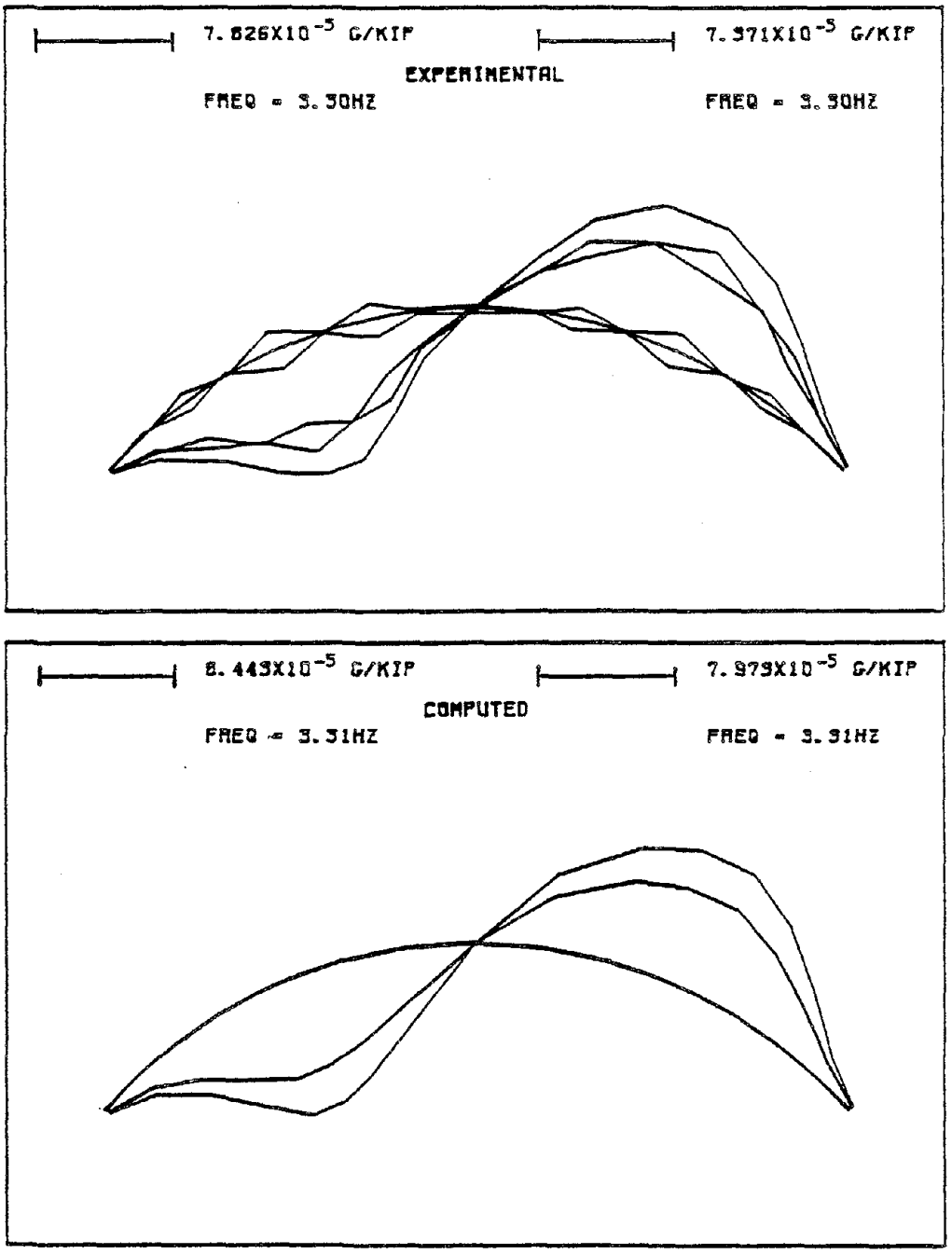

Figure 5.20 Comparison of the dam crest response shapes for the first antisymmetric resonance determined experimentally and computed numerically using an incompressible water model.

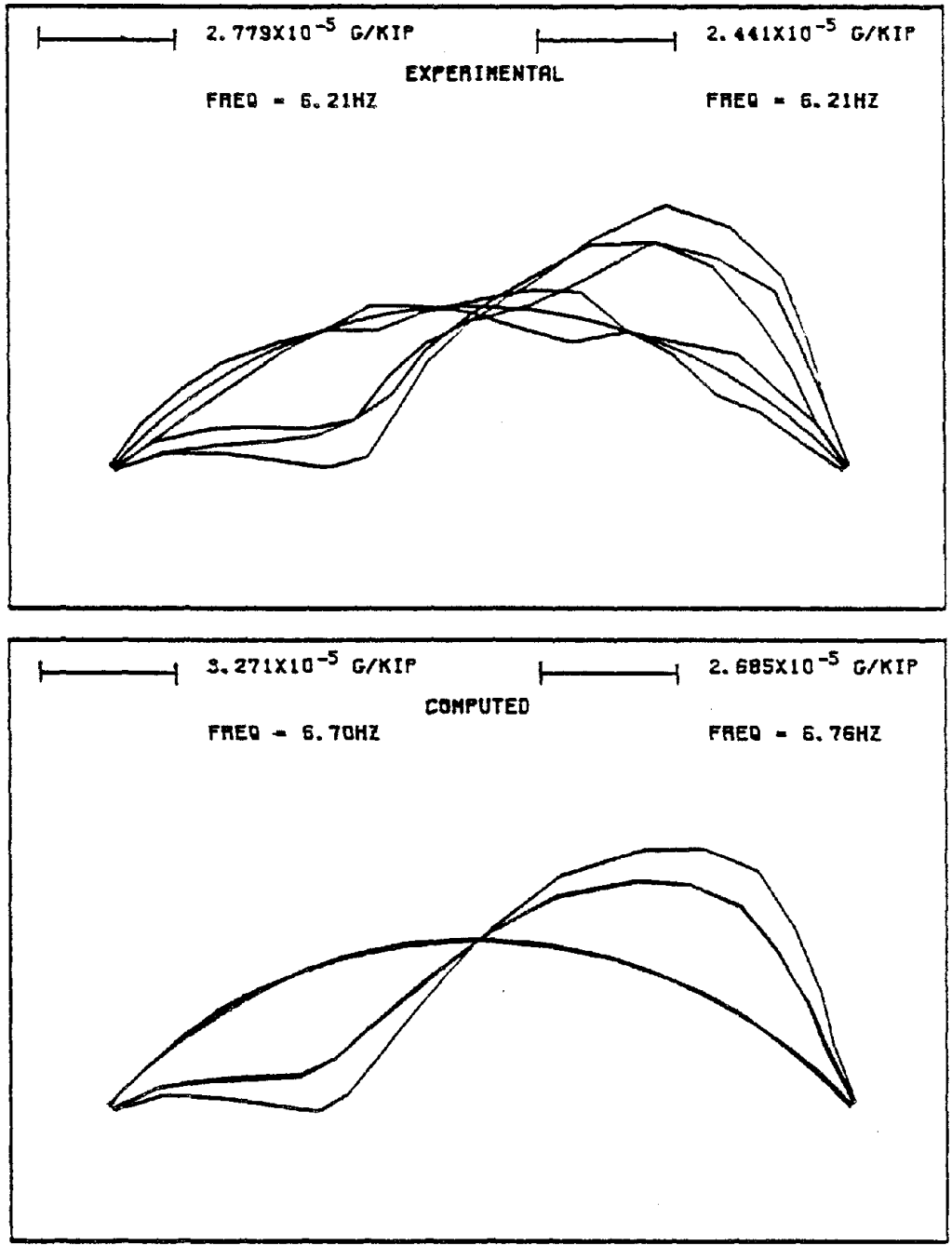

Figure 5.21 Comparison of the dam crest response shapes for the second antisymmetric resonance determined experimentally and computed numerically using an incompressible water model.

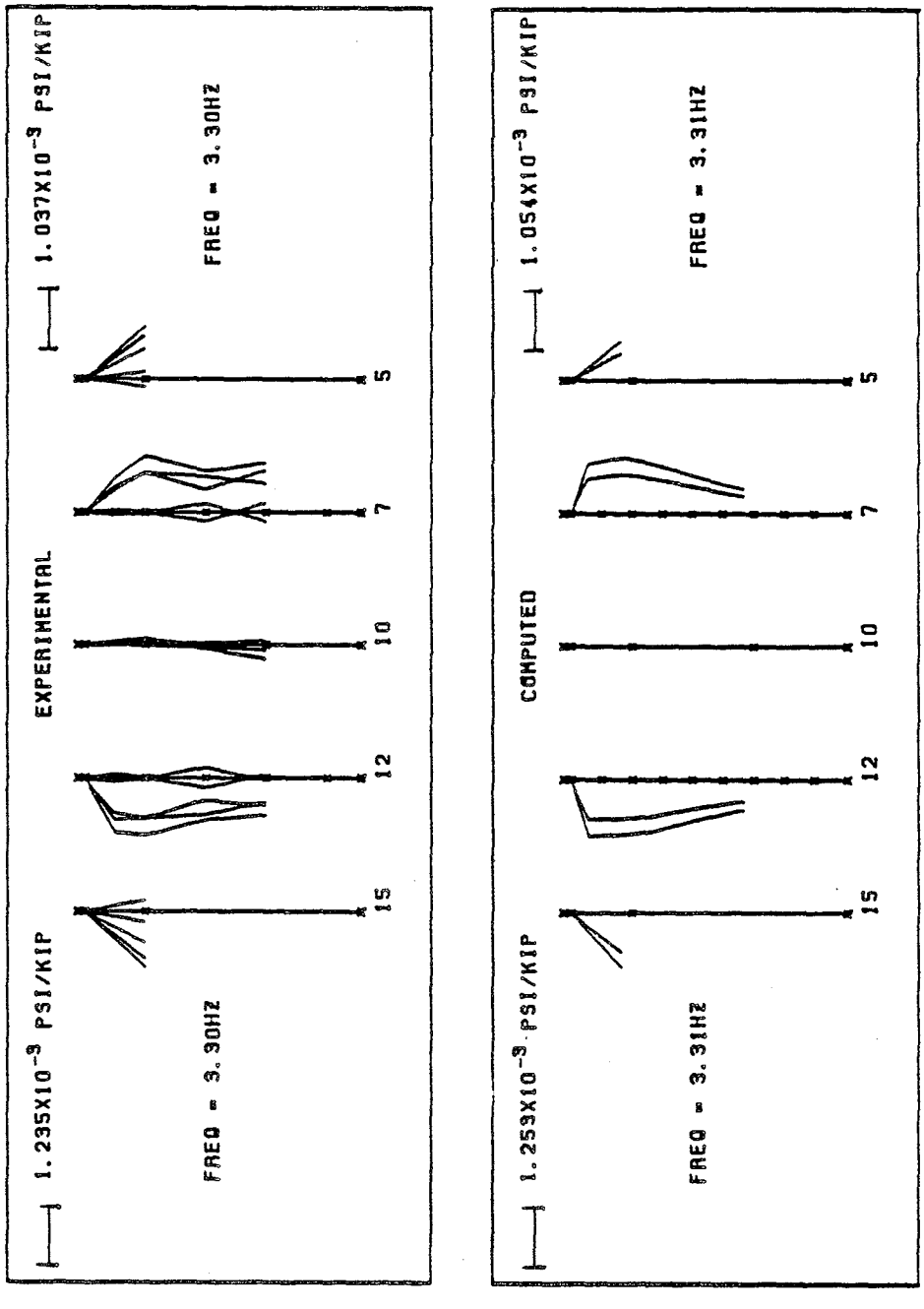

Figure 5.22 Comparison of the pressure profiles for the first antisymmetric resonance determined experimentally and computed numerically using an incompressible water model.

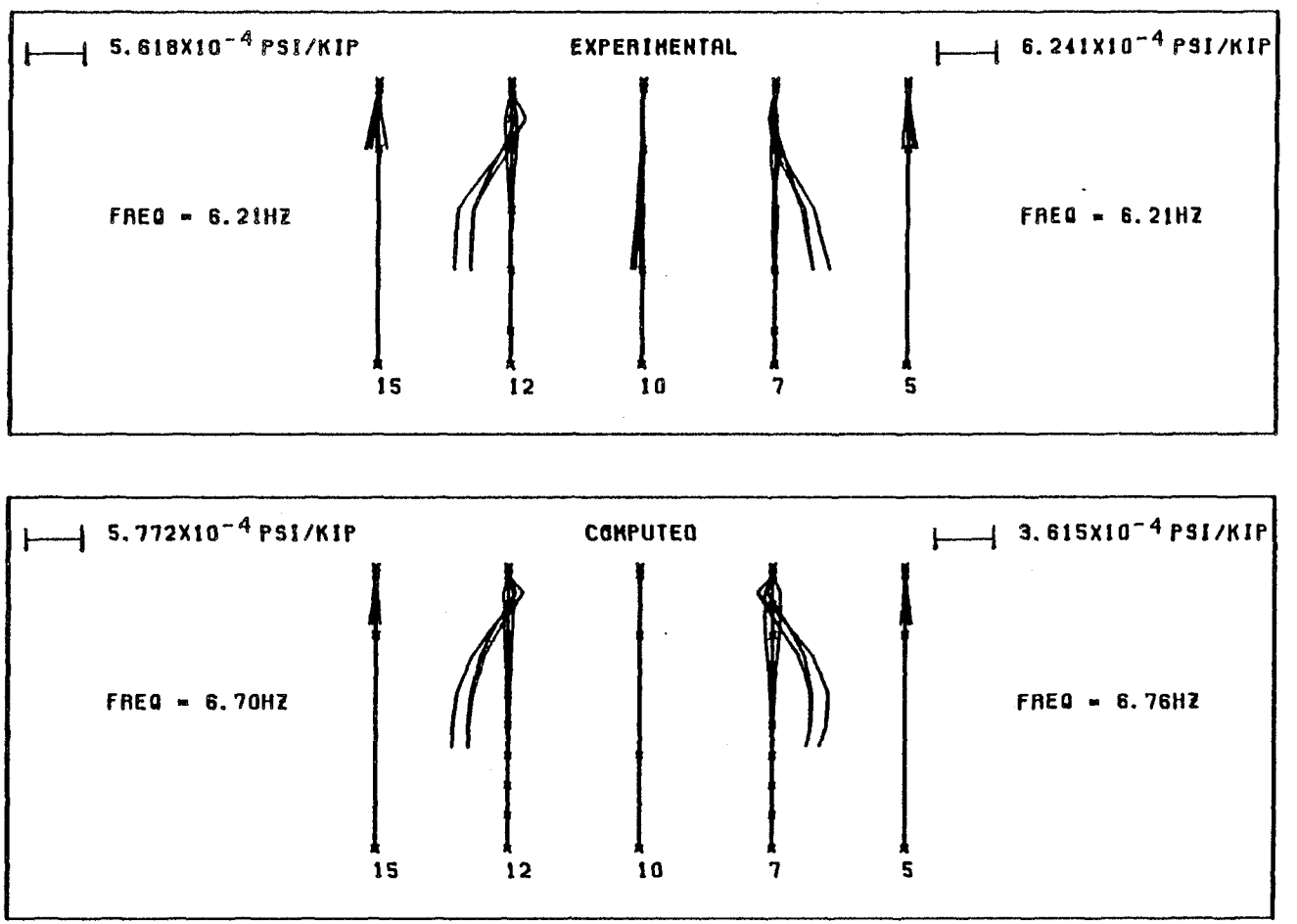

Figure 5.23 Comparison of the pressure profiles for the second antisymmetric resonance determined experimentally and computed numerically using an incompressible water model.

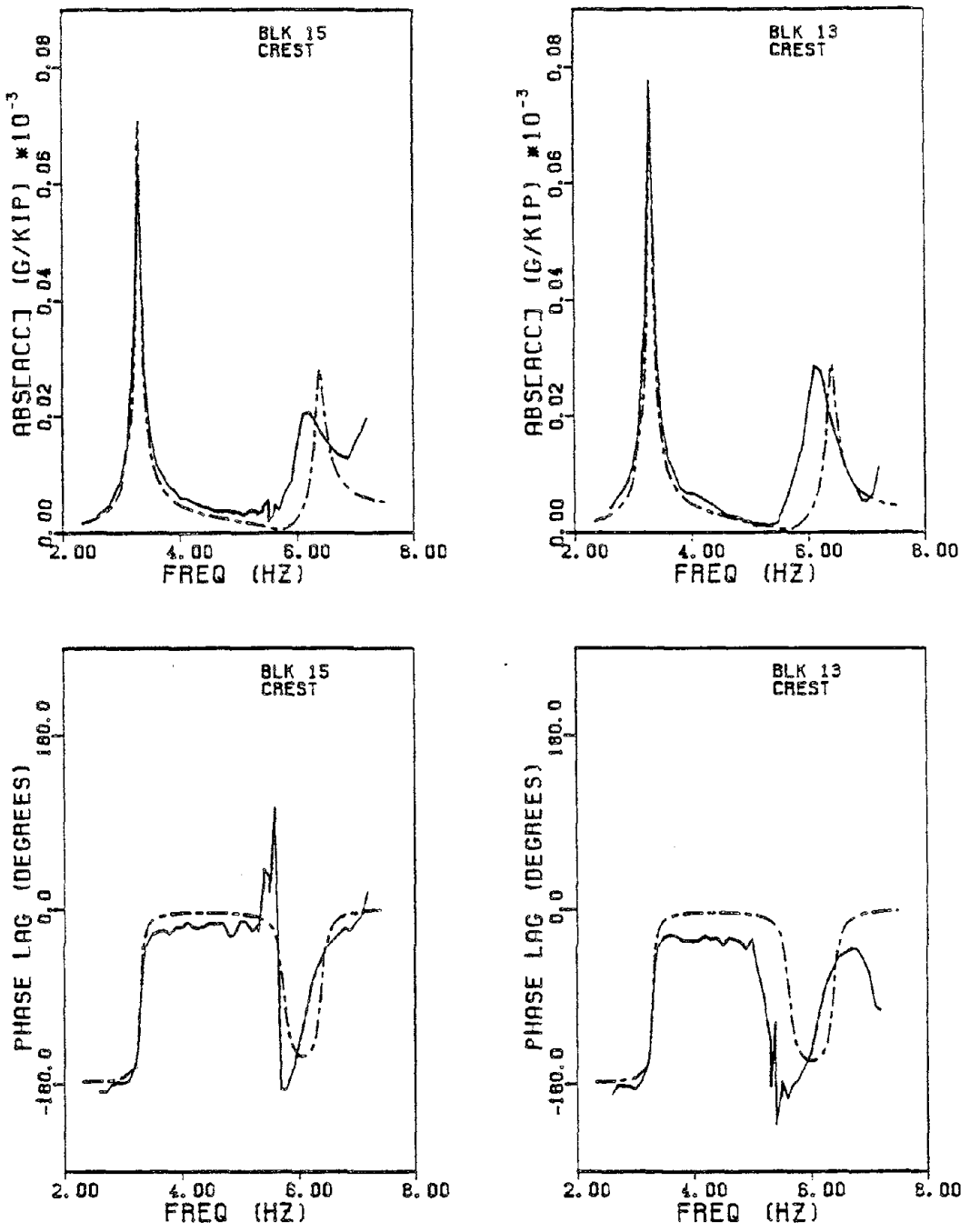

Figure 5.24 Measured and computed frequency response curves obtained for the antisymmetric shake at Blocks 15 and 13 on the dam crest. Shown are the radial components of acceleration and phase. The solid curves represent the experimental data and the dashed curves denote the computed response. A compressible water model was used in the analysis.

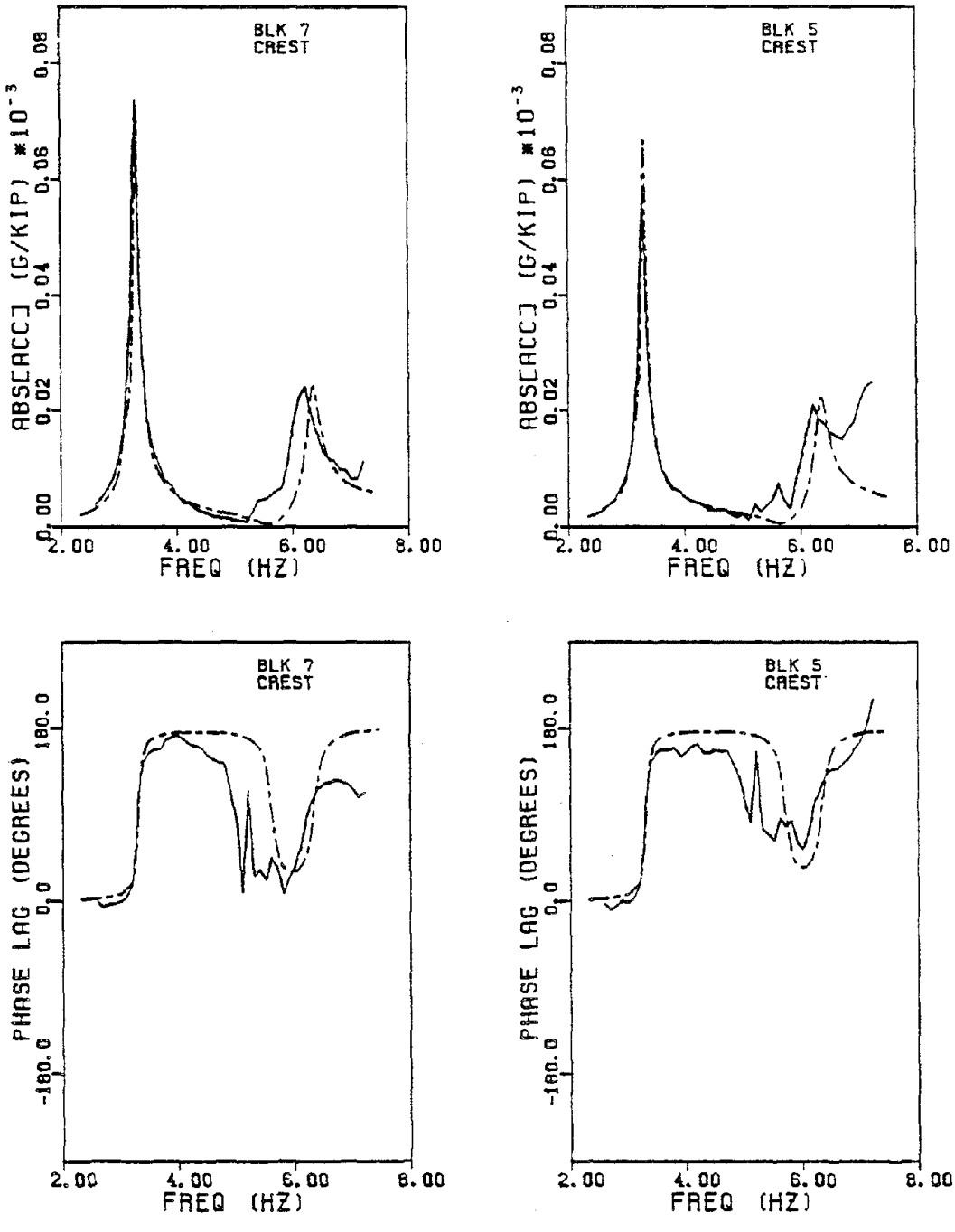

Figure 5.25 Measured and computed frequency response curves obtained for the antisymmetric shake at Blocks 7 and 5 on the dam crest. Shown are the radial components of acceleration and phase. The solid curves represent the experimental data and the dashed curves denote the computed response. A compressible water model was used in the analysis.

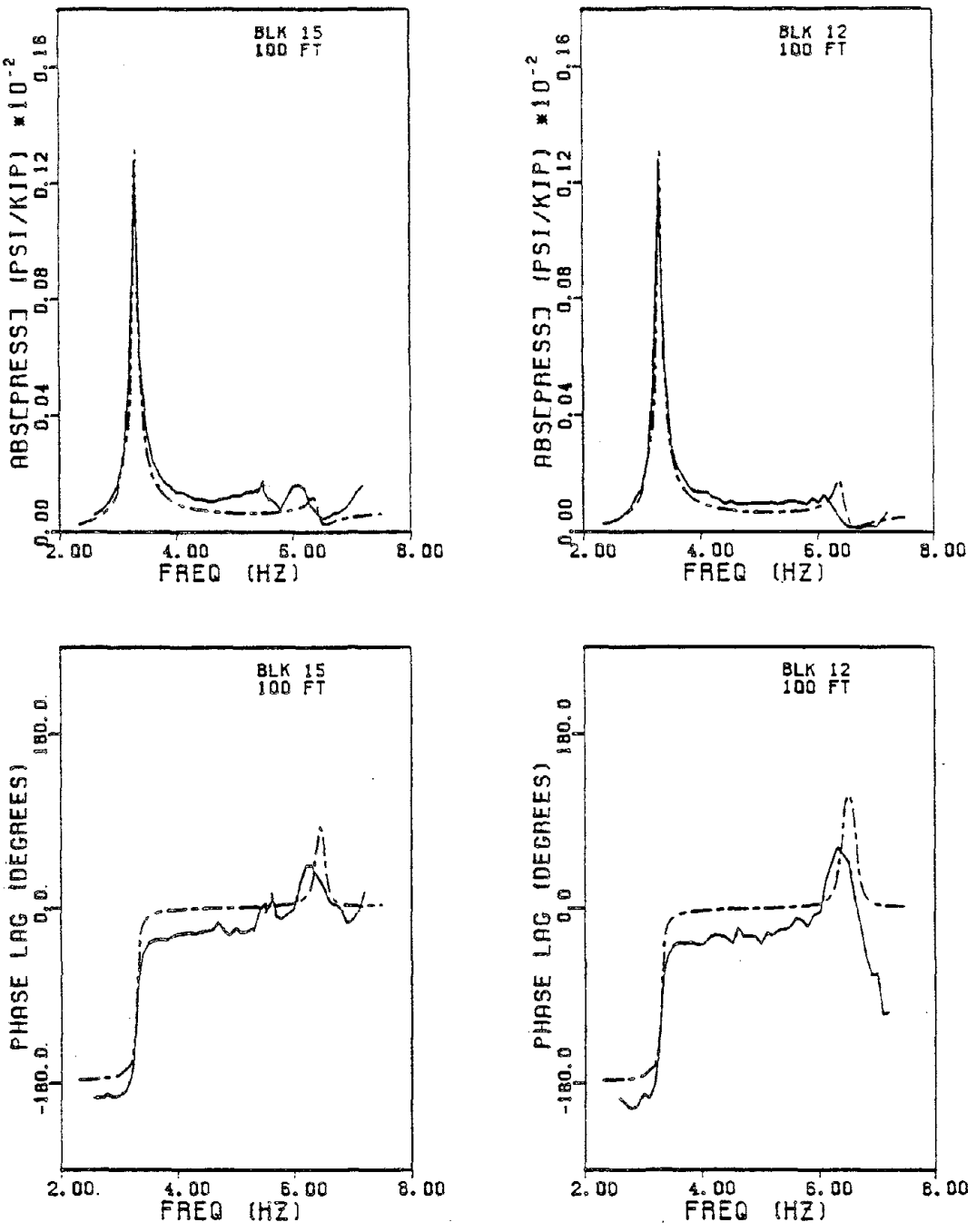

Figure 5.26 Measured and computed frequency response curves for hydrodynamic pressure and phase on the upstream face of the dam at Blocks 15 and 12 at a depth of 100 feet. The responses are obtained for the antisymmetric shake. The solid curves represent the experimental data and the dashed curves denote the computed responses obtained with a compressible water model.

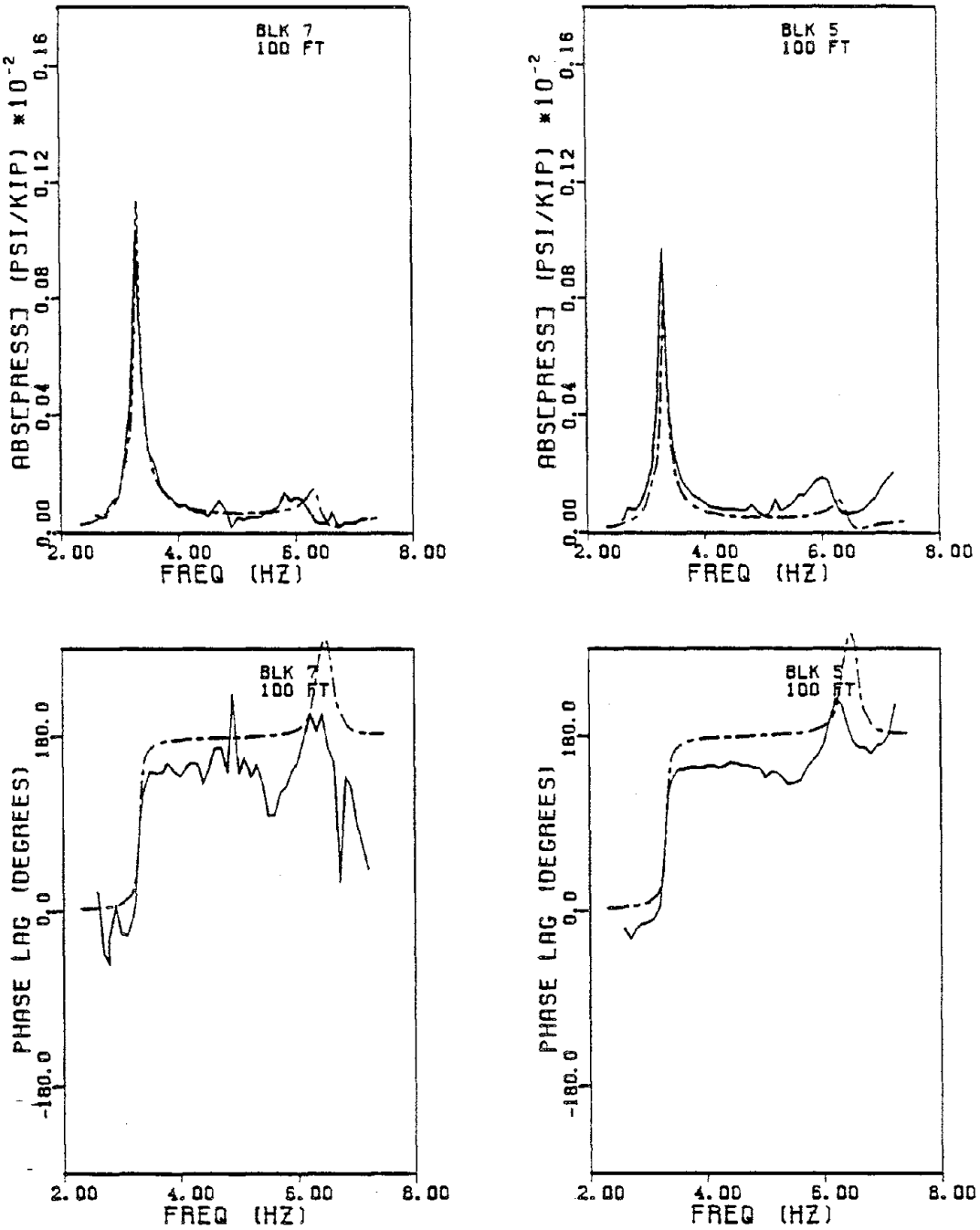

Figure 5.27 Measured and computed frequency response curves for hydrodynamic pressure and phase on the upstream face of the dam at Blocks 7 and 5 at a depth of 100 feet. The responses are obtained for the antisymmetric shake. The solid curves represent the experimental data and the dashed curves denote the computed responses obtained with an incompressible water model.

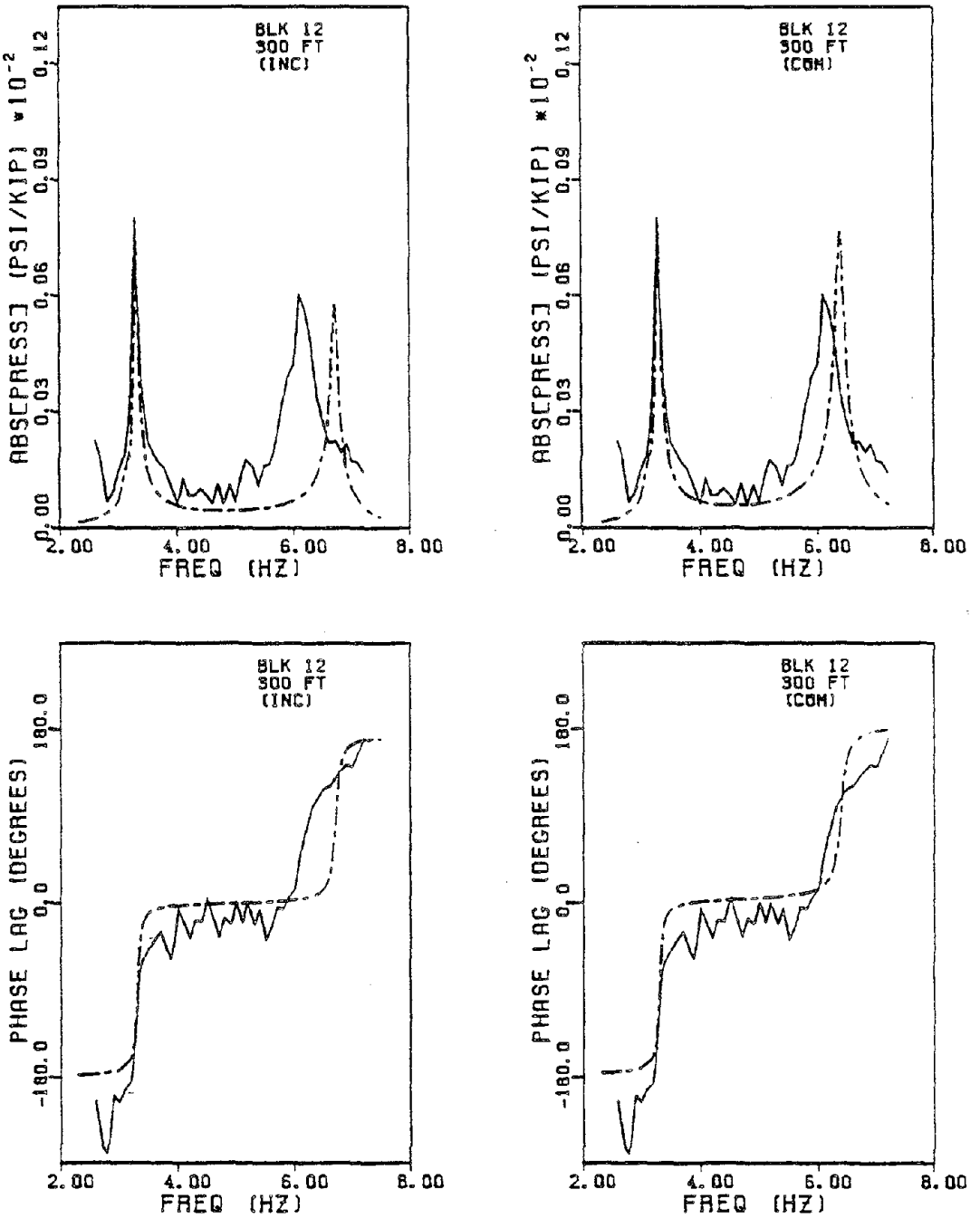

Figure 5.28 Measured and computed frequency response curves for hydrodynamic pressure and phase on the upstream face of the dam at Block 12 at a depth of 300 feet. The responses are obtained for the antisymmetric shake. Comparisons are shown for both incompressible (left) and compressible (right) water models. The solid curves represent the experimental data and the dashed curves denote the computed responses.

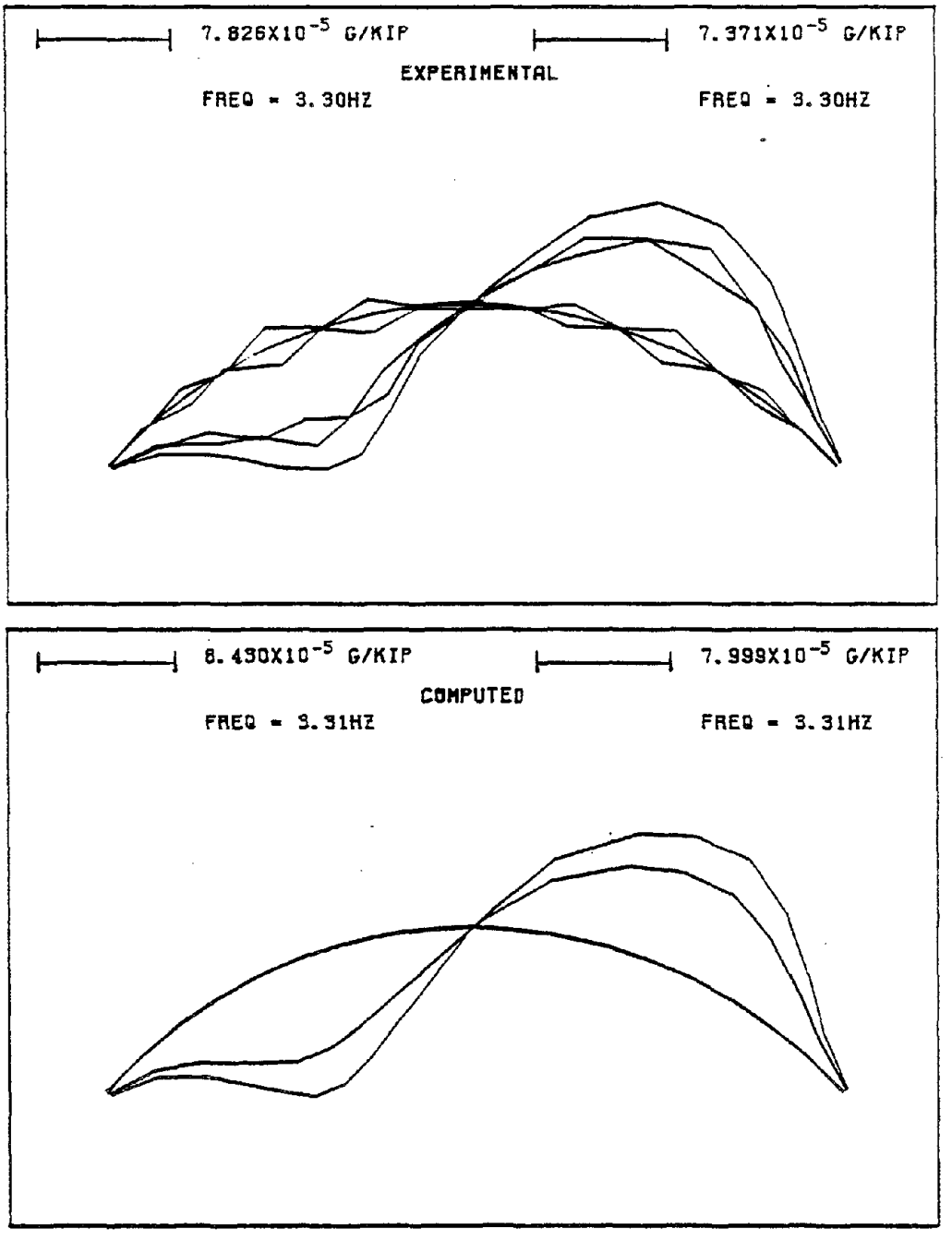

Figure 5.29 Comparison of the dam crest response shapes for the first antisymmetric resonance determined experimentally and computed numerically using a compressible water model.

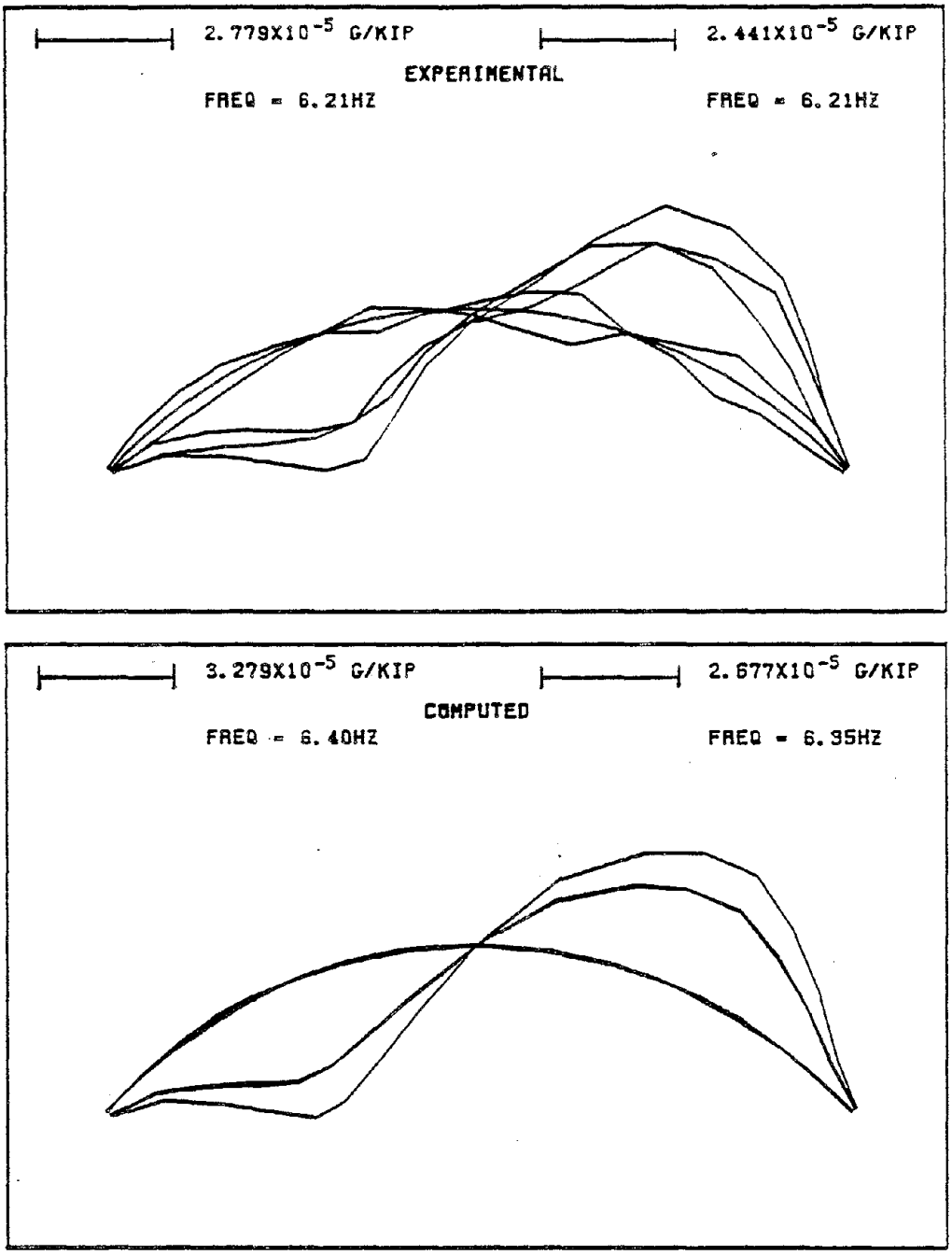

Figure 5.30 Comparison of the dam crest response shapes for the second antisymmetric resonance determined experimentally and computed numerically using a compressible water model.

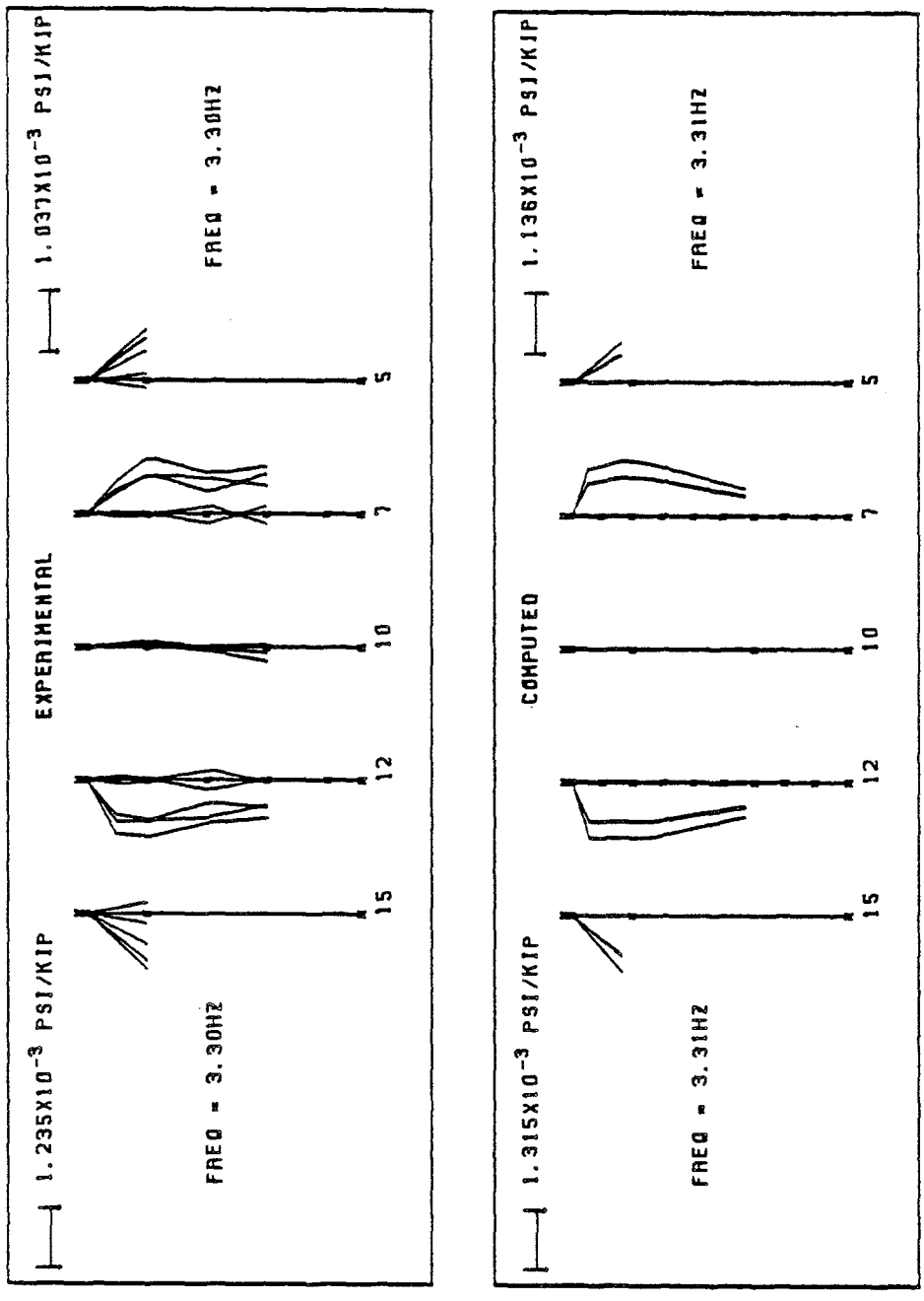

Figure 5.31 Comparison of the pressure profiles for the first antisymmetric resonance determined experimentally and computed numerically using a compressible water model.

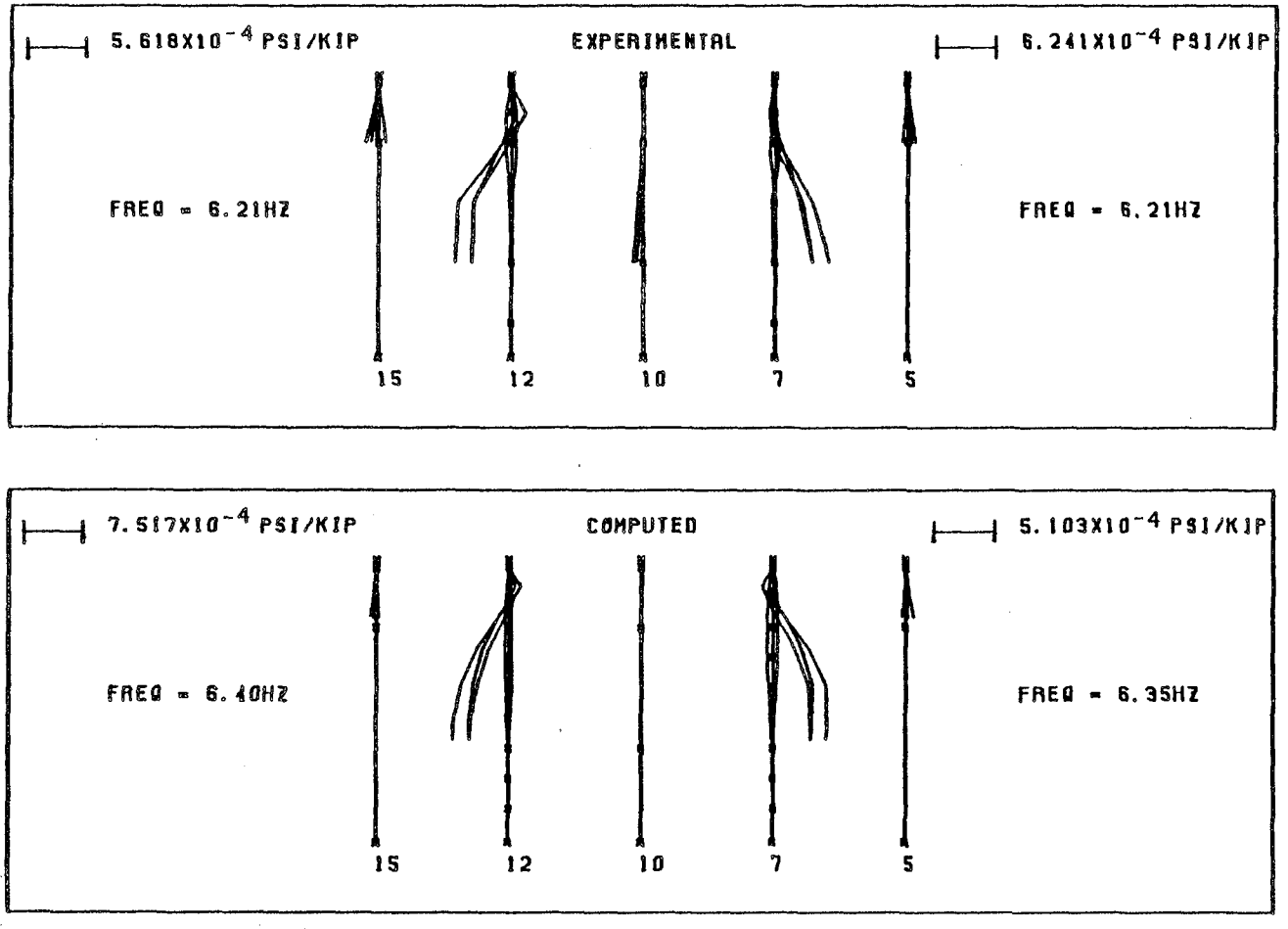

Figure 5.32 Comparison of the pressure profiles for the second antisymmetric resonance determined experimentally and computed numerically using a compressible water model.

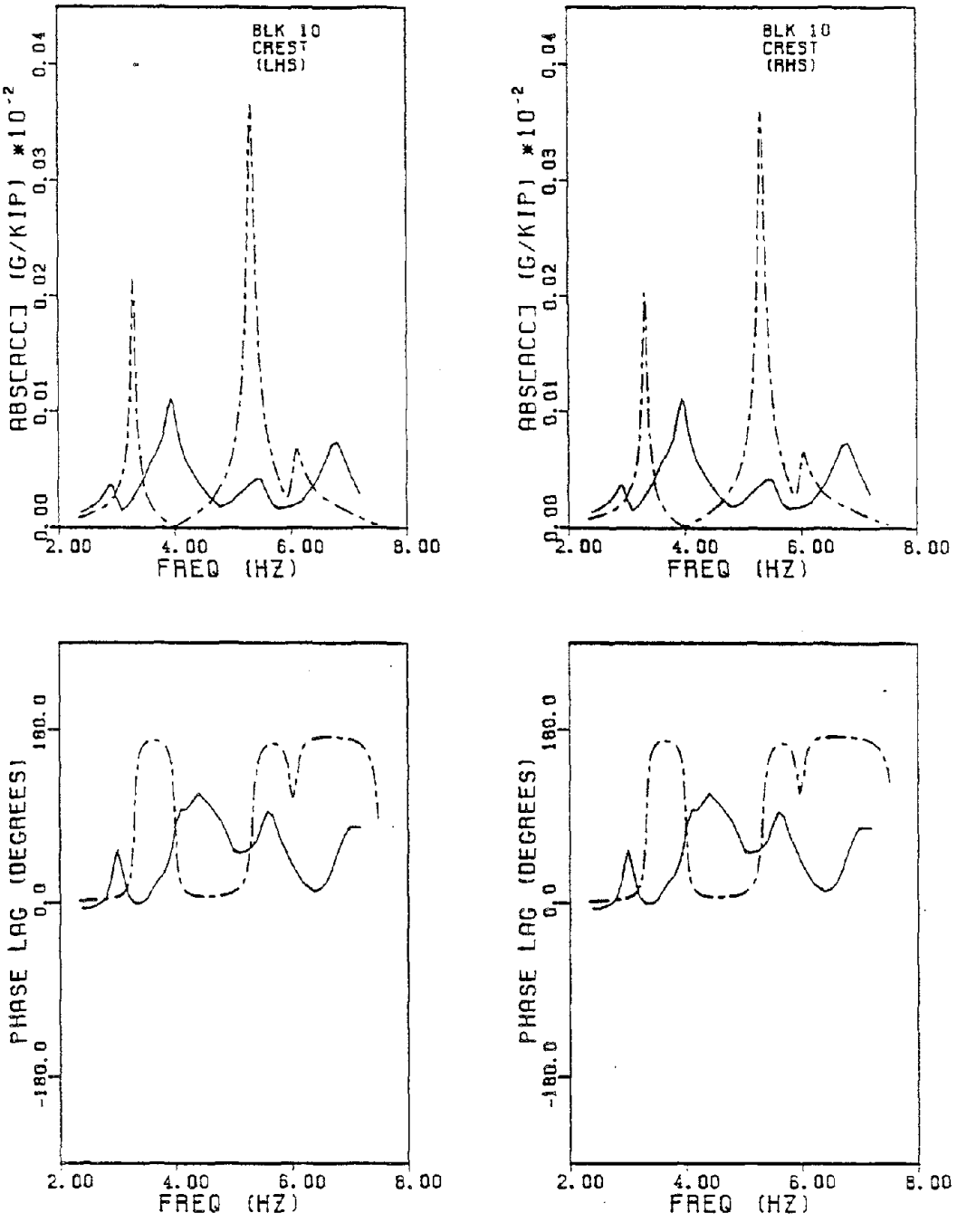

Figure 5.33 Measured and computed frequency response curves obtained for the symmetric shake at Block 10 on the dam crest. Shown are the radial components of acceleration and phase. Comparisons are shown for both LHS (left) and RHS (right) water models. The solid curves represent the experimental data and the dashed curves denote the computed responses. An incompressible water model was used in the analysis.

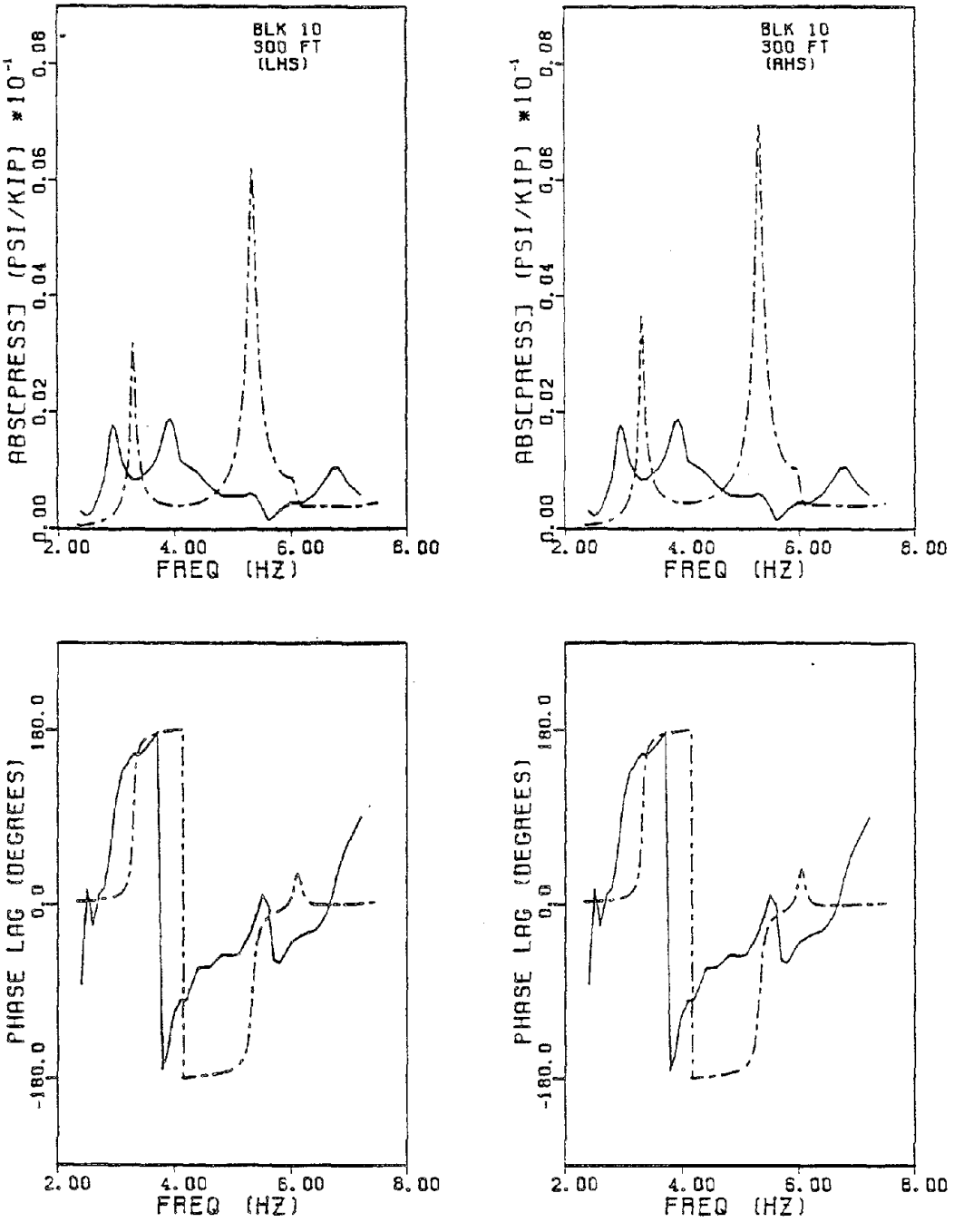

Figure 5.34 Measured and computed frequency response curves for hydrodynamic pressure and phase on the upstream face of the dam at Block 10 at a depth of 300 feet. The responses are obtained for the symmetric shake. Comparisons are shown for both LHS (left) and RHS (right) water models. The solid curves represent the experimental data and the dashed curves denote the computed responses. An incompressible water model was used in the analysis.

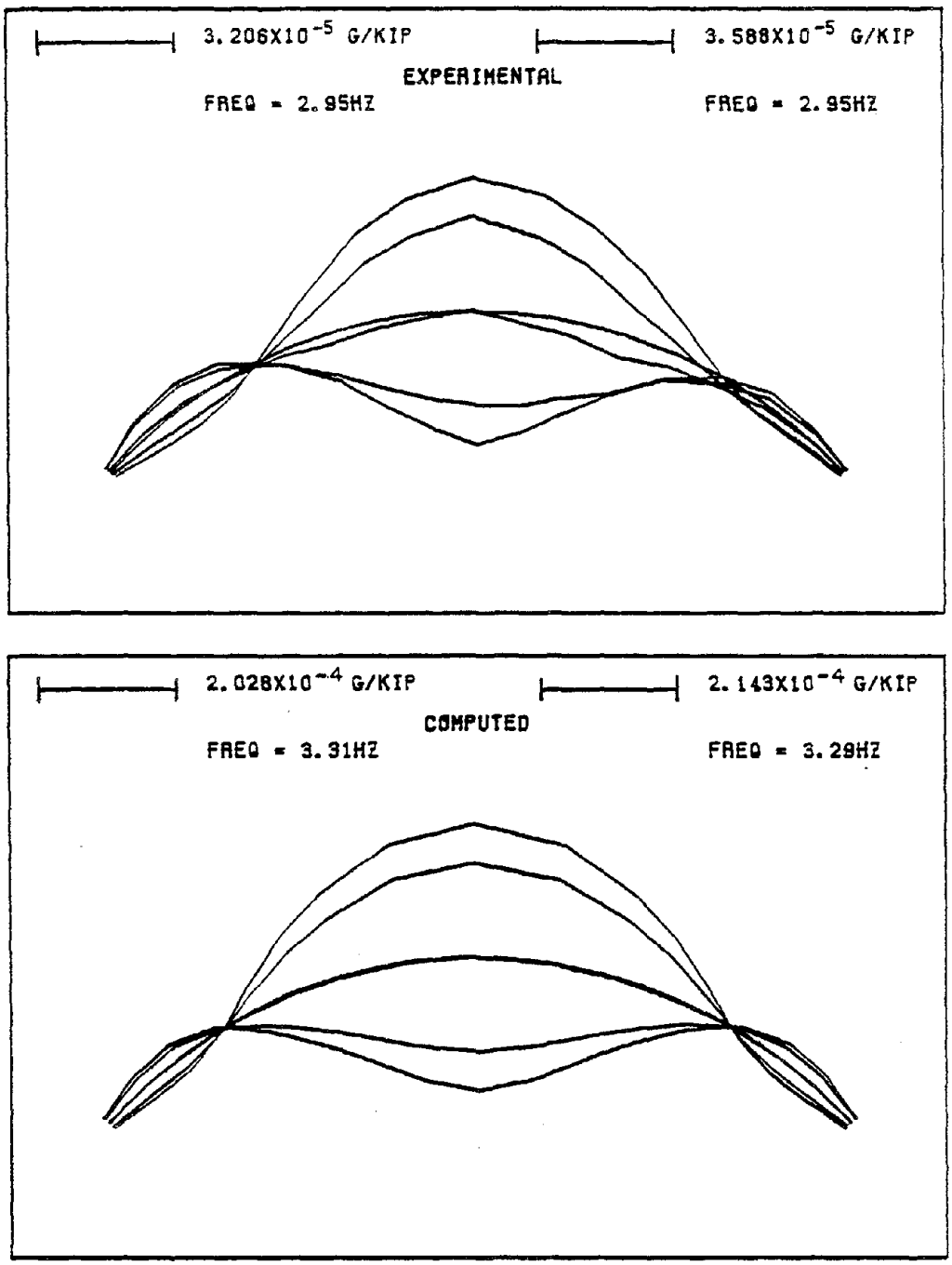

Figure 5.35 Comparison of the dam crest response shapes for the first symmetric resonance determined experimentally and computed numerically using an incompressible water model.

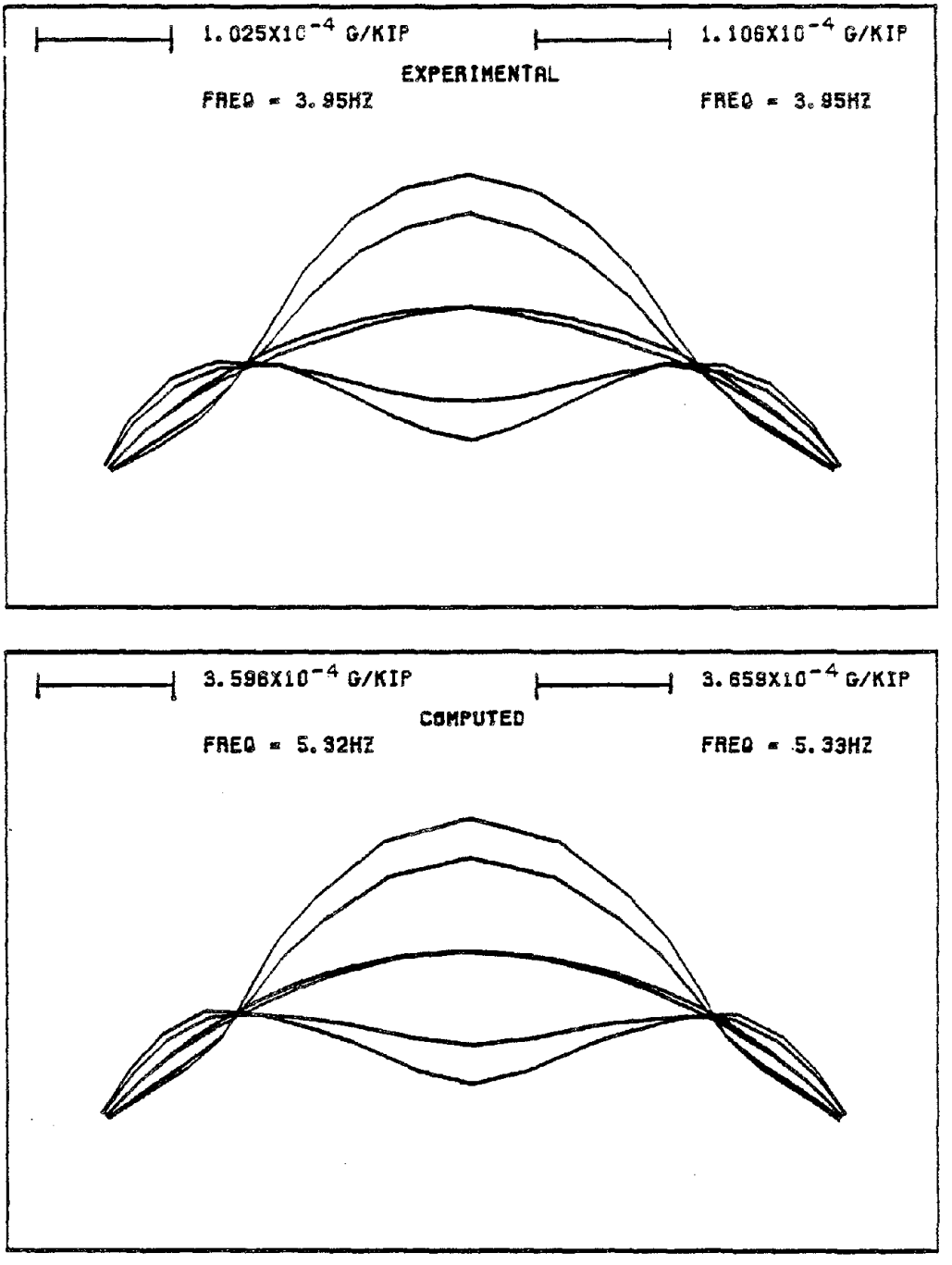

Figure 5.36 Comparison of the dam crest response shapes for the second symmetric resonance determined experimentally and computed numerically using an incompressible water model.

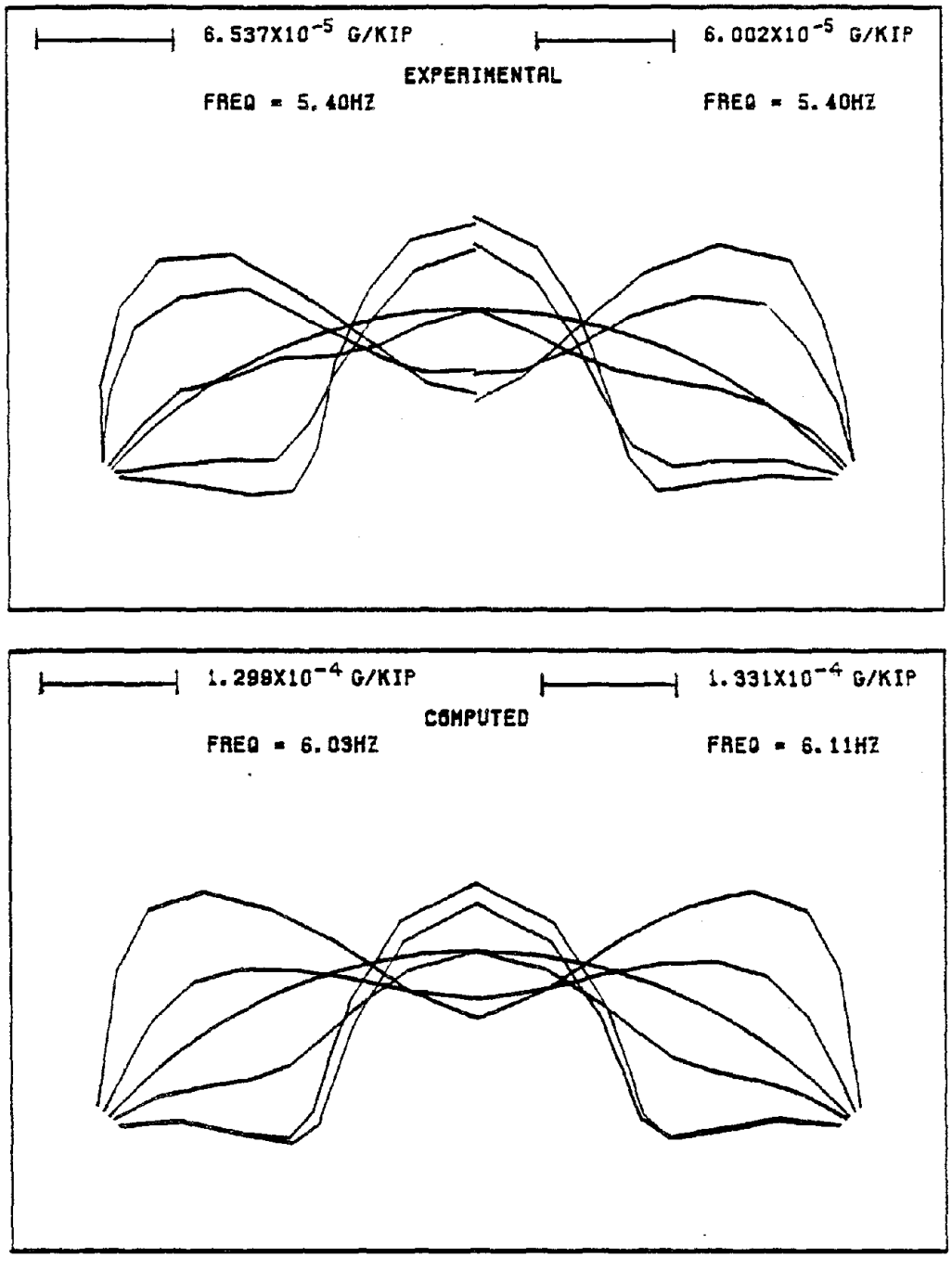

Figure 5.37 Comparison of the dam crest response shapes for the third symmetric resonance determined experimentally and computed numerically using an incompressible water model.

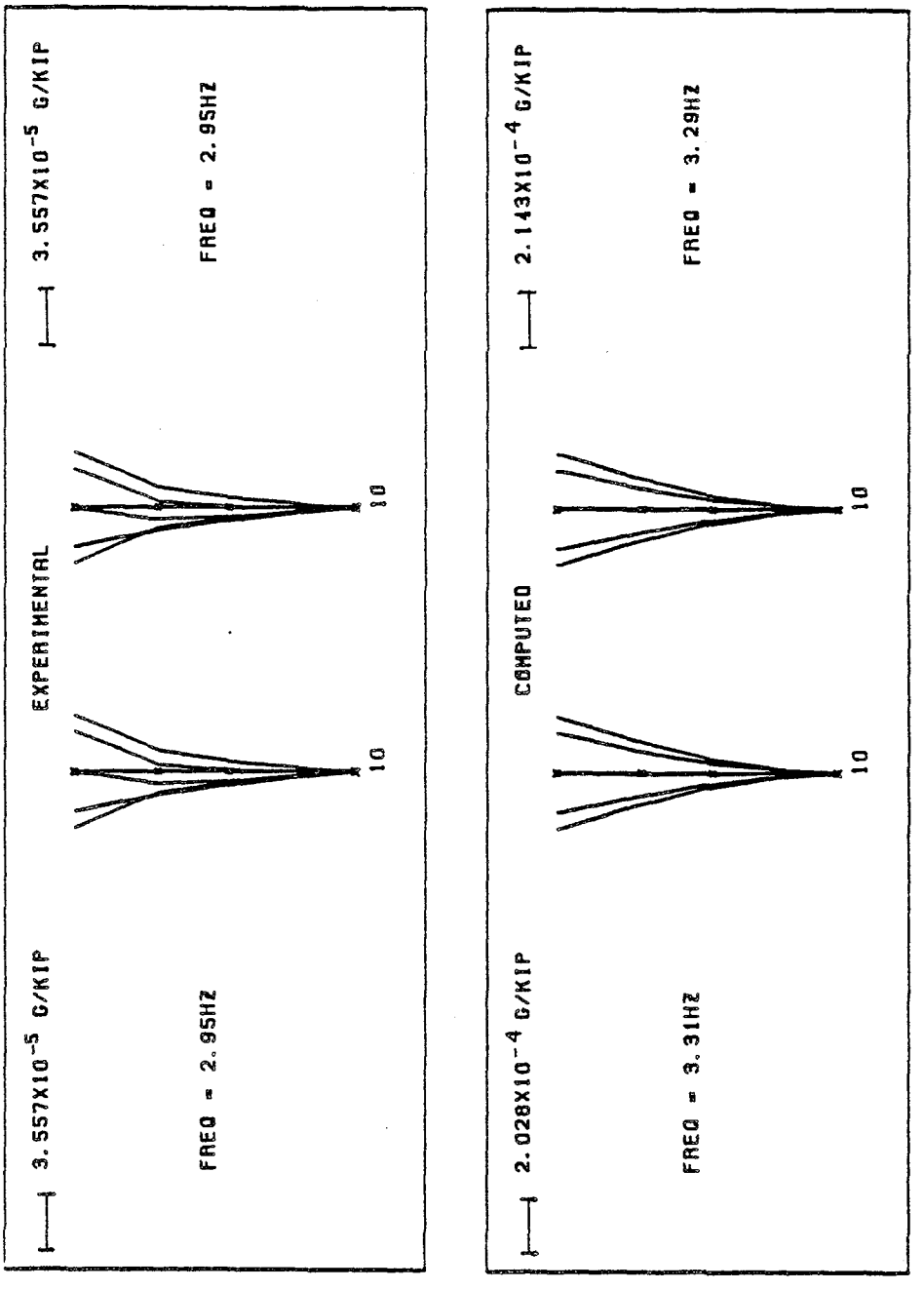

Figure 5.38 Comparison of crown cantilever response shapes for the first symmetric resonance determined experimentally and computed numerically using an incompressible water model.

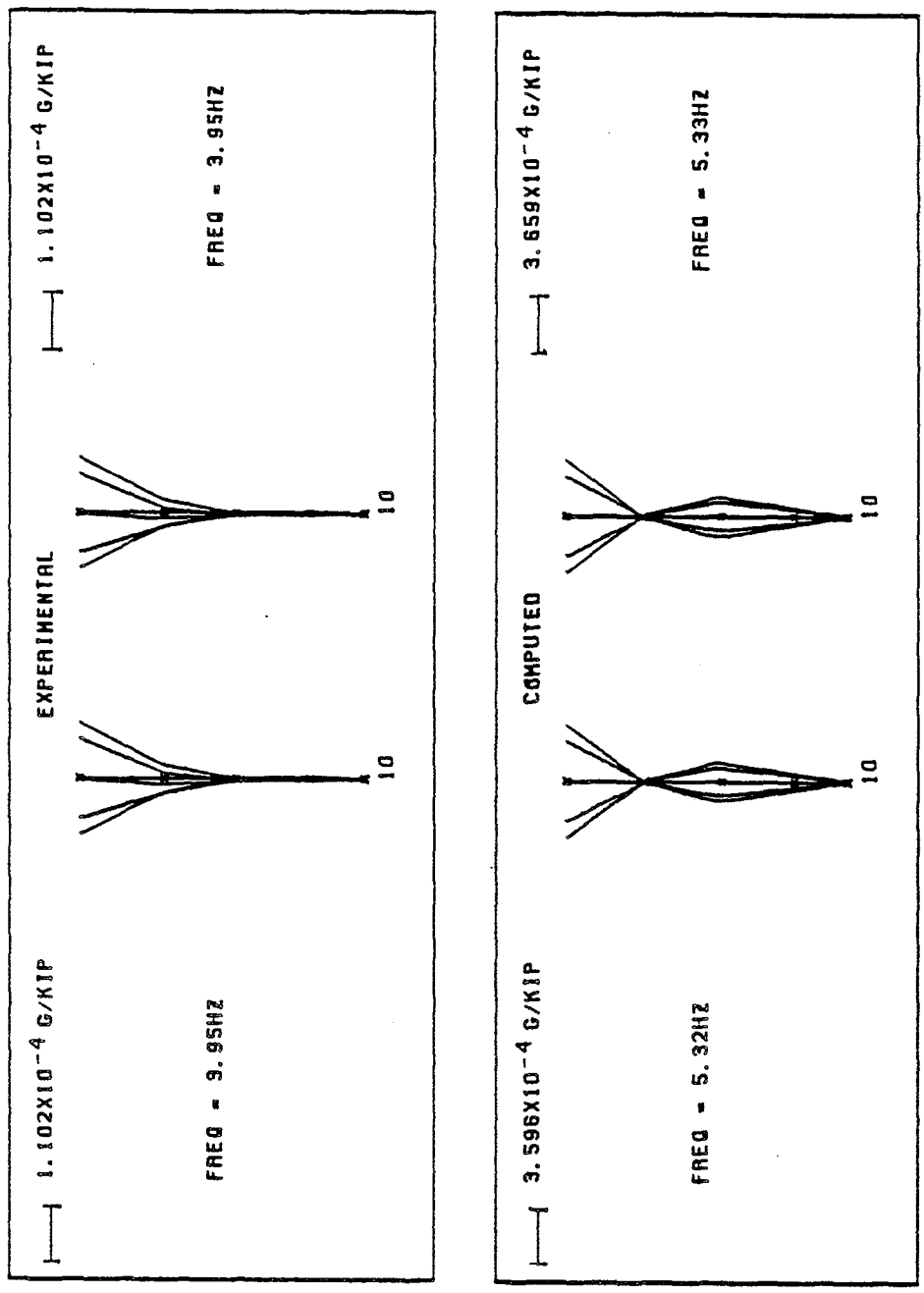

Figure 5.39 Comparison of crown cantilever response shapes for the second symmetric resonance determined experimentally and computed numerically using an incompressible water model.

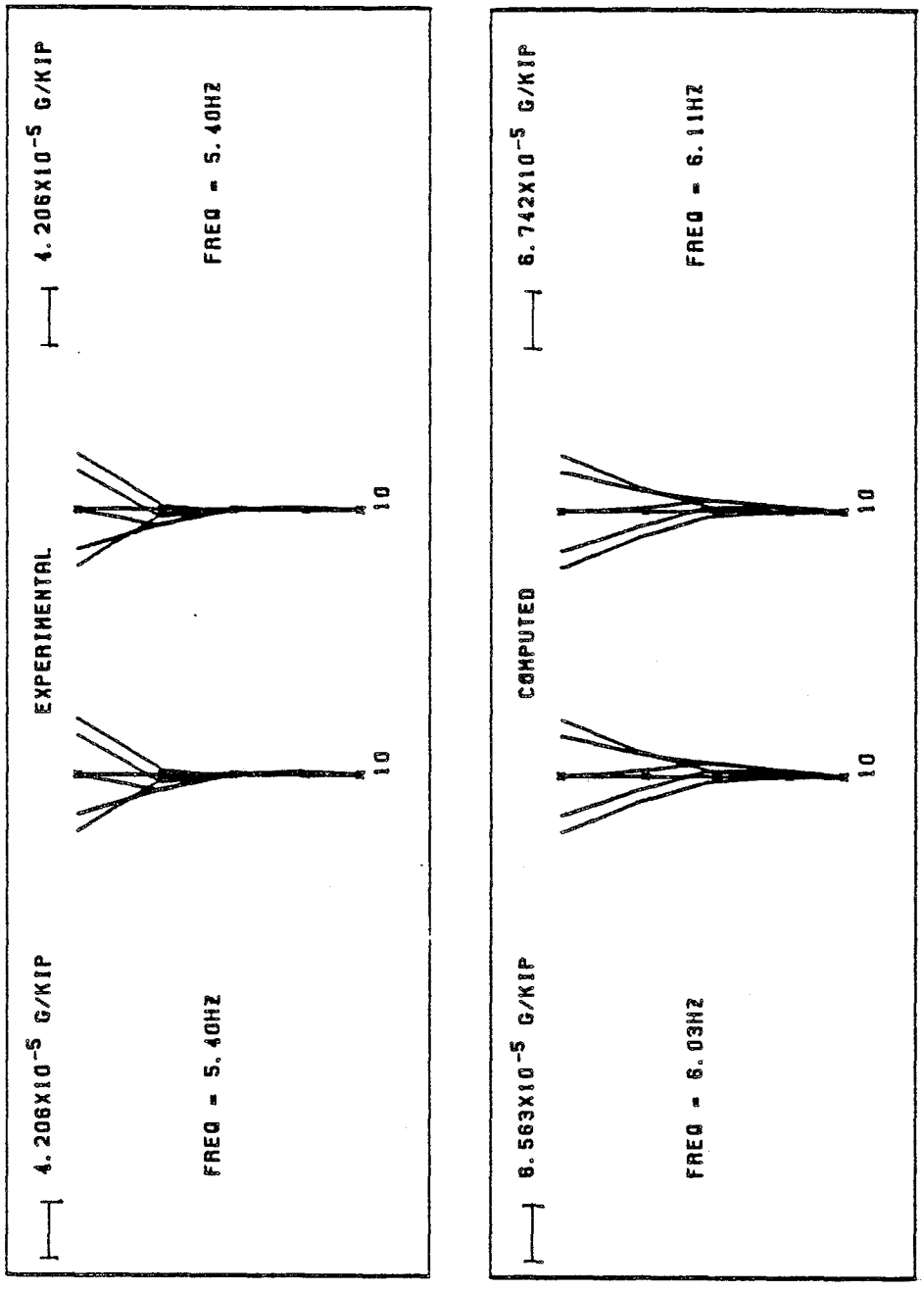

Figure 5.40 Comparison of crown cantilever response shapes for the third symmetric resonance determined experimentally and computed numerically using an incompressible water model.

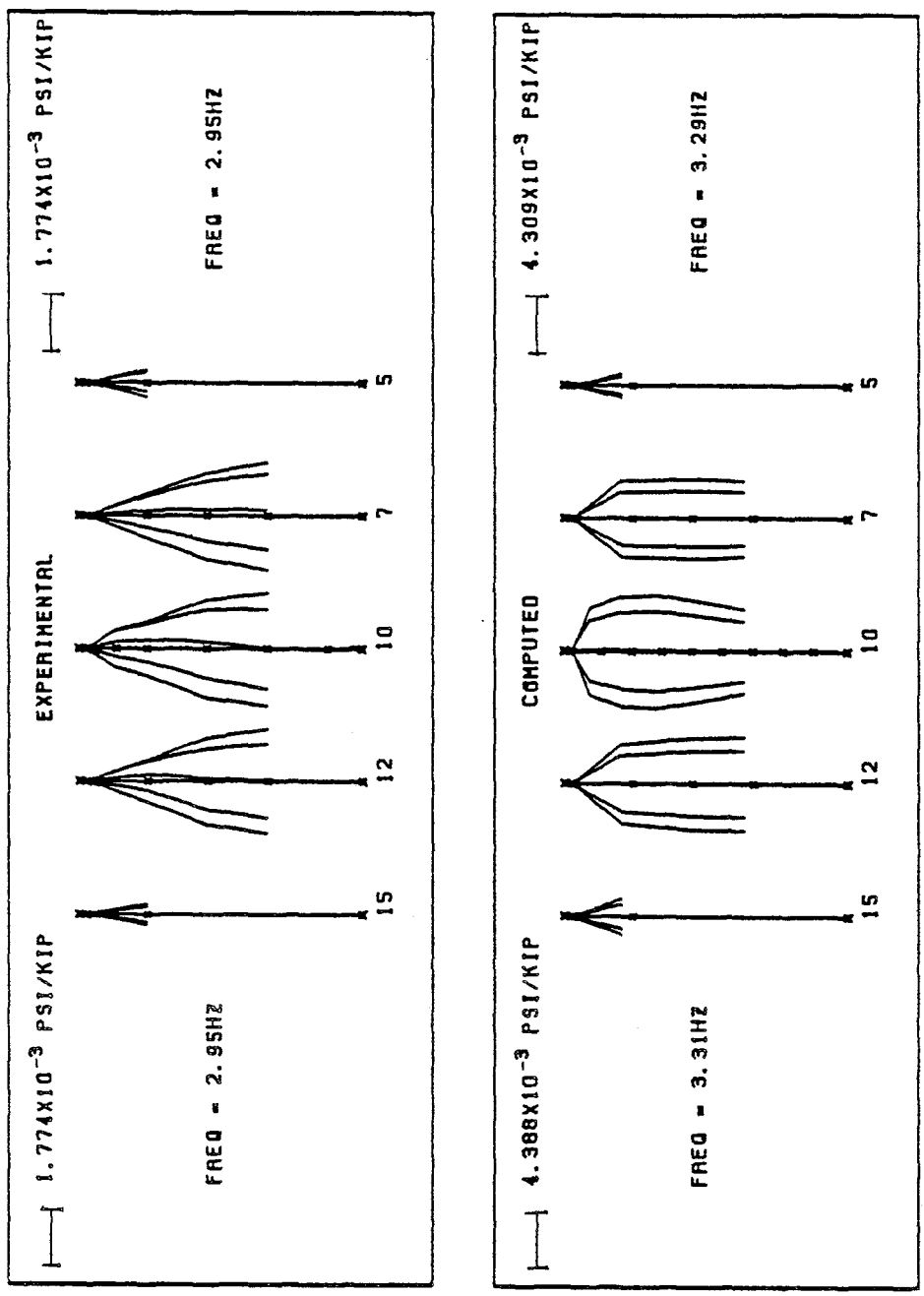

Figure 5.41 Comparison of the pressure profiles for the first symmetric resonance determined experimentally and computed numerically using an incompressible water model.

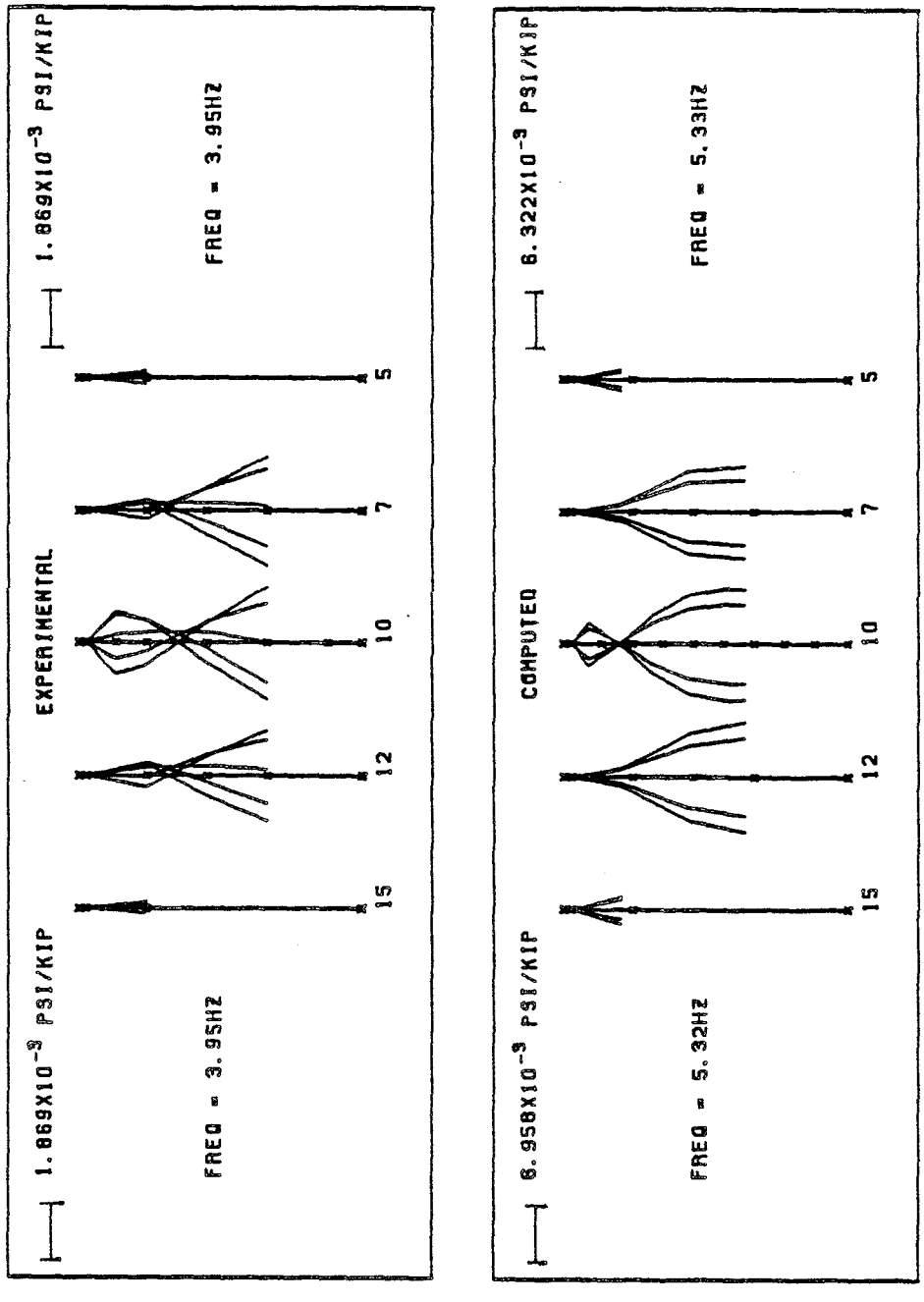

Figure 5.42 Comparison of the pressure profiles for the second symmetric resonance determined experimentally and computed numerically using an incompressible water model.

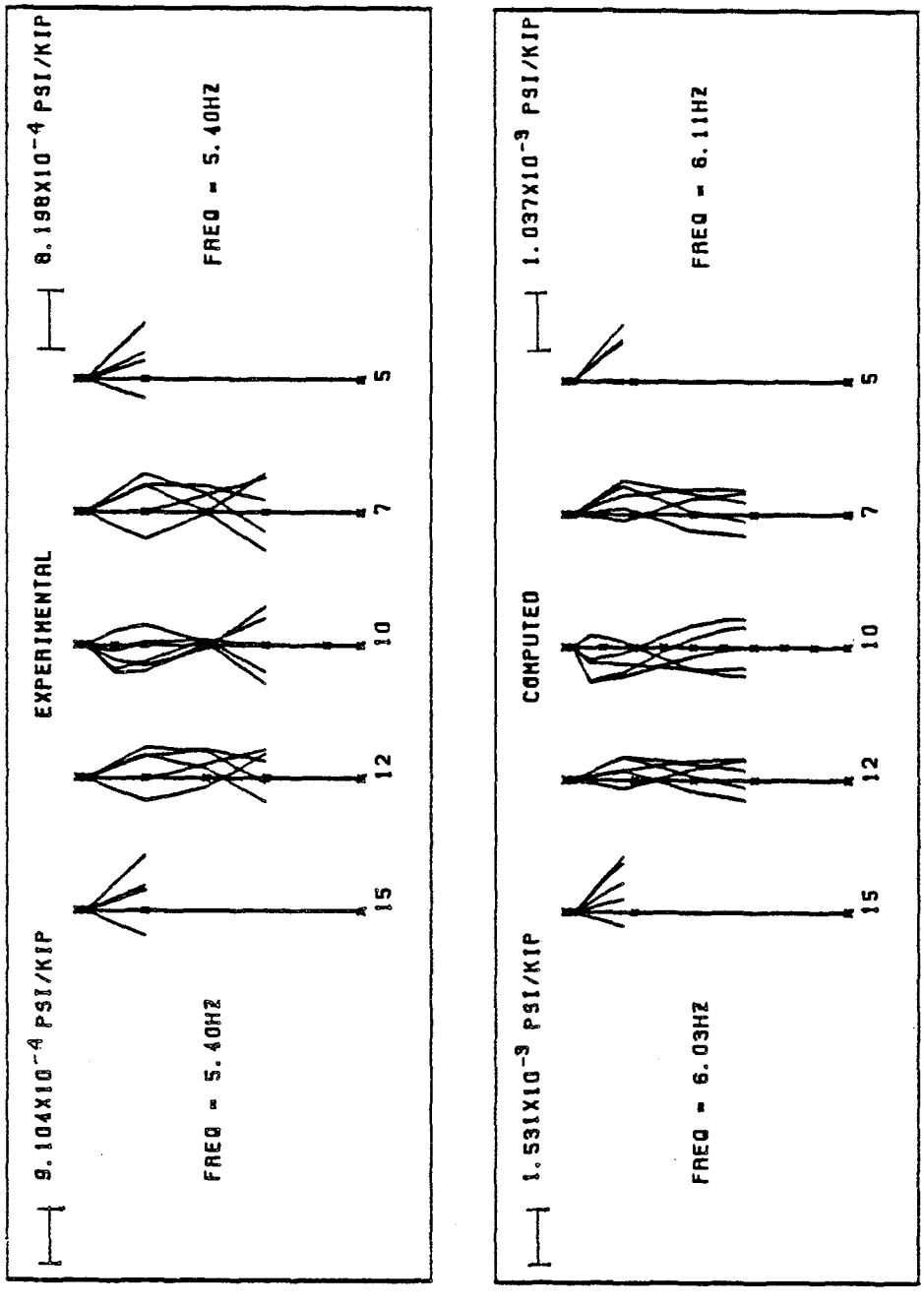

Figure 5.43 Comparison of the pressure profiles for the third symmetric resonance determined experimentally and computed numerically using an incompressible water model.

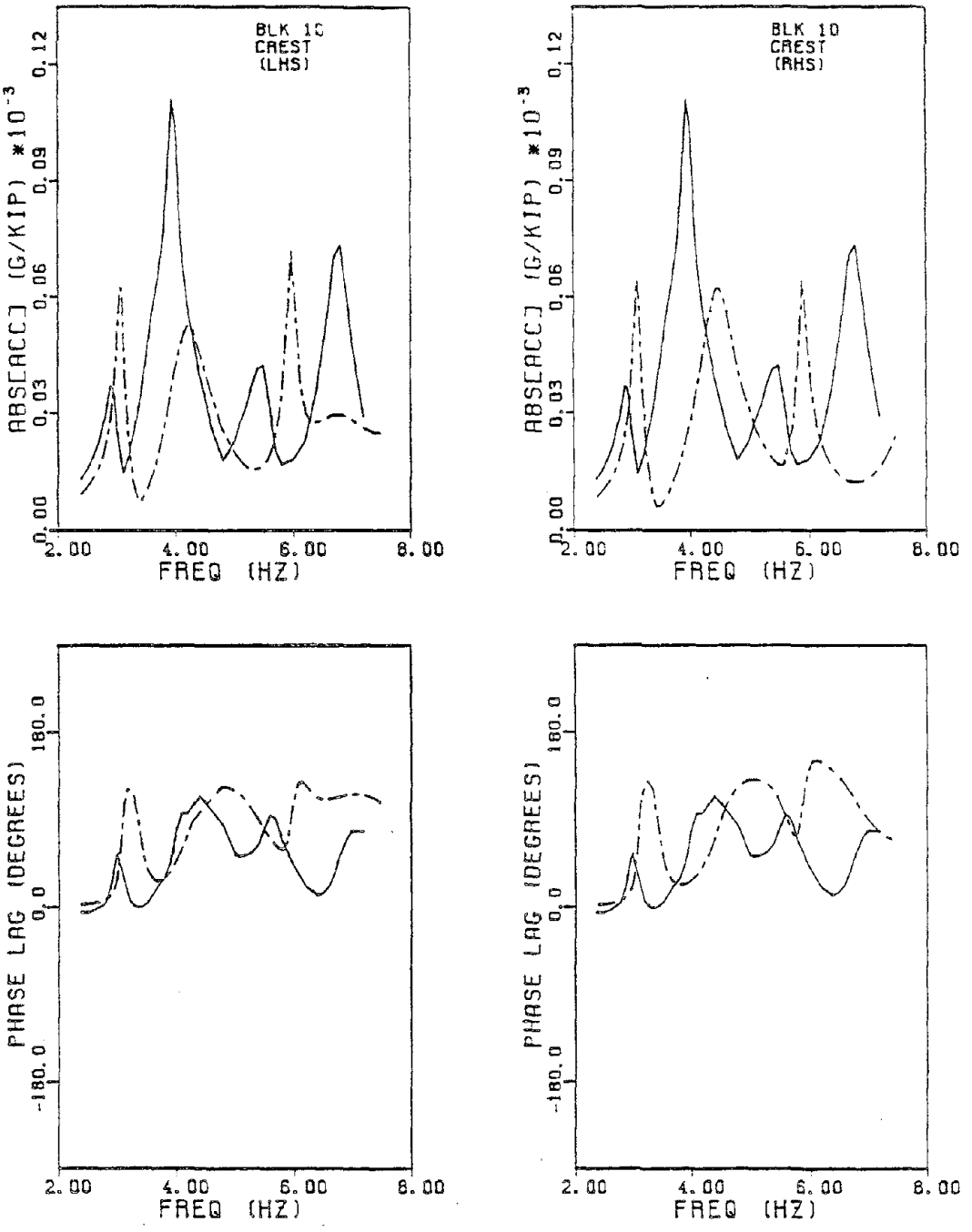

Figure 5.44 Measured and computed frequency response curves obtained for the symmetric shake at Block 10 on the dam crest. Shown are the radial components of acceleration and phase. Comparisons are shown for both LHS (left) and RHS (right) water models. The solid curves represent the experimental data and the dashed curves denote the computed responses. A compressible water model was used in the analysis.

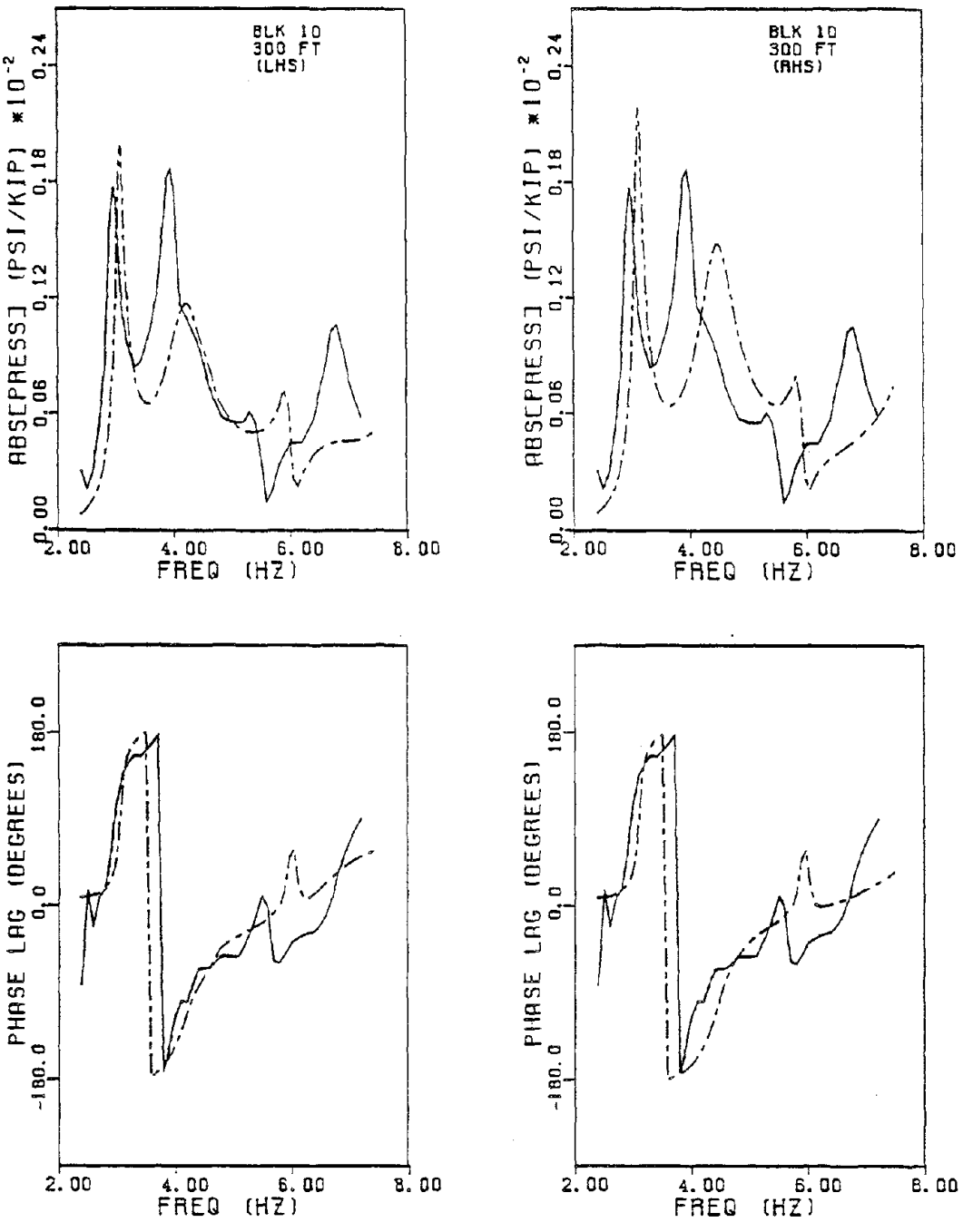

Figure 5.45 Measured and computed frequency response curves for hydrodynamic pressure and phase on the upstream face of the dam at Block 10 at a depth of 300 feet. The responses are obtained for the symmetric shake. Comparisons are shown for both LHS (left) and RHS (right) water models. The solid curves represent the experimental data and the dashed curves denote the computed responses. A compressible water model was used in the analysis.

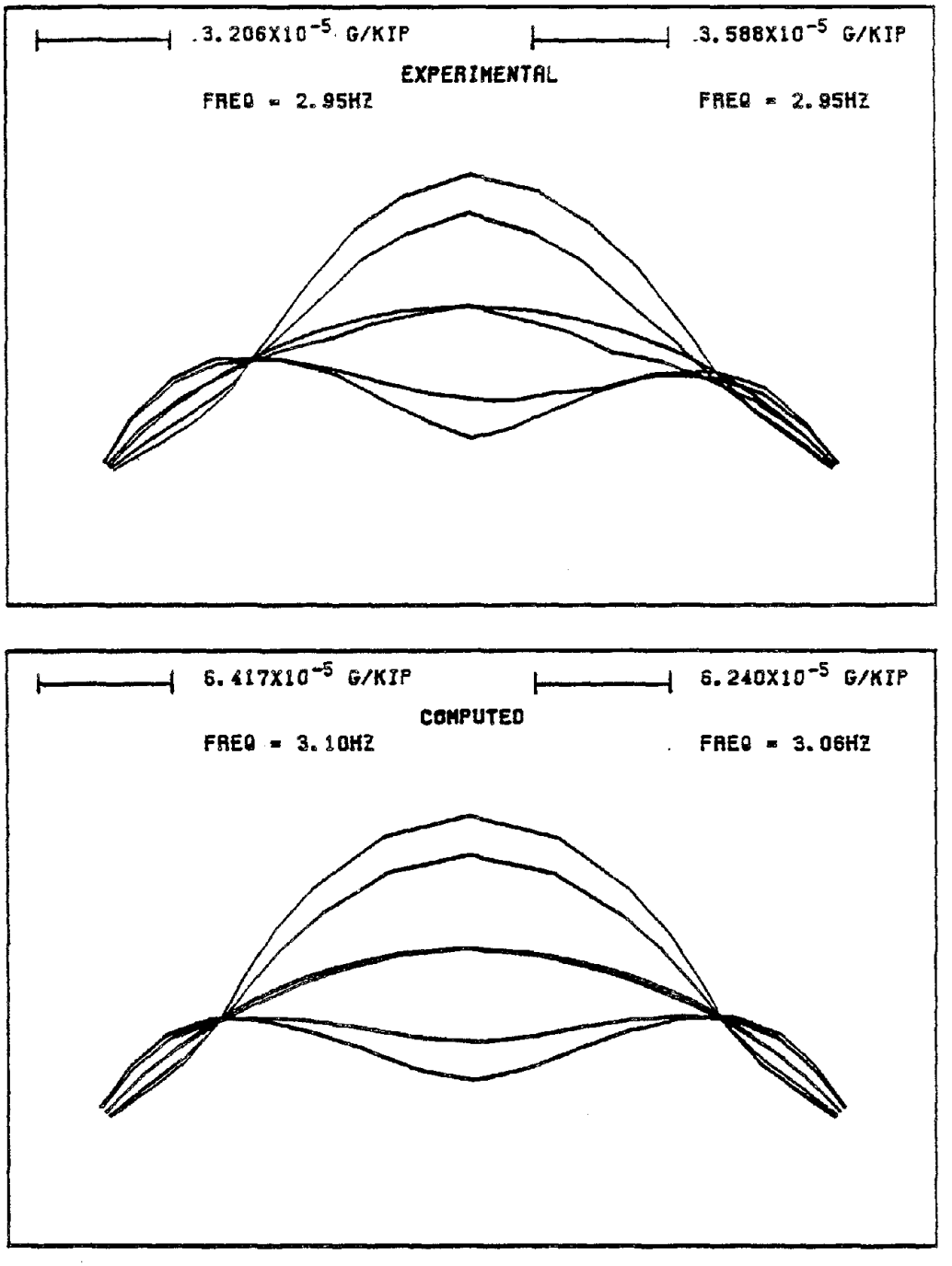

Figure 5.46 Comparison of the dam crest response shapes for the first symmetric resonance determined experimentally and computed numerically using a compressible water model.

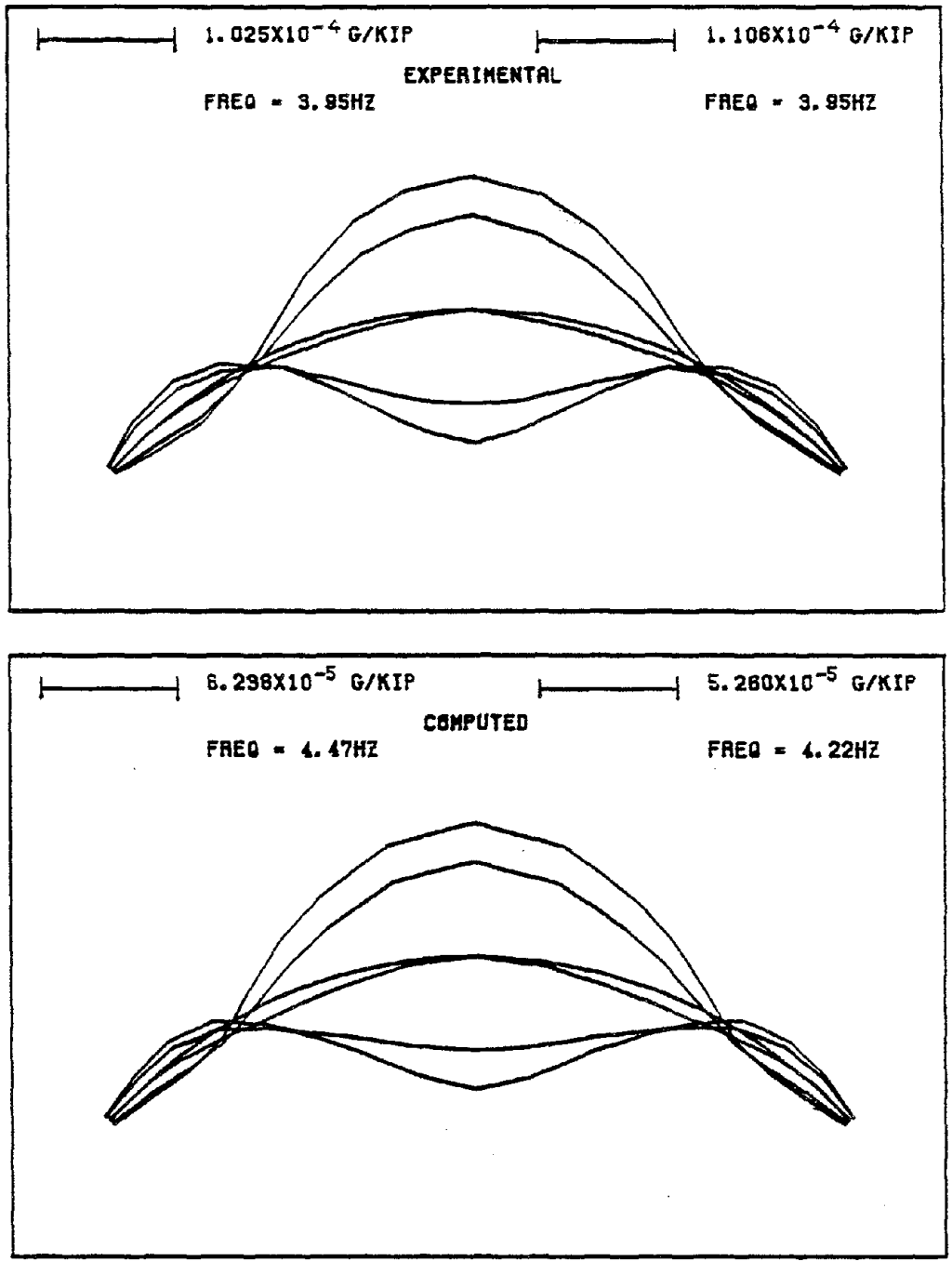

Figure 5.47 Comparison of the dam crest response shapes for the second symmetric resonance determined experimentally and computed numerically using a compressible water model.

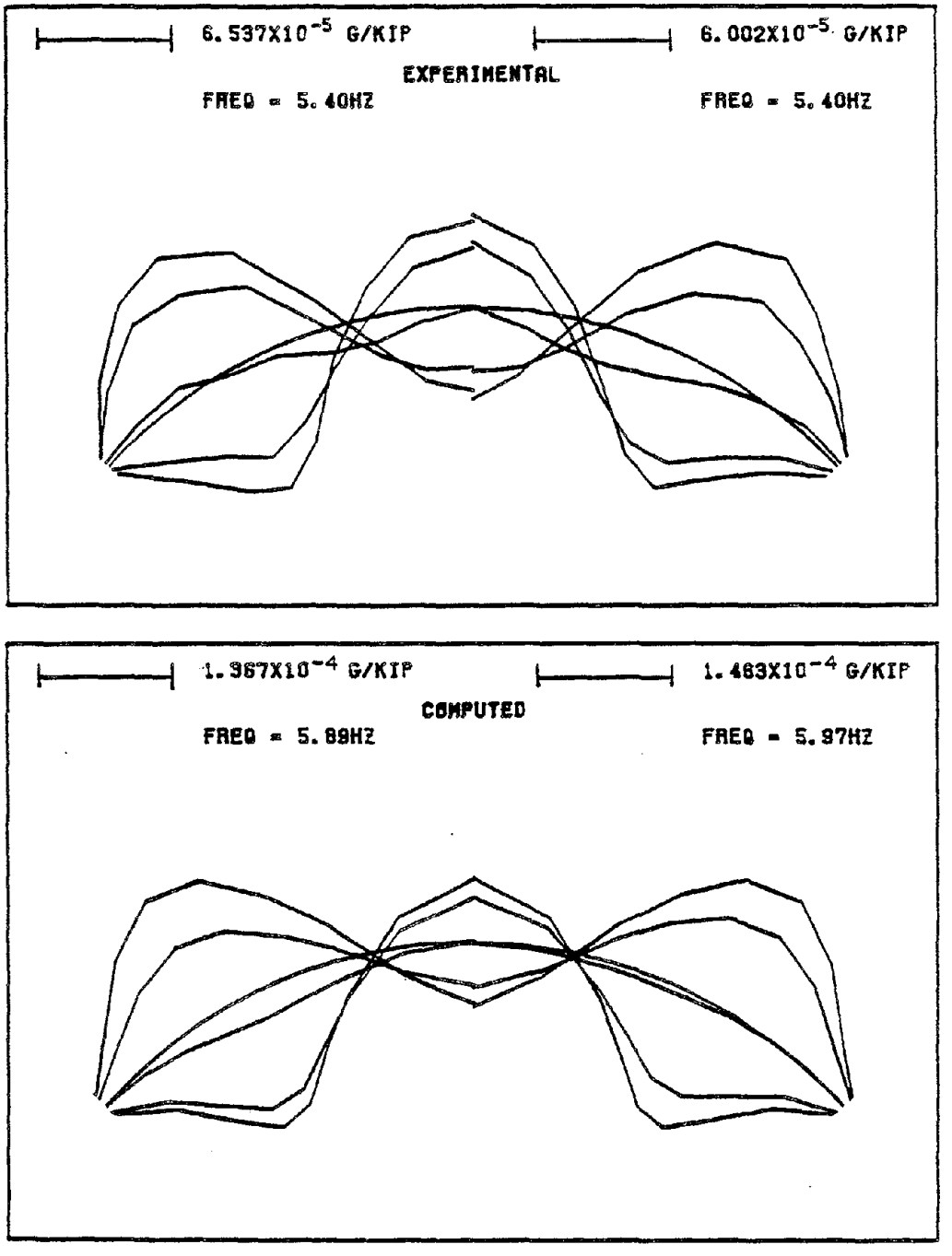

Figure 5.48 Comparison of the dam crest response shapes for the third symmetric resonance determined experimentally and computed numerically using a compressible water model.

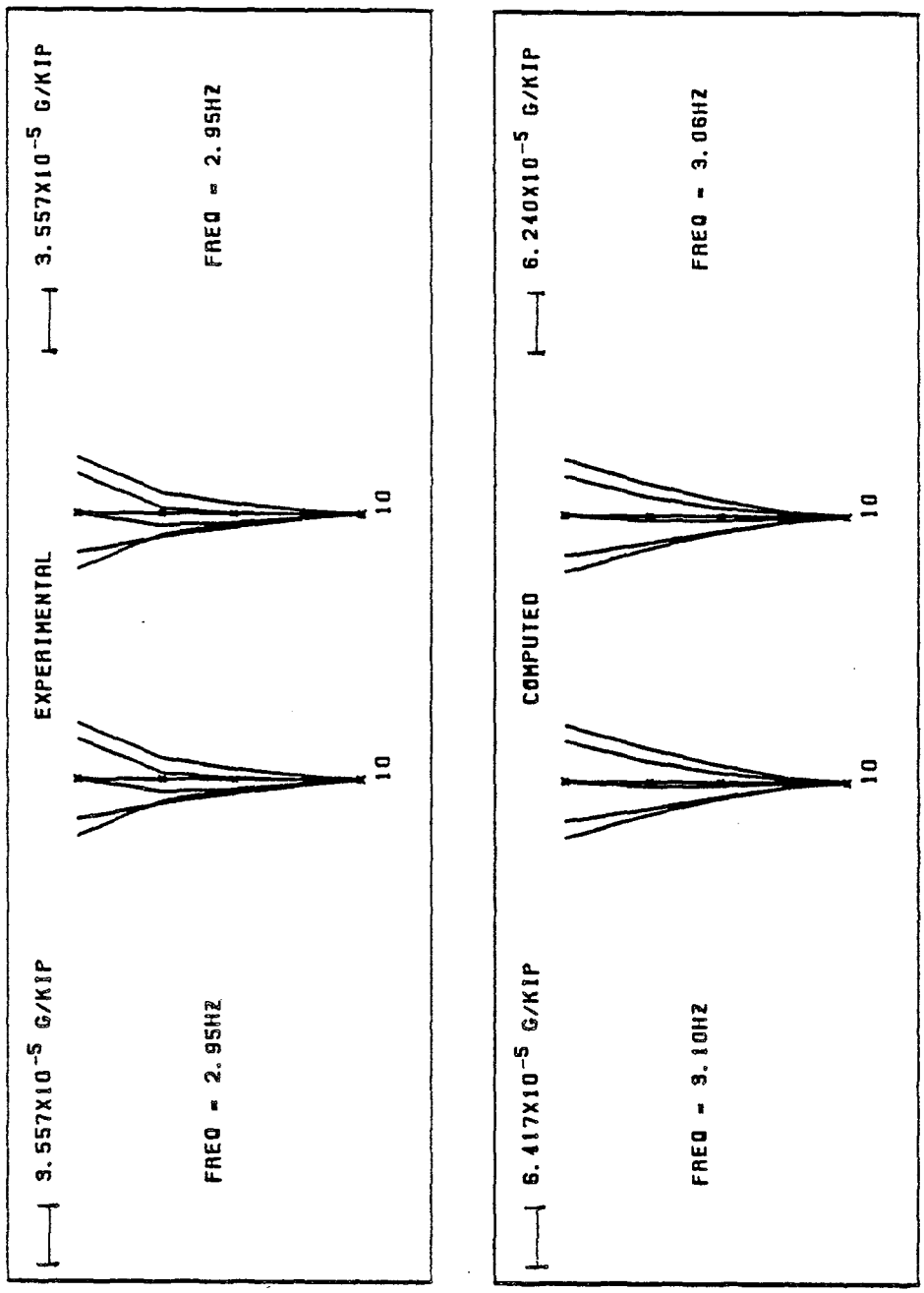

Figure 5.49 Comparison of crown cantilever response shapes for the first symmetric resonance determined experimentally and computed numerically using a compressible water model.

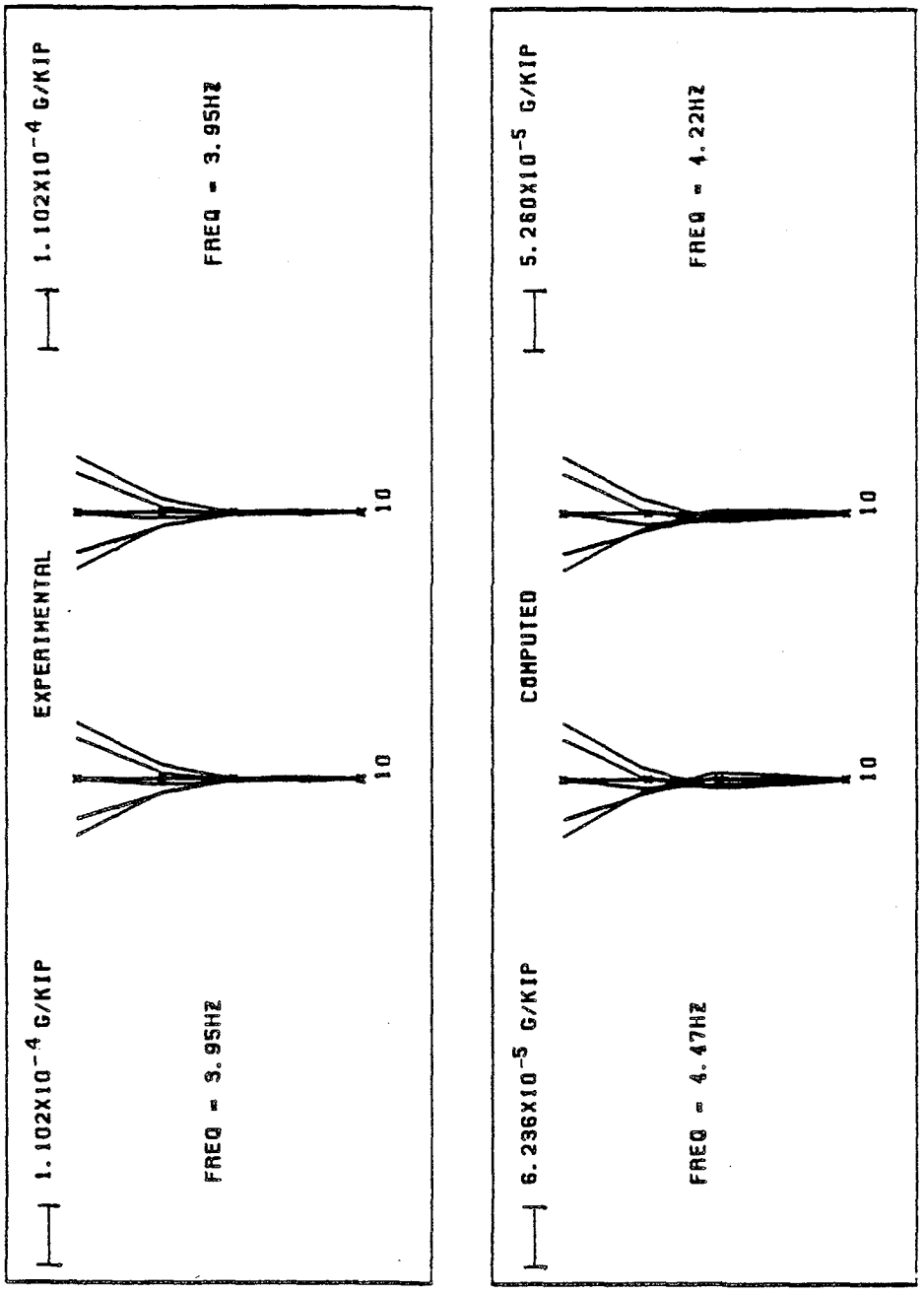

Figure 5.50 Comparison of crown cantilever response shapes for the second symmetric resonance determined experimentally and computed numerically using a compressible water model.

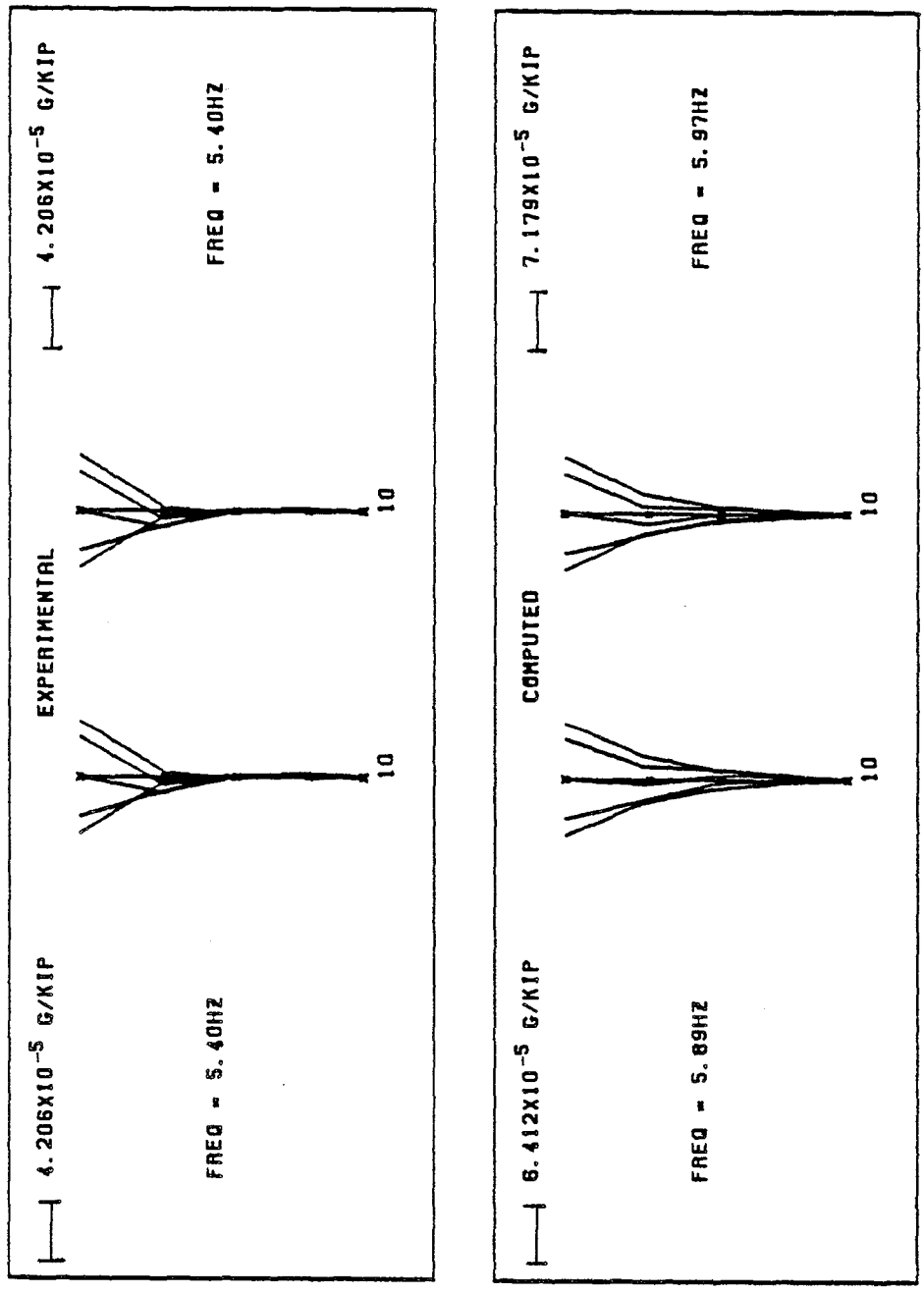

Figure 5.51 Comparison of crown cantilever response shapes for the third symmetric resonance determined experimentally and computed numerically using a compressible water model.

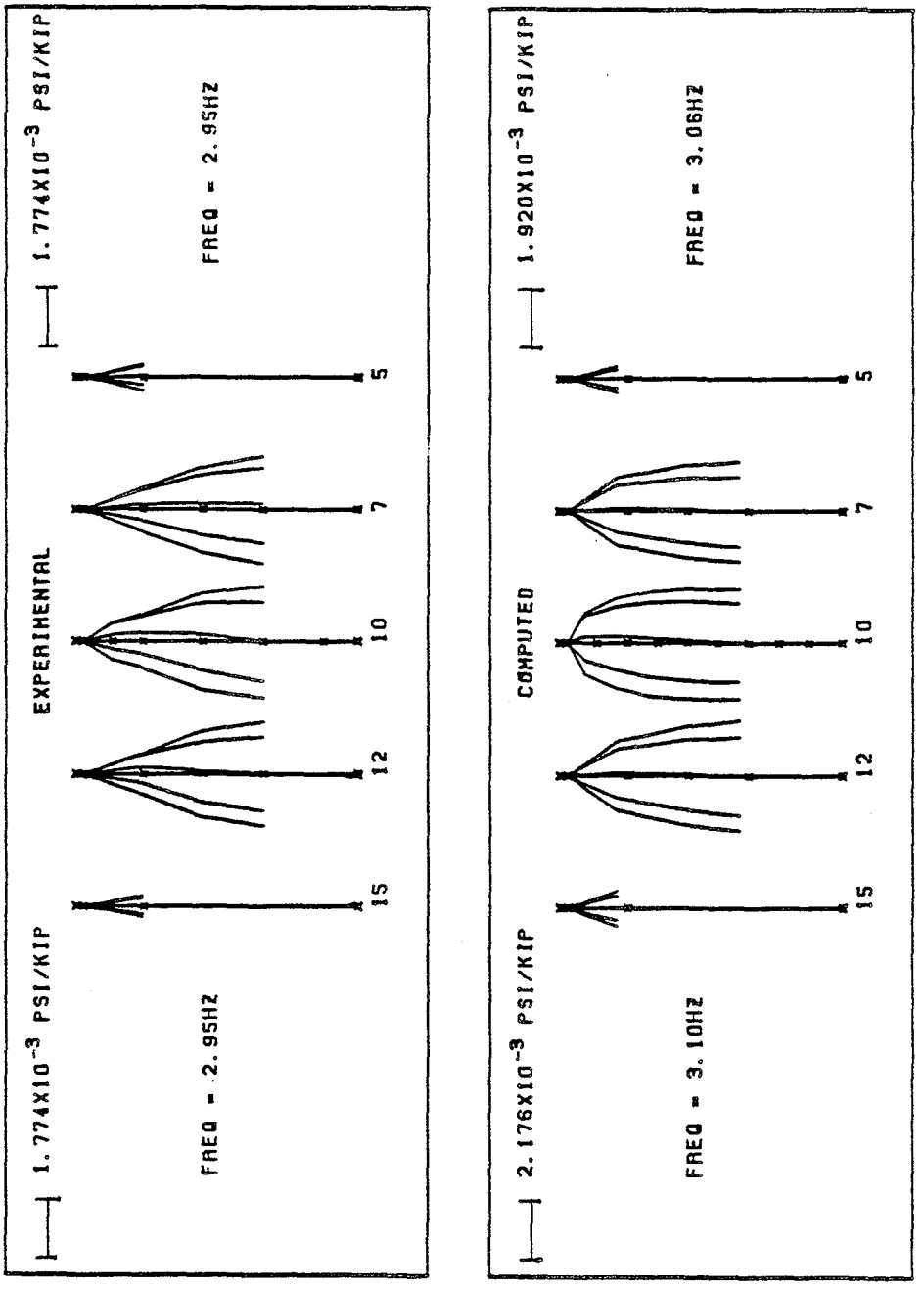

Figure 5.52 Comparison of the pressure profiles for the first symmetric resonance determined experimentally and computed numerically using a compressible water model.

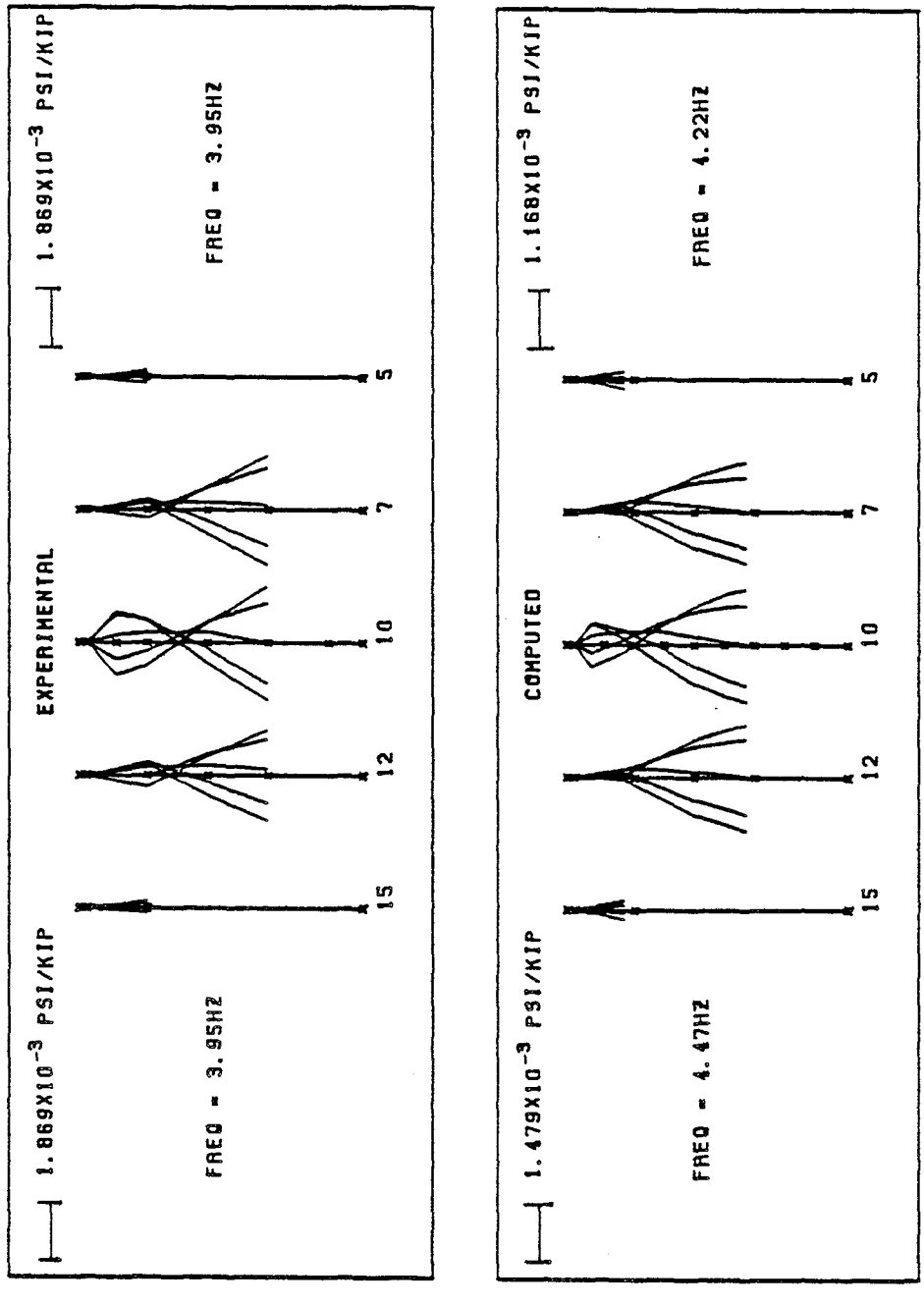

Figure 5.53 Comparison of the pressure profiles for the second symmetric resonance determined experimentally and computed numerically using a compressible water model.

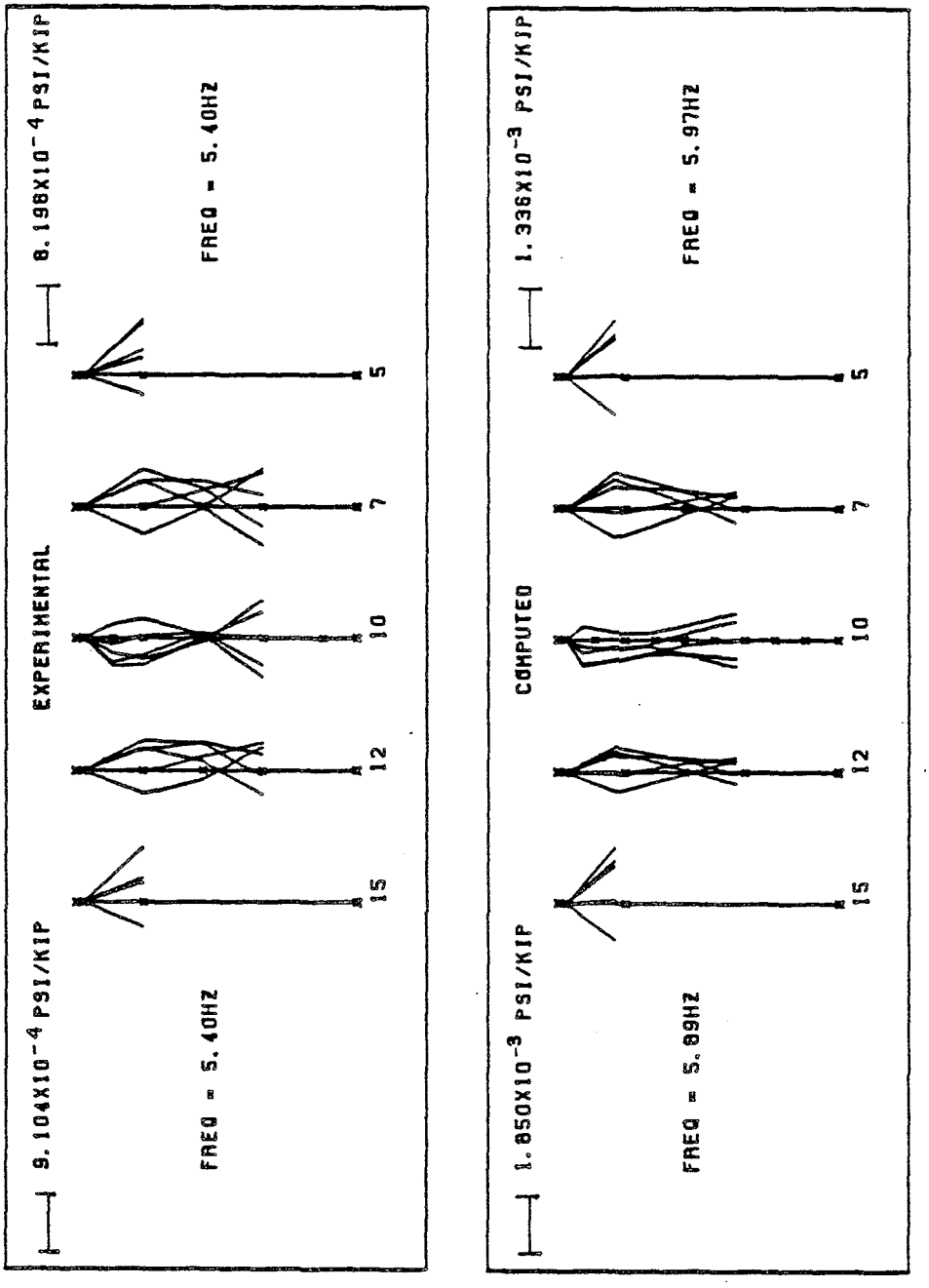

Figure 5.54 Comparison of the pressure profiles for the third symmetric resonance determined experimentally and computed numerically using a compressible water model.

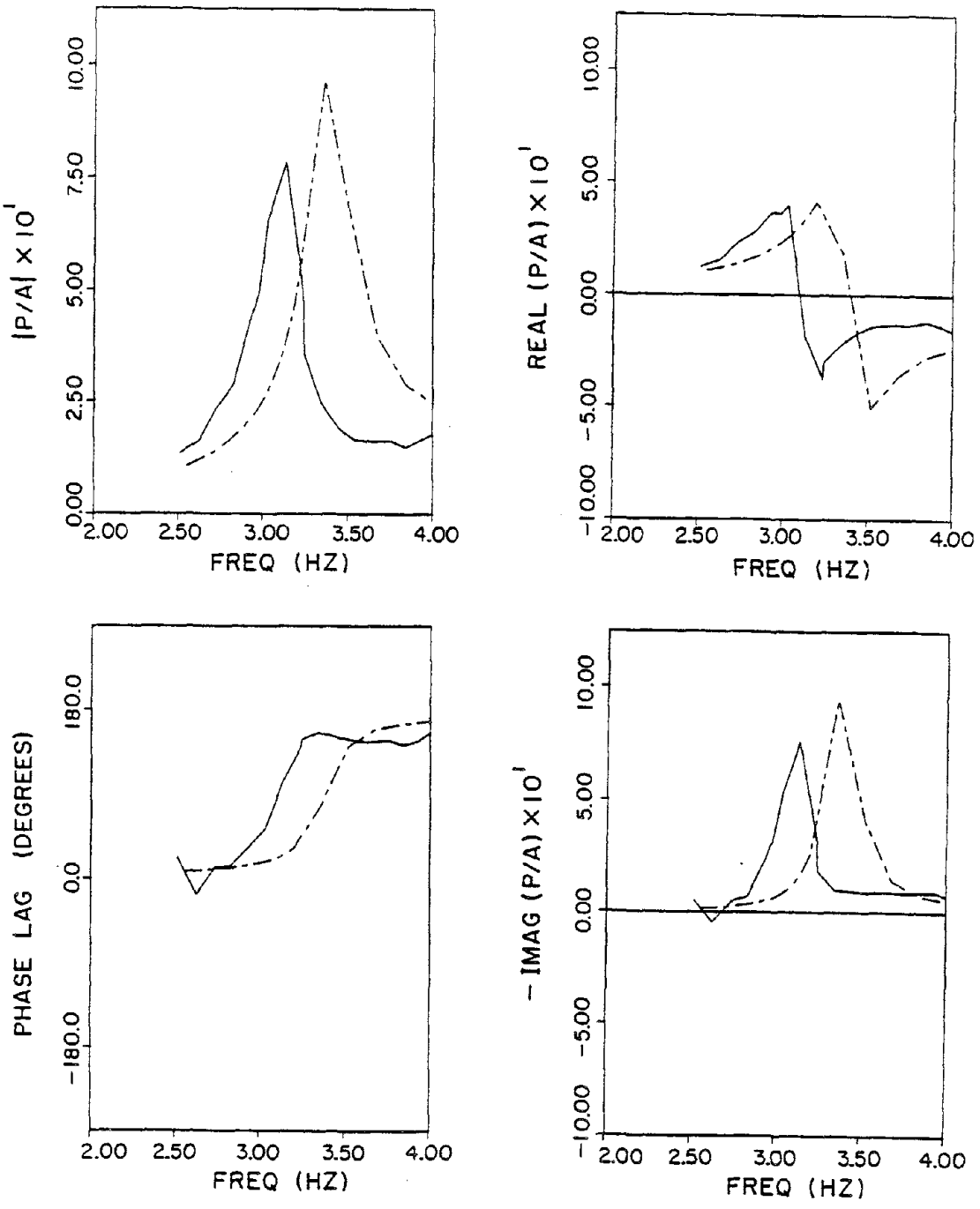

Figure 5.55 Comparison of normalized pressure responses (pressure at Block 10 at a depth of 300 feet divided by the dam acceleration on the crest at Block 10, symmetric shake) determined using both experimental data and computed LHS results with compressible water. Shown are the magnitude, phase, real and imaginary parts. The solid curves represent the normalized quantity obtained from the experimental data and the dashed curves were computed from the numerical results.

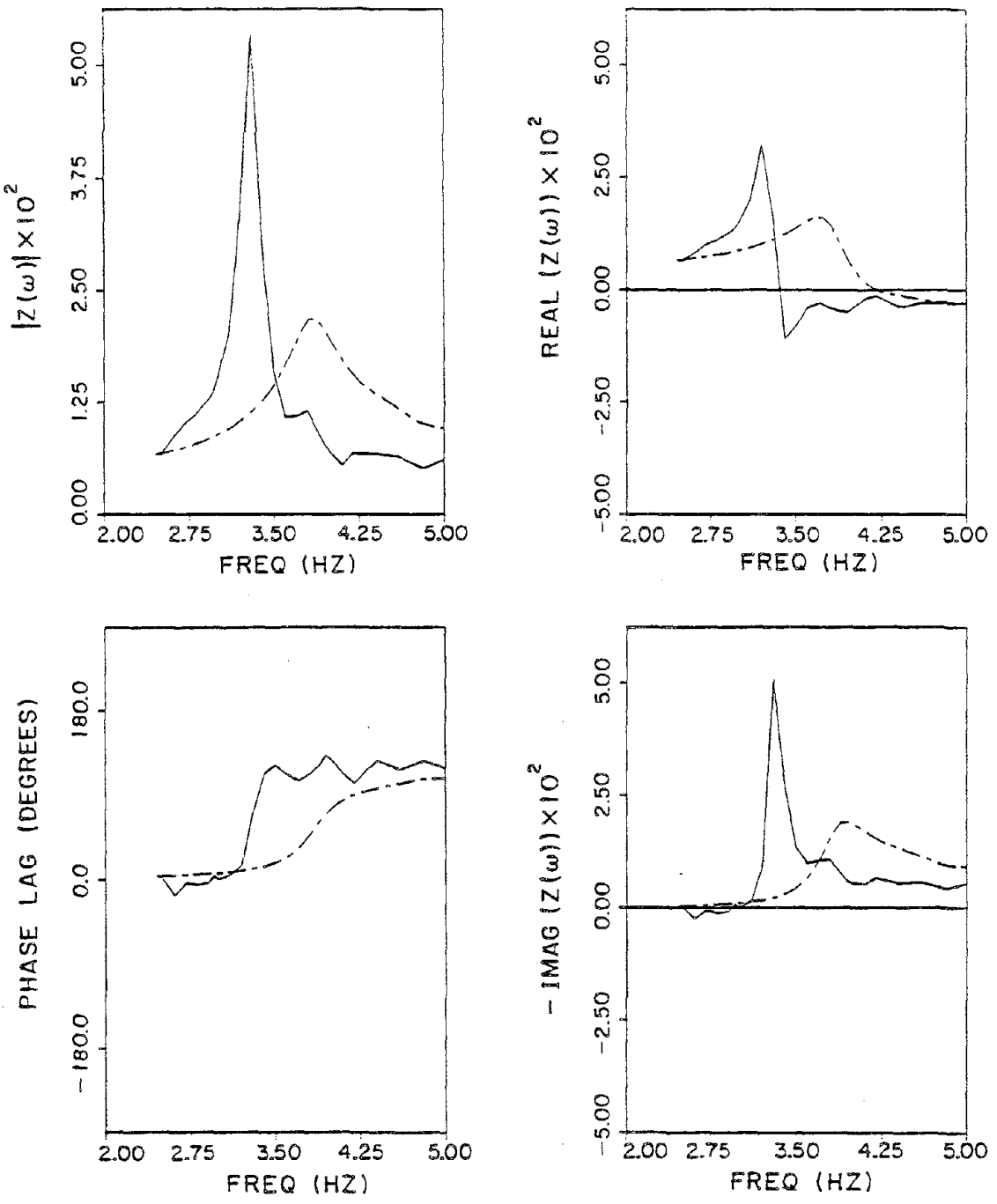

Figure 5.56 Comparison of $Z(\omega)$ determined using both experimental data and computed LHS results. Shown are the magnitude, phase, real and imaginary parts. The solid curves represent the quantity obtained with the experimental data and the dashed curves were computed from the numerical results.

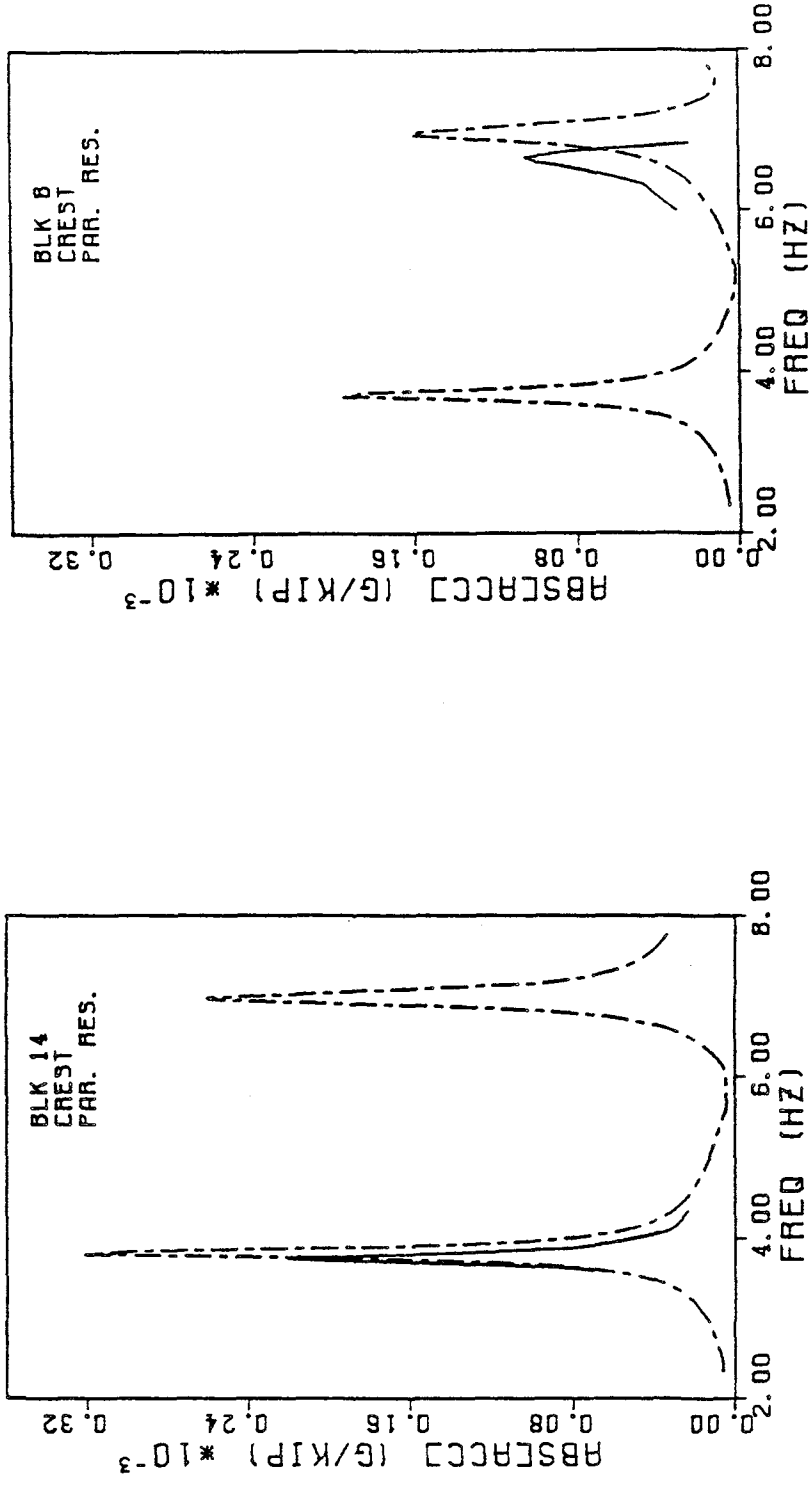

Figure 5.57 UCB 1969 test correlation. Measured and computed frequency response curves obtained for the antisymmetric shake at Blocks 14 and 8 on the dam crest. Shown are the radial components of acceleration and phase. The solid curves represent the experimental data and the dashed curves denote the computed responses. A compressible water model was used in the analysis.

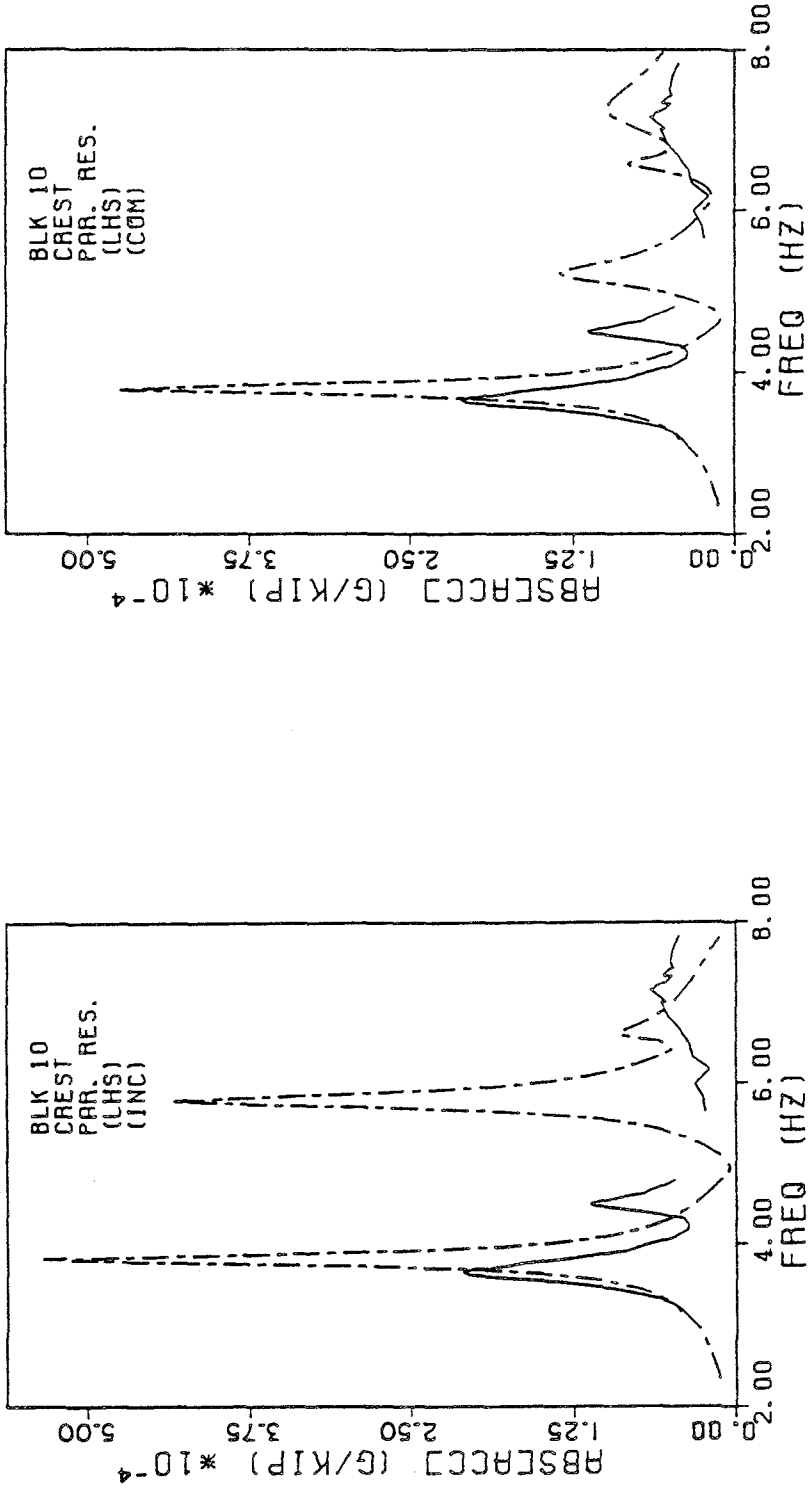

Figure 5.58 UCB 1969 test correlation. Measured and computed frequency response curves obtained for the symmetric shake at Block 10 on the crest. Shown are the radial components of acceleration and phase. Comparisons are shown for both incompressible (left) and compressible (right) water models. The solid curves represent the experimental data and the dashed curves denote the computed responses.

CHAPTER 6

CONCLUSIONS AND FUTURE WORK

6.1 Conclusions

Forced vibration tests and numerical studies carried out at Morrow Point Dam revealed ample evidence of water compressibility effects. The following observations can be made:

A. An attempt to isolate the response of the fundamental water mode appeared to be successful and a strong resonance was observed.

B. Damping values determined by the half-power method from the experimental data at full reservoir were approximately 1.5% for the first two antisymmetric resonances and approximately 4% for the first three symmetric resonances. A possible explanation for the higher damping values in the symmetric response is the added damping associated with water compressibility which is more pronounced in the symmetric case. It is also possible, however, that radiation damping associated with dam-foundation interaction could be greater for symmetric vibration.

C. The fit of the numerical results to the experimental data for the antisymmetric responses at full reservoir resulted in a slightly better match at the observed second antisymmetric resonant frequency of the system when water compressibility was included in the analysis. This frequency is close enough to the fundamental antisymmetric resonance of the water, f^a_{wat}, to be affected by the increased added mass from the water resonance.

D. Prediction of the symmetric data at full reservoir after calibrating the numerical model with the antisymmetric data yielded poor results with the incompressible water model. Inclusion of water compressibility improved the correlation which

is not surprising since the fundamental symmetric frequency of the water, f^s_{wat}, is below the fundamental symmetric frequency of the dam-foundation system, f^s_{dam}, indicating the potential for strong water compressibility effects.

E. Prediction of the symmetric data obtained for the partially full reservoir (water level at 158 feet below the crest) also improved when water compressibility was included. Here, f^s_{wat} is low enough to significantly affect the second symmetric resonant frequency of the system.

The mathematical idealization described in Chapter 4 appears adequate to model the antisymmetric forced vibration response of Morrow Point Dam at any water level. Reasonable choices for Young's moduli and damping values resulted in a good fit to the experimental data. However, water compressibility did not play an important role in the frequency range considered. The ability of the model to reproduce the symmetric responses of Morrow Point Dam, where water compressibility effects are more pronounced, has not been established. No choice of program parameters, E_{rat}, α, or damping values of the dam-foundation system, could have matched the second symmetric resonant peak amplitude because the compressibile water model intoduced too much damping in the frequency interval adjacent to and above f^s_{wat}. In fact, isolation of the fundamental water mode revealed significant differences in the frequency and character of the resonance as obtained from the experimental data and from the numerical results. However, modifications to the water mesh, perhaps including a construction notch around the perimeter of the dam and/or a steepening of the canyon walls, could reduce these differences and possibly lead to adequate agreement in the dam responses. If this can be accomplished, it will imply, however, that the symmetric response of Morrow Point Dam is sensitive to its complicated reservoir geometry because of water compressibility. Other factors, such as through-thickness flexibility of the upstream face of the dam, canyon elasticity, and partially saturated sediments, may also play a role in the

dynamics of the water domain.

6.2 Future Work

Although the experimental and numerical investigations of Morrow Point Dam have led to a better understanding of dam-water interaction effects, further study is needed. For example, the uncertainties regarding the construction notch and the topography of the canyon need to be addressed. To this end, seismic reflection profiling equipment can be used to obtain an acoustical image of the reservoir, which should yield accurate information in regard to the above issues.

Investigations of the damping mechanism associated with the water behavior is also merited. The same equipment used to define the reservoir geometry can be used to measure values of the reflection coefficient, α, along the reservoir bottom. These measurements will also reveal the presence of any significant amounts of sediment deposits, which were not included in the analyses here. In addition, hydrodynamic pressure responses obtained at varying distances from the dam could yield information regarding the damping associated with the propagation of pressure waves in the upstream direction. Finally, a more accurate determination of $Z(\omega)$ could also be made.

While verification of the mathematical idealization using forced vibration testing will be a significant event, it will not imply adequacy for earthquake excitation. Remaining issues include seismic input and the nonlinear effects due to joints, cracks, water cavitation and abutment instability.

REFERENCES

[1] "Design of Arch Dams," United States Department of the Interior, Bureau of Reclamation, 1977.

[2] J. F. Hall and A. K. Chopra, "Dynamic Response of Embankment Concrete—Gravity and Arch Dams Including Hydrodynanic Interaction," Earthquake Engineering Research Center Report No. UCB/EERC-80/39, University of California, Berkeley, October 1980.

[3] K.-L. Fok and A. K. Chopra, "Earthquake Analysis and Response of Concrete Arch Dams," Earthquake Engineering Research Center Report No. UCB/EERC-85/07, University of California, Berkeley, July 1985.

[4] K.-L. Fok, J. F. Hall and A. K. Chopra, "EACD-3D—A Computer Program for Three-Dimensional Earthquake Analysis of Concrete Dams," Earthquake Engineering Research Center Report No. UCB/EERC-86/09, University of California, Berkeley, July 1986.

[5] J. F. Hall, "The Dynamic and Earthquake Behavior of Concrete Dams: Review of Experimental Behavior and Observational Evidence," *Soil Dynamics and Earthquake Engineering*, to appear.

[6] J. S.-H. Kuo, "Fluid-Structure Interactions: Added Mass Computations for Incompressible Fluid," Earthquake Engineering Research Center Report No. UCB/EERC-82/09, University of California, Berkeley, August 1982.

[7] P. J. Deinum, R. Dungar, B. R. Ellis, A. P. Jeary, G. A. L. Reed and R. T. Severn, "Vibration Tests on Emosson Arch Dam, Switzerland," *Earthquake Engineering and Structural Dynamics*, Volume 10, Number 3, May–June 1982.

[8] R. W. Clough, R. M. Stephen, J. S.-H. Kuo, "Dynamic Response Analysis of Techi Dam," Earthquake Engineering Research Center Report No. UCB/EERC-82/11, University of California, Berkeley, August 1982.

[9] R. W. Clough, K.-T. Chang, et al., "Dynamic Response Behavior of Xiang Hong Dian Dam," Earthquake Engineering Research Center Report No. UCB/EERC-84/02, University of California, Berkeley, April 1984.

[10] R. W. Clough, K.-T. Chang, et al., "Dynamic Response Behavior of Quan Shui Dam," Earthquake Engineering Research Center Report No. UCB/EERC-84/20, University of California, Berkeley, November 1984.

[11] R. W. Clough and Y. Ghanaat, "Experimental Study of Arch Dam-Reservoir Interaction," *Proceedings of the Joint China–U.S. Workshop on the Earthquake Behavior of Arch Dams*, Beijing, 1987.

[12] R. Flesch and M. Eiselmayer, "Dynamic *In-Situ* Tests on Kolnbrein Arch Dam

(Austria)," *Proceedings of the 7th World Conference on Earthquake Engineering*, Volume 8, Istanbul, Turkey, 1980.

[13] T. Takahashi, "Results of Vibration Tests and Earthquake Observations on Concrete Dams and their Considerations," *Proceedings of the 8th International Congress on Large Dams*, Question 29, Edinburgh, Scotland, 1964.

[14] D. Rea, C.-Y. Liaw and A. K. Chopra, "Mathematical Models for the Dynamic Analysis of Concrete Gravity Dams," *Earthquake Engineering and Structural Dynamics*, Volume 3, Number 3, January–March 1975.

[15] ANCO Engineers, Inc., "Dynamic Testing of Concrete Dams," Prepared for National Science Foundation, June 1982.

[16] J. G. Bouwkamp, "Forced Vibration Tests of Morrow Point Dam," Report to Bureau of Reclamation, June 1971.

[17] R. M. Stephen, "Forced Vibration Tests, Morrow Point Dam," Service to Industry Report No. 72-15, University of California, Berkeley, December 1972.

[18] Lindvall, Richter and Associates, "Final Report for Investigation and Reanalysis of the Big Tujunga Dam," Report to Los Angeles County Flood Control District, October 1975.

[19] S. Okamoto, N. Yoshida, K. Kato and M. Hakuno, "Dynamic Behavior of an Arch Dam During Earthquakes," Report of the Institute of Industrial Science, Volume 14, No. 2, University of Tokyo, December 1964.

[20] T. Takahashi and C. Tamura, "Field Vibration Tests on Dams—Examples of an Arch Dam and a Rockfill Dam," Some Recent Earthquake Engineering Research and Practice in Japan, Japanese National Committee of the International Association for Earthquake Engineering, Tokyo, Japan, May 1973.

[21] A. Castoldi, "Contribution of the Surveillance to the Evaluation of the Seismic Efficiency of Dams. Example of the Ambiesta Dam," Report No. 112, ISMES, Bergamo, November, 1978 (also, *Seminar on Construction in Seismic Zones*, Bergamo, Italy, 1978).

[22] F. Calciati, et al., "*In-Situ* Tests for the Determination of the Dynamic Characteristics of Some Italian Dams," *Proceedings of the 6th World Conference on Earthquake Engineering*, Volume 3, New Delhi, India, 1977.

[23] G. Oberti and A. Castoldi, "The Use of Models in Assessing the Behavior of Concrete Dams," *Dams and Earthquake*, Institution of Civil Engineers, London, England, 1981 (also ISMES report No. 129, Bergamo, Italy, October 1980).

[24] R. Flesch and M. Eiselmayer, "Dynamic Behavior of Arch Dams," *Proceedings of the 7th European Conference on Earthquake Engineering*, Volume 6, Athens, Greece, 1982.

[25] T. A. Paskalov, J. T. Petrovski and D. V. Jurukovski, "Full-Scale Forced Vibration Studies and Mathematical Model Formulation of Arch Concrete Dams," *Dams and Earthquake*, Institution of Civil Engineers, London, England, 1981 (also *Proceedings of the International Research Conference on Earthquake Engineering*, Skopje, Yugoslavia, 1980).

[26] Z. H. Duron and J. F. Hall, "New Techniques in Forced Vibration Testing," *Experimental and Analytical Methods in Structural Dynamics*, ASCE, April 1986.

[27] R. W. Clough, J. M. Raphael and S. Mojtahedi, "ADAP—A Computer Program for Static and Dynamic Analysis of Arch Dams," Earthquake Engineering Research Center Report No. EERC 73/14, University of California, Berkeley, June 1973.

[28] T. Hatano and T. Nakagawa, "Seismic Analysis of Arch Dams—Coupled Vibrations of Dam Body and Reservoir Water," Central Research Institute of Electric Power Industry, Technical Report, November 1972.

[29] R. Priscu, A. Popovici, L. Ilie and D. Stematiu, "New Aspects in the Earthquake Analysis of Arch Dams," **Criteria and Assumptions for Numerical Analysis of Dams**, D. N. Naylor, et al, editor, Swansea, September 1975.

[30] R. Priscu, A. Popovici, D. Stematiu and C. Stere, " Earthquake Engineering for Large Dams," John Wiley and Sons, 1985.

[31] C. S. Porter and A. K. Chopra, "Dynamic Response of Simple Arch Dams Including Hydrodynamic Interaction," Earthquake Engineering Research Center Report No. UCB/EERC-80/17, University of California, Berkeley, July 1980.

[32] S. Kotsubo, "External Forces on Arch Dams During Earthquakes, Memoirs Faculty of Engineering," Kyushu University, Fu Kuoka, Japan, Volume 20, No. 4, 1961.

[33] P. Chakrabarti and A. K. Chopra, "Earthquake Response of Gravity Dams Including Reservoir Interaction Effects," Earthquake Engineering Research Center Report No. EERC 72/6, University of California, Berkeley, 1972.

[34] "Morrow Point Dam and Powerplant, Technical Record of Design and Construction," United States Department of the Interior, Bureau of Reclamation, Engineering and Research Center, September 1983.

[35] "Concrete Performance in Morrow Point Dam 10-Year Core Report," United States Department of the Interior, Bureau of Reclamation, Engineering and Research Center, No. GR-81-5, March 1981.

[36] "Morrow Point Dam and Power Plant Foundation Investigation," United States Department of the Interior, Bureau of Reclamation, October 1965.

APPENDIX I

A complete and corrected data set from the forced vibration tests conducted on Morrow Point Dam is presented here. No smoothing of the data has been performed and adjacent data points are connected by straight lines. Shown are plots of the magnitude and phase of the response relative to the exciting force versus frequency. Pages 133–143 and 144–149 contain the dam acceleration and water pressure responses, respectively, obtained for the symmetric shake. Similarly, the dam acceleration and water responses obtained for the antisymmetric shake are shown on pages 150–158 and 159–165, respectively. Note that the dam acceleration response is the radial component at each station.

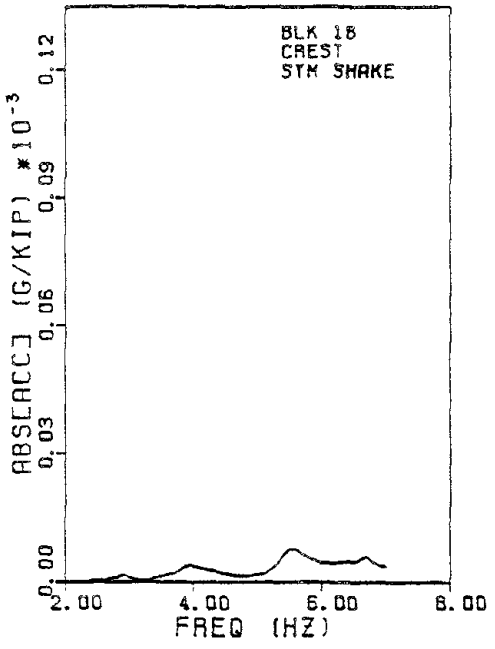
BLK 18
CREST
STM SHAKE
ABSLACC] (G/KIP) *10⁻³
0.00
0.03
0.06
0.09
0.12
2.00
4.00
6.00
8.00
FREQ (HZ)

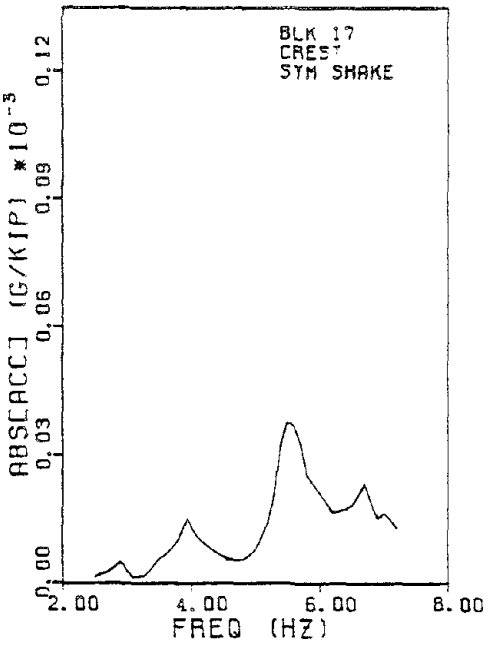
BLK 17
CREST
STM SHAKE
ABSLACC] (G/KIP) *10⁻³
0.00
0.03
0.06
0.09
0.12
2.00
4.00
6.00
8.00
FREQ (HZ)

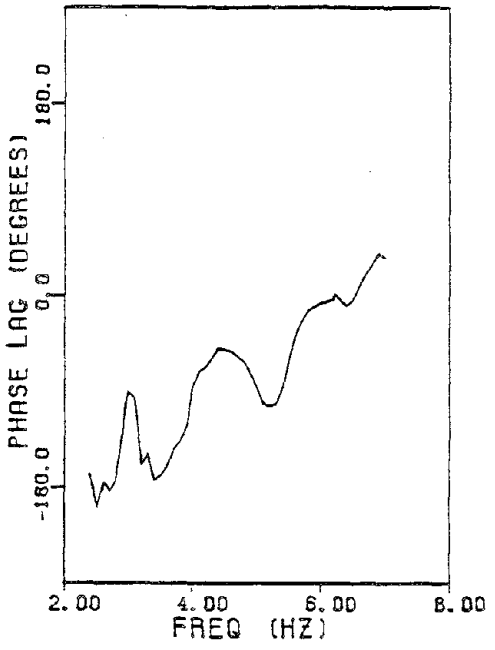
PHASE LAG (DEGREES)
180.0
0.0
-180.0
2.00
4.00
6.00
8.00
FREQ (HZ)

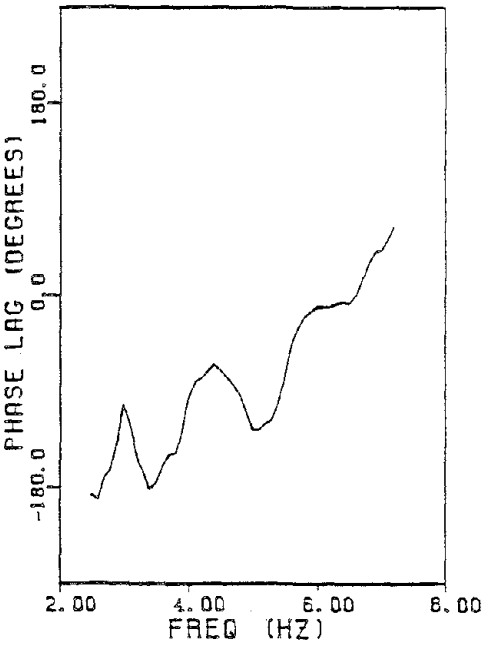
PHASE LAG (DEGREES)
180.0
0.0
-180.0
2.00
4.00
6.00
8.00
FREQ (HZ)

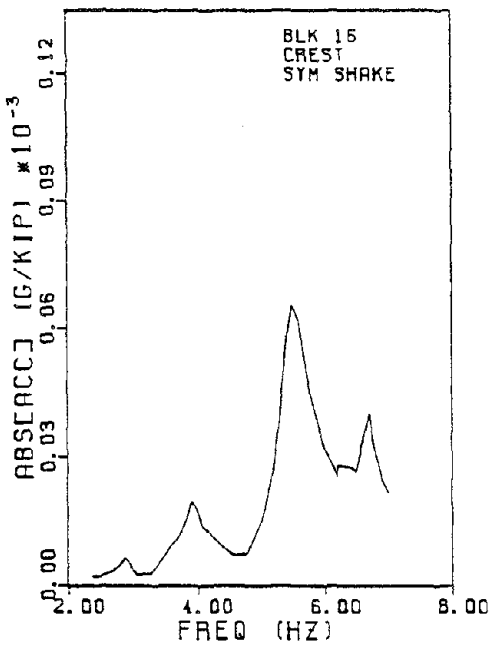
BLK 15
CREST
SYM SHAKE
ABSEACC] (G/KIP) *10^-3
0.00
0.03
0.06
0.09
0.12
2.00
4.00
6.00
8.00
FREQ (HZ)

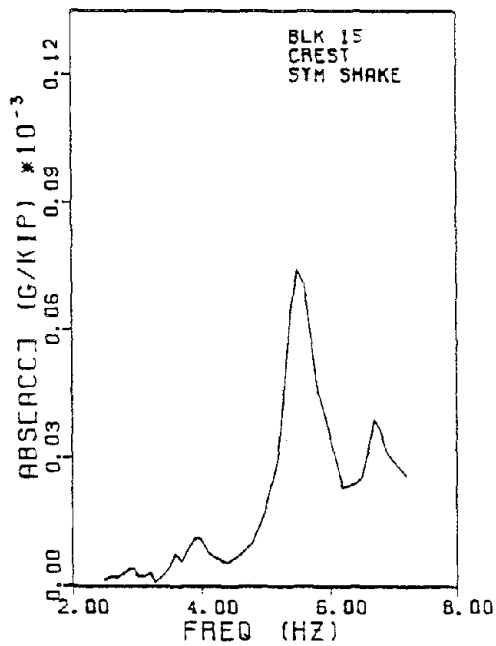
BLK 15
CREST
SYM SHAKE
ABSEACC] (G/KIP) *10^-3
0.00
0.03
0.06
0.09
0.12
2.00
4.00
6.00
8.00
FREQ (HZ)

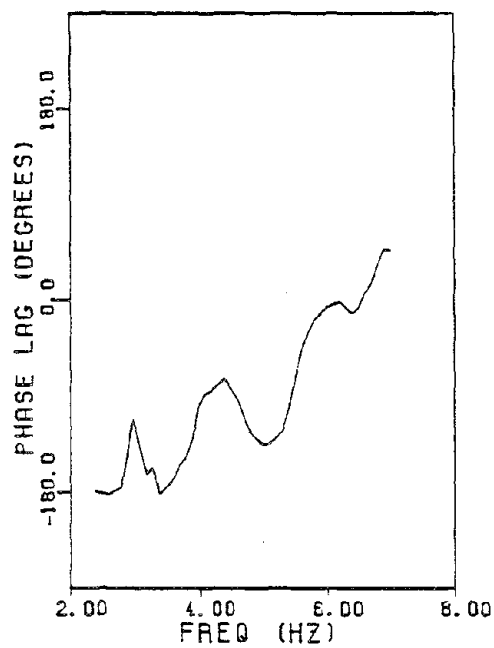
PHASE LAG (DEGREES)
180.0
0.0
-180.0
2.00
4.00
6.00
8.00
FREQ (HZ)

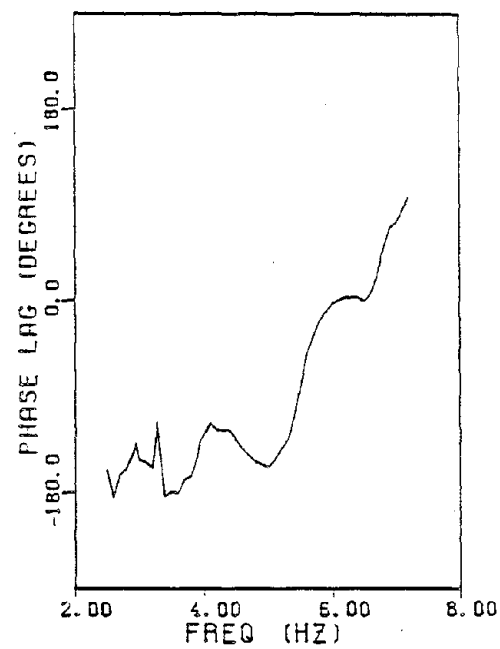
PHASE LAG (DEGREES)
180.0
0.0
-180.0
2.00
4.00
6.00
8.00
FREQ (HZ)

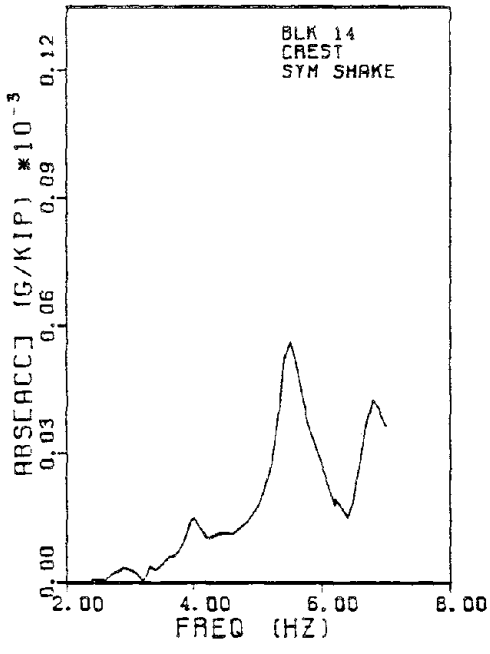
BLK 14
CREST
SYM SHAKE
ABS[ACC] (G/KIP) *10^-3
0.00
0.03
0.06
0.09
0.12
2.00
4.00
6.00
8.00
FREQ (HZ)

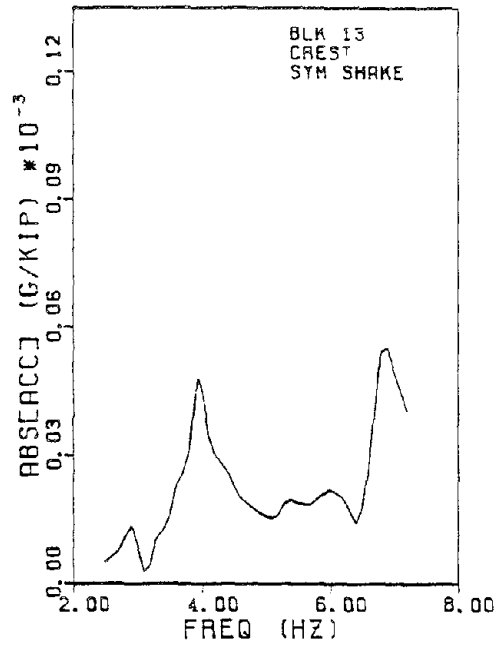
BLK 13
CREST
SYM SHAKE
ABS[ACC] (G/KIP) *10^-3
0.00
0.03
0.06
0.09
0.12
2.00
4.00
6.00
8.00
FREQ (HZ)

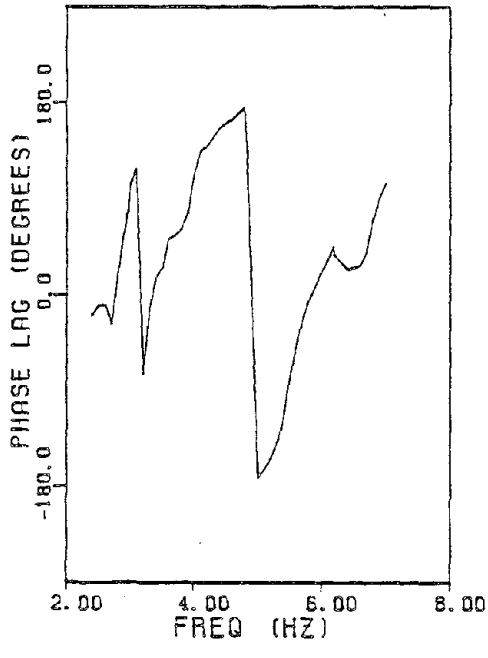
PHASE LAG (DEGREES)
180.0
0.0
-180.0
2.00
4.00
6.00
8.00
FREQ (HZ)

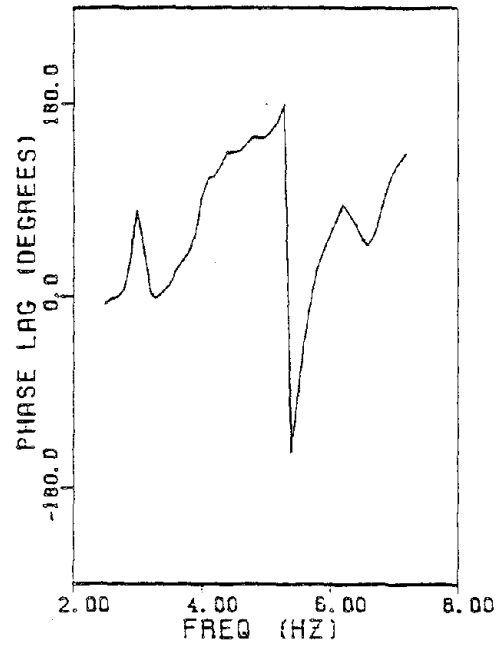
PHASE LAG (DEGREES)
180.0
0.0
-180.0
2.00
4.00
6.00
8.00
FREQ (HZ)

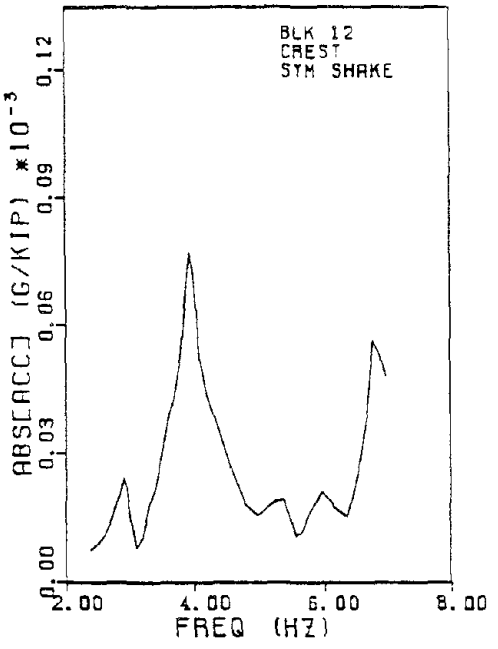
BLK 12
CREST
SYM SHAKE
ABS[ACC] (G/KIP) *10⁻³
0.00
0.03
0.06
0.09
0.12
2.00
4.00
6.00
8.00
FREQ (HZ)

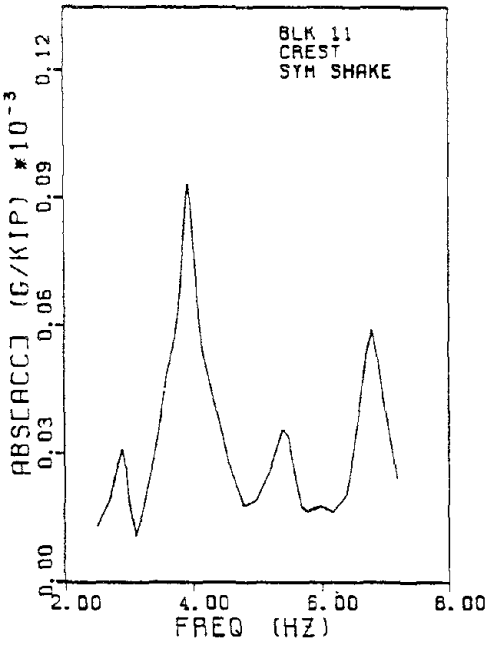
BLK 11
CREST
SYM SHAKE
ABS[ACC] (G/KIP) *10⁻³
0.00
0.03
0.06
0.09
0.12
2.00
4.00
6.00
8.00
FREQ (HZ)

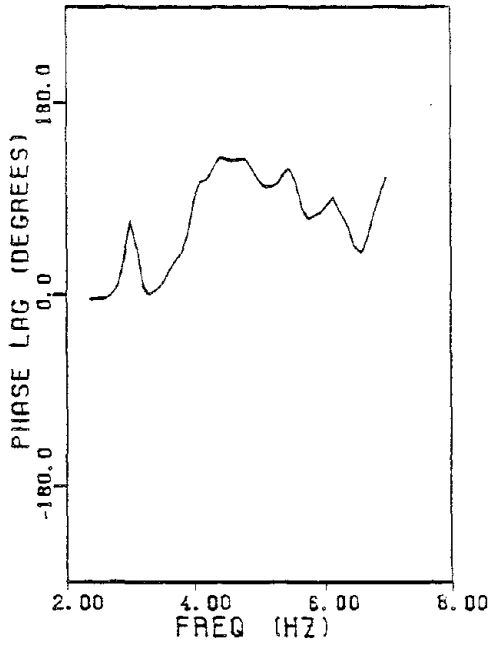
PHASE LAG (DEGREES)
180.0
0.0
-180.0
2.00
4.00
6.00
8.00
FREQ (HZ)

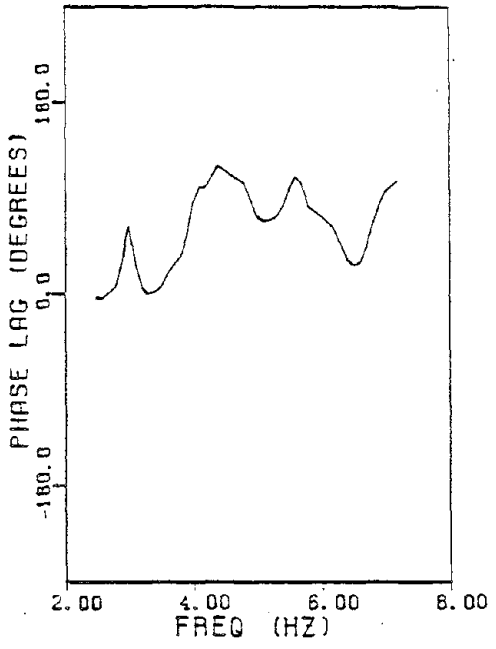
PHASE LAG (DEGREES)
180.0
0.0
-180.0
2.00
4.00
6.00
8.00
FREQ (HZ)

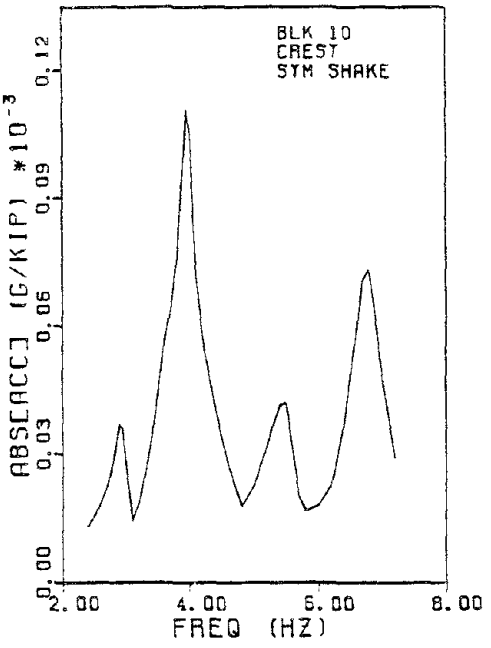
BLK 10
CREST
SYM SHAKE
ABSACCJ (G/KIP) *10⁻³
0.00
0.03
0.06
0.09
0.12
2.00
4.00
6.00
8.00
FREQ (HZ)

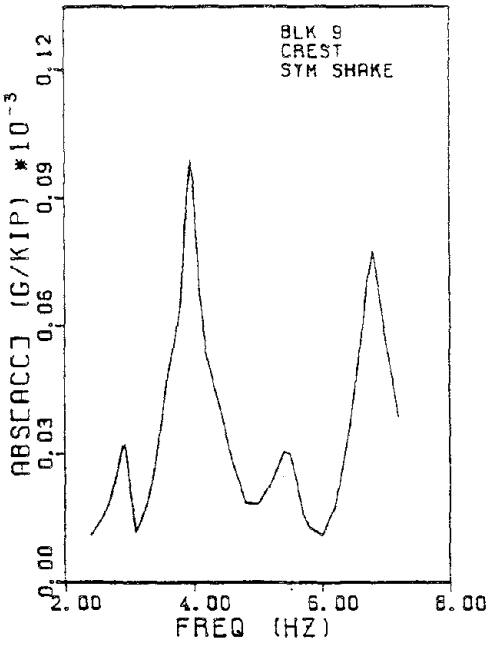
BLK 9
CREST
SYM SHAKE
ABSACCJ (G/KIP) *10⁻³
0.00
0.03
0.06
0.09
0.12
2.00
4.00
6.00
8.00
FREQ (HZ)

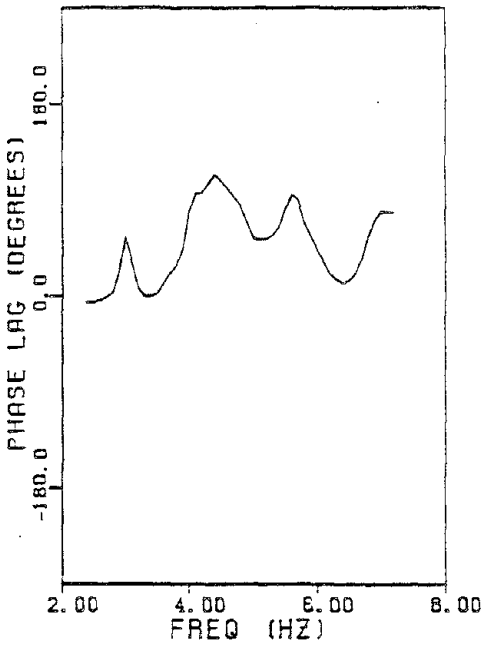
PHASE LAG (DEGREES)
180.0
0.0
-180.0
2.00
4.00
6.00
8.00
FREQ (HZ)

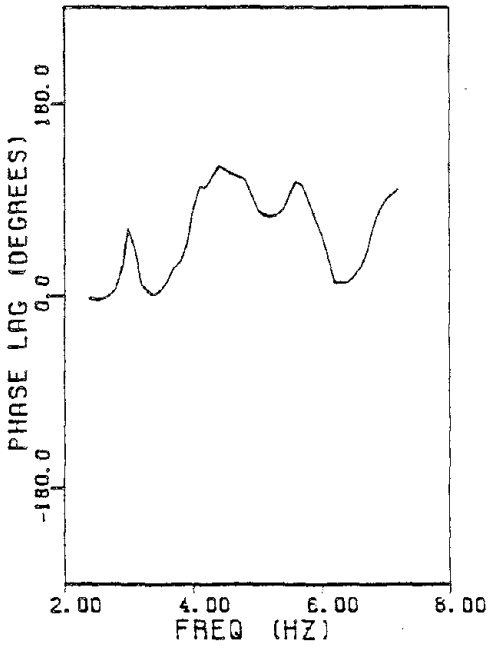
PHASE LAG (DEGREES)
180.0
0.0
-180.0
2.00
4.00
6.00
8.00
FREQ (HZ)

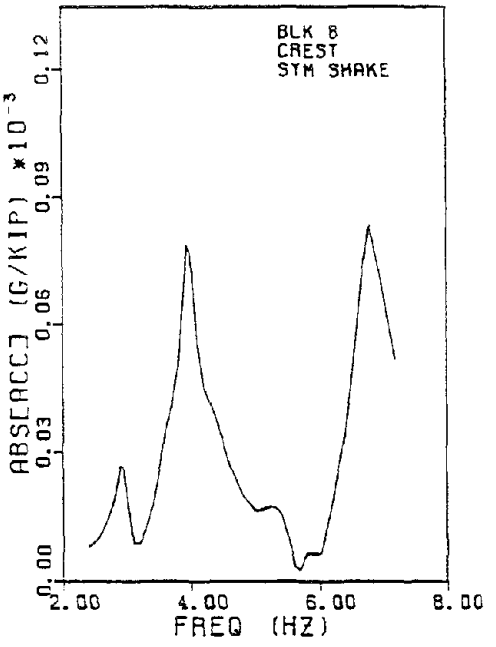
BLK 8
CREST
STM SHAKE
ABSACCJ (G/KIP) *10-3
0.00
0.03
0.06
0.09
0.12
2.00
4.00
6.00
8.00
FREQ (HZ)

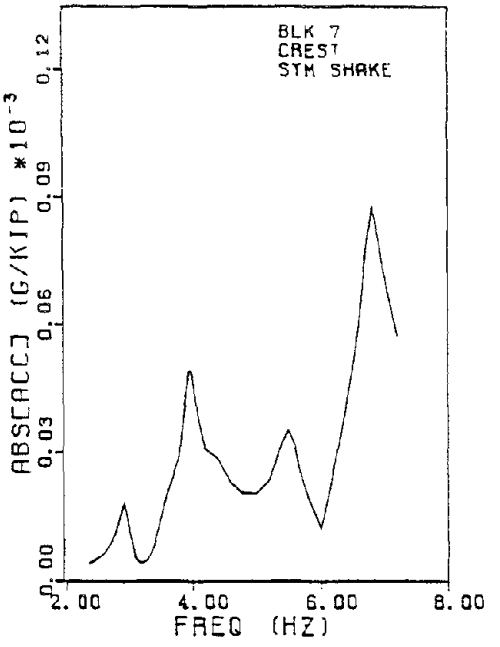
BLK 7
CREST
STM SHAKE
ABSACCJ (G/KIP) *10-3
0.00
0.03
0.06
0.09
0.12
2.00
4.00
6.00
8.00
FREQ (HZ)

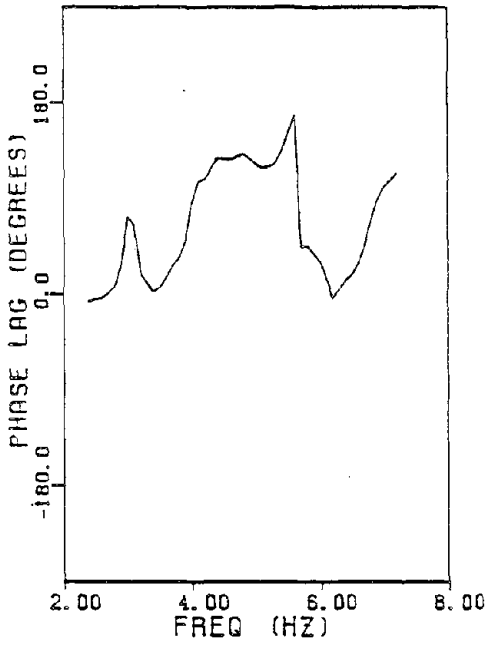
PHASE LAG (DEGREES)
180.0
0.0
-180.0
2.00
4.00
6.00
8.00
FREQ (HZ)

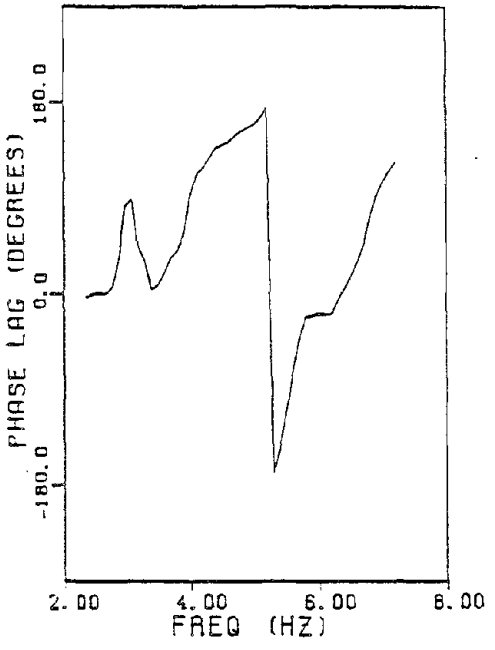
PHASE LAG (DEGREES)
180.0
0.0
-180.0
2.00
4.00
6.00
8.00
FREQ (HZ)

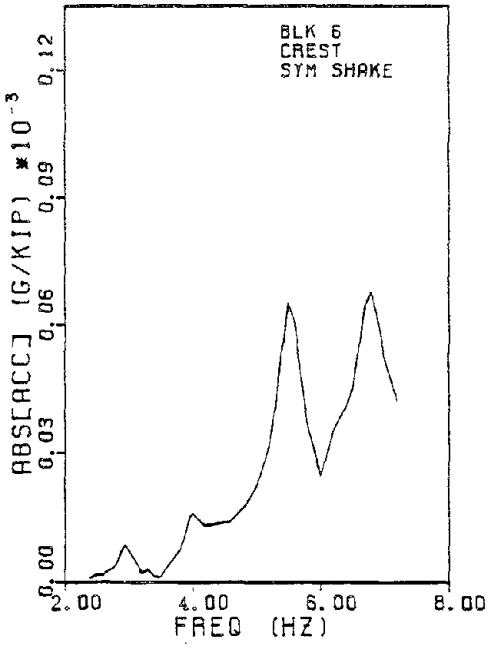
BLK 6
CREST
SYM SHAKE
ABS[ACC] (G/KIP) *10^-3
0.00
0.03
0.06
0.09
0.12
2.00
4.00
6.00
8.00
FREQ (HZ)

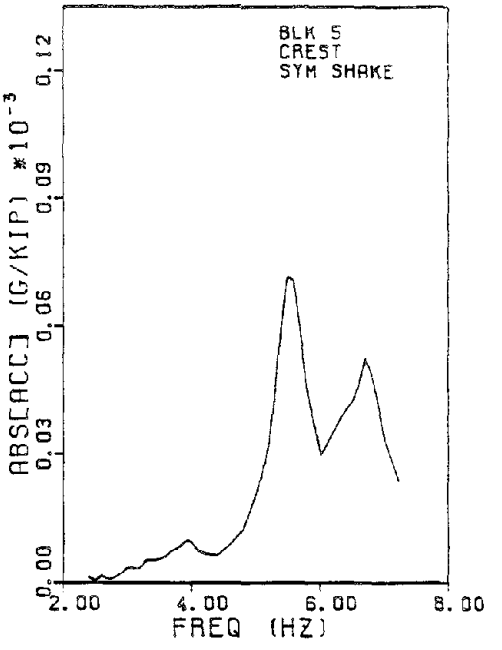
BLK 5
CREST
SYM SHAKE
ABS[ACC] (G/KIP) *10^-3
0.00
0.03
0.06
0.09
0.12
2.00
4.00
6.00
8.00
FREQ (HZ)

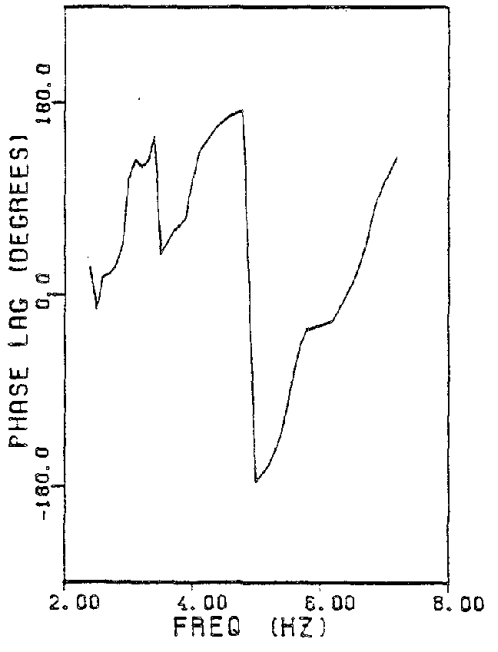
PHASE LAG (DEGREES)
-180.0
0.0
180.0
2.00
4.00
6.00
8.00
FREQ (HZ)

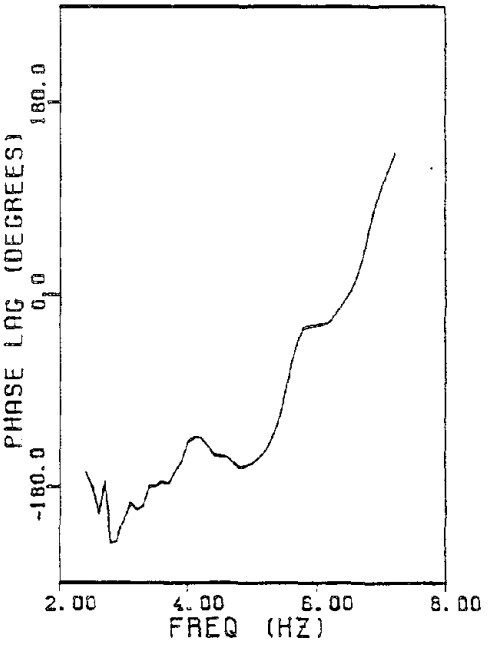
PHASE LAG (DEGREES)
-180.0
0.0
180.0
2.00
4.00
6.00
8.00
FREQ (HZ)

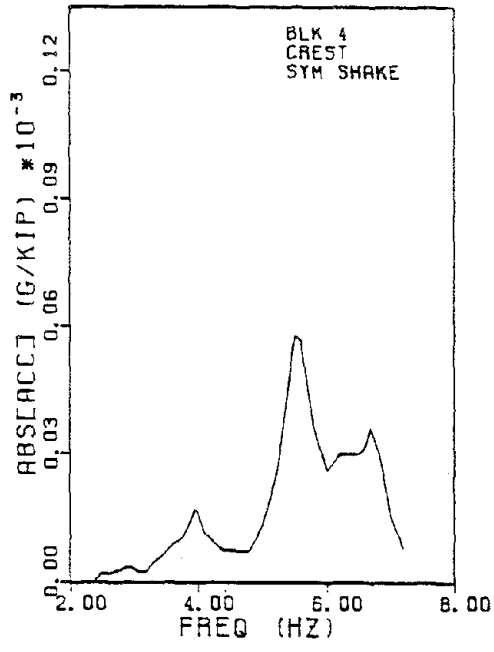
BLK 4
CREST
SYM SHAKE
ABSEACC] (G/KIP) *10-3
0.00
0.03
0.06
0.09
0.12
2.00
4.00
6.00
8.00
FREQ (HZ)

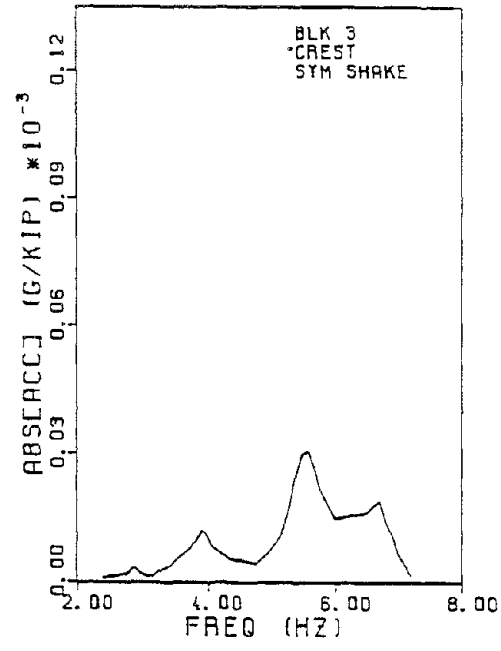
BLK 3
CREST
SYM SHAKE
ABSEACC] (G/KIP) *10-3
0.00
0.03
0.06
0.09
0.12
2.00
4.00
6.00
8.00
FREQ (HZ)

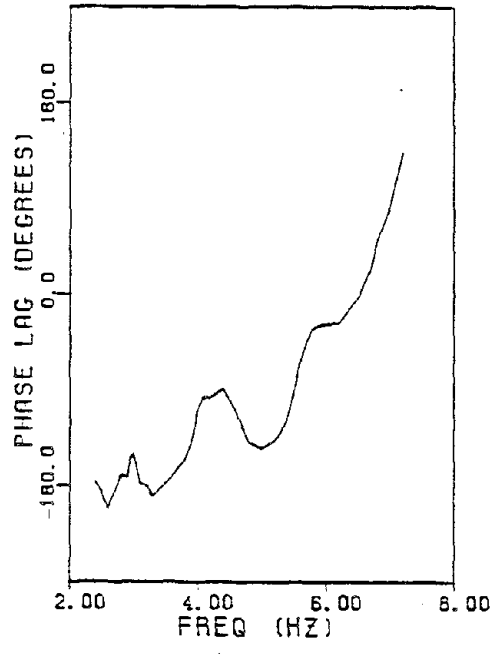
PHASE LAG (DEGREES)
180.0
0.0
-180.0
2.00
4.00
6.00
8.00
FREQ (HZ)

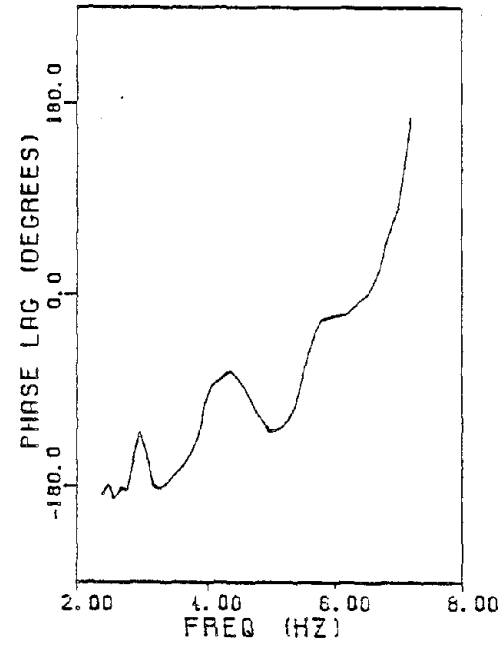
PHASE LAG (DEGREES)
180.0
0.0
-180.0
2.00
4.00
6.00
8.00
FREQ (HZ)

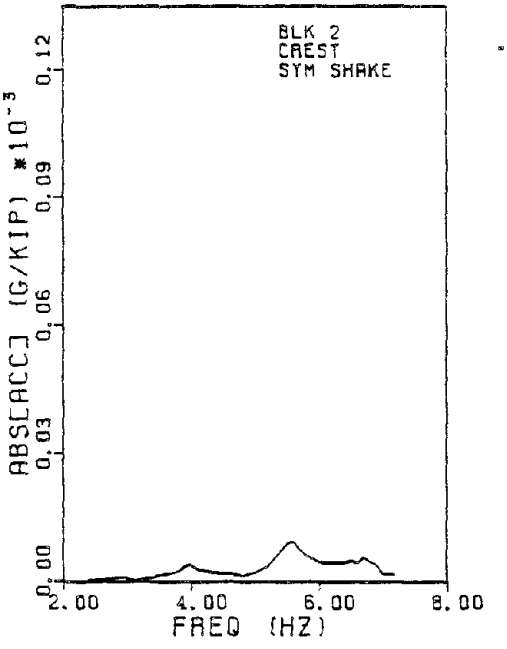
BLK 2
CREST
SYM SHAKE
ABSEACC] (G/KIP) *10^-3
0.00
0.03
0.06
0.09
0.12
2.00
4.00
6.00
8.00
FREQ (HZ)

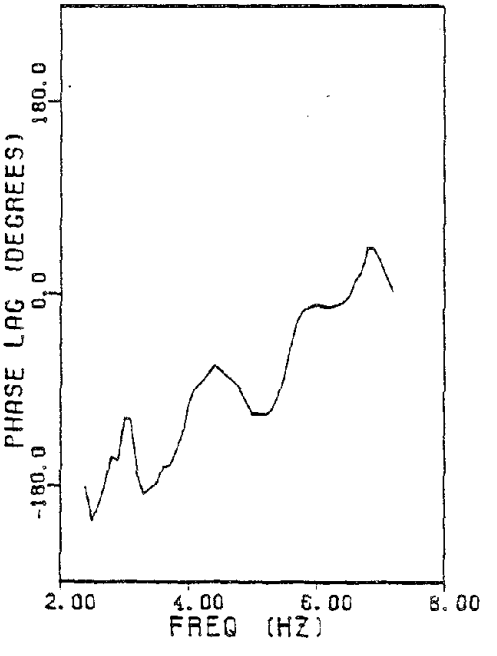
PHASE LAG (DEGREES)
180.0
0.0
-180.0
2.00
4.00
6.00
8.00
FREQ (HZ)

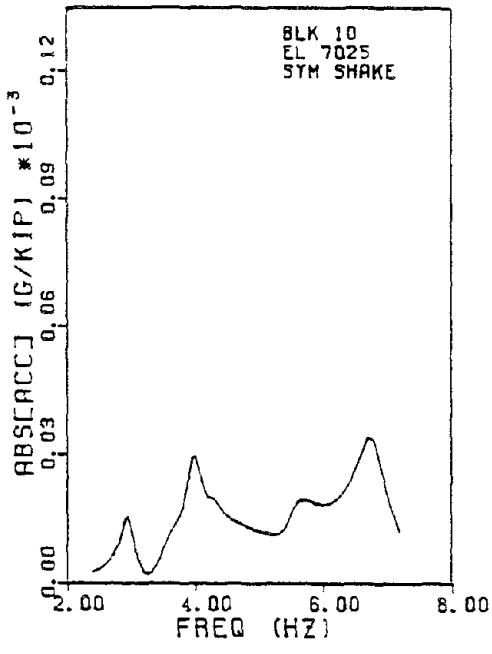
BLK 10
EL 7025
SYM SHAKE
ABS[ACC] (G/KIP) *10⁻³
0.00
0.03
0.06
0.09
0.12
2.00
4.00
6.00
8.00
FREQ (HZ)

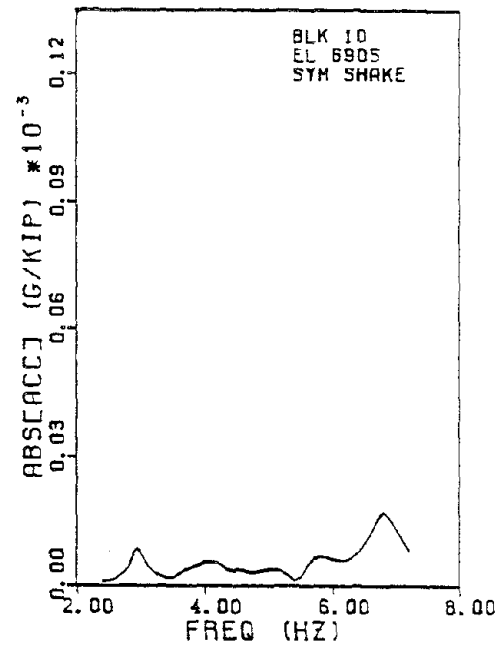
BLK 10
EL 6905
SYM SHAKE
ABS[ACC] (G/KIP) *10⁻³
0.00
0.03
0.06
0.09
0.12
2.00
4.00
6.00
8.00
FREQ (HZ)

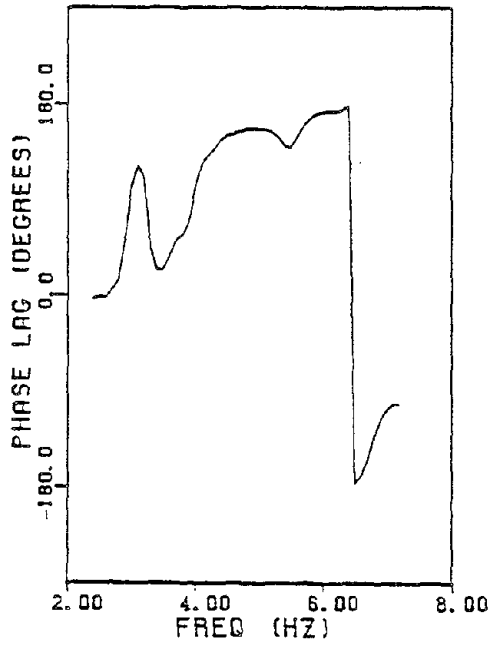
PHASE LAG (DEGREES)
180.0
0.0
-180.0
2.00
4.00
6.00
8.00
FREQ (HZ)

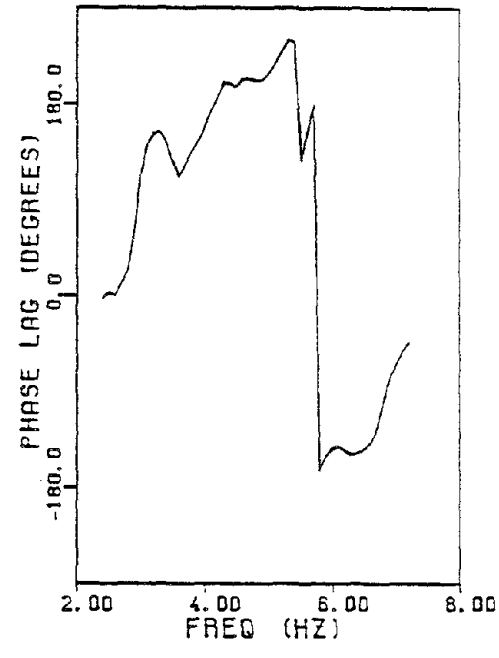
PHASE LAG (DEGREES)
180.0
0.0
-180.0
2.00
4.00
6.00
8.00
FREQ (HZ)

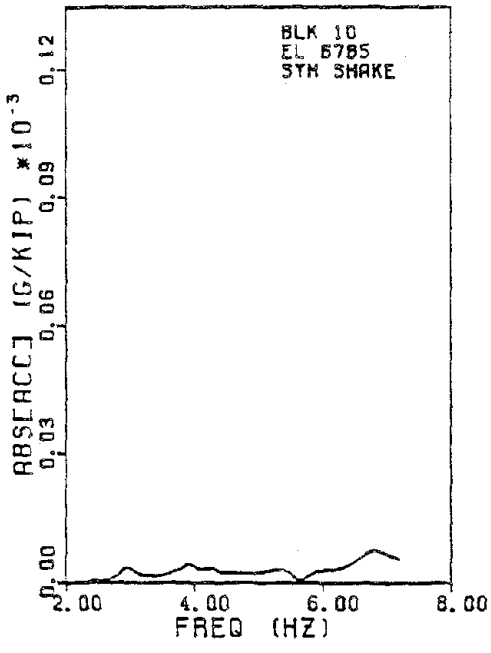
BLK 10
EL 6785
STM SHAKE
ABS[ACC] (G/KIP) *10^-3
0.00
0.03
0.06
0.09
0.12
2.00
4.00
6.00
8.00
FREQ (HZ)

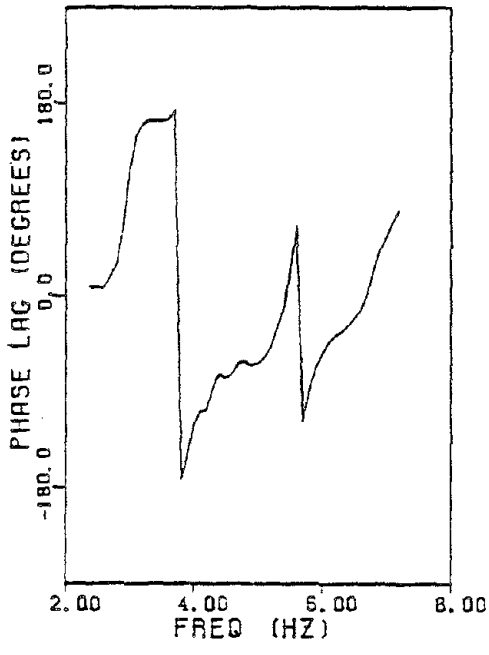
PHASE LAG (DEGREES)
180.0
0.0
-180.0
2.00
4.00
6.00
8.00
FREQ (HZ)

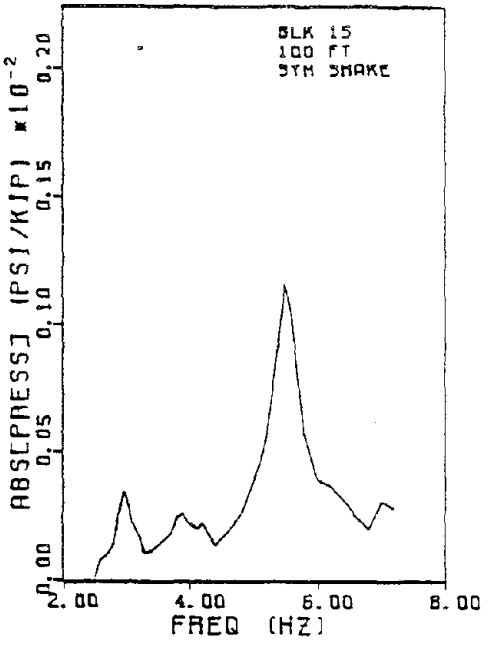
BLK 15
100 FT
SYM SHAKE
ABSCPRESS] (PSI/KIP) *10-2
0.00
0.05
0.10
0.15
0.20
2.00
4.00
6.00
8.00
FREQ (HZ)

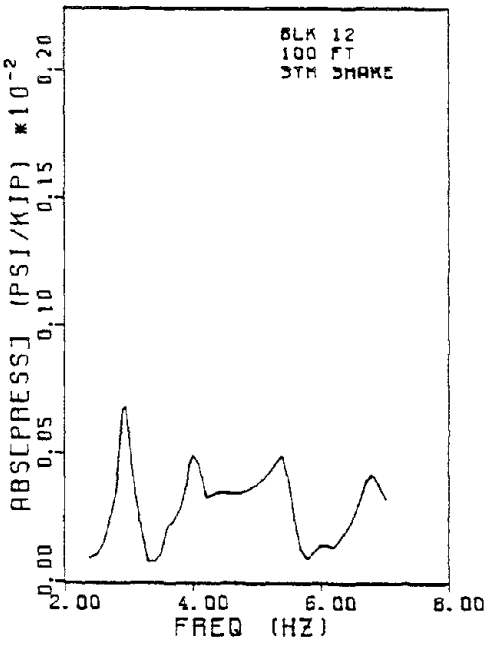
BLK 12
100 FT
SYM SHAKE
ABSCPRESS] (PSI/KIP) *10-2
0.00
0.05
0.10
0.15
0.20
2.00
4.00
6.00
8.00
FREQ (HZ)

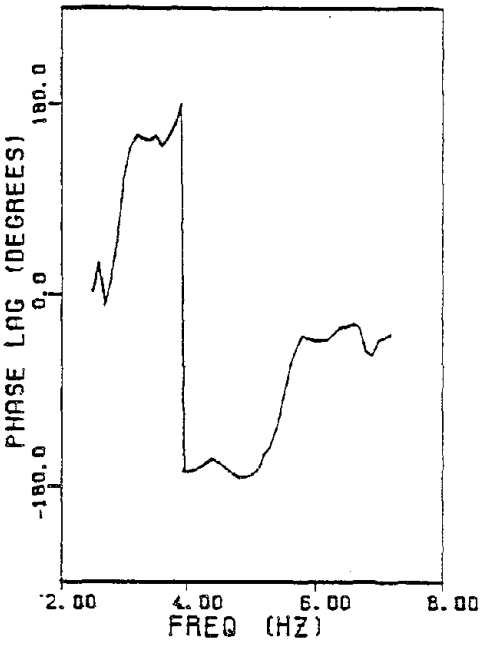
PHASE LAG (DEGREES)
180.0
0.0
-180.0
2.00
4.00
6.00
8.00
FREQ (HZ)

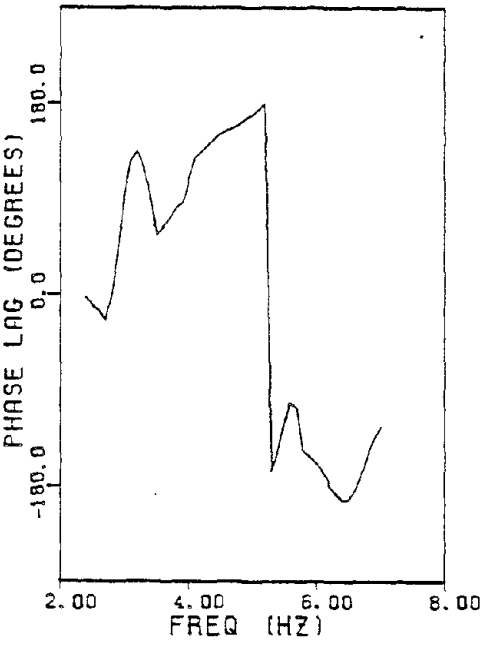
PHASE LAG (DEGREES)
180.0
0.0
-180.0
2.00
4.00
6.00
8.00
FREQ (HZ)

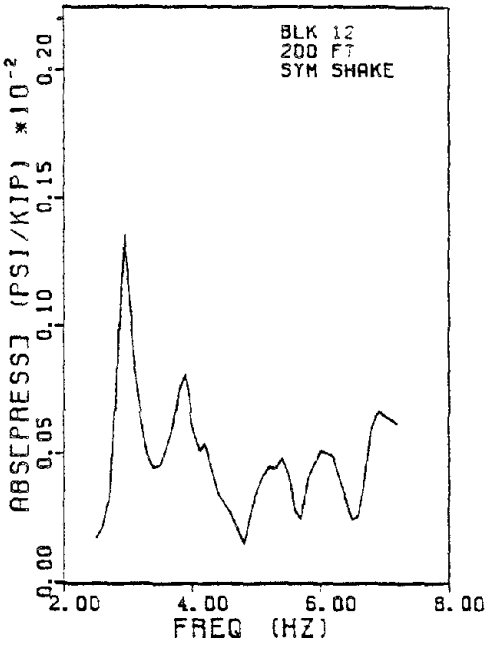
BLK 12
200 FT
SYM SHAKE
ABSCPRESS] (PSI/KIP) *10-2
0.00
0.05
0.10
0.15
0.20
2.00
4.00
6.00
8.00
FREQ (HZ)

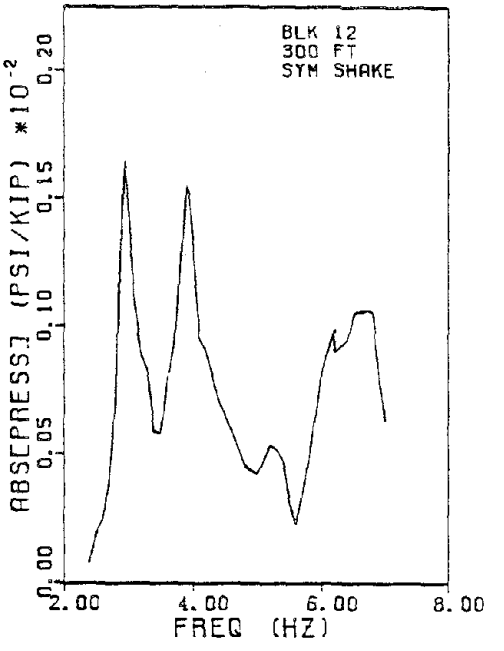
BLK 12
300 FT
SYM SHAKE
ABSCPRESS] (PSI/KIP) *10-2
0.00
0.05
0.10
0.15
0.20
2.00
4.00
6.00
8.00
FREQ (HZ)

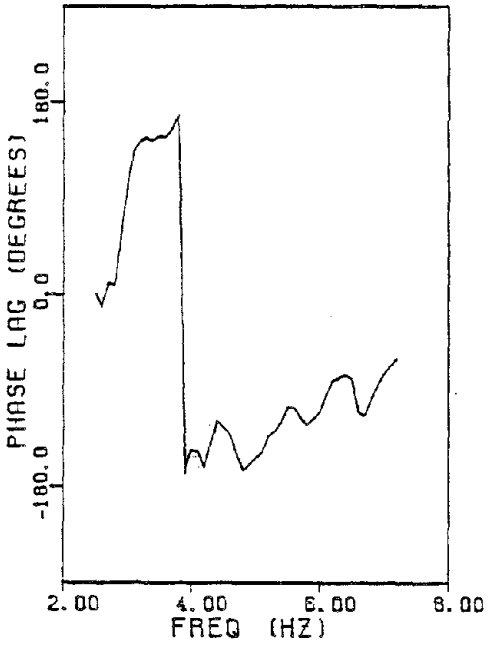
PHASE LAG (DEGREES)
180.0
0.0
-180.0
2.00
4.00
6.00
8.00
FREQ (HZ)

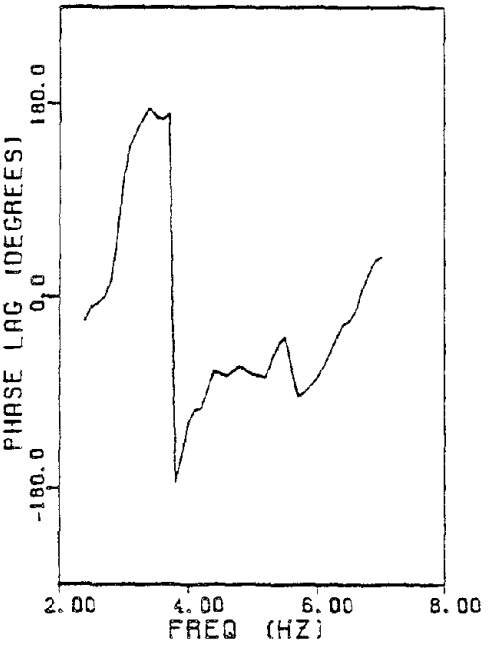
PHASE LAG (DEGREES)
180.0
0.0
-180.0
2.00
4.00
6.00
8.00
FREQ (HZ)

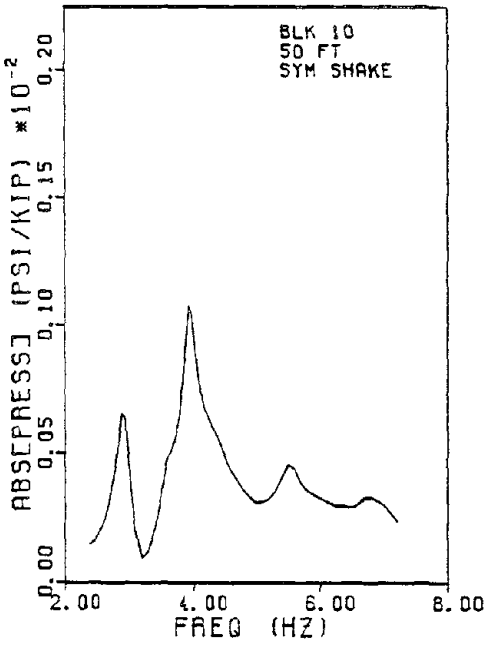
BLK 10
50 FT
SYM SHAKE
ABSPRESS] (PSI/KIP) *10-2
0.00
0.05
0.10
0.15
0.20
2.00
4.00
6.00
8.00
FREQ (HZ)

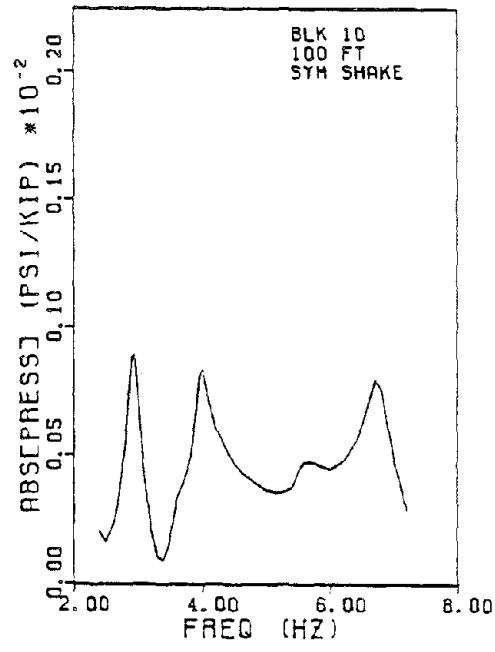
BLK 10
100 FT
SYM SHAKE
ABSPRESS] (PSI/KIP) *10-2
0.00
0.05
0.10
0.15
0.20
2.00
4.00
6.00
8.00
FREQ (HZ)

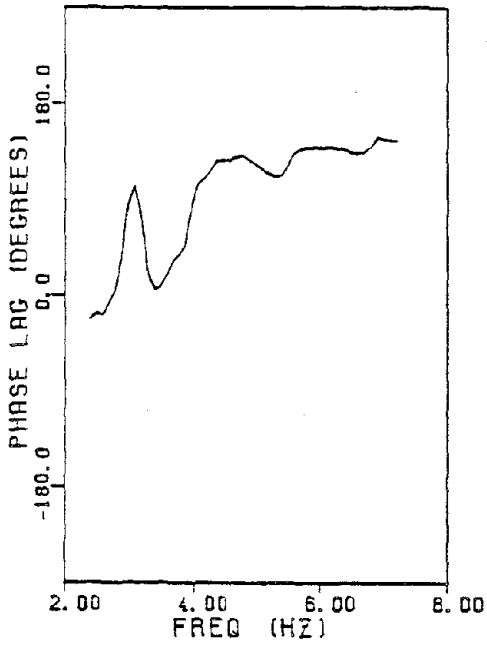
PHASE LAG (DEGREES)
-180.0
0.0
180.0
2.00
4.00
6.00
8.00
FREQ (HZ)

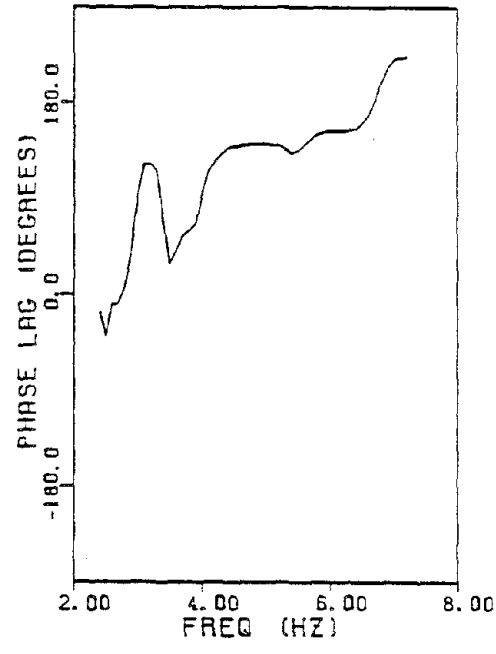
PHASE LAG (DEGREES)
-180.0
0.0
180.0
2.00
4.00
6.00
8.00
FREQ (HZ)

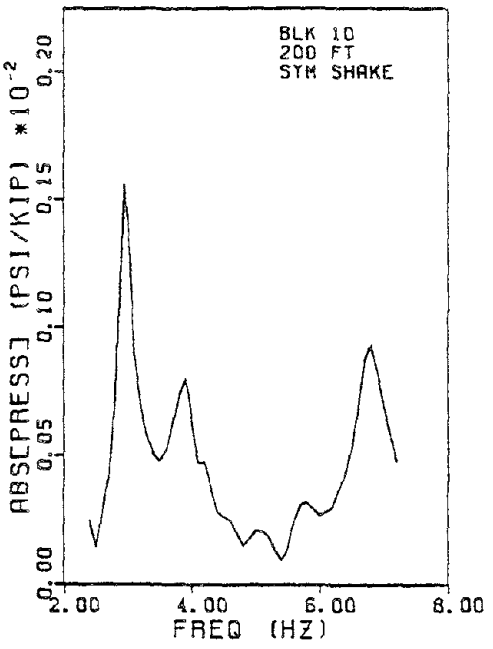
BLK 10
200 FT
SYM SHAKE
ABSCPRESS] (PSI/KIP) *10-2
0.00
0.05
0.10
0.15
0.20
2.00
4.00
6.00
8.00
FREQ (HZ)

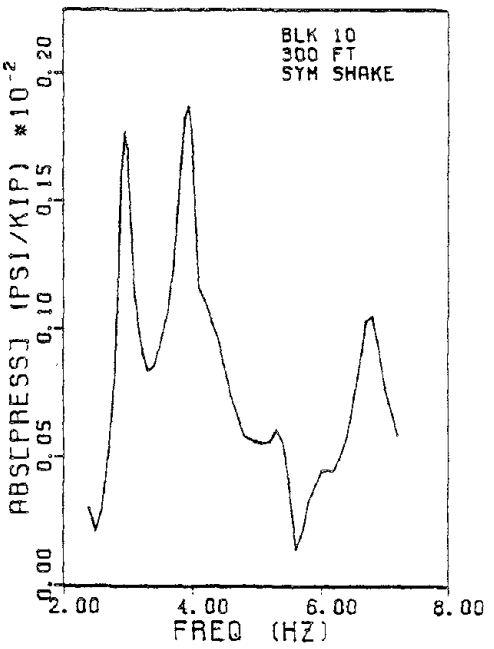
BLK 10
300 FT
SYM SHAKE
ABSCPRESS] (PSI/KIP) *10-2
0.00
0.05
0.10
0.15
0.20
2.00
4.00
6.00
8.00
FREQ (HZ)

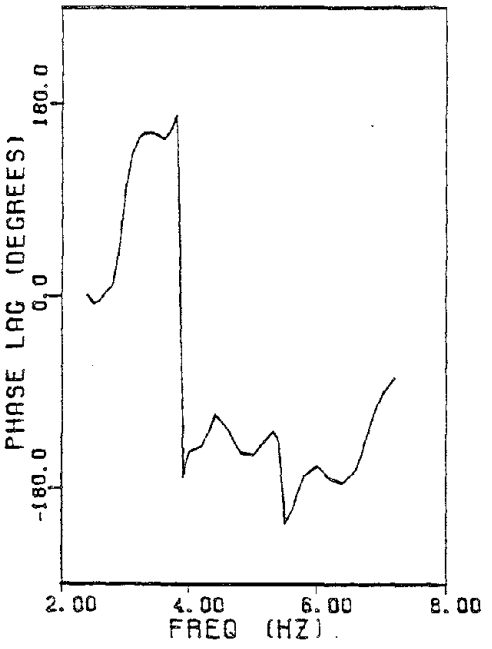
PHASE LAG (DEGREES)
180.0
0.0
-180.0
2.00
4.00
6.00
8.00
FREQ (HZ)

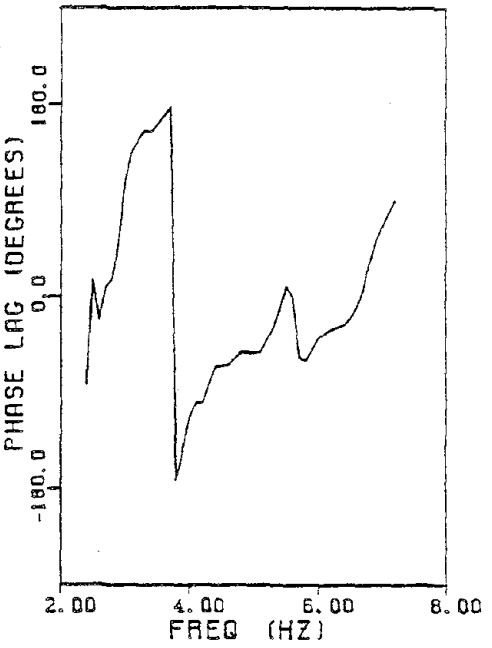
PHASE LAG (DEGREES)
180.0
0.0
-180.0
2.00
4.00
6.00
8.00
FREQ (HZ)

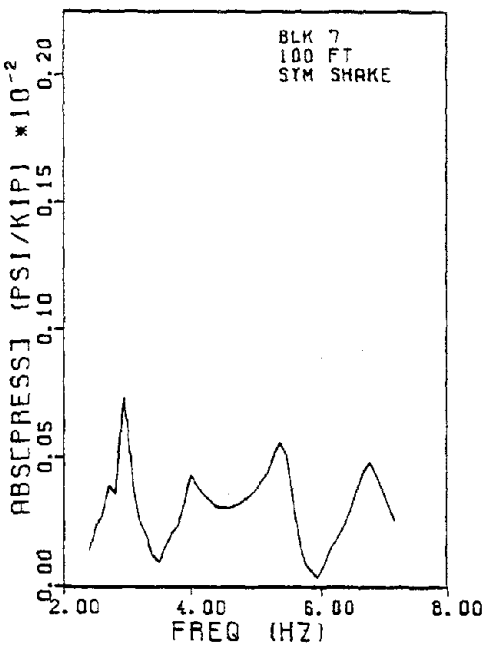
BLK 7
100 FT
STM SHAKE
ABSCPRESS] (PSI/KIP) *10-2
0.00
0.05
0.10
0.15
0.20
2.00
4.00
6.00
8.00
FREQ (HZ)

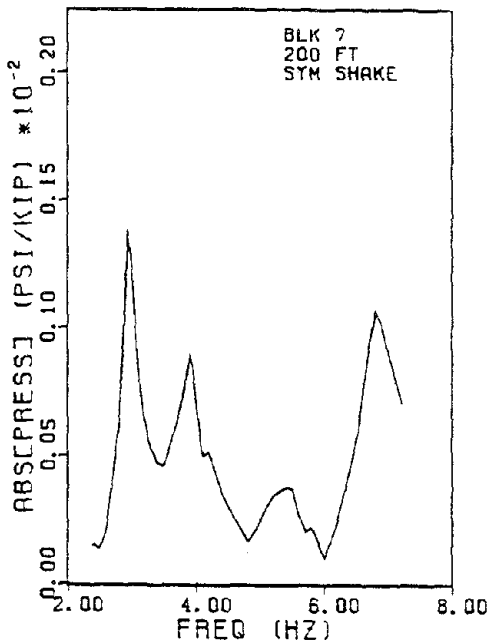
BLK 7
200 FT
STM SHAKE
ABSCPRESS] (PSI/KIP) *10-2
0.00
0.05
0.10
0.15
0.20
2.00
4.00
6.00
8.00
FREQ (HZ)

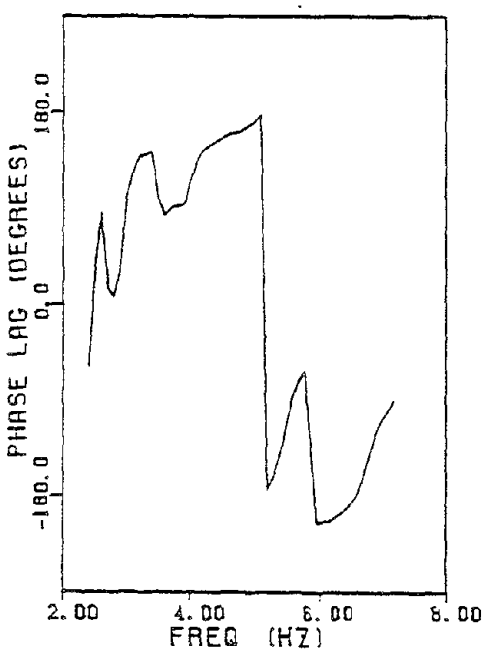
PHASE LAG (DEGREES)
180.0
0.0
-180.0
2.00
4.00
6.00
8.00
FREQ (HZ)

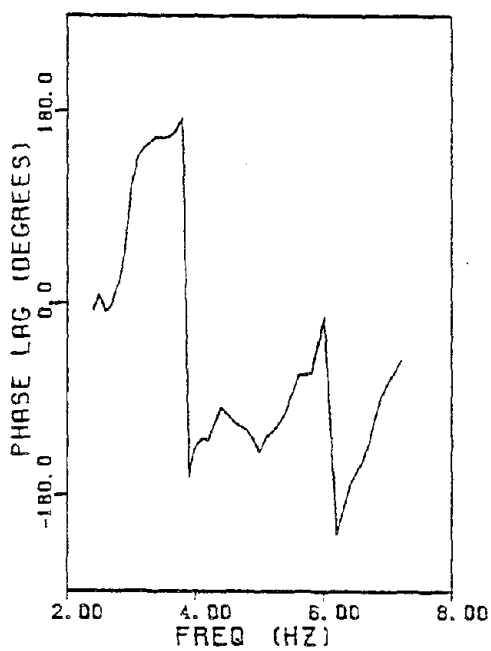
PHASE LAG (DEGREES)
180.0
0.0
-180.0
2.00
4.00
6.00
8.00
FREQ (HZ)

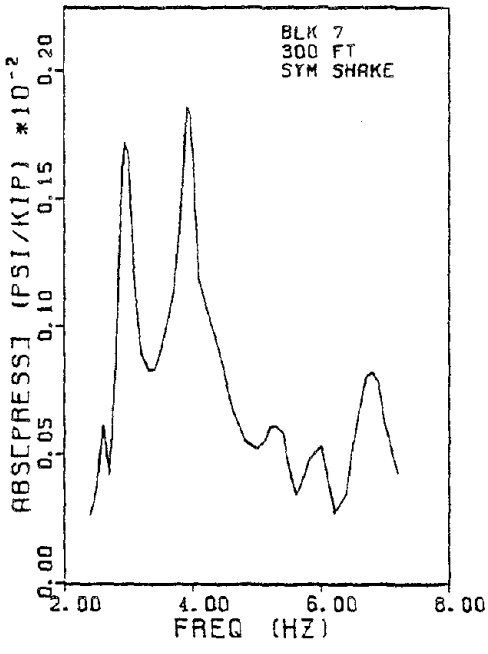
BLK 7
300 FT
SYM SHAKE
ABSCPRESS] (PSI/KIP) *10-2
0.00
0.05
0.10
0.15
0.20
2.00
4.00
6.00
8.00
FREQ (HZ)

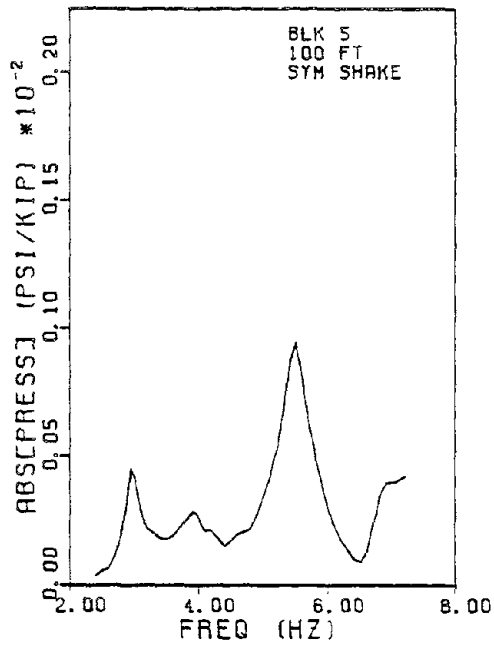
BLK 5
100 FT
SYM SHAKE
ABSCPRESS] (PSI/KIP) *10-2
0.00
0.05
0.10
0.15
0.20
2.00
4.00
6.00
8.00
FREQ (HZ)

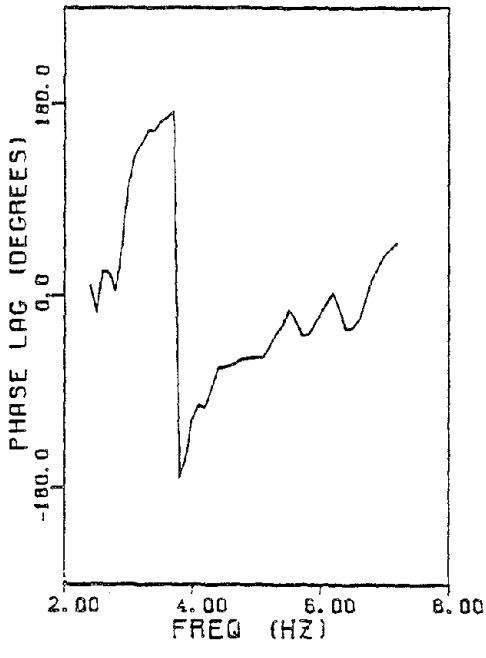
PHASE LAG (DEGREES)
180.0
0.0
-180.0
2.00
4.00
6.00
8.00
FREQ (HZ)

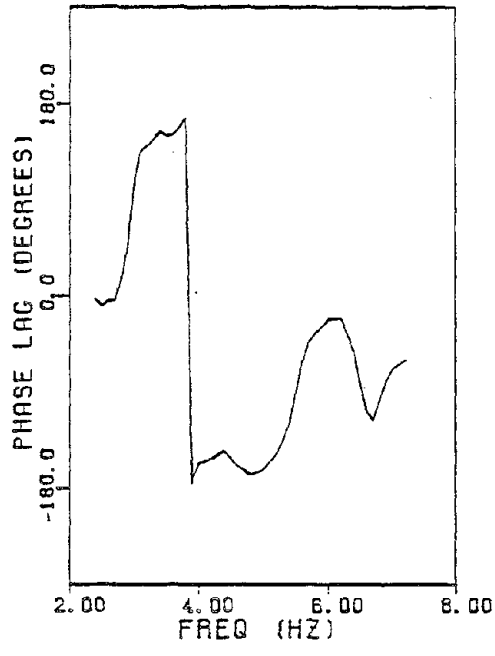
PHASE LAG (DEGREES)
180.0
0.0
-180.0
2.00
4.00
6.00
8.00
FREQ (HZ)

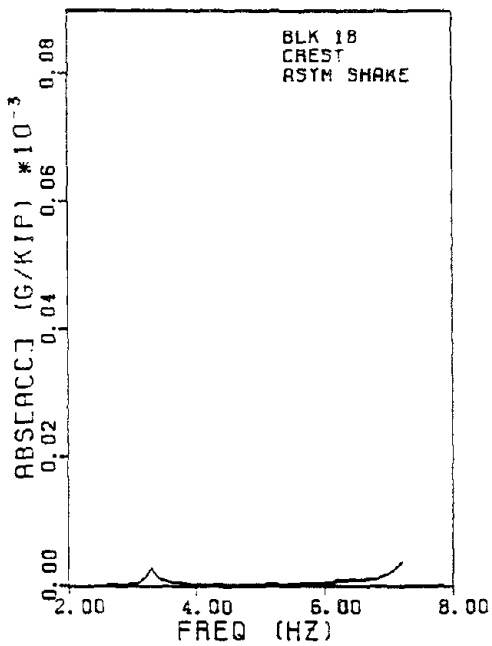
BLK 18
CREST
ASTM SHAKE
ABSACC] (G/KIP) *10⁻³
0.00
0.02
0.04
0.06
0.08
2.00
4.00
6.00
8.00
FREQ (HZ)

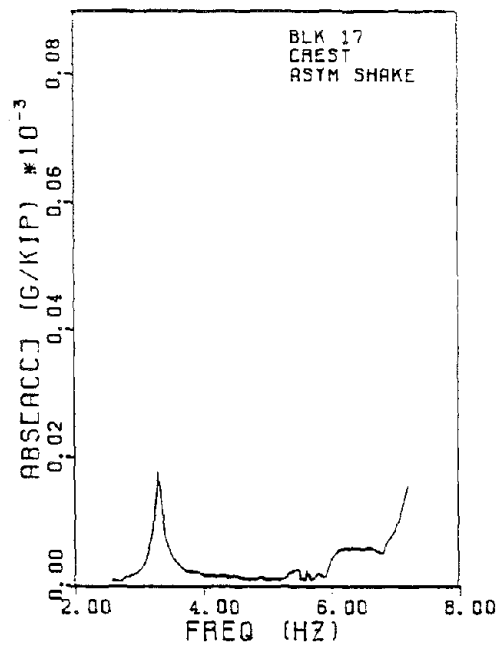
BLK 17
CREST
ASTM SHAKE
ABSACC] (G/KIP) *10⁻³
0.00
0.02
0.04
0.06
0.08
2.00
4.00
6.00
8.00
FREQ (HZ)

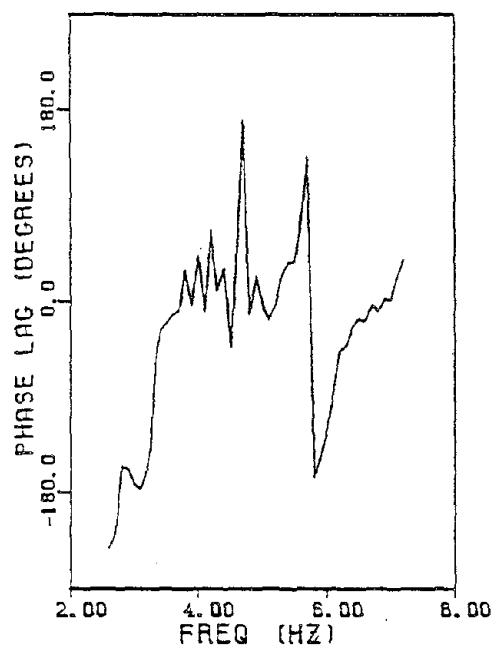
PHASE LAG (DEGREES)
180.0
0.0
-180.0
2.00
4.00
6.00
8.00
FREQ (HZ)

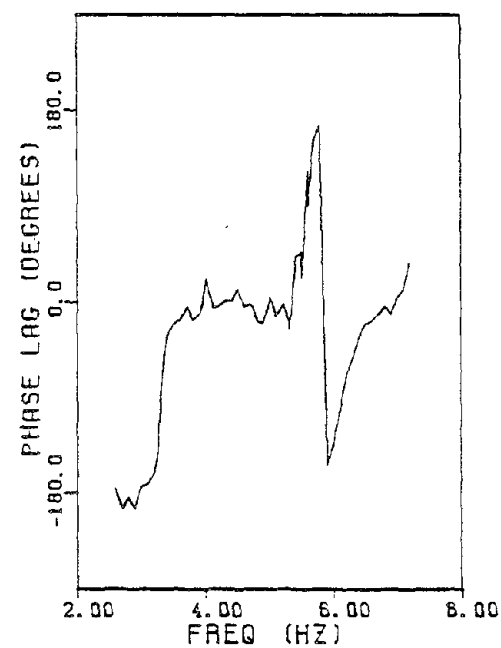
PHASE LAG (DEGREES)
180.0
0.0
-180.0
2.00
4.00
6.00
8.00
FREQ (HZ)

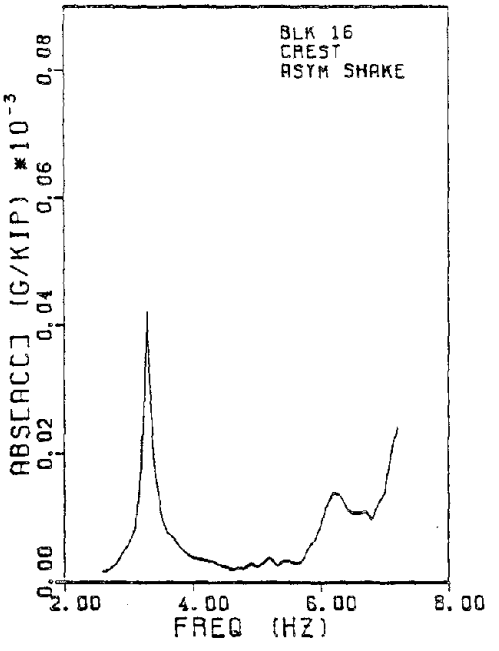
BLK 16
CREST
ASYM SHAKE
ABSEACC] (G/KIP) *10^-3
0.00
0.02
0.04
0.06
0.08
2.00
4.00
6.00
8.00
FREQ (HZ)

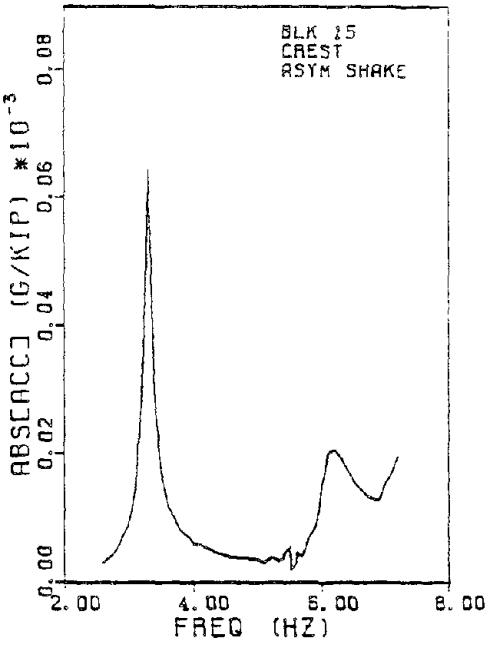
BLK 15
CREST
ASYM SHAKE
ABSEACC] (G/KIP) *10^-3
0.00
0.02
0.04
0.06
0.08
2.00
4.00
6.00
8.00
FREQ (HZ)

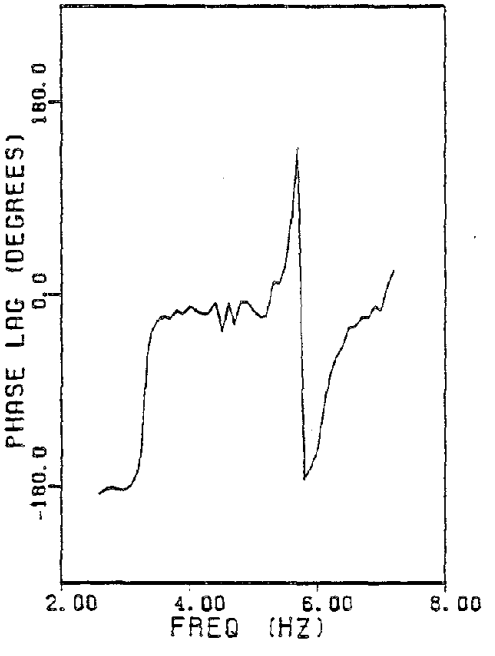
PHASE LAG (DEGREES)
180.0
0.0
-180.0
2.00
4.00
6.00
8.00
FREQ (HZ)

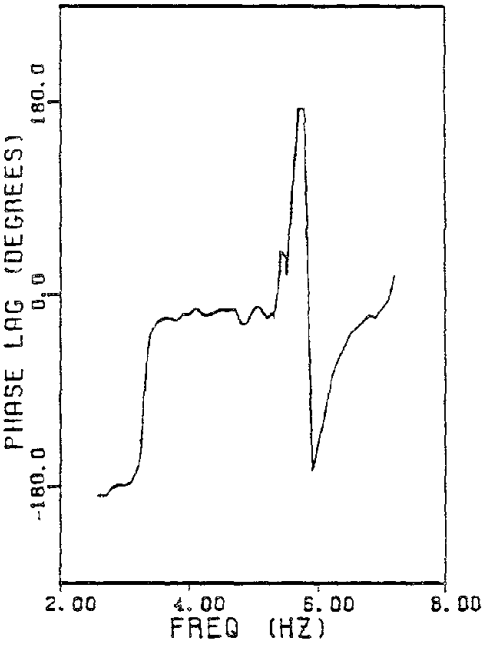
PHASE LAG (DEGREES)
180.0
0.0
-180.0
2.00
4.00
6.00
8.00
FREQ (HZ)

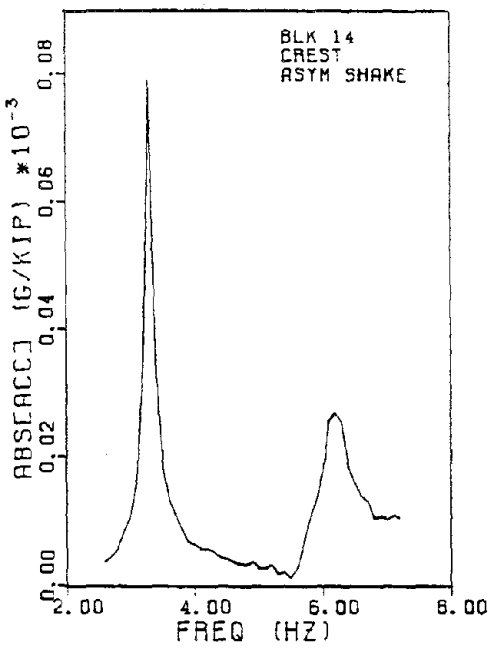
BLK 14
CREST
ASYM SHAKE
ABSEACC] (G/KIP) *10^-3
0.00
0.02
0.04
0.06
0.08
2.00
4.00
6.00
8.00
FREQ (HZ)

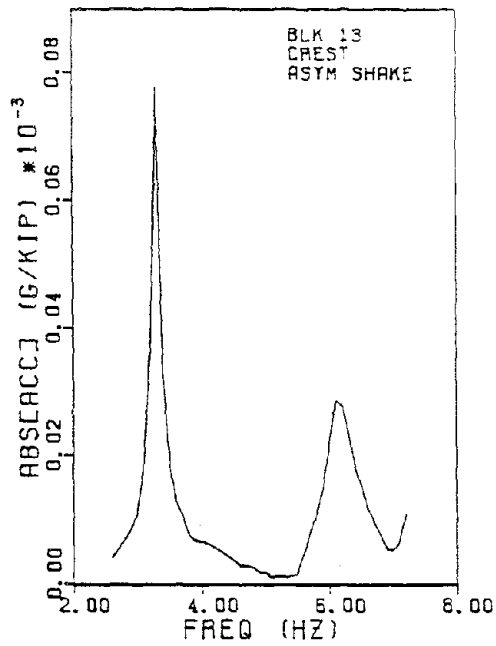
BLK 13
CREST
ASYM SHAKE
ABSEACC] (G/KIP) *10^-3
0.00
0.02
0.04
0.06
0.08
2.00
4.00
6.00
8.00
FREQ (HZ)

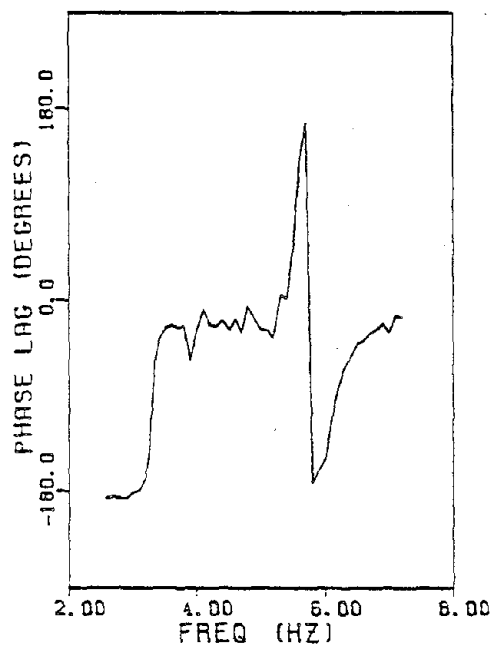
PHASE LAG (DEGREES)
180.0
0.0
-180.0
2.00
4.00
6.00
8.00
FREQ (HZ)

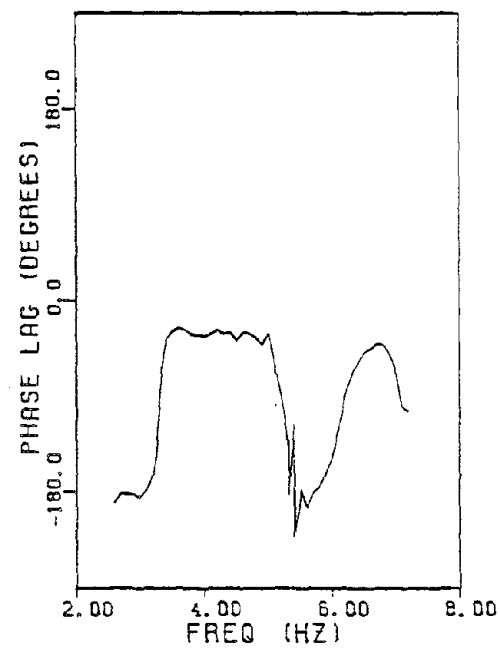
PHASE LAG (DEGREES)
180.0
0.0
-180.0
2.00
4.00
6.00
8.00
FREQ (HZ)

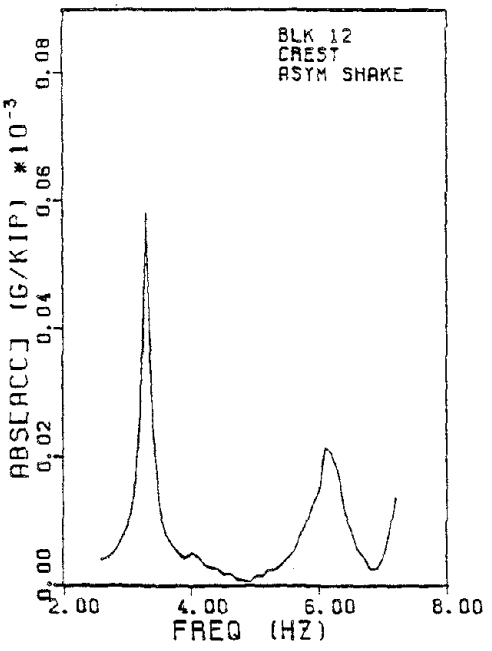
BLK 12
CREST
ASYM SHAKE
ABS[ACC] (G/KIP) *10-3
0.00
0.02
0.04
0.06
0.08
2.00
4.00
6.00
8.00
FREQ (HZ)

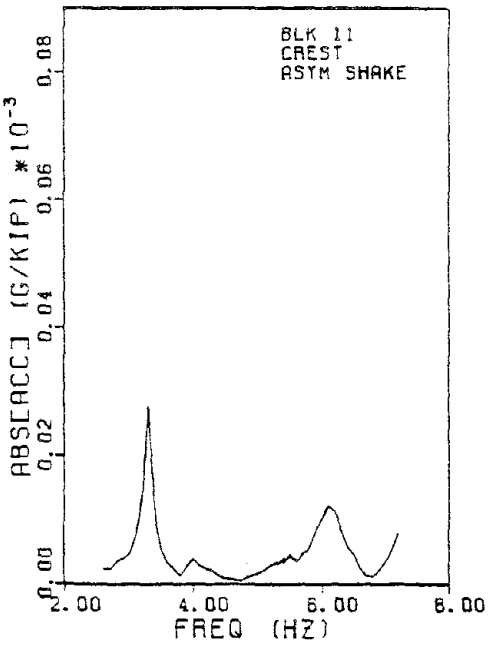
BLK 11
CREST
ASYM SHAKE
ABS[ACC] (G/KIP) *10-3
0.00
0.02
0.04
0.06
0.08
2.00
4.00
6.00
8.00
FREQ (HZ)

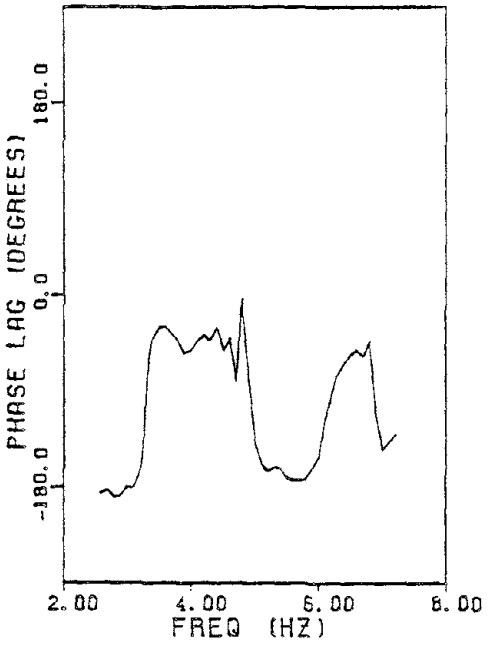
PHASE LAG (DEGREES)
180.0
0.0
-180.0
2.00
4.00
6.00
8.00
FREQ (HZ)

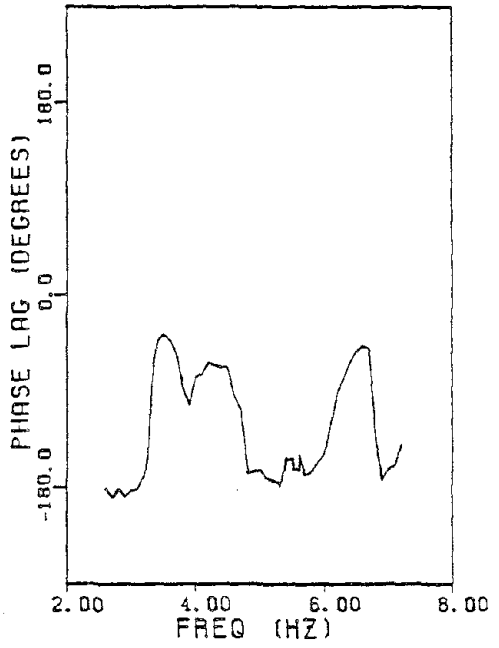
PHASE LAG (DEGREES)
180.0
0.0
-180.0
2.00
4.00
6.00
8.00
FREQ (HZ)

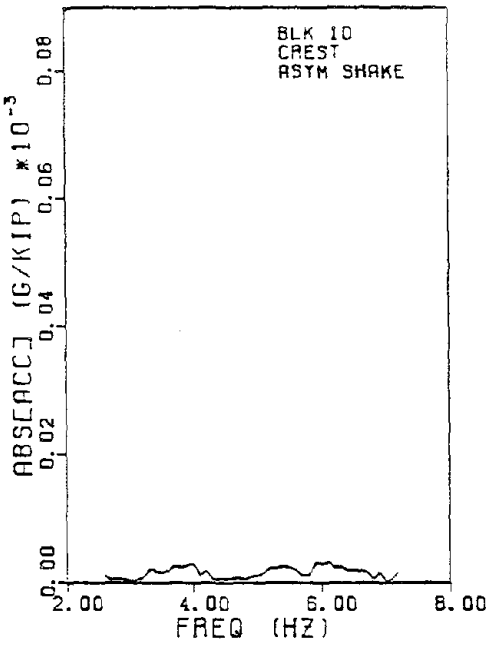
BLK 10
CREST
ASTM SHAKE
ABS[ACC] (G/KIP) *10^-3
0.00
0.02
0.04
0.06
0.08
2.00
4.00
6.00
8.00
FREQ (HZ)

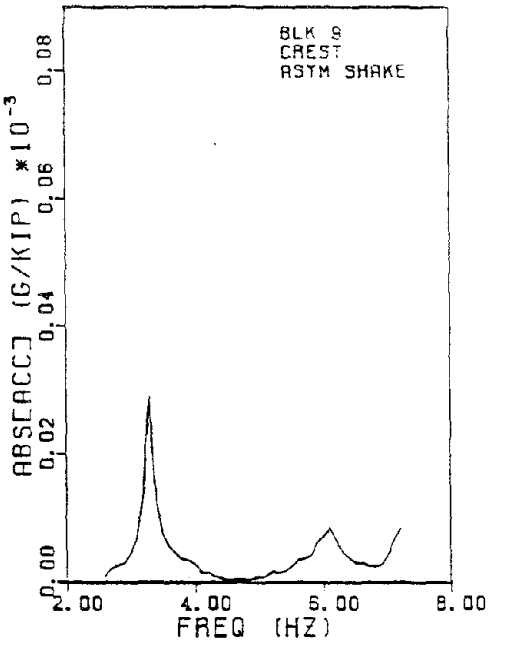
BLK 9
CREST
ASTM SHAKE
ABS[ACC] (G/KIP) *10^-3
0.00
0.02
0.04
0.06
0.08
2.00
4.00
6.00
8.00
FREQ (HZ)

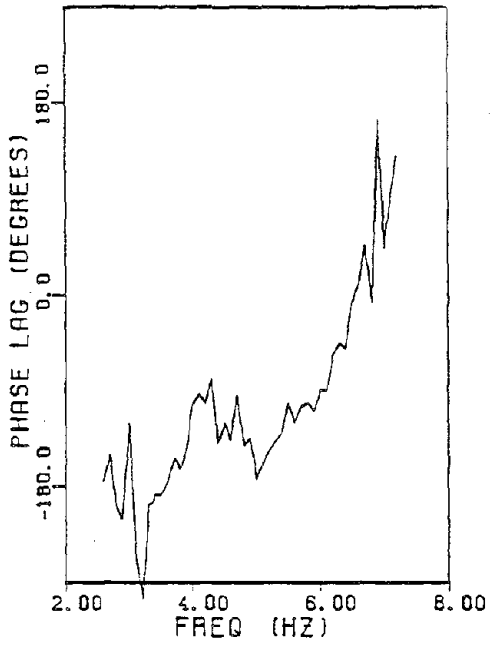
PHASE LAG (DEGREES)
-180.0
0.0
180.0
2.00
4.00
6.00
8.00
FREQ (HZ)

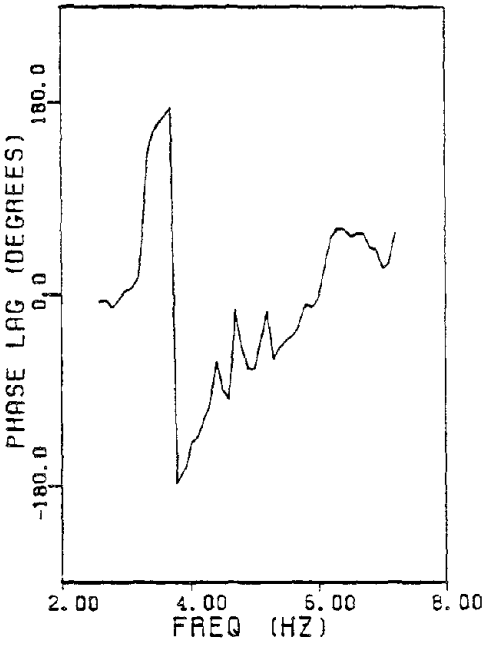
PHASE LAG (DEGREES)
-180.0
0.0
180.0
2.00
4.00
6.00
8.00
FREQ (HZ)

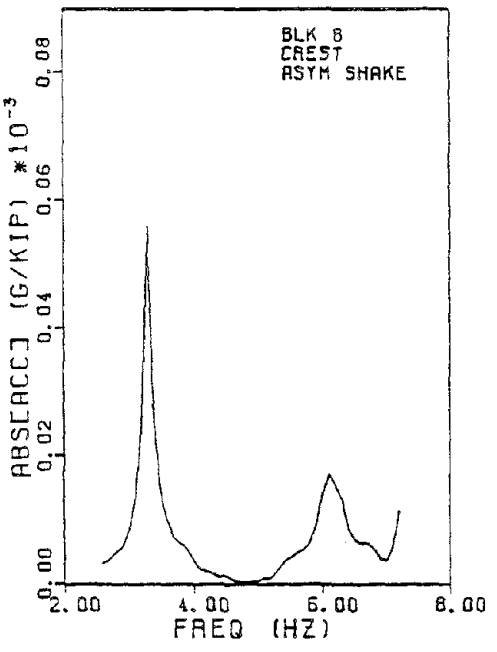
BLK 8
CREST
ASYM SHAKE
ABSIACC] (G/KIP) *10⁻³
0.00
0.02
0.04
0.06
0.08
2.00
4.00
6.00
8.00
FREQ (HZ)

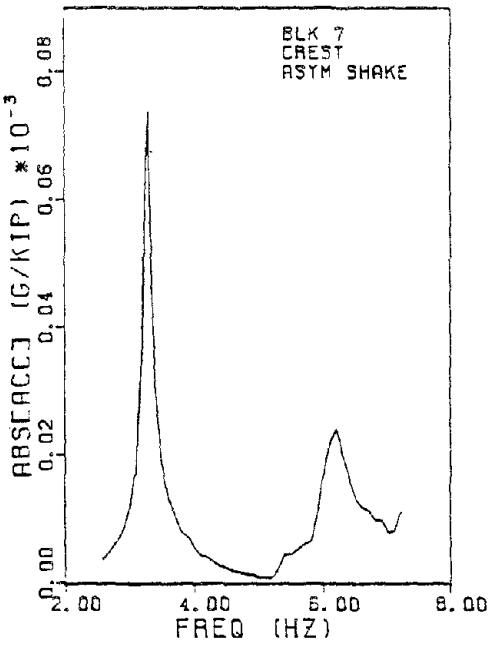
BLK 7
CREST
ASYM SHAKE
ABSIACC] (G/KIP) *10⁻³
0.00
0.02
0.04
0.06
0.08
2.00
4.00
6.00
8.00
FREQ (HZ)

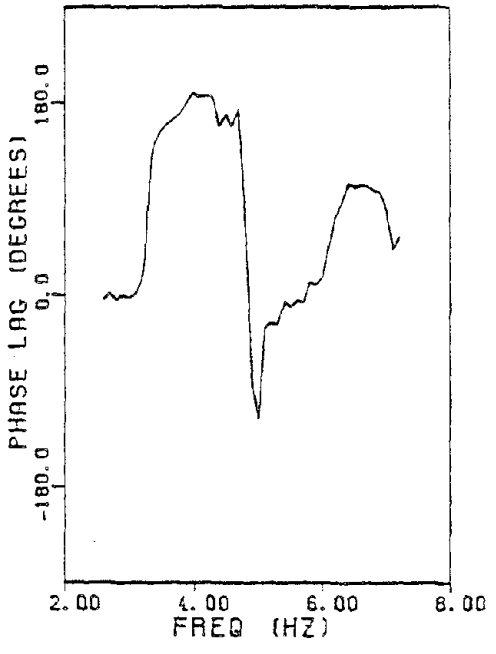
PHASE LAG (DEGREES)
180.0
0.0
-180.0
2.00
4.00
6.00
8.00
FREQ (HZ)

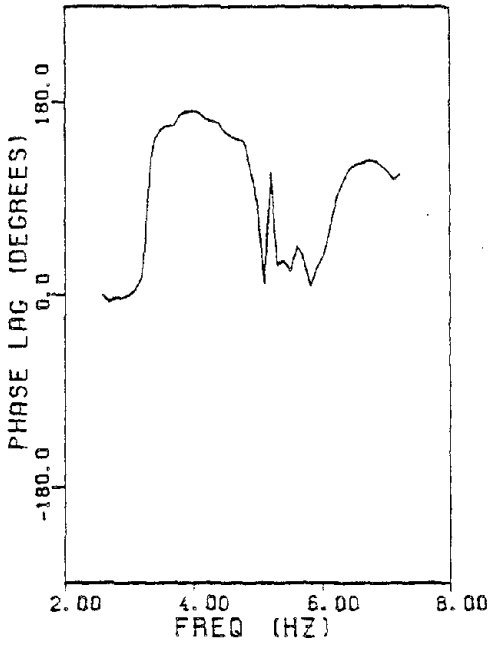
PHASE LAG (DEGREES)
180.0
0.0
-180.0
2.00
4.00
6.00
8.00
FREQ (HZ)

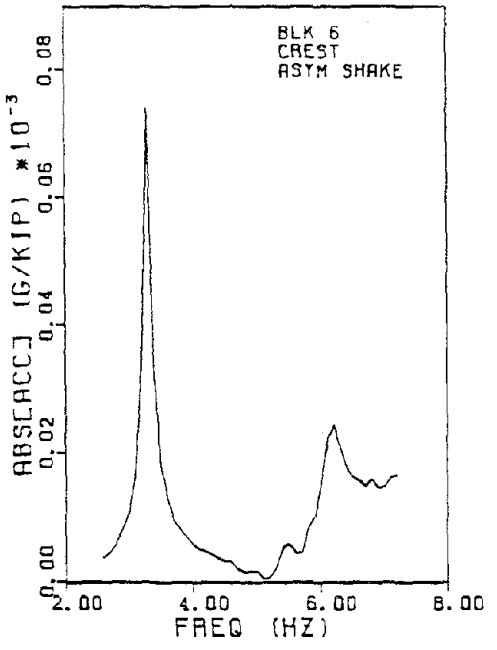
BLK 6
CREST
ASYM SHAKE
ABS[ACC] (G/KIP) *10⁻³
0.00
0.02
0.04
0.06
0.08
2.00
4.00
6.00
8.00
FREQ (HZ)

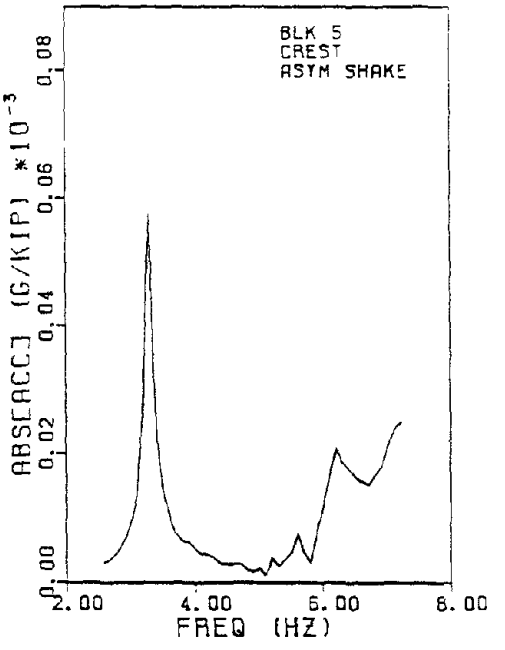
BLK 5
CREST
ASYM SHAKE
ABS[ACC] (G/KIP) *10⁻³
0.00
0.02
0.04
0.06
0.08
2.00
4.00
6.00
8.00
FREQ (HZ)

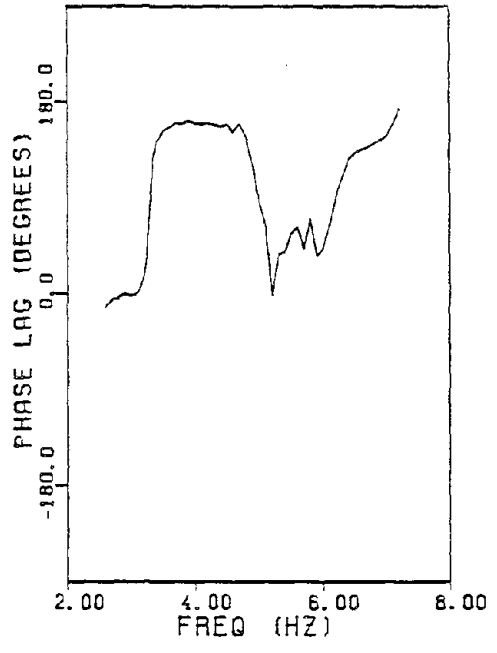
PHASE LAG (DEGREES)
180.0
0.0
-180.0
2.00
4.00
6.00
8.00
FREQ (HZ)

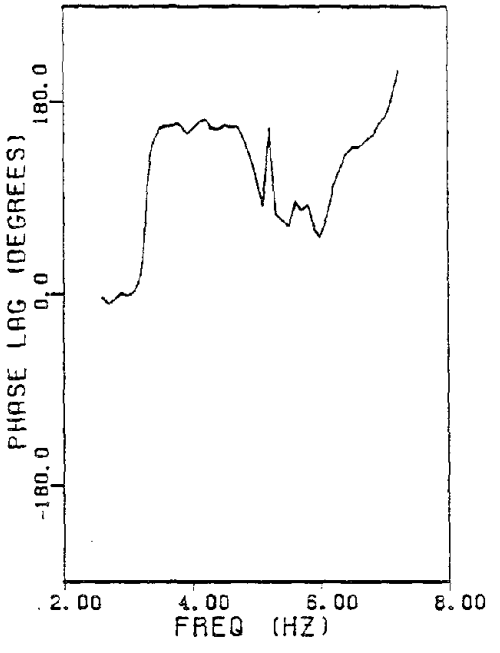
PHASE LAG (DEGREES)
180.0
0.0
-180.0
2.00
4.00
6.00
8.00
FREQ (HZ)

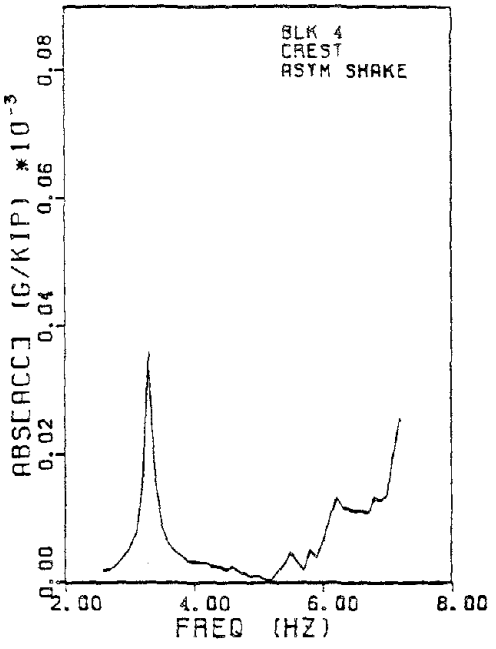
BLK 4
CREST
ASYM SHAKE
ABSEACC] (G/KIP) *10⁻³
0.00
0.02
0.04
0.06
0.08
2.00
4.00
6.00
8.00
FREQ (HZ)

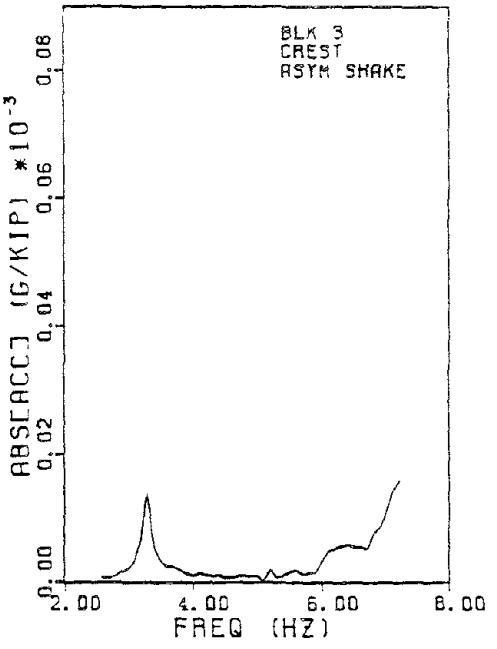
BLK 3
CREST
ASYM SHAKE
ABSEACC] (G/KIP) *10⁻³
0.00
0.02
0.04
0.06
0.08
2.00
4.00
6.00
8.00
FREQ (HZ)

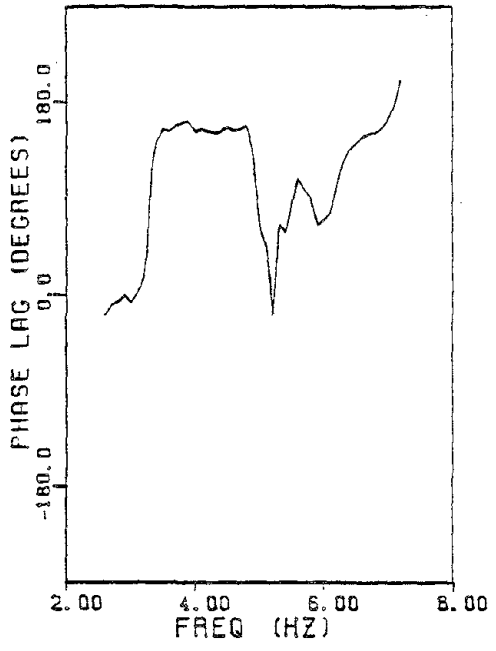
PHASE LAG (DEGREES)
-180.0
0.0
180.0
2.00
4.00
6.00
8.00
FREQ (HZ)

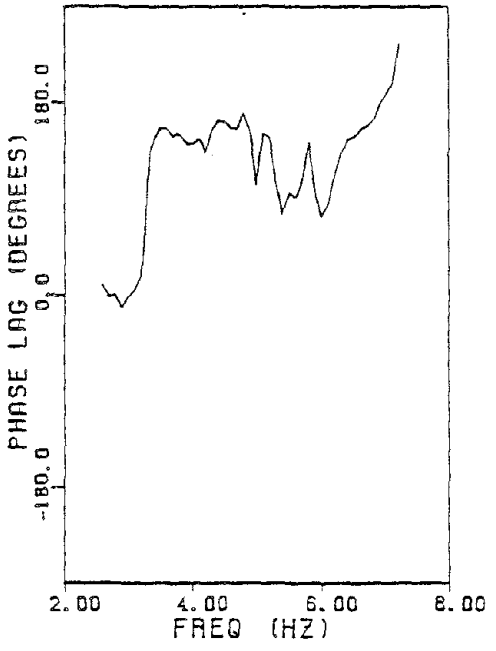
PHASE LAG (DEGREES)
-180.0
0.0
180.0
2.00
4.00
6.00
8.00
FREQ (HZ)

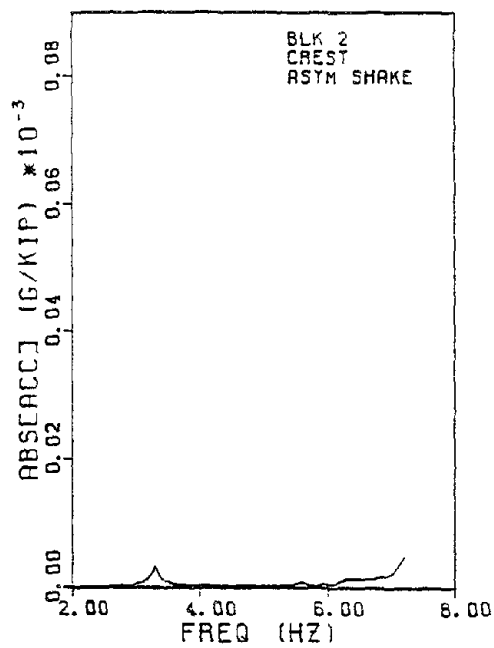
BLK 2
CREST
RSTM SHAKE
ABSACCJ (G/KIP) *10^-3
0.00
0.02
0.04
0.06
0.08
2.00
4.00
6.00
8.00
FREQ (HZ)

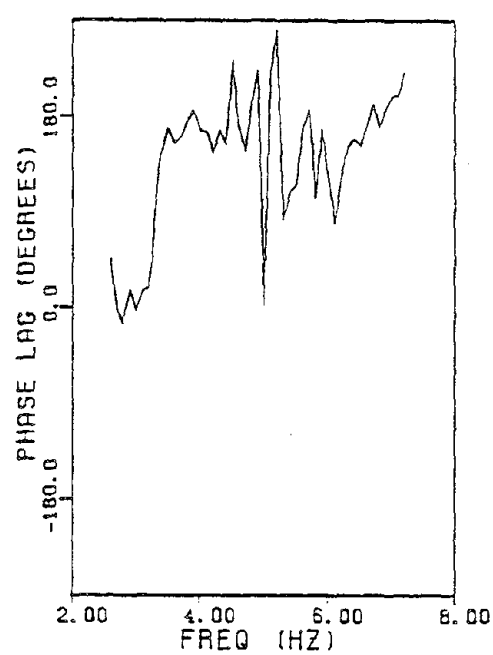
PHASE LAG (DEGREES)
180.0
0.0
-180.0
2.00
4.00
6.00
8.00
FREQ (HZ)

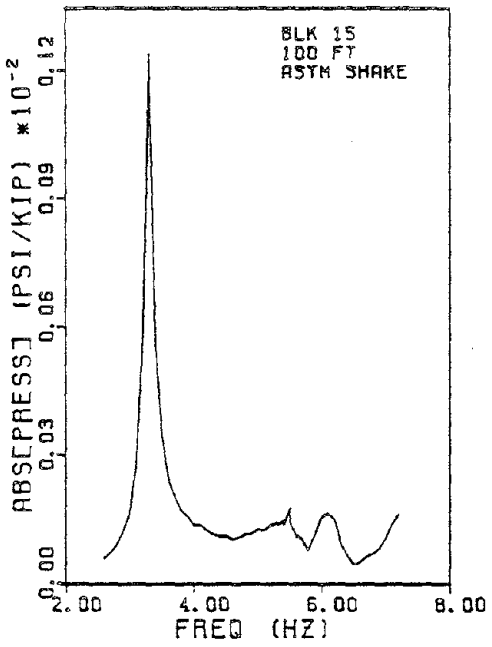
BLK 15
100 FT
ASYM SHAKE
ABSEPRESS] (PSI/KIP) *10^-2
0.00
0.03
0.06
0.09
0.12
2.00
4.00
6.00
8.00
FREQ (HZ)

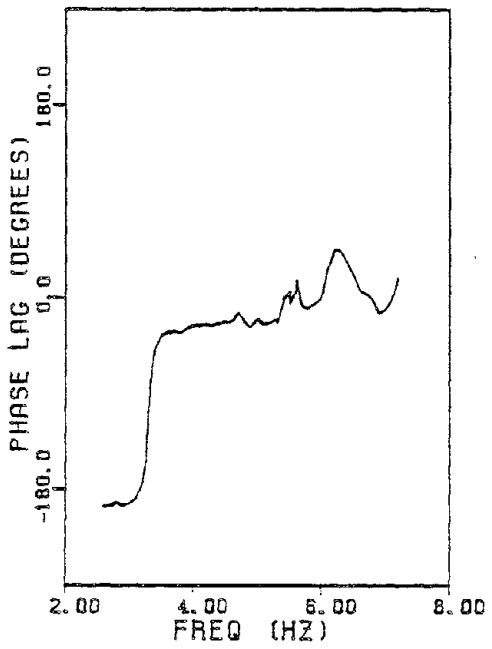
PHASE LAG (DEGREES)
180.0
0.0
-180.0
2.00
4.00
6.00
8.00
FREQ (HZ)

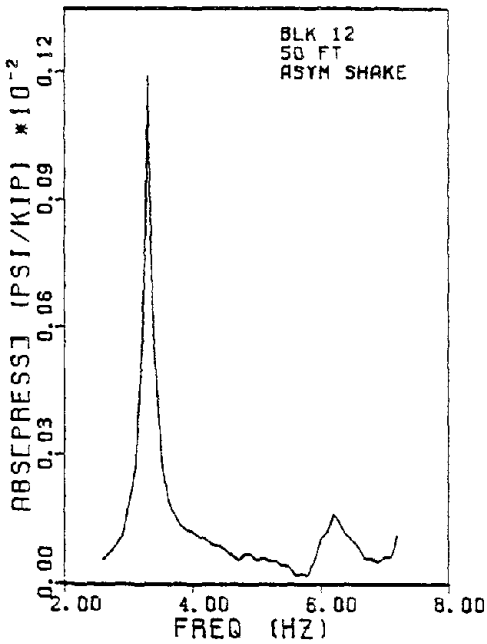
BLK 12
50 FT
ASYM SHAKE
ABSCPRESS] (PSI/KIP) *10⁻²
0.00
0.03
0.06
0.09
0.12
2.00
4.00
6.00
8.00
FREQ (HZ)

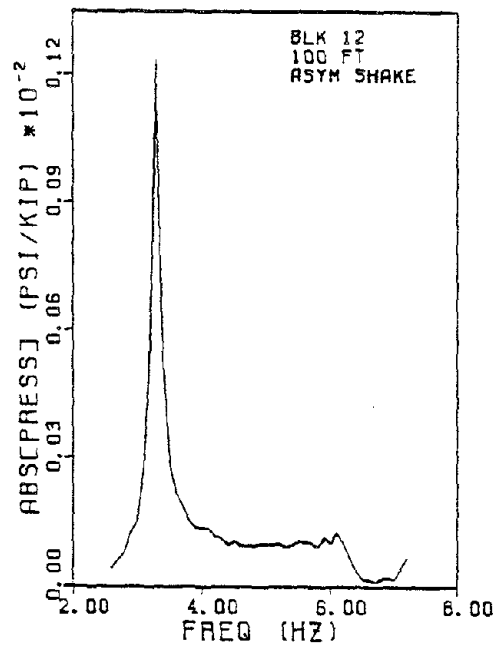
BLK 12
100 FT
ASYM SHAKE
ABSCPRESS] (PSI/KIP) *10⁻²
0.00
0.03
0.06
0.09
0.12
2.00
4.00
6.00
8.00
FREQ (HZ)

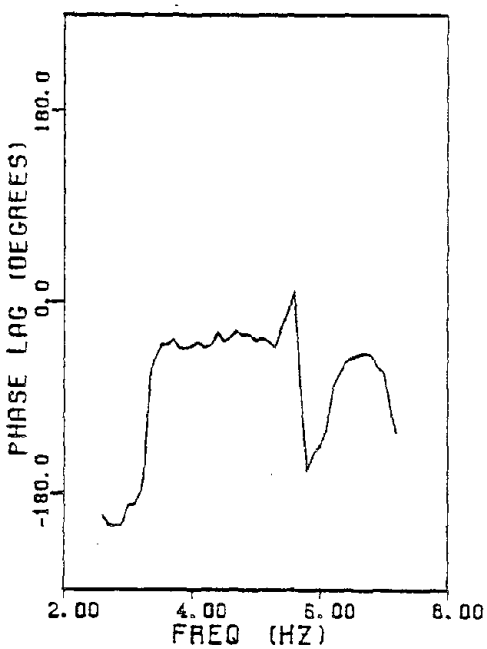
PHASE LAG (DEGREES)
180.0
0.0
-180.0
2.00
4.00
6.00
8.00
FREQ (HZ)

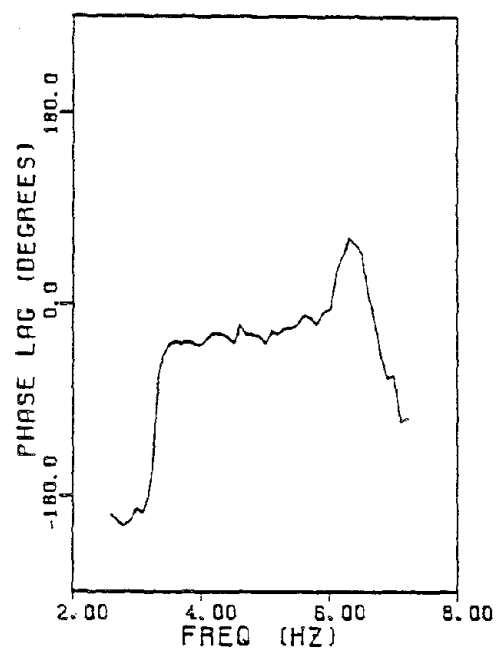
PHASE LAG (DEGREES)
180.0
0.0
-180.0
2.00
4.00
6.00
8.00
FREQ (HZ)

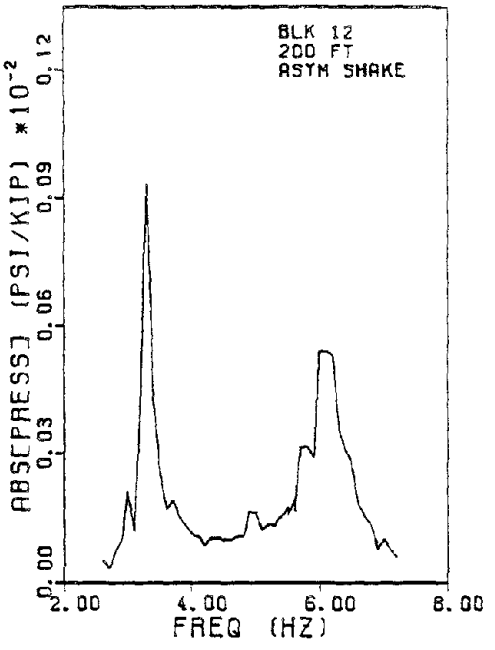
BLK 12
200 FT
ASYM SHAKE
ABS[PRESS] (PSI/KIP) *10^-2
0.00
0.03
0.06
0.09
0.12
2.00
4.00
6.00
8.00
FREQ (HZ)

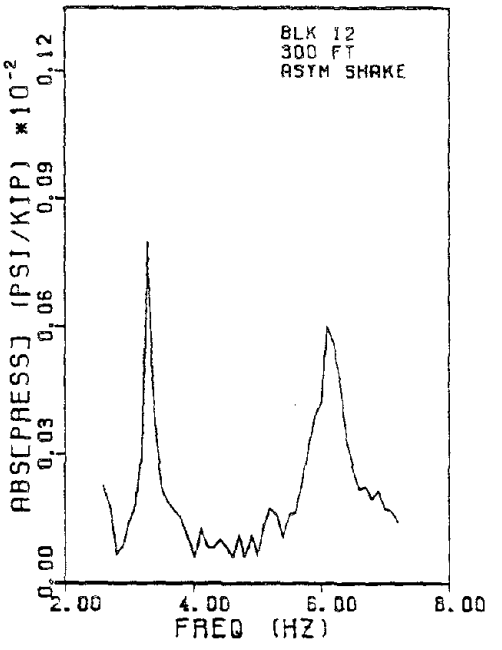
BLK 12
300 FT
ASYM SHAKE
ABS[PRESS] (PSI/KIP) *10^-2
0.00
0.03
0.06
0.09
0.12
2.00
4.00
6.00
8.00
FREQ (HZ)

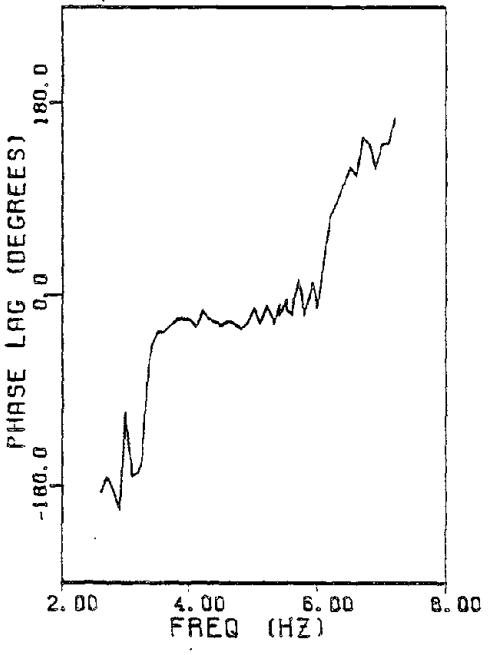
PHASE LAG (DEGREES)
-180.0
0.0
180.0
2.00
4.00
6.00
8.00
FREQ (HZ)

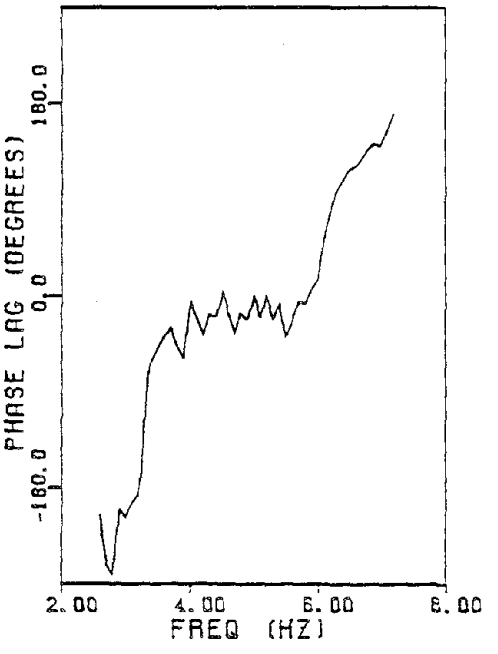
PHASE LAG (DEGREES)
-180.0
0.0
180.0
2.00
4.00
6.00
8.00
FREQ (HZ)

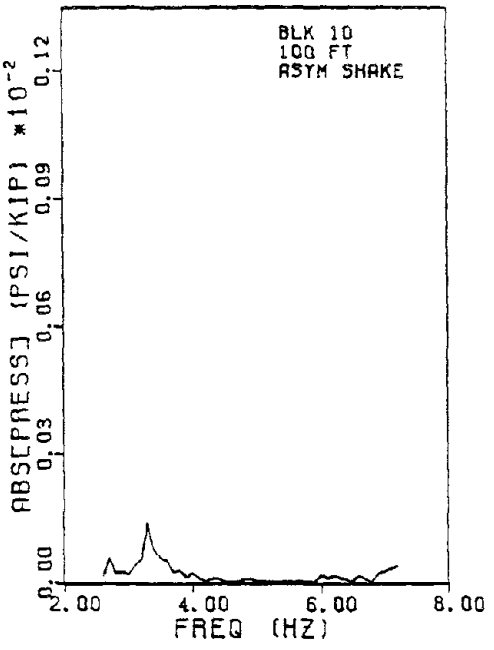
BLK 10
100 FT
ASYM SHAKE
ABS[PRESS] (PSI/KIP) *10⁻²
0.00
0.03
0.06
0.09
0.12
2.00
4.00
6.00
8.00
FREQ (HZ)

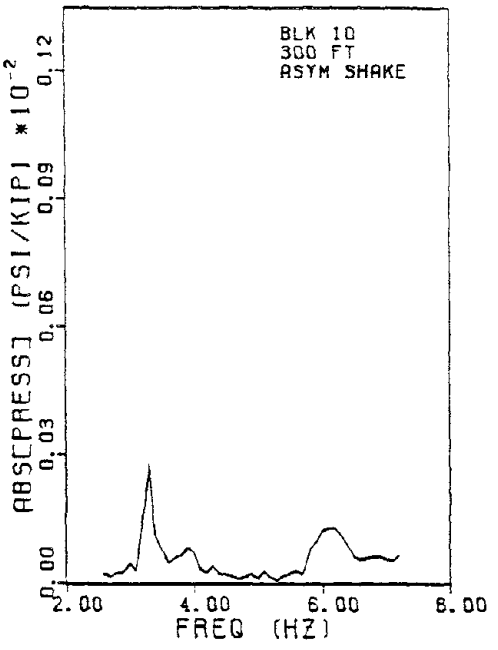
BLK 10
300 FT
ASYM SHAKE
ABS[PRESS] (PSI/KIP) *10⁻²
0.00
0.03
0.06
0.09
0.12
2.00
4.00
6.00
8.00
FREQ (HZ)

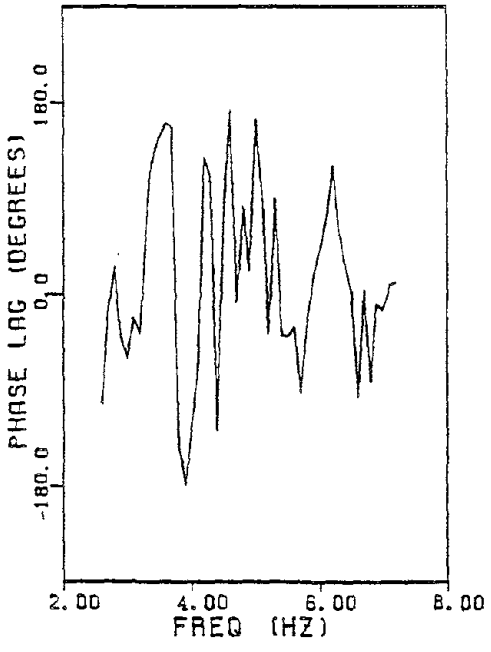
PHASE LAG (DEGREES)
180.0
0.0
-180.0
2.00
4.00
6.00
8.00
FREQ (HZ)

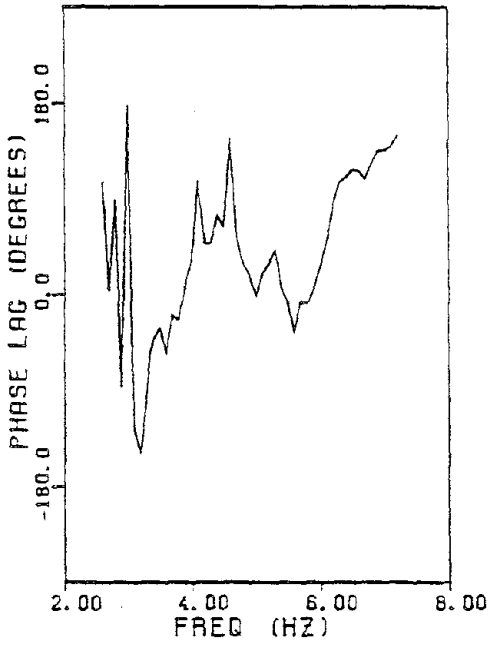
PHASE LAG (DEGREES)
180.0
0.0
-180.0
2.00
4.00
6.00
8.00
FREQ (HZ)

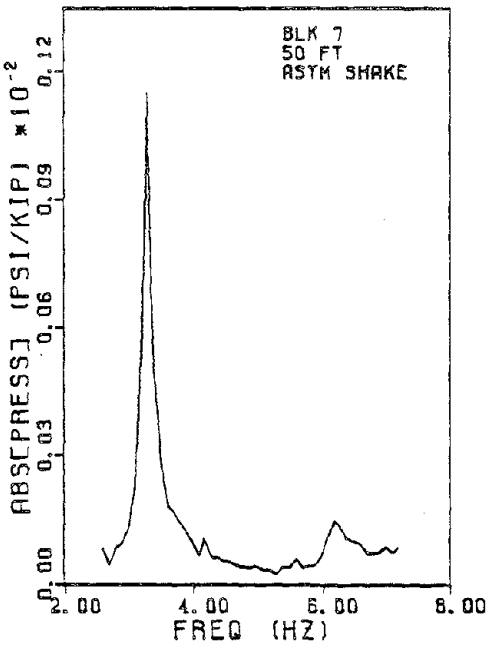
BLK 7
50 FT
ASTM SHAKE
ABS[PRESS] (PSI/KIP) *10^-2
0.00
0.03
0.06
0.09
0.12
2.00
4.00
6.00
8.00
FREQ (HZ)

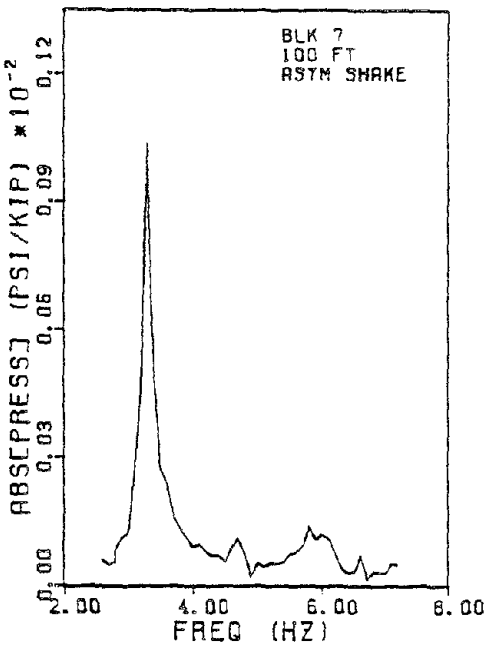
BLK 7
100 FT
ASTM SHAKE
ABS[PRESS] (PSI/KIP) *10^-2
0.00
0.03
0.06
0.09
0.12
2.00
4.00
6.00
8.00
FREQ (HZ)

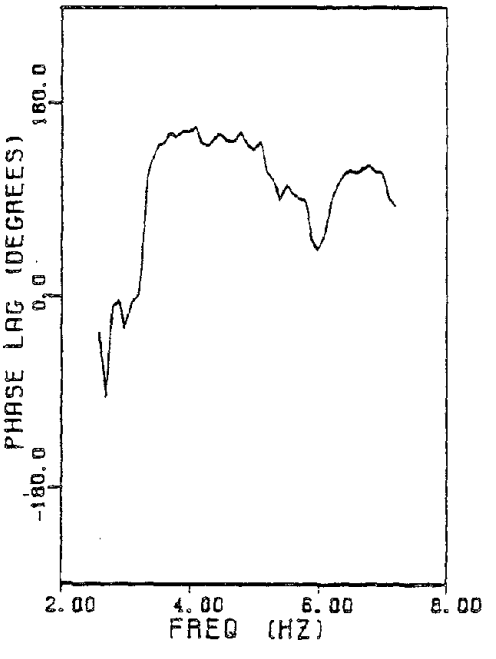
PHASE LAG (DEGREES)
180.0
0.0
-180.0
2.00
4.00
6.00
8.00
FREQ (HZ)

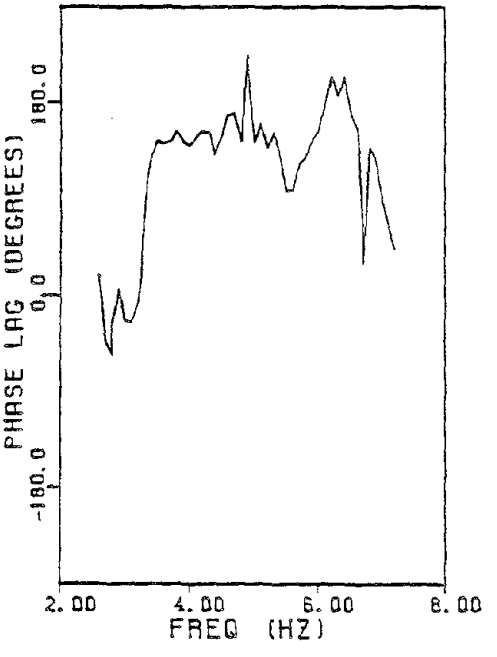
PHASE LAG (DEGREES)
180.0
0.0
-180.0
2.00
4.00
6.00
8.00
FREQ (HZ)

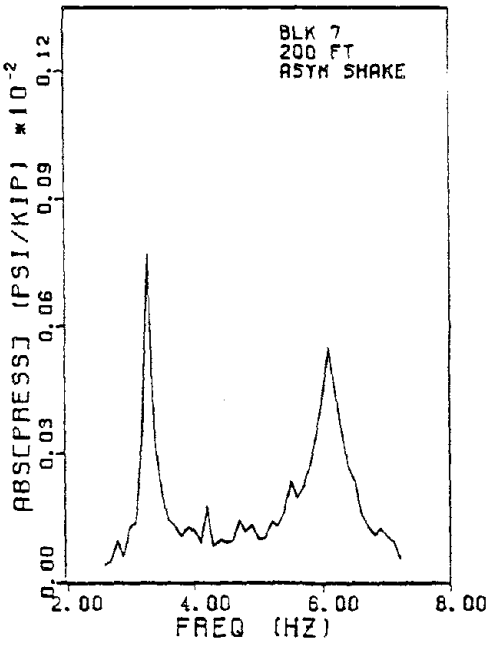
BLK 7
200 FT
ASYM SHAKE
ABS[PRESS] [PSI/KIP] *10^-2
0.00
0.03
0.06
0.09
0.12
2.00
4.00
6.00
8.00
FREQ (HZ)

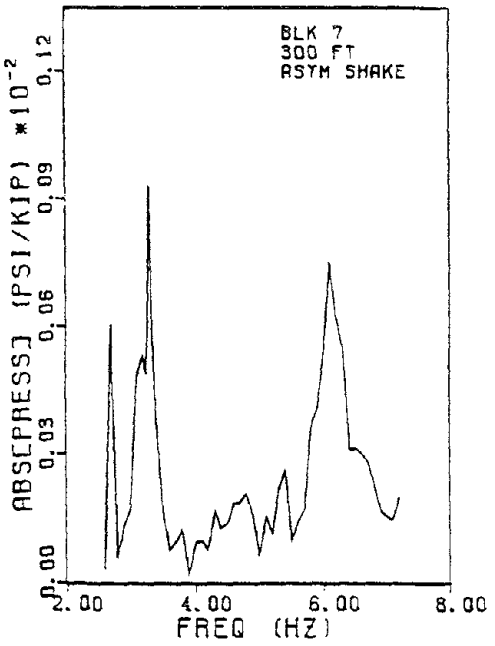
BLK 7
300 FT
ASYM SHAKE
ABS[PRESS] [PSI/KIP] *10^-2
0.00
0.03
0.06
0.09
0.12
2.00
4.00
6.00
8.00
FREQ (HZ)

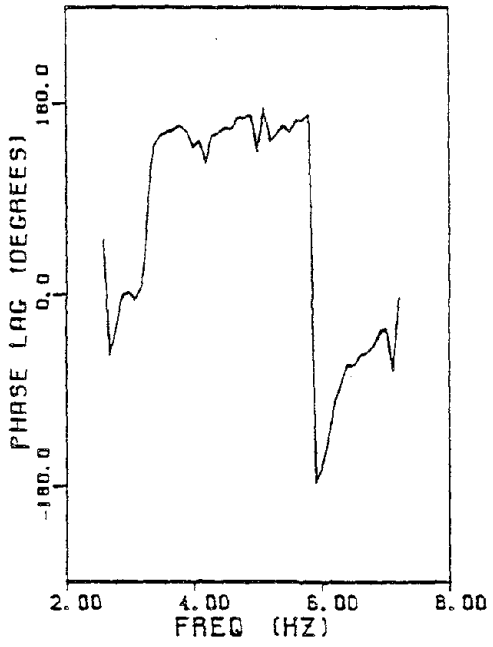
PHASE LAG (DEGREES)
180.0
0.0
-180.0
2.00
4.00
6.00
8.00
FREQ (HZ)

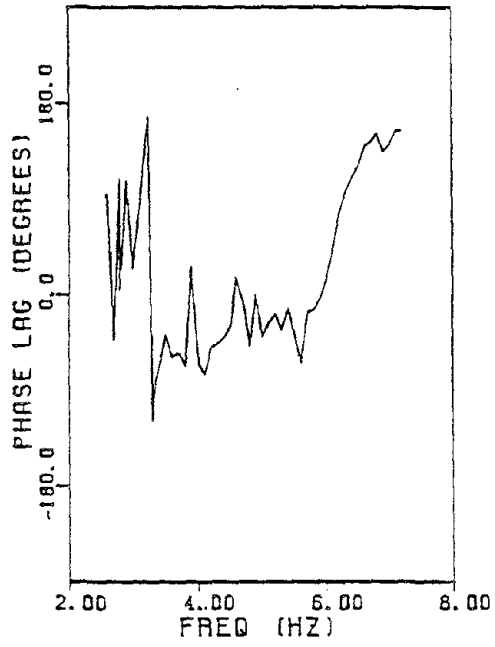
PHASE LAG (DEGREES)
180.0
0.0
-180.0
2.00
4.00
6.00
8.00
FREQ (HZ)

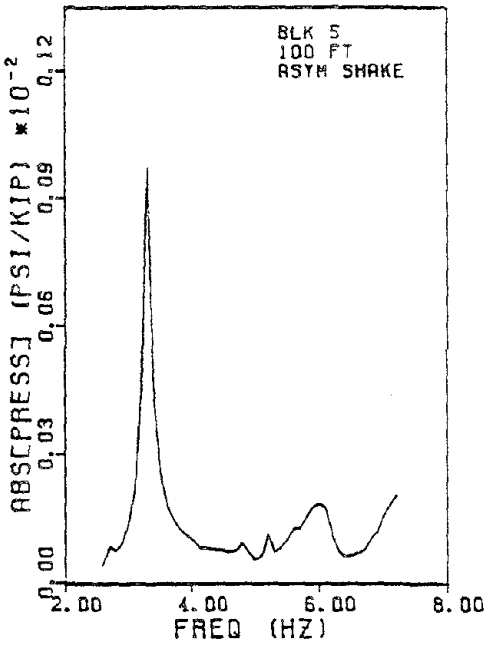
BLK 5
100 FT
ASYM SHAKE
ABSCPRESS] (PSI/KIP) *10^-2
0.00
0.03
0.06
0.09
0.12
2.00
4.00
6.00
8.00
FREQ (HZ)

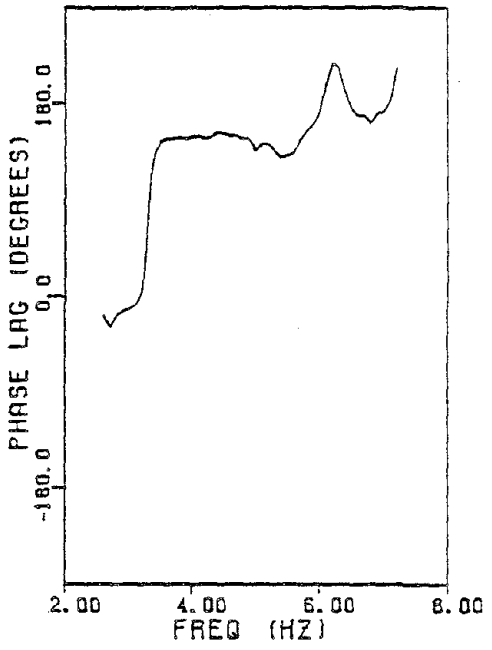
PHASE LAG (DEGREES)
180.0
0.0
-180.0
2.00
4.00
6.00
8.00
FREQ (HZ)

CALIFORNIA INSTITUTE OF TECHNOLOGY

Reports Published

by

Earthquake Engineering Research Laboratory*
Dynamic Laboratory
Disaster Research Center

Note: Numbers in parenthesis are Accession Numbers assigned by the National Technical Information Service; these reports may be ordered from the National Technical Information Service, 5285 Port Royal Road, Springfield, Virginia, 22161. Accession Numbers should be quoted on orders for reports (PB ---- ---). Reports without this information either have not been submitted to NTIS or the information was not available at the time of printing. An N/A in parenthesis indicates that the report is no longer available at Caltech.

1. Alford, J.L., G.W. Housner and R.R. Martel, "Spectrum Analysis of Strong-Motion Earthquake," 1951. (Revised August 1964). (N/A)

2. Housner, G.W., "Intensity of Ground Motion During Strong Earthquakes," 1952. (N/A)

3. Hudson, D.E., J.L. Alford and G.W. Housner, "Response of a Structure to an Explosive Generated Ground Shock," 1952. (N/A)

4. Housner, G.W., "Analysis of the Taft Accelerogram of the Earthquake of 21 July 1952." (N/A)

5. Housner, G.W., "A Dislocation Theory of Earthquakes," 1953. (N/A)

6. Caughey, T.K., and D.E. Hudson, "An Electric Analog Type Response Spectrum," 1954. (N/A)

7. Hudson, D.E., and G.W. Housner, "Vibration Tests of a Steel-Frame Building," 1954. (N/A)

8. Housner, G.W., "Earthquake Pressures on Fluid Containers," 1954. (N/A)

9. Hudson, D.E., "The Wilmot Survey Type Strong-Motion Earthquake Recorder," 1958. (N/A)

10. Hudson, D.E., and W.D. Iwan, "The Wilmot Survey Type Strong-Motion Earthquake Recorder, Part II," 1960. (N/A)

---

* To order directly by phone the number is 703-487-4650.

11. Caughey, T.K., D.E. Hudson, and R.V. Powell, "The CIT Mark II Electric Analog Type Response Spectrum Analyzer for Earthquake Excitation Studies," 1960. (N/A)

12. Keightley, W.O., G.W. Housner and D.E. Hudson, "Vibration Tests of the Encino Dam Intake Tower," 1961. (N/A)

13. Merchant, Howard Carl, "Mode Superposition Methods Applied to Linear Mechanical Systems Under Earthquake Type Excitation," 1961. (N/A)

14. Iwan, Wilfred D., "The Dynamic Response of Bilinear Hysteretic Systems," 1961. (N/A)

15. Hudson, D.E., "A New Vibration Exciter for Dynamic Test of Full-Scale Structures," 1961. (N/A)

16. Hudson, D.E., "Synchronized Vibration Generators for Dynamic Tests of Full-Scale Structures," 1962. (N/A)

17. Jennings, Paul C., "Velocity Spectra of the Mexican Earthquakes of 11 May and 19 May 1962," 1962. (N/A)

18. Jennings, Paul C., "Response of Simple Yielding Structures to Earthquake Excitation," 1963. (N/A)

19. Keightley, Willard O., "Vibration Tests of Structures," 1963. (N/A)

20. Caughey, T.K., and M.E.J. O'Kelly, "General Theory of Vibration of Damped Linear Dynamic Systems," 1963. (N/A)

21. O'Kelly, M.E.J., "Vibration of Viscously Damped Linear Dynamic Systems," 1964. (N/A)

22. Nielsen, N. Norby, "Dynamic Response of Miltistory Buildings," 1964. (N/A)

23. Tso, Wai Keung, "Dynamics of Thin-Walled Beams of Open Section," 1964. (N/A)

24. Keightley, Willard O., "A Dynamic Investigation of Bouquet Canyon Dam," 1964. (N/A)

25. Malhotra, R.K., "Free and Forced Oscillations of a Class of Self-Excited Oscillators," 1964.

26. Hanson, Robert D., "Post-Elastic Response of Mild Steel Structures," 1965.

27. Masri, Sami F., "Analytical and Experimental Studies of Impact Dampers," 1965.

28. Hanson, Robert D., "Static and Dynamic Tests of a Full-Scale Steel-Frame Structures," 1965.

29. Cronin, Donald L., "Response of Linear, Viscous Damped Systems to Excitations Having Time-Varying Frequecy," 1965.

30. Hu, Paul Yu-fei, "Analytical and Experimental Studies of Random Vibration," 1965.

31. Crede, Charles E., "Research on Failure of Equipment when Subject to Vibration," 1965.

32. Lutes, Loren D., "Numerical Response Characteristics of a Uniform Beam Carrying One Discrete Load," 1965. (N/A)

33. Rocke, Richard D., "Transmission Matrices and Lumped Parameter Models for Continuous Systems," 1966. (N/A)

34. Brady, Arthur Gerald, "Studies of Response to Earthquake Ground Motion," 1966. (N/A)

35. Atkinson, John D., "Spectral Density of First Order Piecewise Linear Systems Excited by White Noise," 1967. (N/A)

36. Dickerson, John R., "Stability of Parametrically Excited Differential Equations," 1967. (N/A)

37. Giberson, Melbourne F., "The Response of Nonlinear Multi-Story Structures Subjected to Earthquake Excitation," 1967. (N/A)

38. Hallanger, Lawrence W., "The Dynamic Stability of an Unbalanced Mass Exciter," 1967.

39. Husid, Raul, "Gravity Effects on the Earthquake Response of Yielding Structures," 1967. (N/A)

40. Kuroiwa, Julio H., "Vibration Test of a Multistory Building," 1967. (N/A)

41. Lutes, Loren Daniel, "Stationary Random Response of Bilinear Hysteretic Systems," 1967.

42. Nigam, Navin C., "Inelastic Interactions in the Dynamic Response of Structures," 1967.

43. Nigam, Navin C. and Paul C. Jennings, "Digital Calculation of Response Spectra from Strong-Motion Earthquake Records," 1968.

44. Spencer, Richard A., "The Nonlinear Response of Some Multistory Reinforced and Prestressed Concrete Structures Subjected to Earthquake Excitation," 1968. (N/A)

45. Jennings, P.C., G.W. Housner and N.C. Tsai, "Simulated Earthquake Motions," 1968.

46. "Strong-Motion Instrumental Data on the Borrego Mountain Earthquake of 9 April 1968," (USGS and EERL Joint Report), 1968.

47. Peters, Rex B., "Strong Motion Accelerograph Evaluation," 1969.

48. Heitner, Kenneth L., "A Mathematical Model for Callculation of the Run-Up of Tsunamis," 1969.

49. Trifunac, Mihailo D., "Investigation of Strong Earthquake Ground Motion," 1969. (N/A)

50. Tsai, Nien Chien, "Influence of Local Geology on Earthquake Ground Motion," 1969. (N/A)

51. Trifunac, Mihailo D., "Wind and Microtremor Induced Vibrations of a Twenty-Two Steel Frame Building," EERL 70-01, 1970.

52. Yang, I-Min, "Stationary Random Response of Multidegree-of-Freedom Systems," DYNL-100, June 1970. (N/A)

53. Patula, Edward John, "Equivalent Differential Equations for Nonlinear Dynamic Systems," DYNL-101, June 1970.

54. Prelewicz, Daniel Adam, "Range of Validity of the Method of Averaging," DYNL-102, 1970.

55 Trifunac, M.D., "On the Statistics and Possible Triggering Mechanism of Earthquakes in Southern California," EERL 70-03, July 1970.

56. Heitner, Kenneth Leon, "Additional Investigations on a Mathematical Model for Calculation of Run-Up of Tsunamis," July 1970.

57. Trifunac, Mihailo D., "Ambient Vibration Tests of a Thirty-Nine Story Steel Frame Building," EERL 70-02, July 1970.

58. Trifunac, Mihailo D. and D.E. Hudson, "Laboratory Evaluations and Instrument Corrections of Strong-Motion Accelerographs," EERL 70-04, August 1970. (N/A)

59. Trifunac, Mihailo D., "Response Envelope Spectrum and Interpretation of Strong Earthquake Groun Motion," EERL 70-06, August 1970.

60. Keightley, W.O., "A Strong-Motion Accelerograph Array with Telephone Line Interconnections," EERL 70-05, September 1970.

61. Trifunac, Mihailo D., "Low Frequency Digitization Errors and a New Method for Zero Baseline Correction of Strong-Motion Accelerograms," EERL 70-07, September 1970.

62. Vijayaraghavan, A., "Free and Forced Oscillations in a Class of Piecewise-Linear Dynamic Systems," DYNL-103, January 1971.

63. Jennings, Paul C., R.B. Mathiesen and J. Brent Hoerner, "Forced Vibrations of a 22-Story Steel Frame Building," EERL 71-01, February 1971. (N/A) (PB 205 161)

64. Jennings, Paul C., "Engineering Features of the San Fernando Earthquake of February 9, 1971," EERL 71-02, June 1971. (PB 202 550)

65. Bielak, Jacobo, "Earthquake Response of Building-Foundation Systems," EERL 71-04, June 1971. (N/A) (PB 205 305)

66. Adu, Randolph Ademola, "Response and Failure of Structures Under Stationary Random Excitation," EERL 71-03, June 1971. (N/A) (PB 205 304)

67. Skattum, Knut Sverre, "Dynamic Analysis of Coupled Shear Walls and Sandwich Beams," EERL 71-06, June 1971. (N/A) (PB 205 267)

68. Hoerner, John Brent, "Model Coupling and Earthquake Response of Tall Buildings," EERL 71-07, June 1971. (N/A) (PB 207 635)

69. Stahl, Karl John, "Dynamic Response of Circular Plates Subjected to Moving Massive Loads," DYNL-104, June 1971. (N/A)

70. Trifunac, M.D., F.E. Udwadia and A.G. Brady, "High Frequency Errors and Instrument Corrections of Strong-Motion Accelerograms," EERL 71-05, 1971. (PB 205 369)

71. Furuike, D.M., "Dynamic Response of Hysteretic Systems With Application to a System Containing Limited Slip," DYNL-105, September 1971. (N/A)

72. Hudson, D.E. (Editor), "Strong-Motion Instrumental Data on the San Fernando Earthquake of February 9, 1971," (Seismological Field Survey, NOAA, C.I.T. Joint Report), September 1971. (PB 204 198)

73. Jennings, Paul C. and Jacobo Bielak, "Dynamics of Building-Soil Interaction," EERL 72-01, April 1972. (PB 209 666)

74. Kim, Byung-Koo, "Piesewise Linear Dynamic Systems with Time Delays," DYNL-106, April 1972.

75. Viano, David Charles, "Wave Propagation in a Symmetrically Layered Elastic Plate," DYNL-107, May 1972.

76. Whitney, Albert W., "On Insurance Settlements Incident to the 1906 San Francisco Fire," DRC 72-01, August 1972. (PB 213 256)

77. Udwadia, F.E., "Investigation of Earthquake and Microtremor Ground Motions," EERL 72-02, September 1972. (PB 212 853)

78. Wood, John H., "Analysis of the Earthquake Response of a Nine-Story Steel Frame Building During the San Fernando Earthquake," EERL 72-04, October 1972. (PB 215 823)

79. Jennings, Paul C., "Rapid Calculation of Selected Fourier Spectrum Ordinates," EERL 72-05, November 1972.

80. "Research Papers Submitted to Fifth World Conference on Earthquake Engineering, Rome, Italy, 25-29 June 1973," EERL 73-02, March 1973. (PB 220 431)

81. Udwadia, F.E., and M.D. Trifunac, "The Fourier Transform, Response Spectra and Their Relationship Through the Statistics of Oscillator Response," EERL 73-01, April 1973. (PB 220 458)

82. Housner, George W., "Earthquake-Resistant Design of High-Rise Buildings," DRC 73-01, July 1973. (N/A)

83. "Earthquake and Insurance," Earthquake Research Affiliates Conference, 2-3 April, 1973, DRC 73-02, July 1973. (PB 223 033)

84. Wood, John H., "Earthquake-Induced Soil Pressures on Structures," EERL 73-05, August 1973. (N/A)

85. Crouse, Charles B., "Engineering Studies of the San Fernando Earthquake," EERL 73-04, March 1973. (N/A)

86. Irvine, H.Max, "The Veracruz Earthquake of 28 August 1973," EERL 73-06, October 1973.

87. Iemura, H. and P.C. Jennings, "Hysteretic Response of a Nine-Story Reinforced Concrete Building During the San Fernando Earthquake," EERL 73-07, October 1973.

88. Trifunac, M.D. and V. Lee, "Routine Computer Processing of Strong-Motion Accelerograms," EERL 73-03, October 1973. (N/A) (PB 226 047/AS)

89. Moeller, Thomas Lee, "The Dynamics of a Spinning Elastic Disk with Massive Load," DYNL 73-01, October 1973.

90. Blevins, Robert D., "Flow Induced Vibration of Bluff Structures," DYNL 74-01, February 1974.

91. Irvine, H. Max, "Studies in the Statics and Dynamics of Simple Cable Systems," DYNL-108, January 1974.

92. Jephcott, D.K. and D.E. Hudson, "The Performance of Public School Plants During the San Fernando Earthquake," EERL 74-01, September 1974. (PB 240 000/AS)

93. Wong, Hung Leung, "Dynamic Soil-Structure Interaction," EERL 75-01, May 1975. (N/A) (PB 247 233/AS)

94. Foutch, D.A., G.W. Housner, and P.C. Jennings, "Dynamic Responses of Six Multistory Buildings During the San Fernando Earthquake," EERL 75-02, October 1975. (PB 248 144/AS)

95. Miller, Richard Keith, "The Steady-State Response of Multidegree-of-Freedom Systems with a Spatially Localized Nonlinearity," EERL 75-03, October 1975. (PB 252 459/AS)

96. Abdel-Ghaffar, Ahmed Mansour, "Dynamic Analyses of Suspension Bridge Structures," EERL 76-01, May 1976. (PB 258 744/AS)

97. Foutch, Douglas A., "A Study of the Vibrational Characteristics of Two Multistory Buildings," EERL 76-03, September 1976. (PB 260 874/AS)

98. "Strong Motion Earthquake Accelerograms Index Volume," Earthquake Engineering Research Laboratory, EERL 76-02, August 1976. (PB 260 929/AS)

99. Spanos, P-T.D., "Linearization Techniques for Non-Linear Dynamical Systems," EERL 76-04, September 1976. (PB 266 083/AS)

100. Edwards, Dean Barton, "Time Domain Analysis of Switching Regulators," DYNL 77-01, March 1977.

101. Abdel-Ghaffar, Ahmed Mansour, "Studies of the Effect of Differential Motions of Two Foundations upon the Response of the Superstructure of a Bridge," EERL 77-02, January 1977. (PB 271 095/AS)

102. Gates, Nathan C., "The Earthquake Response of Deteriorating Systems," EERL 77-03, March 1977. (PB 271 090/AS)

103. Daly, W., W. Judd and R. Meade, "Evaluation of Seismicity at U.S. Reservoirs," USCOLD, Committee on Earthquakes, May 1977. (PB 270 036/AS)

104. Abdel-Ghaffer, A.M. and G.W. Housner, "An Analysis of the Dynamic Characteristics of a Suspension Bridge by Ambient Vibration Measurements," EERL 77-01, January 1977. (PB 275 063/AS)

105. Housner, G.W. and P.C. Jennings, "Earthquake Design Criteria for Structures," EERL 77-06, November 1977. (PB 276 502/AS)

106. Morrison, P., R. Maley, G. Brady, R. Porcella, "Earthquake Recordings on or Near Dams," USCOLD, Committee on Earthquakes, November 1977. (PB 285 867/AS)

107. Abdel-Ghaffar, A.M., "Engineering Data and Analyses of the Whittier, California Earthquake of January 1, 1976," EERL 77-05, November 1977. (PB 283 750/AS)

108. Beck, James L., "Determining Models of Structures from Earthquake Records," EERL 78-01, June 1978. (PB 288 806/AS)

109. Psycharis, Ioannis, "The Salonica(Thessaloniki) Earthquake of June 20, 1978," EERL 78-03, October 1978. (PB 290 120/AS)

110. Abdel-Ghaffar, A.M. and R.F. Scott, "An Investigation of the Dynamic Characteristics of an Earth Dam," EERL 78-02, August 1978. (PB 288 878/AS)

111. Mason, Alfred B., Jr., "Some Observations on the Random Response of Linear and Nonlinear Dynamical Systems," EERL 79-01, January 1979. (PB 290 808/AS)

112. Helmberger, D.V. and P.C. Jennings (Organizers), "Strong Ground Motion: N.S.F. Seminar-Workshop," SL-EERL 79-02, February 1978.

113. Lee, David M., Paul C. Jennings and George W. Housner, "A Selection of Important Strong Motion Earthquake Records," EERL 80-01, January 1980. (PB 80 169196)

114. McVerry, Graeme H., "Frequency Domain Identification of Structural Models from Earthquake Records," EERL 79-02, October 1979. (PB-80-194301)

115. Abdel-Ghaffar A.M., R.F.Scott and M.J.Craig, "Full-Scall Experimental Investigation of a Modern Earth Dam," EERL 80-02, February 1980. (PB-81-123788)

116. Rutenberg, Avigdor, Paul C. Jennings and George W. Housner, "The Response of Veterans Hospital Building 41 in the San Fernando Earthquake," EERL 80-03, May 1980. (PB-82-201377)

117. Haroun, Medhat Ahmed, "Dynamic Analyses of Liquid Storage Tanks," EERL 80-04, February 1980. (PB-81-123275)

118. Liu, Wing Kam, "Development of Finite Element Procedures for Fluid-Structure Interaction," EERL 80-06, August 1980. (PB 184078)

119. Yoder, Paul Jerome, "A Strain-Space Plasticity Theory and Numerical Implementation," EERL 80-07, August 1980. (PB-82-201682)

120. Krousgrill, Charles Morton, Jr., "A Linearization Technique for the Dynamic Response of Nonlinear Continua," EERL 80-08, September 1980. (PB-82-201823)

121. Cohen, Martin, "Silent Boundary Methods for Transient Wave Analysis," EERL 80-09, September 1980. (PB-82-201831)

122. Hall, Shawn A., "Vortex-Induced Vibrations of Structures," EERL 81-01, January 1981. (PB-82-201849)

123. Psycharis, Ioannis N., "Dynamic Behavior of Rocking Structures Allowed to Uplift," EERL 81-02, August 1981. (PB-82-212945)

124. Shih, Choon-Foo, "Failure of Liquid Storage Tanks Due to Earthquake Excitation," EERL 81-04, May 1981. (PB-82-215013)

125. Lin, Albert Niu, "Experimental Observations of the Effect of Foundation Embedment on Structural Response," EERL 82-01, May 1982. (PB-84-163252)

126. Botelho, Dirceau L.R., "An Empirical Model for Vortex-Induced Vibrations," EERL 82-02, August 1982. (PB-84-161157)

127. Ortiz, L. Alexander, "Dynamic Centrifuge Testing of Cantilever Retaining Walls," SML 82-02, August 1982. (PB-84-162312)

128. Iwan, W.D., Editor, "Proceedings of the U.S. National Workshop on Strong-Motion Earthquake Instrumentation, April 12-14, 1981, Santa Barbara, California," California Institute of Technology, Pasadena, California, 1981.

129. Rashed, Ahmed, "Dynamic Analysis of Fluid-Structure Systems," EERL 82-03, July 1982. (PB-84-162916)

130. National Academy Press, "Earthquake Engineering Research-1982."

131. National Academy Press, "Earthquake Engineering Research-1982, Overview and Recommendations."

132. Jain, Sudhir Kumar, "Analytical Models for the Dynamics of Buildings," EERL 83-02, May 1983. (PB-84-161009)

133. Huang, Moh-Jiann, "Investigation of Local Geology Effects on Strong Earthquake Ground Motions," EERL 83-03, July 1983. (PB-84-161488)

134. Mcverry, G.H. and J.L. Beck, "Structural Identification of JPL Building 180 Using Optimally Synchronized Earthquake Records." EERL 83-01, August 1983. (PB-84-162833)

135. Bardet, J.P., "Application of Plasticity Theory to Soil Behavior: A New Sand Model," SML 83-01, September 1983. (PB-84-162304)

136. Wilson, John C., "Analysis of the Observed Earthquake Response of a Multiple Span Bridge," EERL 84-01, May 1984. (PB-85-240505/AS)

137. Hushmand, Behnam, "Experimental Studies of Dynamic Response of Foundations," SML 83-02, November 1983. (PB-86-115383/A)

138. Cifuentes, Arturo O., "System Identification of Hysteretic Structures," EERL 84-04, 1984. (PB-240489/AS14)

139. Smith, Kenneth Scott, "Stochastic Analysis of the Seismic Response of Secondary Systems," EERL 85-01, November 1984. (PB-85-240497/AS)

140. Maragakis, Emmanuel, "A Model for the Rigid Body Motions of Skew Bridges," EERL 85-02, December 1984. (PB-85-248433/AS)

141. Jeong, Garrett Duane, "Cumulative Damage of Structures Subjected to Response Spectrum Consistent Random Process," EERL 85-03, January 1985. (PB-86-100809)

142. Chelvakumar, Kasivisvanathan, "A Simple Strain-Space Plasticity Model for Clays," EERL 85-05, 1985. PB-

143. Pak, Ronald Y.S., "Dynamic Response of a Partially Embedded Bar Under Transverse Excitations," EERL 85-04, May 1985. PB-

144. Tan, Thiam-Soon, "Two Phase Soil Study: A. Finite Strain Consolidation, B. Centrifuge Scaling Considerations," SML 85-01, August 1985. PB-

145. Iwan, Wilfred D., Michael A. Moser and Chia-Yen Peng, "Strong-Motion Earthquake Measurement Using a Digital Accelerograph," EERL 84-02, April 1984.

146. Beck, R.T. and J.L. Beck, "Comparison Between Transfer Function and Modal Minimization Methods for System Identification," EERL 85-06, April 1984.

147. Jones, Nicholas Patrick, "Flow-Induced Vibration of Long Structures," DYNL 86-01, May 1986. PB-

148. Peek, Ralf, "Analysis of Unanchored Liquid Storage Tanks Under Seismic Loads," EERL 86-01, April 1986. PB-

149. Paparizos, Leonidas G., "Some Observations on the Random Response of Hysteretic Systems," EERL 86-02. PB-

150. Moser, Michael Anthony, "The Response of Stick-Slip Systems to Random Seismic Excitation," EERL 86-03, September 1986. PB-

151. Burrige, Paul Brian, "Failure of Slopes," SML 87-01, March 1987. PB-

152. Jayakumar, Paramsothy, "Modeling and Identification in Structural Dynamics," EERL 87-01, May 1987. PB-

Strong-Motion Earthquake Accelerograms
Digitized and Plotted Data

Uncorrected Accelerograms

Volume I

Part	Report No.	NTIS Accession No.
A	EERL 70-20	PB 287 847
B	EERL 70-21	PB 196 823
C	EERL 71-20	PB 204 364
D	EERL 71-21	PB 208 529
E	EERL 71-22	PB 209 749
F	EERL 71-23	PB 210 619
G	EERL 72-20	PB 211 357
H	EERL 72-21	PB 211 781
I	EERL 72-22	PB 213 422
J	EERL 72-23	PB 213 423
K	EERL 72-24	PB 213 424
L	EERL 72-25	PB 215 639
M	EERL 72-26	PB 220 554
N	EERL 72-27	PB 223 023
O	EERL 73-20	PB 222 417
P	EERL 73-21	PB 227 481/AS
Q	EERL 73-22	PB 232 315/AS
R	EERL 73-23	PB 239 585/AS
S	EERL 73-24	PB 241 551/AS
T	EERL 73-25	PB 241 943/AS
U	EERL 73-26	PB 242 262/AS
V	EERL 73-27	PB 243 483/AS
W	EERL 73-28	PB 243 497/AS
X	EERL 73-29	PB 243 594/AS
Y	EERL 73-30	PB 242 947/AS

Strong-Motion Earthquake Accelerograms
Digitized and Plotted Data

Corrected Accelerograms and Integrated
Ground Velocity and Displacement Curves

Volume II

Part	Report No.	NTIS Accession No.
A	EERL 71-50	PB 208 283
B	EERL 72-50	PB 220 161
C	EERL 72-51	PB 220 162
D	EERL 72-52	PB 220 836
E	EERL 73-50	PB 223 024
F	EERL 73-51	PB 224 977/9AS
G	EERL 73-52	PB 229 239/AS
H	EERL 74-50	PB 231 225/AS
I	EERL 74-51	PB 232 316/AS
J,K	EERL 74-52	PB 233 257/AS
L,M	EERL 74-53	PB 237 174/AS
N	EERL 74-54	PB 236 399/AS
O,P	EERL 74-55	PB 239 586/AS
Q,R	EERL 74-56	PB 239 587/AS
S	EERL 74-57	PB 241 552/AS
T	EERL 75-50	PB 242 433/AS
U	EERL 75-51	PB 242 949/AS
V	EERL 75-52	PB 242 948/AS
W,Y	EERL 75-53	PB 243 719

Analyses of Strong-Motion Earthquake Accelerograms
Response Spectra

Volume III

Part	Report No.	NTIS Accession No.
A	EERL 72-80	PB 212 602
B	EERL 73-80	PB 221 256
C	EERL 73-81	PB 223 025
D	EERL 73-82	PB 227 469/AS
E	EERL 73-83	PB 227 470/AS
F	EERL 73-84	PB 227 471/AS
G	EERL 73-85	PB 231 223/AS
H	EERL 74-80	PB 231 319/AS
I	EERL 74-81	PB 232 326/AS
J,K,L	EERL 74-82	PB 236 110/AS
M,N	EERL 74-83	PB 236 400/AS
O,P	EERL 74-84	PB 238 102/AS
Q,R	EERL 74-85	PB 240 688/AS
S	EERL 74-86	PB 241 553/AS
T	EERL 75-80	PB 243 698/AS
U	EERL 75-81	PB 242 950/AS
V	EERL 75-82	PB 242 951/AS
W,Y	EERL 75-83	PB 243 492/AS

Analyses of Strong-Motion Earthquake Accelerograms
Fourier Amplitude Spectra

Volume IV

Part	Report No.	NTIS Accession No.
A	EERL 72-100	PB 212 603
B	EERL 73-100	PB 220 837
C	EERL 73-101	PB 222 514
D	EERL 73-102	PB 222 969/AS
E	EERL 73-103	PB 229 240/AS
F	EERL 73-104	PB 229 241/AS
G	EERL 73-105	PB 231 224/AS
H	EERL 74-100	PB 232 327/AS
I	EERL 74-101	PB 232 328/AS
J,K,L,M	EERL 74-102	PB 236 111/AS
N,O,P	EERL 74-103	PB 238 447/AS
Q,R,S	EERL 74-104	PB 241 554/AS
T,U	EERL 75-100	PB 243 493/AS
V,W,Y	EERL 75-101	PB 243 494/AS
Index Volume	EERL 76-02	PB 260 929/AS